



**Multi-scale model analysis of Arctic
surface-atmosphere exchange of
climate-active trace gases**

Johannes G.M. Barten

Propositions

1. Process-based representations of the ozone dry deposition process should be included in atmospheric chemistry and transport models.
(this thesis)
2. Observations of trace gases and aerosols should be included when investigating Arctic warm air intrusions.
(this thesis)
3. Arctic climate change outpaces Arctic climate science.
4. The Arctic Council's decision making inadequately represents its stakeholders.
5. The use of heavy fuel oil in Arctic shipping must be banned immediately.
6. Funding agencies should prioritize exploitation of existing datasets and models over investments in new field campaigns.
7. Flexible working places are not viable at Universities.

Propositions belonging to the thesis, entitled

Multi-scale model analysis of Arctic surface–atmosphere exchange of climate–active trace gases

Johannes Gerardus Martinus Barten

Wageningen, 26 April 2024

Multi-scale model analysis of Arctic surface-atmosphere exchange of climate-active trace gases

Johannes G. M. Barten

Thesis committee

Promotor

Prof. Dr M.C. Krol
Professor of Air Quality and Atmospheric Chemistry
Wageningen University & Research

Co-promotors

Dr L.N. Ganzeveld
Assistant Professor, Meteorology and Air Quality
Wageningen University & Research

Dr G.-J. Steeneveld
Associate Professor, Meteorology and Air Quality
Wageningen University & Research

Other members

Prof. Dr M.J. van der Ploeg, Wageningen University & Research
Prof. Dr S.R. Arnold, University of Leeds, United Kingdom
Prof. Dr R. Bintanja, Royal Netherlands Meteorological Institute (KNMI), De Bilt
Dr J. Stefels, University of Groningen

This research was conducted under the auspices of the Graduate School of Socio-Economic and Natural Sciences of the Environment (SENSE)

Multi-scale model analysis of Arctic surface-atmosphere exchange of climate-active trace gases

Johannes G. M. Barten

Thesis

submitted in fulfilment of the requirements for the degree of doctor
at Wageningen University

by the authority of the Rector Magnificus

Prof. Dr C. Kroeze,

in the presence of the

Thesis Committee appointed by the Academic Board

to be defended in public

on Friday 26 April 2024

at 11 a.m. in the Omnia Auditorium.

Johannes G. M. Barten

Multi-scale model analysis of Arctic surface-atmosphere exchange
of climate-active trace gases,
xiv + 186 pages.

PhD thesis, Wageningen University, Wageningen, the Netherlands (2024)
With references, with summary in English

ISBN 978-94-6447-955-3

DOI <https://doi.org/10.18174/640900>

Summary

The Arctic near-surface atmosphere is warming at nearly four times the rate of the global average. Climate models tend to underestimate the increase in Arctic air temperatures, partially due to a lack of understanding of the myriad of underlying physical and biogeochemical processes and their feedbacks. Nevertheless, the observed increase in Arctic atmospheric and oceanic temperatures resulted in a strong decrease in Arctic sea ice cover, which is expected to continue in future climate. The opening of the Arctic ocean through disappearing sea ice is projected to result in substantial changes in ocean-sea ice-atmosphere exchange of momentum, heat and moisture, as well as climate-active trace gases such as carbon dioxide (CO_2), methane (CH_4) and ozone (O_3). This results in changes in atmospheric concentrations of climate-active trace gases, with uncertain feedbacks to global warming. At the same time, the expected increase in local emissions of trace gases and air pollutants, by developing industry and shipping, poses an additional burden on the Arctic environment. The Arctic atmosphere, which was previously often considered pristine, because of the lack of local sources of air pollutants, faces significant changes in the coming decades.

Atmospheric chemistry and transport models show many deficiencies in accurately representing observed concentrations of climate-active trace gases in the Arctic troposphere. Fundamental processes controlling the burden of trace gases in the Arctic troposphere are often represented in a simplified manner. Additionally, very few long-term observational monitoring sites are present in the Arctic, which challenges evaluation and further development of these models. This thesis introduces a comprehensive approach, using novel observations and state-of-the-art modelling techniques, to advance understanding of local and large-scale processes controlling trace gases in the Arctic atmosphere. A methodology is applied that integrates to a maximum extent Arctic atmospheric observations with process-based model experiments. A hierarchy of coupled meteorological-chemical modelling systems allows for upscaling of observed and simulated conditions at the measurement scale ($\sim 10\text{--}1000\text{ m}$) to the representative footprint of airborne observations ($\sim 1\text{--}10\text{ km}$) and the grid resolution of global-scale chemistry-climate models ($> 100\text{ km}$) to assess the impact of long-term Arctic and global climate change. This thesis specifically focuses on, but does not limit itself to, the further development, evaluation

and application of process-based representations of surface exchange processes of climate-active trace gases in models.

Chapter 2 focuses on the O_3 dry deposition process to the Arctic ocean. Tropospheric O_3 acts as both a greenhouse gas and air pollutant, and plays an important role in atmospheric oxidation chemistry. The dry deposition process, i.e., the removal by the Earth's surface, is one of the main removal pathways of tropospheric O_3 . The O_3 dry deposition process to oceans in atmospheric chemistry and transport models is commonly represented by a so-called constant surface uptake resistance approach, not accounting for specific process-based drivers. However, observational studies have indicated the role of solubility, waterside turbulent transport and O_3 reacting with ocean water reactants such as iodide. The hypothesis is that O_3 deposition to the Arctic Ocean, having a relatively low O_3 reactivity, is overestimated in current models with consequences for the concentrations, lifetime and long-range transport of O_3 . To this end, 3D coupled meteorology-atmospheric chemistry model simulations are set up, with the simplified constant resistance approach and with a process-based approach, accounting for the before-mentioned environmental drivers. These model simulations are evaluated against surface O_3 observations at 25 pan-Arctic sites. Chapter 2 shows that the process-based approach leads to a better prediction of the magnitude and temporal variability in surface O_3 concentrations, compared to the simplified approach. The spatial variability in oceanic O_3 deposition mostly expresses the sensitivity of the O_3 -iodide reaction in the oceanic surface layer. The temporal variability in oceanic O_3 deposition results from differences in waterside turbulent transport, driven by changes in near-surface wind speed.

Chapter 3 focuses on the O_3 dry deposition process to the Arctic sea ice and snow surface, and on quantifying the O_3 budget in the Planetary Boundary Layer (PBL), i.e. the atmospheric layer in direct interaction with the surface. Chapter 3 aims to 1) arrive at an improved quantification of Arctic sea ice/snow O_3 deposition for various meteorological conditions and 2) to evaluate the contribution of dry deposition and other processes on the temporal variability of O_3 concentrations over sea ice. Here, novel year-round O_3 surface flux observations over the Arctic sea ice are used, as part of the Multidisciplinary drifting Observatory for the Study of Arctic Climate (MOSAIC) expedition (<https://mosaic-expedition.org/>). This most extensive Arctic measurement campaign in history featured the research vessel *Polarstern* docking itself into the Arctic sea ice, and passively drifting with the Arctic sea ice for a full year. The O_3 flux observations are complemented by supporting observations of a meteorological tower, and radiosondes to observe the vertical structure of the atmosphere. Additionally, model simulations with a 1D atmospheric chemistry and meteorological model are performed, following the track of the *Polarstern*. The observed O_3 deposition to the Arctic sea ice/snow surface is up to a factor of 10 smaller than currently used in models. In winter, the modelled PBL O_3 budget is governed by dry deposition at the surface, compensated for by downward turbulent transport of

O_3 towards the surface. Advection, i.e., long-range transport of O_3 , posed a substantial, mostly negative contribution to the modelled PBL O_3 budget in summer. Especially during episodes with low wind speeds and a shallow PBL, the O_3 dry deposition process is a significant sink of O_3 in the Arctic PBL.

From Chapter 3 it became clear that 1D models lack appropriate constraints during synoptically driven events, such as warm air intrusions, when large-scale processes dominate over local processes. Synoptic scale warm air intrusions transport anomalous amounts of heat and moisture to the Arctic. This enhanced transport can also bring elevated concentrations of aerosols and trace gases to the Central Arctic, where local emissions are generally absent. Furthermore, Arctic warm air intrusions are expected to increase in frequency and duration in future climate. **Chapter 4** focuses on the long-range transport of O_3 , and other trace gases, as a result of an Arctic warm air intrusion event observed during the MOSAiC campaign. This specific warm air intrusion contained episodes with a similar increase in temperature and humidity, but showing distinct differences in observed trace gas concentrations. A 3D coupled meteorology–atmospheric chemistry model is set up to simulate this warm air intrusion event, and to evaluate the sensitivity of 3D simulated meteorology and trace gas concentrations on horizontal model resolution and PBL parameterization scheme. The first episode of the warm air intrusion was dominated by southeasterly wind coming from the Eurasian mainland, with elevated concentrations of air pollutants. The second episode was dominated by southerly wind, coming from the Atlantic Ocean, with lower concentrations of air pollutants. These distinct differences in 3D simulated tracer footprints for the two warm air intrusion events were further supported by MOSAiC observations, and Lagrangian back-trajectory model simulations tracing the air back in time. Some improvement of model performance is found by increasing the horizontal model resolution (3 km versus 27 km) while results show no clear preference for PBL parameterization scheme. A comparison of simulated and observed atmospheric trace gas concentrations can help identify source regions and the transport pathway during Arctic warm air intrusions.

Chapters 2 to 4 mostly concerned local- and large-scale forcings on the composition of the Arctic atmosphere, on hourly to monthly timescales. **Chapter 5** connects the previously used observations and modelling techniques to timescales relevant for Arctic climate. This is considering the increasing environmental and socio-economic pressure on the Arctic region, with unknown consequences for the exchange of climate-active trace gases and composition of the Arctic atmosphere. Surface continuous and flask observations of eight trace gases were taken during the MOSAiC campaign. Additionally, these observations were compared with 18-years (2003–2021) of state-of-the-art reanalysis data from the Copernicus Atmosphere Monitoring Service (CAMS). The objectives of this chapter were two-fold: 1) to address the representativeness of reanalysis data with respect to local observations and 2) to put the year-round observations of MOSAiC in the context of inter-annual variability and extremes on the climate timescale.

Chapter 5 highlights strengths and weaknesses of chemical reanalysis products in representing the full seasonal cycle of in-situ observations. Finally, Chapter 5 presents the results of the first year-round CO₂ and CH₄ flux observations over the Arctic sea ice. Both for CO₂ (uptake) and CH₄ (emission), these new flux observations indicate among the lowest ice-atmosphere and ocean-atmosphere fluxes compared to previous literature.

Results of this thesis, as summarized in **Chapter 6**, contribute to understanding the surface exchange of climate-active trace gases, and further cycling in the Arctic atmosphere, using a combination of novel in-situ observations and a variety of state-of-the-art modelling techniques. Specifically, the thesis provides new insights on the role of local- versus long-range controls on the composition of the Arctic atmosphere, on a broad range of spatial and temporal scales. Chapter 6 also provides an outlook for future research related to observing and modelling the surface-exchange and, composition of the Arctic atmosphere. I specifically discuss flux observations over a heterogeneous ocean-sea ice-snow surface and coupled meteorology-atmospheric chemistry modelling in the Arctic PBL. Here, I argue that the way forward is an interdisciplinary approach focusing on detailed process understanding, combining observations and modelling tools at various spatial and temporal scales. To conclude, I argue that the complexity of the consequences of Arctic climate change require collaborative efforts in both the scientific and political domains. Fostering synergy between scientific disciplines, leveraging existing data, and embracing cooperative international initiatives are key to assess, and potentially mitigate the intricate challenges posed by Arctic climate change.

Samenvatting

De atmosfeer vlak bij het oppervlak van de Arctis warmt op bij bijna vier keer de snelheid van het wereldwijde gemiddelde. Klimaatmodellen hebben de neiging om de toename van de luchttemperatuur in de Arctis te onderschatten, deels vanwege een gebrek aan begrip van de talloze onderliggende fysieke en biogeochemische processen en hun terugkoppelingen. Desondanks heeft de waargenomen toename van de atmosferische en oceanische temperaturen in de Arctis geleid tot een sterke afname van de ijsbedekking in de Arctische oceaan, welke naar verwachting zal doorzetten gezien de geprojecteerde klimaatverandering. Het openen van de Arctische oceaan door verdwijnend zee-ijs wordt verwacht grote veranderingen te veroorzaken in de uitwisseling van momentum, warmte en vocht, evenals klimaat-actieve sporengassen zoals koolstofdioxide (CO_2), methaan (CH_4) en ozon (O_3), tussen oceaan, zee-ijs en atmosfeer. Dit leidt tot veranderingen in de atmosferische concentraties van klimaat-actieve sporengassen, met onzekere terugkoppelingen naar de geprojecteerde wereldwijde opwarming. Tegelijkertijd vormt de verwachte toename van lokale emissies van sporengassen en luchtverontreinigende stoffen door de ontwikkeling van industrie en scheepvaart een aanvullende belasting voor het Arctische milieu. De Arctische atmosfeer, die eerder vaak als zeer schoon werd beschouwd vanwege het ontbreken van lokale bronnen van luchtverontreiniging, staat de komende decennia voor aanzienlijke veranderingen.

Atmosferische chemie- en transportmodellen tonen veel tekortkomingen bij het nauwkeurig weergeven van waargenomen concentraties van klimaat-actieve sporengassen in de Arctische troposfeer. Fundamentele processen die de belasting van sporengassen in de Arctische troposfeer bepalen, worden vaak op een vereenvoudigde manier gerepresenteerd. Bovendien zijn er maar heel weinig langdurige observatiestations aanwezig in de Arctis, wat de evaluatie en verdere ontwikkeling van deze modellen bemoeilijkt. Deze scriptie introduceert een uitgebreide aanpak, met behulp van nieuwe waarnemingen en moderne modelleringstechnieken, om het begrip van lokale en grootschalige processen die sporengassen in de Arctische atmosfeer regelen, te bevorderen. Er wordt een methodologie toegepast die Arctisch atmosferische waarnemingen maximaal integreert met op proces gebaseerde modelexperimenten. Een hiërarchie van gekoppelde meteorologisch-chemische modelleringssystemen maakt het mogelijk om

waargenomen en gesimuleerde omstandigheden op de meetschaal ($\sim 10\text{--}1000\text{ m}$) op te schalen naar het representatieve bereik van luchtwaarnemingen ($\sim 1\text{--}10\text{ km}$) en de resolutie van mondiale chemie-klimaatmodellen ($> 100\text{ km}$) om de impact van langdurige Arctische en wereldwijde klimaatverandering te beoordelen. Deze scriptie richt zich specifiek op, maar beperkt zich niet tot, de verdere ontwikkeling, evaluatie en toepassing van op proces gebaseerde representaties van oppervlakte-uitwisselingsprocessen van klimaat-actieve sporengassen in modellen.

Hoofdstuk 2 richt zich op het proces van droge depositie van O_3 naar de Arctische oceaan. Troposferisch O_3 fungeert zowel als een broeikasgas als een luchtverontreinigende stof en speelt een belangrijke rol in de atmosferische oxidatiechemie. Het droge depositiesproces, d.w.z. de verwijdering door het aardoppervlak, is een van de belangrijkste verwijderingsroutes van troposferisch O_3 . Het droge depositiesproces van O_3 naar oceanen in atmosferische chemie- en transportmodellen wordt vaak voorgesteld door een zogenaamde constante oppervlakte-weerstandsbepaling, waarbij geen rekening wordt gehouden met specifieke op proces gebaseerde drijfveren. Observatiestudies hebben echter gewezen op de rol van oplosbaarheid, turbulent transport aan de waterspiegel en O_3 die reageert met reactanten zoals jodide in het oceaanwater. De hypothese is dat de depositie van O_3 naar de Arctische oceaan, met een relatief lage O_3 -reactiviteit, wordt overschat in huidige modellen met gevolgen voor de concentraties, levensduur en langeafstandstransport van O_3 . Hiertoe worden 3D-gekoppelde meteorologie-atmosferische chemiemodelsimulaties opgezet, met de vereenvoudigde constante weerstandsbepaling en met een op proces gebaseerde bepaling die rekening houdt met de eerder genoemde drijfveren. Deze modelsimulaties worden geëvalueerd aan de hand van oppervlakte- O_3 -waarnemingen op 25 Arctische locaties. Hoofdstuk 2 toont aan dat de op proces gebaseerde bepaling leidt tot een betere voorspelling van de hoogte en de temporele variabiliteit in oppervlakte- O_3 -concentraties in vergelijking met de vereenvoudigde bepaling. De ruimtelijke variabiliteit in de depositie van O_3 drukt voornamelijk de gevoeligheid van de O_3 -jodide-reactie in de oceanische oppervlaktelaag uit. De temporele variabiliteit in de depositie van O_3 is het gevolg van verschillen in turbulent transport aan de waterspiegel, veroorzaakt door veranderingen in de windsnelheid nabij het oppervlak.

Hoofdstuk 3 richt zich op het proces van droge deposities van O_3 naar het oppervlak van Arctisch zee-ijs en sneeuw, en op het kwantificeren van het O_3 -budget in de atmosferische grenslaag, d.w.z. de atmosferische laag die direct in interactie staat met het oppervlak. Hoofdstuk 3 heeft tot doel 1) te komen tot een verbeterde kwantificering van O_3 -depositie naar Arctisch zee-ijs/sneeuwoppervlak voor verschillende meteorologische omstandigheden en 2) om de bijdrage van droge depositie en andere processen aan de tijdelijke variabiliteit van O_3 -concentraties over zee-ijs te evalueren. Hier worden nieuwe continue O_3 -fluxwaarnemingen over het Arctische zee-ijs gebruikt als onderdeel van de Multidisciplinary Drifting Observatory for the Study of Arctic Climate (MOSAIC)-expeditie (<https://mosaic-expedition.org/>). Deze meest

uitgebreide meetcampagne in de geschiedenis van de Arctis omvatte het onderzoeksschip *Polarstern*, dat zichzelf vastvroor in het Arctische zee-ijs en een volledig jaar meedreef met het Arctische zee-ijs. De O_3 -fluxwaarnemingen worden aangevuld met ondersteunende waarnemingen van een meteorologische toren en radiosondes om de verticale structuur van de atmosfeer te observeren. Bovendien worden modelsimulaties uitgevoerd met een 1D-atmosferisch chemie- en meteorologisch model, waarbij de drijfroute van de *Polarstern* wordt gevolgd. De waargenomen O_3 -depositie naar het Arctische zee-ijs/sneeuwoppervlak is tot een factor 10 kleiner dan momenteel gebruikt wordt in modellen. In de winter wordt het gemodelleerde O_3 -budget in de grenslaag voornamelijk bepaald door droge depositie aan het oppervlak, gecompenseerd door neerwaarts turbulent transport van O_3 naar het oppervlak. Advectie, d.w.z. het langeafstandstransport van O_3 , leverde in de zomer een aanzienlijke, meestal negatieve bijdrage aan het gemodelleerde O_3 -budget in de grenslaag. Vooral tijdens periodes met lage windsnelheden en een ondiepe grenslaag is het droge depositiesproces van O_3 een significante verliespost van O_3 in de Arctische grenslaag.

Uit Hoofdstuk 3 bleek dat 1D-modellen geen passende randvoorwaarden hebben tijdens synoptisch gestuurde gebeurtenissen, zoals warme luchtinbraken, waarbij grootschalige processen domineren over lokale processen. Synoptische schaal warme luchtinbraken transporteren abnormale hoeveelheden warmte en vocht naar de Arctis. Dit toegenomen transport kan ook verhoogde concentraties aerosolen en sporengassen naar het Centraal Arctisch gebied brengen, waar lokale emissies over het algemeen afwezig zijn. Bovendien wordt verwacht dat Arctische warme luchtinbraken in toekomstig klimaat in frequentie en duur zullen toenemen. **Hoofdstuk 4** richt zich op het langeafstandstransport van O_3 en andere sporengassen als gevolg van een Arctische warme luchtinbraak die tijdens de MOSAiC-campagne werd waargenomen. Deze specifieke warme luchtinbraak bevatte episoden met een vergelijkbare temperatuur- en vochtigheidstoename, maar vertoonde verschillen in waargenomen sporengasconcentraties. Een 3D gekoppeld meteorologie-atmosferische chemiemodel wordt opgezet om deze warme luchtinbraak te simuleren en de gevoeligheid van 3D-gesimuleerde meteorologie en sporengasconcentraties voor horizontale modelresolutie en grenslaag-parameterisatieschema te evalueren. De eerste episode van de warme luchtinbraak werd gedomineerd door zuidoostelijke wind die van het Euraziatische vasteland kwam, met verhoogde concentraties luchtverontreinigende stoffen. De tweede episode werd gedomineerd door zuidelijke wind die van de Atlantische Oceaan kwam, met lagere concentraties van sporengassen. Deze duidelijke verschillen in 3D-gesimuleerde voetafdrukken voor de twee warme luchtinbraakevenementen werden verder ondersteund door MOSAiC-waarnemingen en "back-trajectory" modellen die de lucht terug in de tijd volgen. Enige verbetering van de modelprestaties wordt gevonden door de horizontale modelresolutie te verhogen (3 km versus 27 km), terwijl de resultaten geen duidelijke voorkeur tonen voor het grenslaag-parameterisatieschema. Een vergelijking van gesimuleerde en waargenomen

atmosferische sporengasconcentraties kan helpen bij het identificeren van bronregio's en de transportroute tijdens Arctische warme luchtinbraken.

Hoofdstukken 2 tot 4 behandelden voornamelijk lokale en grootschalige invloeden op de samenstelling van de Arctische atmosfeer, op tijdschalen in de orde van uren tot maanden. **Hoofdstuk 5** verbindt de eerder gebruikte waarnemingen en modelleringstechnieken met tijdschalen die relevant zijn voor het Arctische klimaat. Dit is in overweging genomen gezien de toenemende milieudruk en sociaal-economische druk op het Arctische gebied, met onbekende gevolgen voor de uitwisseling van klimaat-actieve sporengassen en de samenstelling van de Arctische atmosfeer. In-situ observaties van acht sporengassen werden genomen tijdens de MOSAiC-campagne. Bovendien werden deze observaties vergeleken met 18 jaar (2003-2021) moderne reanalysegegevens van de Copernicus Atmosphere Monitoring Service (CAMS). De doelstellingen van dit hoofdstuk waren tweeledig: 1) de representativiteit van reanalyse-gegevens met betrekking tot lokale waarnemingen in kaart te brengen en 2) de jaarlijkse waarnemingen van MOSAiC in de context te plaatsen van inter-jaarlijkse variabiliteit en extremen op de klimaat-tijdschaal. Hoofdstuk 5 benadrukt de sterke en zwakke punten van chemische reanalyseproducten bij het weergeven van de volledige seizoenscyclus van in-situ observaties. Ten slotte presenteert hoofdstuk 5 de resultaten van de eerste jaarlijkse CO₂ en CH₄ fluxwaarnemingen over het Arctische zee-ijs. Zowel voor CO₂ (opname) als CH₄ (emissie) geven deze nieuwe fluxwaarnemingen aan dat ze tot de laagste ijs-atmosfeer en oceaan-atmosfeerfluxen behoren in vergelijking met eerdere literatuur.

Resultaten van deze scriptie, zoals samengevat in **Hoofdstuk 6**, dragen bij aan het begrip van de oppervlakte-uitwisseling van klimaat-actieve sporengassen en verdere cycli in de Arctische atmosfeer, met gebruikmaking van een combinatie van nieuwe in-situ waarnemingen en verschillende moderne modelleringstechnieken. In het bijzonder biedt de scriptie nieuwe inzichten in de rol van lokale versus langeafstandsprocessen op de samenstelling van de Arctische atmosfeer, op verschillende ruimtelijke en temporele schalen. Hoofdstuk 6 biedt ook een vooruitzicht voor toekomstig onderzoek met betrekking tot het observeren en modelleren van de oppervlakte-uitwisseling en samenstelling van de Arctische atmosfeer. Hier betoog ik dat de complexiteit van de gevolgen van klimaatverandering in de Arctis samenwerkende inspanningen vereist, zowel op wetenschappelijk als politiek gebied. Het bevorderen van synergie tussen wetenschappelijke disciplines, het benutten van bestaande gegevens en het omarmen van samenwerkingsinitiatieven op internationaal niveau zijn essentieel om de complexe uitdagingen van klimaatverandering in de Arctis te beoordelen en mogelijk te verminderen.

Contents

	Page
Summary	v
Samenvatting	ix
Contents	xiii
Chapter 1 Introduction	1
Chapter 2 Role of oceanic ozone deposition in explaining temporal variability in surface ozone at High Arctic sites	27
Chapter 3 Low ozone dry deposition rates to sea ice during the MOSAiC field campaign: Implications for the Arctic boundary layer ozone budget	59
Chapter 4 Simulations of long-range transport of trace gases by a warm intrusion event observed during the MOSAiC field campaign	87
Chapter 5 Near-surface atmospheric composition during the MOSAiC field campaign: A long-term comparison with 18 years of reanalysis product	111
Chapter 6 General Discussion and Outlook	131
References	145
About the author	179
Acknowledgements	181

Chapter 1

Introduction



Disclaimer:

Similar to the cover of this thesis, every chapter features a randomly generated image based on the title or contents of the chapter using artificial intelligence. These images are merely an artistic representation and do not represent any scientific meaning.

1.1 The Arctic: A fast-changing region

The word *Arctic* is derived from the Greek word ἀρκτικός (*Arktikós*), meaning *northern* or *near the Bear*, referring to the constellation *Ursa Major* (Great Bear) or *Ursa Minor* (Little Bear). The Arctic is the Northern most part of the Earth and is often referred to as the area north of the Arctic circle at 66°33'N (Fig. 1.1). The Arctic ocean lies in the center and is for a large part surrounded by landmasses. This is in sharp contrast with the Antarctic, which is a landmass completely surrounded by ocean waters. In winter, the Arctic ocean is dominantly covered by sea ice which stretches all the way from Asia to North America, while in summer the majority of the Arctic ocean is ice free (Fig. 1.1). The Arctic features many unique ecosystems (CAFF, 2013) and species of flora, fauna and micro-organisms (Walker et al., 2005; Thomas, 2020), of which the most prominent example is the *Ursus maritimus* (Polar bear). Also, the Arctic is home to many indigenous communities throughout North America, Scandinavia, Finland and Northern Russia (Nuttall, 2005). Traditionally, economic activity in the Arctic is low compared to other parts of the world. In recent decades, economic activity has seen a sharp increase in the form of new or intensified maritime trade routes from the Atlantic Basin to the Bering Strait, mining activities and the exploitation of gas and oil fields (Jungsberg et al., 2019). Current estimates of available oil and gas resources in the Arctic amount to 413.23 billion barrels of oil equivalent, of which about 50% is located in Russian territories (Keil, 2014).

The Arctic is a fast-changing region in terms of its natural environment, and economic and geopolitical development. Many of these changes are closely related to climate change and the resulting decrease in sea ice cover. The consequences of climate change, originating from an increase in anthropogenic greenhouse gas emissions, are becoming increasingly evident in the Arctic (AMAP, 2021b). These consequences are apparent in many environmental records such as: increase in near-surface air temperature (Comiso and Hall, 2014; Vikhamar-Schuler et al., 2016), decline in permafrost (Romanovsky et al., 2010; Yumashev et al., 2019), retreat of the Arctic sea ice (Comiso et al., 2008; Perovich and Richter-Menge, 2009) and changes in atmospheric dynamics (Shepherd, 2016; Ogawa et al., 2018) and ecology (Arrigo and van Dijken, 2011; Årthun et al., 2018). Conflicting geopolitical interests, expanding exploitation of natural resources and increasing activities on Arctic shipping routes portend an ever-increasing pressure on the Arctic (AMAP, 2021a). Further environmental impacts appear unpreventable and are already becoming increasingly evident (Corbett et al., 2010; Arnold et al., 2016; Law et al., 2017) in the vulnerable Arctic ecosystem.

The Arctic near-surface atmosphere is warming at nearly four times the rate of the global average, a process often referred to as Arctic amplification (Rantanen et al., 2022). Arctic amplification likely follows from a multitude of feedbacks and mechanisms of which the importance of each component is often debated (Dai et al., 2019). Climate models tend to underestimate

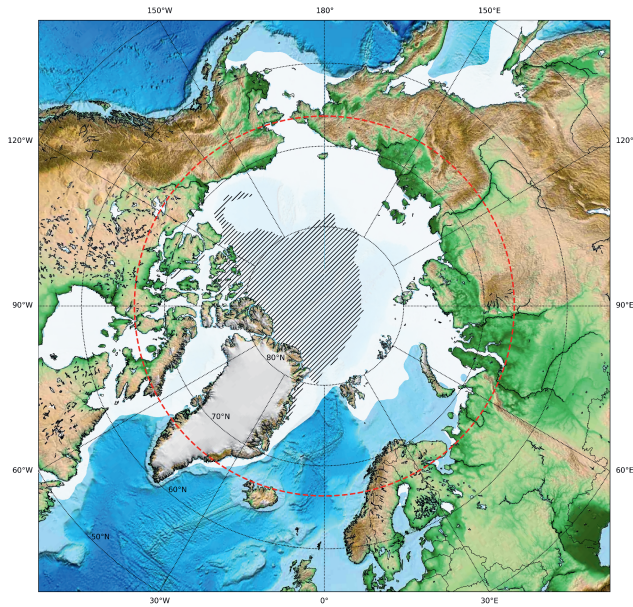


Figure 1.1: Map of the Arctic including the Arctic circle ($66^{\circ}33'N$, red), the 2020 sea ice maximum (white) and 2020 sea ice minimum (black hashed) from ERA5 (Hersbach et al., 2020).

the increase in Arctic temperatures partially due to a lack of understanding of the myriad of underlying processes and physical feedbacks (Pithan and Mauritsen, 2014). Nevertheless, the observed increase in Arctic atmospheric and oceanic temperatures (Timmermans et al., 2018) resulted in a strong decrease in Arctic sea ice cover over the last decades (Fig. 1.2a). The Arctic sea ice extent shows a strong seasonality and year-to-year variation dependent on specific atmospheric conditions (Fang and Wallace, 1994). However, the retreat of the sea ice is clearly apparent in the trends of the winter maximum and summer minimum sea ice cover (Fig. 1.2b). In winter, the sea ice extent is decreasing by about -0.33 million km^2 decade $^{-1}$ while in summer the trend is about -0.68 million km^2 decade $^{-1}$, derived from satellite observations from 1972 to 2022 (Fig. 1.2b). This decrease amounts to about 8 and 17 times the surface area of the Netherlands per decade, respectively. Climate model simulations suggest that effectively ice-free summer conditions could occur around 2050 depending on the carbon emission scenarios (Notz, 2020; Diebold and Rudebusch, 2021).

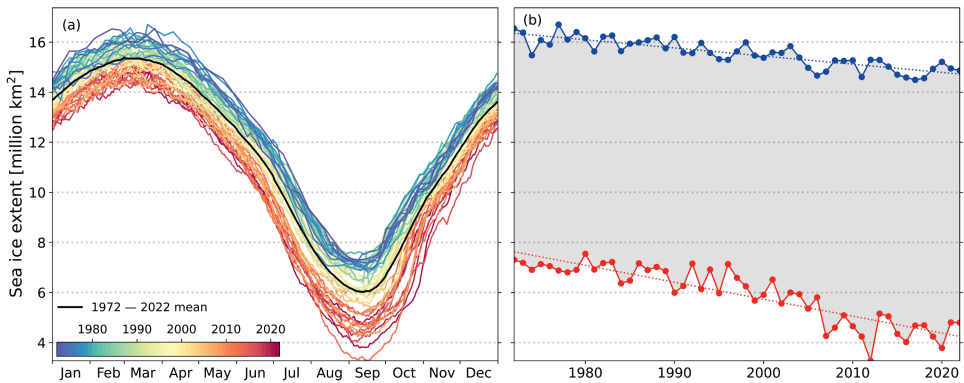


Figure 1.2: (a) Yearly cycle in Arctic sea ice extent [million km²] colored per year and (b) temporal evolution of the sea ice maximum (blue) and sea ice minimum (red) from 1972 to 2022 including linear trends (dashed) based on satellite observations following the method of Spreen et al. (2008).

1.2 Theoretical framework

The opening of the Arctic ocean through disappearing sea ice is expected to result in substantial changes in ocean–sea ice–atmosphere exchange of momentum, energy and moisture but also of climate–active trace gases, with uncertain feedbacks to global warming (McGuire et al., 2009; Parmentier et al., 2013). The climate–active trace gases I refer to in this context are carbon dioxide (CO₂), methane (CH₄), ozone (O₃) and dimethylsulfide (DMS). CO₂, CH₄ and O₃ affect climate through their role as greenhouse gases, whereas O₃ also affects climate through its role in the atmosphere’s oxidizing capacity, determining the lifetime of other trace gases such as CH₄ and DMS. DMS acts as a key precursor in the formation of sulphate aerosols, affecting climate through the direct and indirect aerosol impacts on the Earth’s energy balance (Levy et al., 2013). Additionally, the expected increase in local emissions of trace gases and air pollutants (Granier et al., 2006; Law et al., 2017; Schmale et al., 2018), by developing industry and shipping, poses an additional burden on the Arctic environment. The Arctic atmosphere, which was previously often considered pristine, because of the lack of local sources of air pollutants, faces significant changes in the coming decades.

Trace gases occur in the Earth’s atmosphere at relatively low quantities. As an example, pre-industrial global CO₂ levels amounted to about 280 parts per million (ppm), equivalent to 0.028% of the total composition of the atmosphere. Other trace gases occur at even lower quantities, in the order of parts per billion (ppb) or even parts per trillion (ppt). Although trace gases occur at low quantities in the Earth’s atmosphere, they have a substantial effect on the Earth’s climate and the quality of the air we breathe.

Even though the Arctic atmosphere is often considered pristine, it is strongly connected to emissions and transport from the mid-latitudes. Especially trace gases that have a long lifetime, i.e. on the order of months to years, can be transported over a long distance by advection, and reach areas where local emissions are lacking. In contrast, concentrations of a trace gas which have a short lifetime, i.e. on the order of hours to weeks, are generally mostly reflecting to a larger extent the role of local processes such as in-situ emissions and vertical mixing conditions.

This thesis investigates the role of local– versus large–scale effects on the composition of the Arctic atmosphere (see Fig. 1.3). I mainly focus, but do not limit myself, to the understanding of underlying processes that ultimately determine the fate of O_3 in the Arctic atmosphere. I especially focus on the role of O_3 deposition to the Arctic ocean and snow–and ice surfaces. I propose a methodology that optimally integrates novel observations with process-based modeling at multiple spatial and temporal scales. In Sect. 1.2.1–1.2.3 I will introduce in more detail the theoretical framework of this thesis, including relevant processes and concepts. Thereafter, I will introduce observations of the Arctic atmosphere in Sect. 1.3 and atmospheric chemistry and transport models in Sect. 1.4. In Sect. 1.5 I will finalize this introduction with the research questions answered in the different chapters.

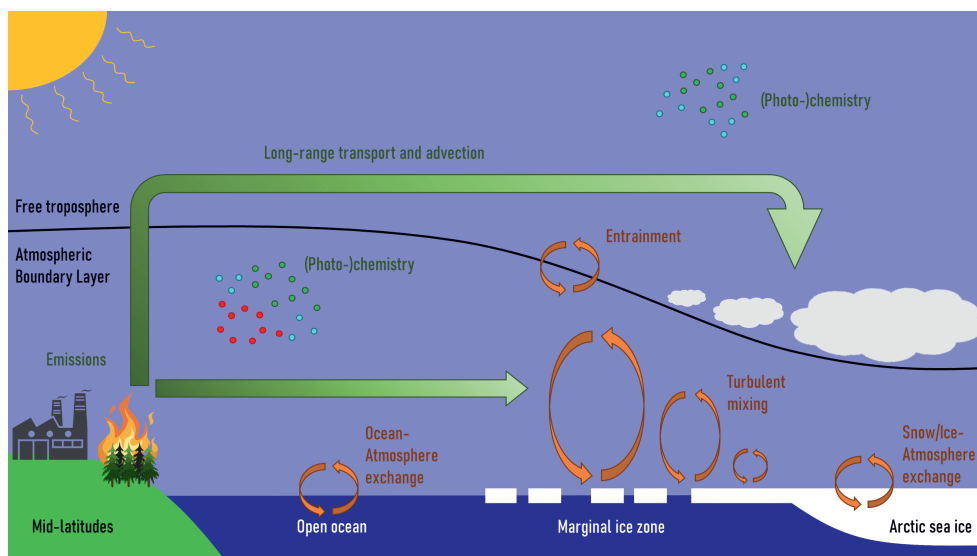


Figure 1.3: Schematic illustration of physical and chemical processes relevant for this thesis research on understanding and modeling chemical composition of the Arctic atmosphere.

1.2.1 Arctic tropospheric ozone

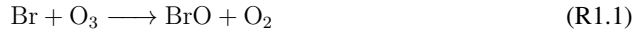
In the stratosphere (~ 10 – 50 km above the Earth's surface), O_3 plays an important role in protecting us from harmful solar ultraviolet (UV) radiation. In the *ozone layer* (at ~ 30 km altitude), all of the highly energetic so-called UV-C and most of the UV-B radiation are absorbed by O_3 molecules. Exposure to elevated amounts of UV radiation is very harmful to living organisms (Lucas et al., 2008; Watson et al., 2016) and therefore stratospheric O_3 is often considered *good ozone* by maintaining habitable living conditions on Earth.

In the troposphere (from the surface up to ~ 8 – 10 km altitude), O_3 is often considered as *bad ozone* especially in the context of O_3 as an air pollutant with enhanced concentrations relative to those for pristine conditions. Due to its oxidative character it is harmful to human health (Nuvolone et al., 2018), plant growth (Ainsworth et al., 2012; Emberson, 2020) and artificial materials (Shen and Gao, 2018). Additionally, tropospheric O_3 is the third most important anthropogenic greenhouse gas after carbon dioxide (CO_2) and methane (CH_4) by absorbing radiation and redirecting it back to the Earth's surface (Gorshchev et al., 2014; Checa-Garcia et al., 2018). Additionally, O_3 has indirect effects on the climate as a precursor of the hydroxyl radical (OH) which determines the lifetime of CH_4 , and many other reduced compounds acting as precursors of further oxidized products and aerosols, in the atmosphere (Stevenson et al., 2020). Background levels of O_3 in the Arctic troposphere are about 30–40 ppb and its atmospheric lifetime is about 23 ± 8 days (Derwent et al., 2018).

The sources of tropospheric O_3 are chemical production and stratosphere-to-troposphere exchange. The sinks of tropospheric O_3 are chemical destruction and removal to the Earth's surface, often referred to as *dry deposition* (Young et al., 2018; Tarasick et al., 2019). O_3 is a secondary air pollutant because it is not emitted directly into the atmosphere, but chemically produced as a function of the concentration of the emitted precursors. O_3 forms as the result a series of chemical reactions involving carbon monoxide (CO) and hydrocarbons, such as volatile organic compounds (VOCs) and CH_4 , in the presence of nitrogen oxides ($NO_x = NO + NO_2$) and solar radiation (Jacob, 2000).

In the Arctic, observations of tropospheric O_3 concentrations have indicated an increasing trend up to the early 2000s. This upward trend has been leveling off (Oltmans et al., 2013; Cooper et al., 2014) or decreasing at individual sites (Cooper et al., 2020) in the last decade (2010–2020). The upward trend up to the early 2000s can be attributed to increased emissions of precursors in the mid-latitudes (Cooper et al., 2014; Lin et al., 2017). Additionally, increased stratosphere-to-troposphere exchange was suggested to also contribute to the upward trend (Pausata et al., 2012). Local emissions of O_3 precursors, such as NO_x emissions from increasing shipping activities, are expected to become an important source of Arctic tropospheric O_3 (Marelle et al., 2016; Law et al., 2017).

A prominent feature of the seasonal cycle of Arctic tropospheric O_3 are Ozone Depletion Events (ODEs) in spring. Tropospheric O_3 depletion is caused by catalytic reactions with halogens such as bromine (Br), iodine (I) and chlorine (Cl). Of these halogens, the reaction with Br is often considered as the main removal pathway of O_3 following (Barrie et al., 1988):



The net result of the reactions R1.1 and R1.2 is



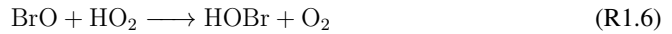
Additionally, bromine oxide (BrO) can self-react and form Br_2 in the reaction



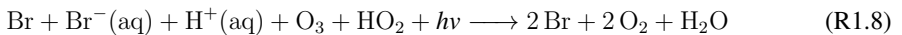
and convert back to Br by the photolysis of Br_2 following



The Br in the reactions above is involved in a null-cycle and therefore, the rate at which O_3 is ultimately destroyed is determined by the rate at which BrO reacts with other species (Halfacre et al., 2014). Halogens, mostly in the form of Br_2 , are released from the Arctic snowpack, blowing snow and sea salt aerosols (Pratt, 2019). This occurs particularly during spring, when temperatures are still low, yet radiation is strong enough for photo-chemical reactions. While the BrO self-reaction in R1.4 only regenerates gas-phase Br atoms, Br is also involved in multi-phase chemical reactions on surfaces such as the snow-ice surface, snowflakes and aerosols (Pratt, 2019) in the following reactions:



Together with R1.1 and R1.5 this results in the net reaction:



This is referred to as *bromine explosion* and indicates that aqueous-phase bromine is converted to gas-phase bromine which then ultimately leads to more O₃ destruction.

During an ODE, the O₃ mixing ratio can drop below 1 ppb in a time-span of several hours (Jacobi et al., 2010). These ODEs, related to the emissions and gas- and heterogeneous chemistry involving Br, have been observed at multiple sites throughout the Arctic (Simpson et al., 2007; Halfacre et al., 2014; Thompson et al., 2017). Recently, Benavent et al. (2022) also showed a major contribution of iodine chemistry to Arctic O₃ destruction. The term ozone depletion *event* can be up to discussion since this feature of observing consistently low O₃ can persist for several days (Jacobi et al., 2010) in the lowest kilometer of the atmosphere and occur at horizontal spatial scales of hundreds of kilometers (Halfacre et al., 2014). Rather, it seems that these events appear to be normal state of Arctic spring alternated with elevated levels of O₃ being observed due to the passage of dynamically active synoptic systems (Cao et al., 2016).

1.2.2 The Arctic Planetary Boundary Layer

The previously discussed details on Arctic tropospheric O₃ chemistry are to a large extent controlled by processes occurring near the surface in the Arctic Planetary Boundary Layer (PBL). The PBL or Atmospheric Boundary Layer (ABL) is the atmospheric layer closest to the Earth's surface which is under direct influence of the surface below (Stull, 1988). At small scales, the PBL is relevant for the local exchange and further cycling of trace gases (Lin et al., 2008) while at the larger scale the PBL influences meso-scale and synoptic weather phenomena (Banks et al., 2016). The boundary layer features *turbulent eddies* that transport heat, moisture, momentum and trace gases throughout the boundary layer. The depth of the PBL is characterized by the size of the largest eddies which are typically in the order of 1–2 km for daytime conditions in the mid-latitudes. Production of atmospheric turbulence can be divided in buoyant production and shear production. Turbulence from buoyant production follows from heating of the surface by solar radiation causing a statically unstable situation. Shear production follows from vertical wind speed differences. Because the wind speed at the surface is zero this creates a hydro-dynamically unstable situation.

The Arctic PBL is generally marked by strongly stratified conditions (Esau and Sorokina, 2009). A lack of turbulence results in very shallow PBLs which are typically in the order of 10–300 m deep (Kral et al., 2021). The Arctic is characterized by a strong seasonal cycle in incoming solar radiation. Even in summer, when solar radiation is available for 24 hours per day, the relatively high albedo of the snow and ice surface makes that the available energy to heat the surface and overcome the strong vertical temperature inversions near the surface, is limited. These temperature inversions — an increase of temperature with height — are very characteristic of the Arctic PBL (Tjernström et al., 2019). Therefore, buoyant production is restricted and

turbulence in the Arctic PBL is mainly governed by shear production (van der Linden et al., 2020). Presence of leads, openings in the Arctic sea ice as a result of stress, can though provide an additional source of energy to generate buoyant turbulent production by opening of the warm Arctic ocean ($-2\text{ }^{\circ}\text{C}$) under the cold Arctic atmosphere (up to $-40\text{ }^{\circ}\text{C}$) (Qu et al., 2019; Li et al., 2020).

The dynamics in the Arctic PBL strongly regulate the exchange of trace gases between the atmosphere and the underlying surface. Additionally, the concentration of trace gases and aerosols emitted into the atmosphere strongly depend on the depth of the PBL. Stably stratified PBLs often feature strong vertical gradients in concentrations of trace gases alongside the gradients of potential temperature, wind speed and direction and humidity (Kupiszewski et al., 2013). The presence of fully developed turbulence will then homogenize the vertical structure of the PBL to a large extent. Additionally, turbulent eddies, moving air masses upward from the surface, may overshoot the height of the PBL, mixing in air from the free troposphere into the PBL. This process is referred to as *entrainment* (see Fig. 1.3). Generally, a potential temperature inversion is present at the PBL top, which decouples the PBL from the free troposphere. Often, these two atmospheric layers — the PBL and the free troposphere — have a different atmospheric composition due to their different origin of air masses (Orbe et al., 2015) and physical and chemical processes. Entrainment causes these two air masses to mix, affecting the concentration of trace gases in the PBL.

Dynamics and exchange processes in the Arctic PBL are also of relevance for the larger Arctic system. It regulates the exchange of energy and water vapour affecting Arctic low cloud cover (Wu and Lee, 2012; Kay et al., 2016). Low clouds increase the net available energy at the surface by an additional longwave radiative forcing (Shupe and Intrieri, 2004). This additional energy has been suggested to result in an accelerated Arctic sea ice decline in spring (Huang et al., 2019). Current state-of-the-art weather and climate models have many shortcomings in a realistic representation of the stably stratified Arctic PBL (Holtzlag et al., 2013; Sandu et al., 2013; Sedlar et al., 2020). Consequently, this results in biases in the large-scale system, including cloud processes and feedbacks impacting the radiation and energy balance. This motivates to improve our understanding of the PBL using an approach that integrates to a maximum extent novel observations and state-of-the-art weather and climate models.

1.2.3 Surface exchange of climate-active trace gases

As mentioned before, the turbulence in the PBL controls to a large extent the exchange of trace gases between the atmosphere and the underlying surface. The exchange of trace gases is expressed as a flux, representing how much uptake or emissions of a certain gas occurs per surface area over a certain time period [$\text{kg m}^{-2} \text{s}^{-1}$]. This exchange flux is driven by concentration

gradients between the atmosphere and the underlying surface, where the flux is directed from high to low concentrations. This flux can be observed, or calculated in model experiments. The lack of turbulent mixing can strongly decouple the surface from the overlying atmosphere and pose a barrier for the exchange of trace gases (Helmig et al., 2007b; Carpenter et al., 2012). In the Arctic, these surface fluxes can be up to several orders of magnitude smaller than in the mid-latitudes, which complicates the measurement of these fluxes, which will be discussed later in Sect. 1.3.1.

The atmosphere–ocean and atmosphere–ice surface exchange of the two most important greenhouse gases CO_2 and CH_4 is bi-directional as a function of the partial pressure gradient between the atmosphere and the surface water or sea ice. The Arctic ocean is generally deemed to be a sink of CO_2 (Arrigo et al., 2010; Bates et al., 2011), even though some shelf seas are hypothesized to become a relatively strong source of CO_2 in a future warmer climate (Semiletov et al., 2007). In the Arctic ocean, CO_2 partial pressures in the surface water are lower, especially in open waters, leading to a net CO_2 flux into the ocean. With a diminishing sea ice extent, a larger area of surface waters with low CO_2 partial pressures opens up and may take up even more CO_2 from the atmosphere. However, observational studies also suggest a less effective uptake due to low primary productivity in the central basin, reaching a quick equilibrium of CO_2 uptake due to increased stratification and lower solubility due to warmer ocean waters (Cai et al., 2010).

Sea ice generally restricts the exchange between the ocean and the overlying atmosphere. However, Kotovitch et al. (2016) found in a laboratory study that sea ice is still permeable after freeze-up. CO_2 fluxes from the atmosphere into the sea ice as well as fluxes from sea ice to the atmosphere have been observed (Parmentier et al., 2013) and fluxes approach zero with increasing snow thickness. The magnitude and direction of CO_2 fluxes between sea ice and atmosphere in a future climate remain unknown. It is also not certain how the exchange of CH_4 between the Arctic ocean, sea ice and atmosphere will evolve in a changing climate. In aerobic ocean surface water, CH_4 super-saturation is common, following from biological production (Damm et al., 2010; Jacques et al., 2021). Furthermore, CH_4 emissions from the Arctic ocean to the atmosphere have been observed in areas with fractional sea ice cover and near open leads (Kort et al., 2012).

Surface exchange of O_3 , predominantly reflecting removal of O_3 by the surface is a significant sink ($\sim 25\%$) of tropospheric O_3 (Lelieveld and Dentener, 2000). This process is often referred to as O_3 deposition or O_3 dry deposition. The deposition of O_3 to the ocean, snow and ice surfaces is generally much slower compared to other natural surfaces (Hardacre et al., 2015). However, due to the large surface area, O_3 deposition to these surfaces still poses an important contribution to the total O_3 budget (Ganzeveld et al., 2009). On the local scale, O_3 dry deposition is an important process which determines the magnitude and variability in PBL O_3 concentrations

in remote areas (Monks et al., 2000; Conley et al., 2011).

The reduced sea ice cover is expected to alter O_3 deposition to the Arctic ocean dependent on changes in the oceanic surface-layer composition. O_3 in the surface waters is being mainly removed through its reactions with dissolved organic carbon and halogens (Sarwar et al., 2016). These reactions between O_3 and halogens result in the release by the ocean water of halogen oxidation products that can further catalytically destroy O_3 inducing a negative feedback mechanism (Prados-Roman et al., 2015). Our current understanding of the processes involved in O_3 deposition to the Arctic ocean and sea ice, and its further consequences for the Arctic O_3 budget, has been hampered by limited observations. This thesis will focus on process-understanding of O_3 deposition to these surfaces by using novel observations and modeling techniques introduced in Sect. 1.3 and 1.4.

1.3 Observations of the Arctic atmosphere

Observational coverage of the Arctic atmosphere is very limited compared to other regions in the world. As an example, measurements of surface O_3 concentrations are collected at 26 sites North of the Arctic circle ($66^{\circ}33'N$, Fig. 1.1), of which some sites are already out of service. This is in sharp contrast with ~ 3400 and ~ 4300 locations over land in North America and Europe, respectively (Schultz et al., 2017; Fleming et al., 2018). Long-term monitoring sites of O_3 concentrations, or other atmospheric variables, are limited to the Arctic land-surface which only enables us to understand a part small part of the entire Arctic system. One of the reasons for this limited coverage is the inaccessibility of large parts of the Arctic. Furthermore, the development and maintenance costs of these surface stations is high, especially in remote areas.

Remote sensing techniques such as satellites can only partially cover these observational gaps (Arnold et al., 2016). Typically, satellite observations of trace gases retrieve the abundance of trace gases based on the difference of the solar radiation spectrum and the radiation spectrum reflected by the Earth's surface. Different trace gases each absorb a specific part or multiple parts of the entire wavelength spectrum. However, due to the absence of solar radiation in Arctic winter, remote sensing techniques which rely on solar radiation are only useful in summer months. Additionally, many satellite observations are obstructed by clouds (Worden et al., 2013; Boersma et al., 2018) which can be very persistent in the Arctic (Shupe et al., 2011; Gierens et al., 2020; Silber and Shupe, 2022). Active remote sensing techniques rely on active emission of wavelengths often not contained in the solar radiation spectrum. For example, active microwave remote sensing can be used to study the extent and age of the sea ice (Forster et al., 2001; Melsheimer et al., 2022).

Additional observational coverage of the central Arctic atmosphere comes from dedicated field campaigns. An example of a field campaign can be intensive sampling of the vertical structure of the Arctic atmosphere using aircrafts. Some examples of such short-term measurements relying on airborne observations include The Arctic Research of the Composition of the Troposphere from Aircraft and Satellites (ARCTAS) (Jacob et al., 2010), Airborne Extensive Regional Observations in Siberia (AEROSIB) (Paris et al., 2009) and the Polar Study using Aircraft, Remote Sensing, Surface Measurements and Models, Climate, Chemistry, Aerosols and Transport (POLARCAT) (Law et al., 2014).

Observations of the PBL dynamics over sea ice often rely on ship based field campaigns, e.g., the Surface Heat Budget of the Arctic Ocean experiment (SHEBA) (Persson et al., 2002) and the Arctic Summer Cloud Ocean Study (ASCOS) (Tjernström et al., 2014). These ship based field campaigns are typically centered around an icebreaker sailing through, or drifting with the Arctic sea, with sensors on the ship and deployable sensors on the Arctic sea ice. Ship- and airborne field campaigns are naturally very expensive and require a large coordinated effort of multiple research institutes. Additionally, due to logistical reasons, they commonly focus on the spring and summer seasons causing an incomplete understanding of the seasonal cycle of the central Arctic atmosphere. Also, they mostly have a specific focus and do not fully consider the interdisciplinary aspect including the many feedbacks and interactions in the natural Arctic system.

1.3.1 The Multidisciplinary drifting Observatory for the Study of Arctic Climate expedition

In September 2019, the German icebreaker *RV Polarstern*, operated by the Alfred Wegener Institute (AWI), set sail to the Arctic and docked itself into the Arctic sea ice for a full year. This drift was inspired by the explorer and scientist *Fridtjof Nansen* who hoped to reach the North Pole in 1893 by letting his wooden sailing-ship *Fram* drift with the Arctic sea ice. From October 2019 to September 2020, the Multidisciplinary drifting Observatory for the Study of Arctic Climate expedition (MOSAiC) collected observations of the central Arctic atmosphere (Shupe et al., 2022), ocean (Rabe et al., 2022), sea ice and snow (Nicolaus et al., 2022), biogeochemistry and ecology. The overarching goal of MOSAiC was to better understand the causes and consequences of Arctic climate change from an interdisciplinary perspective and to use these observations for improved model representation. MOSAiC is up to this point, the largest central Arctic field campaign by participation of hundreds of researchers from ~20 countries.

The campaign was organized around five *Legs* in between which personnel onboard the *RV Polarstern* was exchanged (Fig. 1.4a). About 100 m to 2000 m away from the *RV Polarstern* the

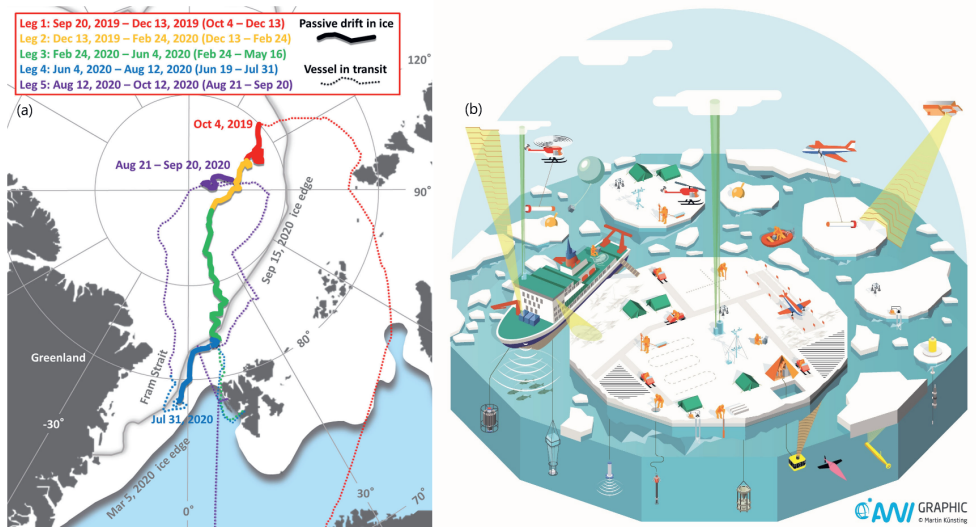


Figure 1.4: (a) Passive drift and active transit path of the RV *Polarstern* including the 5 different legs (adapted from Shupe et al. (2022)) and (b) graphical representation of the MOSAiC observatory (Graphic by: Alfred Wegener Institute/Martin Künsting)

Central Observatory was built. The Central Observatory was subdivided into many different areas with a specific scientific focus such as *Met City* (Meteorological City) and *Ocean City*. The top deck of the RV *Polarstern* itself also contained a broad array of sensors and containers. Furthermore, in the labs aboard samples collected in the field were analyzed. The Central Observatory was complemented by a *Distributed Network* of buoys and other automated sensors up to ~ 40 km away from the RV *Polarstern* (Hoppmann et al., 2022). The intention of this Distributed Network was to connect the detailed local scale observations at the Central Observatory, to the typical size of a grid cell of Numerical Weather Prediction models. Another tool to bridge the local and regional scales was the deployment of the *Polar 5* and *Polar 6* aircrafts. The *Polar 5* and *Polar 6* performed two flight campaigns from Svalbard to the Central Observatory (Herber et al., 2021) in summer. Unfortunately, the planned flights in spring had to be cancelled due to the outbreak of the Coronavirus Disease 2019 (COVID-19) outbreak. Additionally, existing remote sensing observations from satellites have been used to connect the local MOSAiC Central Observatory observations to the regional Arctic scale (Krumpen et al., 2021).

Many novel observational techniques were applied during MOSAiC, which were previously not yet applied in the Central Arctic. For example, the use of drones and uncrewed aircrafts (Hamilton et al., 2022), tethered balloons (Lonardi et al., 2022) and ground-based remote sensing instruments set up on the sea ice (Demir et al., 2021) have provided another wealth of

observations. A graphical representation of the MOSAiC observatory can be found in Fig. 1.4b. The campaign features two major data gaps due to logistical reasons. For the exchange between Leg 3 and Leg 4, the *RV Polarstern* had to pick up personnel and material from Svalbard. Some automated sensors continued collecting observations on the sea ice and *RV Polarstern*, but the majority of the sensors was packed and reinstalled after the exchange. At the end of Leg 4 the *RV Polarstern* was already in the marginal ice zone due to the faster ice drift than predicted. After Leg 4 the *RV Polarstern* set sail North to set up a new Central Observatory close to the geographic North Pole for Leg 5. Below, I will introduce the most important sensors and observational datasets that are used in this study.

Meteorological data

Near-surface meteorological variables were collected on a meteorological tower set up on the sea ice as part of the Central Observatory, located ~ 300 – 500 m away from the *RV Polarstern*. This tower includes, but is not limited to, measurements of air temperature, relative humidity, wind speed and wind direction. These measurements were made at nominal heights of 2, 6 and 10 m on a 10 m high tower. Additionally, a 30 m high tower was set up to observe the same variables at 30 m height. This tower broke down due to deformation of the ice floe resulting from a storm event in November. The tower was later rebuilt to a height of 23 m. Similar measurements were performed onboard the *RV Polarstern* at a height of 29 m. However, these observations are possibly influenced by the ship itself and are therefore only used for gap-filling of missing data, after a careful comparison with the observations on the sea ice which are assumed to be undisturbed from the ship and other artificial structures.

The meteorological tower provides continuous and detailed observations of the atmospheric surface layer. However, the observations do not provide any information of the synoptic background conditions and vertical profiles of the upper atmosphere. Therefore, radiosondes were launched every 6 hours. A radiosonde is a small instrument package suspended below a helium filled balloon. This instrument package features measurements of air temperature, relative humidity, pressure and its position using a Global Positioning System (GPS). Approximately once a week, the radiosonde was equipped with an O_3 sensor. By tracking its location the wind speed and wind direction is calculated. The temporal frequency of these observations was increased to 3 hours for periods that were of particular interest, such as the passage of storms. The radiosondes were launched from the sea ice or the deck of *RV Polarstern* and reached altitudes of up to 30 km. During the transit periods (Fig. 1.4a) launching of the radiosondes continued as usual from the deck of *RV Polarstern*. Due to their fast ascent after release, the measurements close to the surface are subject to a high uncertainty.

Observations of trace gases and surface fluxes

Near-surface mole fractions of trace gases were measured aboard *RV Polarstern* in three sea-container laboratories (Angot et al., 2022d). These observations include concentrations of carbon dioxide (CO_2), methane (CH_4), nitrous oxide (N_2O), carbon monoxide (CO), ozone (O_3), dimethylsulfide (DMS), sulphur dioxide (SO_2), elemental mercury ($\text{Hg}(0)$) and a selection of Volatile Organic Compounds (VOCs). The inlet height of the samplers was $\sim 18\text{--}25$ m above the ice surface. Some of these measurements have been performed in multiple containers. Additionally, duplicate measurements of CO_2 and CH_4 concentrations and fluxes have been performed on the meteorological tower on the sea ice. This redundancy allows for cross-calibration of the different sensors and gap-filling during periods of technical issues and maintenance. Because the measurements have been performed on the *RV Polarstern*, the observations are subject to influences of local air pollution. Therefore, many of the datasets have been subject to quality assessment and quality control. Parts of the dataset were filtered to exclude the role of local air pollution from the ship exhaust (Beck et al., 2022).

Measurements of surface fluxes of O_3 , CO_2 , CH_4 and DMS have been performed on the *RV Polarstern* bow crane extending approximately 5 m in front of the ship's bow. These fluxes are observed using a so-called *Eddy-Covariance* system. This Eddy-Covariance system is a combination of a 3D sonic anemometer and a gas analyzer. The anemometer measures the wind speed in three directions using ultrasonic sound waves at a frequency of typically 20 Hz. A gas analyzer with a similar high-frequency is needed to infer the surface fluxes.

The vertical mass-flux of a trace gas X (F_X , [$\text{kg m}^{-2} \text{s}^{-1}$]) is defined as the time-average of the concurrent vertical wind speed (w , [m s^{-1}]) and the concentration of trace gas X (c_X , [kg m^{-3}]):

$$F_X = \overline{w \cdot c_X}. \quad (1.1)$$

The instantaneous values of w and c_x can be decomposed, using *Reynolds decomposition*, in a mean (\overline{w} and $\overline{c_X}$) plus the deviation around the mean (w' and c'_X). Therefore, Eq. 1.1 rewrites to:

$$F_X = \overline{(\overline{w} + w') \cdot (\overline{c_X} + c'_X)} = \overline{\overline{w} \cdot \overline{c_X}} + \overline{w' \cdot \overline{c_X}} + \overline{\overline{w} \cdot c'_X} + \overline{w' \cdot c'_X}. \quad (1.2)$$

Because the mean of a deviation is by definition zero, the second and third terms on the right hand side of Eq. 1.2 are zero. Another assumption made is that the mean vertical flow (\overline{w}) is assumed to be negligible for horizontal homogeneous terrain (Mauder et al., 2021). Therefore, the first term on the right hand side of Eq. 1.2 can be ignored to arrive at the final formulation

of the surface flux of a gas X :

$$F_X = \overline{w' \cdot c'_X}. \quad (1.3)$$

This equation represents the covariance of the vertical wind speed and concentration of gas X . If a turbulent eddy is moving up ($w' > 0$) and is enriched in gas X ($c'_X > 0$), the instantaneous flux will be positive. Additionally, turbulent eddies moving downwards ($w' < 0$) which are depleted in gas X ($c'_X < 0$) will also result in a positive instantaneous flux. By averaging these instantaneous fluctuation co-variances over a longer time-window (typically ~ 15 minutes), the total flux can be calculated. In the previous example, the positive flux represents an emission of trace gas X . In contrast, upward moving eddies ($w' > 0$) can be depleted in gas X ($c'_X < 0$). Similarly, downward moving eddies ($w' < 0$) can be enriched in gas X ($c'_X > 0$). This will result in a negative flux that represents deposition of gas X to the surface.

1.4 Atmospheric chemistry and transport models

Observations are inherently limited in time and space. Additionally, many quantities and processes can not be observed using contemporary measurement techniques. Therefore, numerical models are commonly used tools to study the environment. Examples include, but are not limited to, forecasting, understanding fundamental processes, quantifying local- or global scale budgets, and sensitivity studies to certain input parameters or forcing scenarios. An atmospheric model is a mathematical description of our understanding of the physics of the natural system. Atmospheric models are built around the governing equations of conservation of mass, momentum and energy. These equations describe the rate of change of the atmospheric state variables wind, temperature and moisture over time. In atmospheric models they are numerically solved by discretizing time and space into a finite number of discrete elements or volumes.

1.4.1 Fundamentals of atmospheric chemistry and transport models

Historically, atmospheric chemistry models and numerical weather prediction models have been developed separately because they were treated as different disciplines (Baklanov et al., 2014). Atmospheric chemistry models were often run in a so-called *offline* mode. In an offline setup, the output of a weather prediction model was used to drive the atmospheric chemistry model. It was recognized that the weather strongly influences air quality through advection, turbulent transport, photo-chemistry, precipitation and many other factors. However, atmospheric composition can alter the radiation budget directly or indirectly through cloud formation, and thus affects the weather forecast itself. This motivated the development of *online* atmospheric chemistry and transport models (e.g. Grell et al., 2005; Korsholm et al., 2008; Schaap et al., 2008; Knote et al.,

2011). In an online setup, atmospheric physics and chemistry are calculated at the same time and on the same model grid accounting for a two-way feedback. A downside of this online setup is that it is computationally much more expensive than using an offline setup. In a similar fashion, atmospheric models have been coupled to physical (sea-)ice, snow and ocean models to fully consider the role of temporal and spatially resolved dynamics in the atmosphere, cryosphere and ocean, relevant for climate change assessments (Moore and Gordon, 1994; Roberts et al., 2019) and sea ice prediction (Mikolajewicz et al., 2005; Ren et al., 2021), generally referred to as *Earth System Models*.

Atmospheric chemistry and transport models can be divided into so-called *Lagrangian* and *Eulerian* models. Lagrangian models follow a parcel of air in time, as it moves through the atmosphere. For example, Lagrangian models are used to study dispersion of a plume of air pollution downwind of a specific point- or area source. In addition, Lagrangian models are also applied to assess the evolution of air masses being transported from an upwind area to a specific location in back-trajectory analysis. For example, back-trajectory analysis is applied to explain observed sharp increases in the concentration of a certain gas and identifying the potential location and magnitude of the source.

Eulerian models are fixed in space and calculate the physical and chemical processes for a specific control volume. This control volume can either be one box (*box model*), an array of vertically stacked boxes (*1D or Single Column model*) or a three-dimensional array of boxes (*3D model*). Most weather prediction and climate models are examples of 3D Eulerian models. In each grid box, the temporal rate of change of the concentration of a certain trace gas X can be calculated by accounting for all its sources and sinks following:

$$\frac{\Delta X}{\Delta t} = \left[\frac{\Delta X}{\Delta t} \right]_{\text{advection}} + \left[\frac{\Delta X}{\Delta t} \right]_{\text{turbulence}} + \left[\frac{\Delta X}{\Delta t} \right]_{\text{chemistry}} + \left[\frac{\Delta X}{\Delta t} \right]_{\text{emissions}} + \left[\frac{\Delta X}{\Delta t} \right]_{\text{deposition}}. \quad (1.4)$$

The left side of the Eq. 1.4 represents the total tendency of the concentration of gas X over time Δt . The right side of Eq. 1.4 represents the contribution by each individual process explaining the net tendency of the concentration of gas X . These processes can either be a source, represented by a positive contribution of this term to the equation, or provide a sink of gas X , represented by a negative tendency term. Often, these individual processes can be a source or a sink depending on the specific state of the atmosphere. For example, for a site located North of a factory that emits a certain gas X , and the wind blowing from the South, air with a higher concentration of gas X is advected to the site, implying a positive advection term in Eq. 1.4. In contrast, if the wind blows from the North where the air is depleted in trace gas X , the advection term can be negative. If one would know the concentration of gas X at

timestep t and let a model calculate the contribution of each source and sink term in Eq. 1.4 for timestep Δt , one would know the concentration at the next timestep $t + \Delta t$. The choice of the model timestep is very important in the set up of the model. On the one hand, if the time steps are too large, the model may become numerically unstable. On the other hand, small timesteps require a lot of computational resources.

At the same time, an appropriate model grid spacing has to be selected. Eulerian models have grid boxes in three dimensions with a certain grid length Δx , Δy and Δz . By reducing the grid length, and thus increasing the resolution, one is able to resolve smaller features of the atmospheric flow. However, when increasing the model resolution by a factor of 10, the number of grid points increases by 1000, and thus requires much more computational resources. At the same time, the time step of the model depends on the selected grid size. Higher resolution models require smaller time steps, because a parcel of air is not allowed to travel across a grid cell during a single timestep, also known as the *Courant-Friedrichs-Lewy criterion*. Atmospheric flow occurs at a wide range of scales, and thus not every process can be completely resolved by the model. Therefore, processes that occur at scales smaller than the grid spacing, or are too complex to physically represent, are parameterized. Parameterizations are simplified representations of a physical process. An atmospheric chemistry and transport model often consists of many parameterization schemes each representing one individual component of the entire system. Examples of processes that are often parameterized are radiation, turbulence, clouds, surface-atmosphere exchange, surface emissions and atmospheric chemistry.

The choice of model archetype and model setup is dependent on the research questions and objectives (Warner, 2011). Model simulations can be very useful to answer questions such as *"What is the contribution of process Y on the concentration of gas X?"* or *"How much will the concentration of gas X increase in the future under certain climate scenarios?"*. Models can provide information of processes that can not or have not been observed. For example, using observations you might only be able to measure the concentration of a certain gas X while a model can give you information of each individual process driving the rate of change (Eq. 1.4). Furthermore, models provide information on the full temporal and spatial coverage, where observations are often limited to a certain location, footprint and time period. However, models are limited by our fundamental understanding of the processes, which is often not completely represented in its model representation. Moreover, models require accurate initial and boundary conditions, which often are obtained from observations. Because of their full spatial and temporal coverage, models are often perceived as accurate. However, a model can never fully represent the natural system and can only approximate at best. Therefore, atmospheric chemistry and transport models are not a tool on its own, but can become useful tools when combined with observations. Evaluating model results against observations is key to understand the behaviour of models, assess their strengths and weaknesses, and formulate paths for further

model development. Only then a model can be used to further understand observations and processes or to use the model for a forecast.

1.4.2 Multi-scale modeling approach

Despite continuous model development in the last 20 years, atmospheric chemistry and transport models show many deficiencies in accurately representing observed concentrations of climate-active trace gases in the Arctic troposphere (Whaley et al., 2022, 2023). Very few long-term monitoring sites are present in the Arctic, which complicates evaluation and further development of these models. Furthermore, fundamental processes controlling the burden of trace gases in the Arctic troposphere, such as surface-atmosphere exchange of trace gases, are often represented in an oversimplified manner. Accurately representing turbulent transport in the Arctic PBL, and further cycling of trace gases in discretized model layers, appears challenging due to the prevalent strongly stratified conditions over the Arctic sea ice.

This thesis focuses on the role of local versus large-scale contributions to the MOSAiC observed climate-active trace gas fluxes and concentrations. I apply a methodology that integrates to a maximum extent observations of the Arctic atmosphere with process-based model experiments. I link the observations at a range of scales to the scale of regional– to global–scale atmospheric chemistry and transport modeling systems. Therefore, I rely on the application of models on different spatial and temporal scales. Here, I apply box models, 1D models and 3D models to support the observations (Fig. 1.5). Specifically, I focus on the application and development of a 1D and a 3D modeling system coupled to box-model representations of the surface exchange of trace gases.

The 1D model being applied is the Single-Column atmospheric chemistry and meteorological Model (SCM) (Ganzeveld et al., 2002, 2008; Kuhn et al., 2010; Seok et al., 2013; Barten et al., 2020) which is basically a 1D version of the global chemistry–climate model ECHAM/MESSy Atmospheric Chemistry (EMAC) (Jöckel et al., 2006). An advantage of the SCM is that it is computationally cheap to run. This makes it suitable for model simulations over a long period. Another application of the SCM is sensitivity analysis. In sensitivity analysis one changes certain parameters, initial or boundary conditions to investigate the effect on a certain process of interest. Because the SCM only simulates the physical and chemical processes in one column, certain assumptions have to be made on the conditions at the boundaries of the model domain. This is done in the general set-up of the modeling experiments with the 1D forcing simulated state-variables such as wind speed, moisture, temperature and some of the concentrations of long-lived trace gases to the same state-variables of 3D reanalysis data on meteorology and atmospheric composition (see Sect. 1.4.3). The SCM is especially well suited to study local-scale processes such as surface-atmosphere exchange of trace gases and further cycling of these

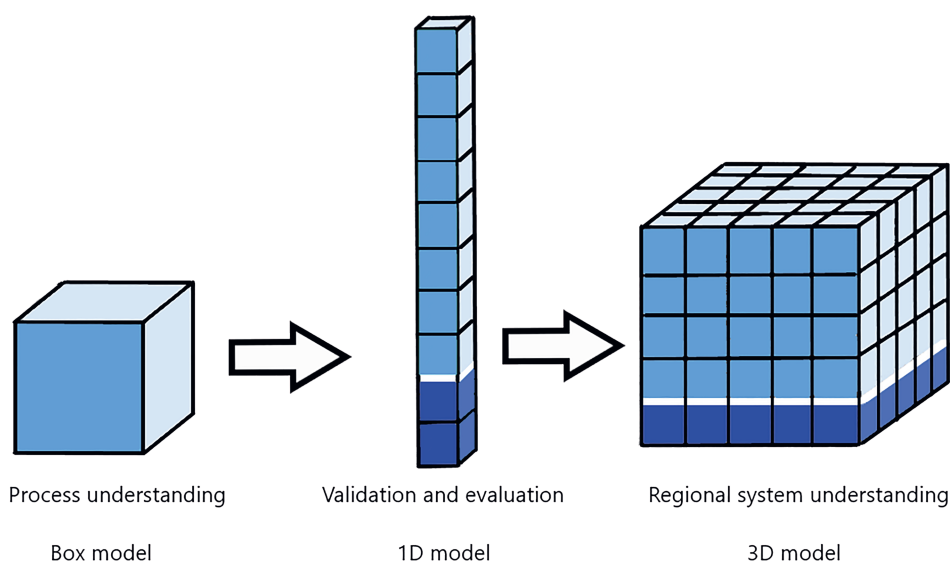


Figure 1.5: Schematic illustration of application of box models, 1D models and 3D models.

trace gases in the PBL.

The 3D model being applied is the Weather Research and Forecasting (WRF) (Skamarock et al., 2019) model coupled to Chemistry (–Chem) (Grell et al., 2005) and optimized for Polar regions (Polar–) (Bromwich et al., 2013), hereafter Polar-WRF-Chem. The Polar-WRF-Chem model is often used to study regional-scale processes and Arctic tropospheric chemistry (Sessions et al., 2011; Herrmann et al., 2021; Marelle et al., 2021). These 3D model simulations require a relatively large amount of computational resources and are typically run over time spans of one week to one month. However, they are very useful to study large-scale events such as the long-range transport of air pollution from the mid-latitudes to the Arctic, which can not be studied in a 1D setup.

This hierarchy of coupled surface–PBL meteorological–chemical modeling systems (Fig. 1.5) allows upscaling of simulated and observed exchange fluxes at a measurement scale (~ 10 – 1000 m) to the representative footprint of airborne observations (~ 1 – 10 km) and the grid-resolution of global-scale chemistry-climate models (> 100 km) to assess the impact of long-term Arctic and global climate change. Furthermore, this thesis focuses on the further development, evaluation and application of process-based model representations of surface exchange of climate-active trace gases in models.

1.4.3 Reanalysis data

Atmospheric reanalysis products are a combination of atmospheric models and observations of the atmosphere. At its core, reanalysis products are based on model simulations. Observational products are assimilated in these model simulations for a specified time span, which is typically about 3–12 hours. These observations are then used to secure that the model simulated metrics are very similar to those observations. Some examples of assimilated data to constrain 3D meteorological and atmospheric chemistry models are in-situ surface observations, radiosondes, and observations from satellites, buoys, aircrafts and ships. Reanalysis products commonly go back several decades, depending on the amount of data that is available. For example, the European Centre for Medium-Range Weather Forecasts Reanalysis version 5 (ERA5) (Hersbach et al., 2020) meteorological reanalysis is available from 1959 while the Copernicus Atmosphere Monitoring Service (CAMS) (Inness et al., 2019) chemical composition reanalysis is available from 2003. This is mainly because the CAMS reanalysis heavily relies on satellite observations of the composition of the atmosphere that got a significant boost at the beginning of this century. Similar to models, reanalysis products come in many different forms, resolution and degree of complexity (Lindsay et al., 2014; Bromwich et al., 2018). They provide full temporal and spatial coverage of many atmospheric variables and are often considered as representative datasets to study trends (Marshall et al., 2018). However, due to their observational constraints, the accuracy of reanalysis products can vary significantly depending on the location, time period and variable considered. Especially in the Arctic, where limited amount of observations are available to constrain these reanalysis products, significant biases in reanalysis data with independent observations still occur (Alexeev et al., 2012; Lindsay et al., 2014; Liu and Key, 2016).

In this thesis, I use reanalysis products as initial and boundary conditions for the local- and regional-scale modeling studies on climate-active trace gas exchange and further cycling in the Arctic troposphere. Furthermore, I use them to study trends in the composition of the Arctic atmosphere and compare them to independent observations, to address the accuracy of reanalysis products in the Arctic. Another application of reanalysis datasets I apply here is nudging model simulations to these reanalysis datasets. Nudging is a simplified form of data assimilation that adjusts model predictions towards another data source. This can either be observations, another model simulation or, in this case, reanalysis data. Because of the non-linear behaviour of the atmosphere, model simulations become less accurate over time. Therefore, adjustment of free-running model simulations to reanalysis datasets is needed to maintain reliable model estimates for longer simulations. Additionally, nudging also secures that the model simulations represent optimally the changes in synoptic conditions and atmospheric composition also reflected in the field observations (Pithan et al., 2023).

1.4.4 Modeling of ozone dry deposition

The dry deposition process of O_3 is strongly parameterized in atmospheric chemistry and transport models. Originally developed by Wesely (1989), the dry deposition velocity of O_3 (V_{d,O_3}) [$m\ s^{-1}$] is calculated using a resistance-in-series approach as

$$V_{d,O_3} = \frac{1}{r_a + r_b + r_c}, \quad (1.5)$$

where r_a represents the aerodynamic resistance [$s\ m^{-1}$], r_b represents the quasi-laminar sublayer resistance [$s\ m^{-1}$] and r_c represents the surface resistance [$s\ m^{-1}$]. This deposition velocity is then multiplied by the O_3 mixing ratio in the atmospheric surface layer ($[O_3]_{atmosphere}$) [$kg\ m^{-3}$] to arrive at the total O_3 flux (F_{O_3}) [$kg\ m^{-2}\ s^{-1}$] using

$$F_{O_3} = -V_{d,O_3} \cdot [O_3]_{atmosphere}. \quad (1.6)$$

This calculation of the O_3 surface deposition flux in Eq. 1.6 assumes a surface substrate O_3 concentration of zero. Furthermore, an assumption made is that the dry deposition velocity reflects the overall exchange velocity along the pathway, up to the point where all O_3 is removed. Both r_a and r_b strongly depend on the stability of the atmosphere and are calculated using variables such as wind speed. If wind speeds are low, the PBL is very stable and mixing is suppressed. This causes a decoupling of the surface to which O_3 is deposited and the atmosphere. Throughout this thesis, a positive flux refers to an emission from the surface to the atmosphere, whereas a negative flux refers to removal by, or deposition to the surface.

Observations of O_3 deposition over many different surfaces have indicated that uptake and final destruction of O_3 in the surface substrate is generally the limiting term. This implies that the surface resistance r_c is typically the largest resistance determining the magnitude of O_3 deposition. In atmospheric chemistry and transport models, r_c is often represented using a constant value to snow, ice and water surfaces independent of environmental factors. This is despite the fact that observations show a dependency of O_3 deposition and actual removal by the surface on multiple environmental drivers (Chang et al., 2004; Helmig et al., 2012a,b; Martino et al., 2012). In this thesis, I will evaluate those commonly applied dry deposition parameterizations to snow, ice and water surfaces and complement these by using more process-based model representations of O_3 dry deposition including estimations of r_c based on environmental drivers.

1.5 Research questions and thesis outline

As a summary of the above, I have identified several knowledge gaps in the understanding of the budgets of climate active trace gases, and the challenges related to their modeling and observations. The MOSAiC campaign, covering a full year of both polar day and night conditions, offers a unique opportunity to bring the understanding of Arctic atmospheric composition a step further.

Application of the modeling systems to address the MOSAiC objectives relies on implementation, further improvement and extensive evaluation of more process-based representations of ocean–atmosphere and sea ice–atmosphere exchange of climate–active trace gases. These representations have already been partly evaluated at a site-scale (Helmig et al., 2012b) and global scale (Ganzeveld et al., 2009) for a range of meteorological and biogeochemical conditions but not yet in detail for the Arctic environment. The MOSAiC observations provide a unique opportunity to further evaluate and improve these process-based representations of climate–active trace gas exchange and to assess implications of the diminishing sea ice cover for Arctic photochemistry and PBL dynamics. Our modeling activity also complements other MOSAiC experimental studies, e.g., planned airborne observations of concentrations of climate–active trace gases. Interpretation of these concentration measurements in terms of surface fluxes requires an inversion that accounts for PBL dynamics and chemical cycling along the transfer pathway from the surface to the altitude of these observations.

In the Sections 1.1–1.4 I have introduced the relevant concepts, processes, and observational and modeling frameworks. Below, I will define the focus and research questions of Chapters 2–5.

Chapter 2 focuses on the representation of the O_3 dry deposition process to the Arctic ocean in meso-scale 3D atmospheric chemistry and transport models. Currently, the representation of oceanic O_3 deposition in models is oversimplified, with unknown consequences for simulated surface O_3 concentrations. I will compare the skill score for a commonly applied oversimplified parameterization, and a process-based model representation accounting for various environmental drivers of ocean water O_3 uptake. These model simulations will be compared with surface O_3 observations over the Arctic land surface. I will focus on the ability of the model to explain the magnitude and temporal variability of these observations. The research questions of Chapter 2 are as follows:

- How well does a commonly applied (constant resistance) parameterization compare to the results of a process-based model representation of oceanic O_3 dry deposition?
- What is the role of oceanic ozone dry deposition in explaining the magnitude and temporal

variability of pan-Arctic surface O_3 ?

Chapter 3 focuses on the O_3 dry deposition process to the Arctic sea ice. Due to limited observations, the magnitude of O_3 deposition and consequences for the PBL O_3 budget over sea ice is unknown. In this chapter, I apply a 1D model to support analysis of the one year of O_3 flux observations over the Arctic sea ice during MOSAiC. I subsequently use the model and other complementary observations to quantify the role of dry deposition and other relevant processes on the observed O_3 concentrations in the PBL. In Chapter 3, I will answer the following research questions:

- Can I quantify the removal of O_3 by dry deposition the Arctic sea ice?
- What is the contribution of O_3 dry deposition and other processes to the observed temporal variability of O_3 over the Arctic sea ice?

Where Chapters 2 and 3 are mostly concerned with the removal of O_3 by the surface, Chapter 4 will deal with long-range transport of O_3 and other gases during a central Arctic warm air intrusion event in April 2020. I will apply a 3D atmospheric chemistry and transport model to simulate this event, evaluate the impact of various settings of the model and compare these with observations collected during MOSAiC. I will focus on the role of local– versus large–scale effects controlling the transport and further cycling of trace gases. The research questions of Chapter 4 are as follows:

- How well does a 3D atmospheric chemistry and transport model represent a central Arctic warm air intrusion considering the role of local– versus large–scale processes controlling Arctic O_3 ?
- What is the sensitivity of model simulated meteorology and trace gas concentrations to horizontal spatial resolution and selected PBL parameterization schemes?

Chapter 5 will deal with the long-term changes in Arctic atmospheric composition of climate-active trace gases and other relevant trace gases. I will put the MOSAiC observations in context of the past 18 years using a chemical reanalysis dataset. The main objectives of this chapter are twofold. Firstly, to quantify the ability of large–scale reanalysis products to represent these local–scale observations. Secondly, another objective is to address the representativeness of MOSAiC compared to the current climate. This will elucidate whether the conditions observed during MOSAiC are normal or anomalous. Additionally, I will study the magnitude and variability of CO_2 and CH_4 fluxes observed during MOSAiC. Hence, the following research questions will be answered in Chapter 5:

- Are MOSAiC observed trace gas concentrations representative for the past 18 years?
- How well do reanalysis datasets represent trace gas concentrations observed during MO-

SAiC?

- What is the magnitude and variability in surface CO₂ and CH₄ fluxes during MOSAiC?

In Chapter 6 I will summarize the findings of this thesis and directly answer the research questions defined above. Thereafter, these findings are placed into context of other research. Furthermore, the current state-of-the-art of topics relevant to this thesis will be discussed, and future perspectives and research directions will be provided.

Chapter 2

Role of oceanic ozone deposition in explaining temporal variability in surface ozone at High Arctic sites



This chapter is based on:

J. G. M. Barten, L. N. Ganzeveld, G.-J. Steeneveld and M. C. Krol (2021). Role of oceanic ozone deposition in explaining temporal variability in surface ozone at High Arctic sites. *Atmospheric Chemistry and Physics*, 21, 10229–10248. DOI: 10.5194/acp-21-10229-2021

Abstract

Dry deposition is an important removal mechanism for tropospheric ozone (O_3). Currently, O_3 deposition to oceans in atmospheric chemistry and transport models (ACTMs) is generally represented using constant surface uptake resistances. This occurs despite the role of solubility, waterside turbulence and O_3 reacting with ocean water reactants such as iodide resulting in substantial spatiotemporal variability in O_3 deposition and concentrations in marine boundary layers. We hypothesize that O_3 deposition to the Arctic Ocean, having a relatively low reactivity, is overestimated in current models with consequences for the tropospheric concentrations, lifetime and long-range transport of O_3 . We investigate the impact of the representation of oceanic O_3 deposition to the simulated magnitude and spatiotemporal variability in Arctic surface O_3 .

We have integrated the Coupled Ocean-Atmosphere Response Experiment Gas transfer algorithm (COAREG) into the mesoscale meteorology and atmospheric chemistry model Polar-WRF-Chem (WRF) which introduces a dependence of O_3 deposition on physical and biogeochemical drivers of oceanic O_3 deposition. Also, we reduced the O_3 deposition to sea ice and snow. Here, we evaluate WRF and CAMS reanalysis data against hourly averaged surface O_3 observations at 25 sites (latitudes $> 60^\circ N$). This is the first time such a coupled modeling system has been evaluated against hourly observations at pan-Arctic sites to study the sensitivity of the magnitude and temporal variability in Arctic surface O_3 on the deposition scheme. We find that it is important to nudge WRF to the ECMWF ERA5 reanalysis data to ensure adequate meteorological conditions to evaluate surface O_3 .

We show that the mechanistic representation of O_3 deposition over oceans and reduced snow/ice deposition improves simulated Arctic O_3 mixing ratios both in magnitude and temporal variability compared to the constant resistance approach. Using COAREG, O_3 deposition velocities are in the order of 0.01 cm s^{-1} compared to $\sim 0.05 \text{ cm s}^{-1}$ in the constant resistance approach. The simulated monthly mean spatial variability in the mechanistic approach (0.01 to 0.018 cm s^{-1}) expresses the sensitivity to chemical enhancement with dissolved iodide, whereas the temporal variability (up to $\pm 20\%$ around the mean) expresses mainly differences in waterside turbulent transport. The mean bias for six sites above $70^\circ N$ reduced from -3.8 to 0.3 ppb with the re-

sion to ocean and snow/ice deposition. Our study confirms that O_3 deposition to high-latitude oceans and snow/ice is generally overestimated in ACTMs. We recommend that a mechanistic representation of oceanic O_3 deposition is preferred in ACTMs to improve the modeled Arctic surface O_3 concentrations in terms of magnitude and temporal variability.

2.1 Introduction

Tropospheric ozone (O_3) is the third most important greenhouse gas and a secondary air pollutant negatively affecting human health (Nuvolone et al., 2018) and plant growth (Ainsworth et al., 2012) due to its oxidative character. O_3 shows a large spatiotemporal variability due to its relatively short lifetime (3–4 weeks) in the free troposphere compared to other greenhouse gases. Its main sources are chemical production and entrainment from the stratosphere. Its main sinks are chemical destruction and deposition to the Earth’s surface (Young et al., 2018; Tarasick et al., 2019). Understanding the Arctic O_3 budget is of particular interest because its remote location implies that anthropogenic sources and sinks are generally absent. This implies that these Arctic O_3 observations allow us to determine large-scale trends in tropospheric O_3 (Helmig et al., 2007c; Gaudel et al., 2020; Cooper et al., 2020). In the Arctic, routine tropospheric O_3 observations indicate an increasing trend up to the early 2000s which has been leveling off (Oltmans et al., 2013; Cooper et al., 2014) or decreasing at individual sites (Cooper et al., 2020) in the last decade. This upward trend can be attributed to increased emissions of precursors in the midlatitudes (Cooper et al., 2014; Lin et al., 2017), but stratosphere-to-troposphere transport may also have played a role (Pausata et al., 2012). Local emissions of precursors are expected to become an important source of Arctic O_3 concentrations due to the warming Arctic climate and increasing local economic activity (Marelle et al., 2016; Law et al., 2017). This underlines the need for understanding the sources and sinks of Arctic tropospheric O_3 and to accurately representing them in atmospheric chemistry and transport models (ACTMs).

On the global scale, dry deposition accounts for $\sim 25\%$ of the total sink term (Lelieveld and Dentener, 2000) in ACTM simulations and is especially important for the O_3 budget in the atmospheric boundary layer (ABL). Dry deposition in ACTMs is often represented as a resistance in series approach (Wesely, 1989). Herein, the total resistance r_t consists of three serial resistances: the aerodynamic resistance (r_a) representing turbulent transport to the surface, the quasi-laminar sublayer resistance (r_b) representing diffusion close to the surface and the surface resistance (r_s) expressing the efficiency of removal by the surface. The dry-deposition velocity (V_d) is then evaluated as the reciprocal of r_t . The r_a term mainly depends on the stability of the atmosphere and friction velocity (u_*) (Padro, 1996; Toyota et al., 2016). The r_b term also scales with u_* and varies with the diffusivity of the chemical species (Wesely and Hicks, 2000). Low-solubility gases like O_3 have a high r_s , in comparison to the relatively small $r_a + r_b$ term, which dominates the magnitude of the O_3 dry-deposition velocity (V_{d,O_3}). Thus, accurately representing the surface uptake efficiency of O_3 is crucial. During episodes of low wind speeds, the $r_a + r_b$ term can pose an additional restriction on the exchange of O_3 with oceans (Fairall et al., 2007).

Observed O_3 deposition to oceans (e.g., Chang et al., 2004; Clifford et al., 2008; Helmig et al.,

2012b) and coastal waters (e.g., Gallagher et al., 2001) is relatively slow ($\sim 0.01\text{--}0.1\text{ cm s}^{-1}$). However, oceanic O_3 is relevant for the global O_3 deposition budget due to the large surface area of water bodies (Ganzeveld et al., 2009; Hardacre et al., 2015). Recent experimental and modeling studies indicate the spatiotemporal variability in oceanic O_3 uptake efficiency (Ganzeveld et al., 2009; Helmig et al., 2012b; Luhar et al., 2018). However, most ACTMs often use a constant O_3 surface uptake efficiency of 2000 cm s^{-1} to water bodies, proposed by Wesely (1989), resulting in a simulated ocean V_{d,O_3} of $\sim 0.05\text{ cm s}^{-1}$. The observed V_{d,O_3} shows a larger variability including also a dependency on wind speed and sea surface temperature (SST) (Helmig et al., 2012b). The turbulence-driven enhancement by wind speed (Fairall et al., 2007) is complemented by a strong chemical enhancement of oceanic O_3 deposition associated with its chemical destruction through the oxidation of ocean water reactants such as dissolved iodide and dissolved organic matter (DOM) (Chang et al., 2004). Mechanistic O_3 deposition representations in models include the physical and biogeochemical drivers of the exchange of O_3 in surface waters (Fairall et al., 2007, 2011; Ganzeveld et al., 2009; Luhar et al., 2017, 2018). Dissolved iodide is deemed to be the main reactant of O_3 in surface waters (Chang et al., 2004) and therefore often applied in these representations. Some studies only consider dissolved iodide as a reactant (Luhar et al., 2017; Pound et al., 2019), whereas Ganzeveld et al. (2009) also included DOM as one reactant contributing to the chemical enhancement of oceanic O_3 deposition. These mechanistic deposition representations appeared to be crucial for O_3 dry-deposition modeling, the marine ABL O_3 concentrations and the potentially involved feedback mechanisms such as the release of halogen compounds as a function of O_3 deposition (Prados-Roman et al., 2015).

Up until now, earlier studies on global-scale oceanic O_3 deposition (Ganzeveld et al., 2009; Luhar et al., 2017) evaluated monthly mean surface O_3 observations (Pound et al., 2019). The implementation of these mechanistic exchange methods in ACTMs, in particular the method proposed by Luhar et al. (2018) using a two-layer model representation (compared to a bulk layer version by Ganzeveld et al., 2009), results in a $\sim 50\%$ reduction in the global mean V_{d,O_3} which affects the tropospheric O_3 burden (Pound et al., 2019). The mechanistic representation in Pound et al. (2019) especially results in a simulated decrease in V_{d,O_3} to cold polar waters with relatively low reactivity. Simulated V_{d,O_3} can be as low as 0.01 cm s^{-1} compared to the commonly applied V_{d,O_3} of 0.05 cm s^{-1} in the constant surface uptake resistance approach (Pound et al., 2019). However, the hypothesized deposition reduction to cold waters is expected to substantially affect Arctic ABL O_3 concentrations on relatively short timescales (sub-monthly) and potentially improve operational Arctic O_3 forecasts, e.g., the air quality forecasts by the Copernicus Atmosphere Monitoring Service (CAMS) (Inness et al., 2019).

The evaluation of simulated oceanic O_3 deposition in the Arctic is hampered by a lack of O_3 ocean–atmosphere flux observations and consequently relies on a comparison of simulated and

observed surface O_3 concentrations not only regarding the magnitude but in particular the temporal variability. We hypothesize that on synoptic timescales these concentrations are controlled by temporal variability in the main physical drivers of oceanic O_3 deposition, e.g., atmospheric and waterside turbulence mainly as a function of wind speed. Chemical enhancement of, e.g., iodide to O_3 deposition is anticipated to control the long-term (months) baseline level of V_{d,O_3} more associated with anticipated long-term (e.g., seasonal) changes in ocean water biogeochemical conditions (Sherwen et al., 2019). This evaluation of Arctic spatiotemporal O_3 concentrations aims to better understand the role of ocean and sea ice deposition as a potentially important but also uncertain sink impacting Arctic air pollution (Arnold et al., 2016). Furthermore, the projected opening of the Arctic Ocean, as a result of climate change, urges us to improve our understanding of Arctic Ocean–atmosphere exchange.

We aim to identify and quantify the impact of a mechanistic representation of O_3 deposition in explaining observed hourly Arctic surface O_3 concentrations, both in terms of magnitude and temporal variability. A mesoscale coupled meteorology–atmospheric chemistry model is evaluated against a large dataset of pan-Arctic O_3 observations at a high-resolution (hourly) timescale for the end of summer 2008. Using a much higher spatial and temporal resolutions compared to other global modeling studies, we aim to evaluate to what extent the role of spatiotemporal variability in O_3 deposition explains observed surface O_3 concentrations particularly regarding temporal variability. We also indicate the role of meteorology in simulating these O_3 concentrations by nudging the simulated synoptic conditions towards an atmospheric reanalysis dataset.

2.2 Methods

2.2.1 Regional coupled meteorology–chemistry model

We use the Weather Research and Forecasting model (v4.1.1) coupled to chemistry (Chem) (Grell et al., 2005) and optimized for Polar regions (Hines and Bromwich, 2008). Polar-WRF-Chem (hereafter WRF) is a non-hydrostatic mesoscale numerical weather prediction and atmospheric chemistry model used for operational and research purposes. Figure 2.1 shows the selected study area including the locations of surface O_3 observational sites selected for this study (more information in Sect. 2.2.5). WRF is set up with a polar projection centered at 90° N, 250×250 horizontal grid points (30×30 km resolution) and 44 vertical levels up to 100 hPa, with a finer vertical grid spacing in the ABL and lower troposphere. The simulation period is 8 August to 7 September 2008 including 3 d of spin-up. This end-of-summer 2008 period is chosen (1) to limit the role of active halogen chemistry during springtime (Pratt et al., 2013; Thompson et al., 2017; Yang et al., 2020) and (2) the additional availability of O_3 observations in the High Arctic

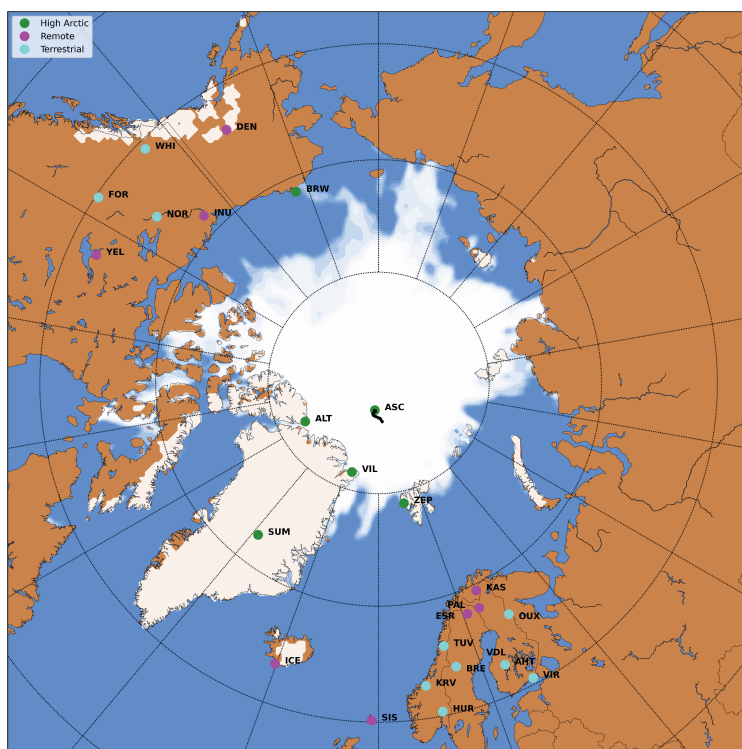


Figure 2.1: WRF domain including sea ice and snow cover at the start of the simulation. Locations with surface observations O_3 are indicated in green (High Arctic), magenta (Remote) and cyan (Terrestrial) (see Sect. 2.2.5). The drifting path of the ASCOS campaign during the simulation is indicated with the black line.

over sea ice from the Arctic Summer Cloud Ocean Study (ASCOS) campaign (Paatero et al., 2009). The ECMWF ERA5 meteorology ($0.25^\circ \times 0.25^\circ$) (Hersbach et al., 2020) and CAMS reanalysis chemistry ($0.75^\circ \times 0.75^\circ$) (Inness et al., 2019) products are used for the initial and boundary conditions. Boundary conditions, SSTs and sea ice fractions are updated every 3 h to these reanalysis products to allow for the sea ice retreat during the simulation. Other relevant parameterization schemes and emission datasets have been listed in Table A.1.1 and are mostly based on Bromwich et al. (2013).

2.2.2 Nudging to ECMWF ERA5

The first WRF simulation, without any adjustments to O_3 deposition, indicated that WRF was misrepresenting the temporal variability in surface O_3 observations, most prominently starting from a few days into the simulation. We hypothesize that this misrepresentation is

caused by deviations in the synoptic conditions in the free-running WRF simulation. This was confirmed with a comparison of simulated and satellite observed wind speeds above oceans at a spatial resolution of $0.25^\circ \times 0.25^\circ$ (Wentz and Meissner, 2004). To overcome the impact of this deficiency on our O_3 study, nudging is applied to ensure an optimal model evaluation with observations. Hence, WRF is nudged every 3 h to the ECMWF ERA5 specific humidity, temperature and wind fields in the free troposphere with nudging coefficients of 1×10^{-5} , 3×10^{-4} and $3 \times 10^{-4} \text{ s}^{-1}$, respectively.

2.2.3 Representation of ocean–atmosphere gas exchange

The Coupled Ocean-Atmosphere Response Experiment (COARE) (Fairall et al., 1996) has been developed to study physical exchange processes (sensible heat, latent heat and momentum) at the ocean–atmosphere interface. Later, COARE has been extended to include the exchange of gaseous species such as O_3 , dimethyl sulfide (DMS) and carbon dioxide (CO_2) (Fairall et al., 2011). Many studies have used the COARE Gas transfer algorithm (COAREG) in combination with eddy-covariance measurements to study the effects of wind speed and sea state on ocean–atmosphere gas exchange (e.g., Helmig et al., 2012b; Blomquist et al., 2017; Bell et al., 2017; Porter et al., 2020). Furthermore, the COAREG algorithm has also been previously used in global O_3 modeling studies (Ganzeveld et al., 2009). The choice for COAREG is further motivated by the consistent coupling with other species such as DMS.

Here we use COAREG version 3.6, which is extended with a two-layer scheme for surface resistance compared to the previous version described by Fairall et al. (2007, 2011). The two-layer scheme is similar to Luhar et al. (2018) building upon a first application of a one-layer version of COAREG by Ganzeveld et al. (2009). In that study, chemical enhancement of ocean O_3 deposition by its reaction with iodide was considered using a global climatology of ocean surface water concentrations of nitrate serving as a proxy for oceanic iodide concentrations (I_{aq}^-). Besides nitrate, satellite-derived chlorophyll- α concentrations have been used as a proxy for I_{aq}^- (Oh et al., 2008). Since then, alternative parameterizations of oceanic I_{aq}^- have been proposed (e.g., MacDonald et al., 2014) using SST as a proxy for this reactant. In COAREG, chemical reactivity of O_3 with I_{aq}^- is present through the depth of the oceanic mixing layer. O_3 loss by waterside turbulent transfer is negligible in the top water layer (few micrometers), but is accounted for in the underlying water column. The waterside turbulent transfer term is especially relevant for relatively cold waters because the chemical enhancement term is then relatively low (Fairall et al., 2007; Ganzeveld et al., 2009; Luhar et al., 2017). The last two important waterside processes that determine the total O_3 deposition are molecular diffusion and solubility of O_3 in seawater which both depend on the SST. In Appendix A.2 we list the formulation of the air side and waterside resistance terms in the COAREG routine applied in this study and show the sensitivity to the environmental factors wind speed, SST and I_{aq}^- for typical

Arctic conditions.

The COAREG algorithm is coupled such that WRF provides the meteorological and SST input for the COAREG routine. In turn, the COAREG calculated ocean–atmosphere exchange velocities are used in the WRF model to calculate the oceanic O_3 deposition flux replacing the default oceanic O_3 deposition fluxes calculated by the Wesely (1989) scheme reflecting use of the default constant r_s of 2000 s m^{-1} . For grid boxes with fractional sea ice cover, COAREG replaces the Wesely deposition scheme for the fraction that is ice free. Note that in this study, only O_3 ocean–atmosphere exchange is represented by COAREG not having modified simulations of ocean–atmosphere exchange of other compounds (e.g., DMS).

Moreover, we apply the monthly mean I_{aq}^- distribution by Sherwen et al. (2019) ($0.125^\circ \times 0.125^\circ$ resolution) which applies a machine learning approach, namely the random forest regressor algorithm (Pedregosa et al., 2011), using various physical and chemical variables such as SST, nitrate, salinity and mixed layer depth. This distribution replaces the previously applied I_{aq}^- estimations only using SST (Chance et al., 2014; MacDonald et al., 2014). At high latitudes, these I_{aq}^- distributions are highly uncertain due to the limited number of observations. The choice for Sherwen et al. (2019) is motivated by the most accurate representation of observed I_{aq}^- by the introduction of other predictors besides SST. Furthermore, this product will be further updated with newly available measurements. Figure A.3.1 shows the spatial distribution of I_{aq}^- used in the calculation of the O_3 deposition velocities. Using the Sherwen et al. (2019) distribution for August/September we found I_{aq}^- concentrations ranging between 30 and 80 nM for the open oceans up to 130 nM in coastal waters. In MacDonald et al. (2014) and Chance et al. (2014), I_{aq}^- is solely a function of SST which leads to I_{aq}^- in the order of 5 to 50 nM and thus low reactivity and O_3 deposition velocities.

2.2.4 Deposition to snow and ice

Reported atmosphere–snow gas exchange spans a wide range of observed O_3 deposition velocities. Some studies even report episodes of negative deposition fluxes (emissions) over snow or sea ice (Zeller, 2000; Helmig et al., 2009; Muller et al., 2012). Clifton et al. (2020a) recently summarized observed O_3 deposition velocities to snow having a range of -3.6 to 1.8 cm s^{-1} with most of the observations indicating a deposition velocity between 0 and 0.1 cm s^{-1} for multiple snow-covered surfaces (e.g., grass, forest and sea ice). Generally, O_3 concentrations in the interstitial air of the snowpack are lower than in the air above making the snowpack not a direct source of O_3 in terms of emissions (Clifton et al., 2020a). However, the emissions of O_3 precursors from the snowpack can enhance O_3 production in the very stable atmosphere above the snowpack (Clifton et al., 2020a). Helmig et al. (2007b) investigated the sensitivity of a global chemistry and tracer transport model to the prescribed O_3 deposition velocity and found the best

agreement between modeled and observed O_3 concentrations at four Arctic sites by applying deposition velocities in the order of $0.00\text{--}0.01\text{ cm s}^{-1}$. Following Helmig et al. (2007b) we have increased the O_3 surface uptake resistance (r_s) for snow and ice land use classes to 10^4 s m^{-1} . This corresponds to total deposition velocities of $\leq 0.01\text{ cm s}^{-1}$, which is a reduction of $\sim 66\%$ compared to the Wesely deposition routine that is the default being applied in WRF (Grell et al., 2005).

2.2.5 Observational data of surface ozone

The new modeling setup, including nudging to ECMWF ERA5 and the revised O_3 deposition to snow, ice and oceans, is evaluated against observational data of pan-Arctic surface O_3 concentrations. We expect that the different representation of O_3 deposition mostly affects O_3 concentrations in the ABL. Therefore, we evaluate our simulations against hourly averaged surface O_3 observations from 25 measurement sites above 60° N . These sites are further categorized in three site selections: “High Arctic”, “Terrestrial” and “Remote”. High Arctic refers to sites having latitudes $> 70^\circ\text{ N}$ and for which we expect that the deposition footprint is a combination of ocean and sea ice (e.g., Helmig et al., 2007c). The Terrestrial sites are located below 70° N and show a clear diurnal cycle in observed O_3 . Sites are characterized as Terrestrial when the average observed minimum nighttime mixing ratio is $> 8\text{ ppb}$ smaller than the average observed maximum daytime mixing ratio during the ~ 1 month of simulation. This criterion is based on a preparatory analysis of the observational data, footprint and site characteristics. The Remote sites have been identified as such based on their location below 70° N and showing no clear diurnal cycle in O_3 concentrations. The analysis also includes the observations during the Arctic Summer Cloud Ocean Study (ASCOS) campaign, when the icebreaker *Oden* was located in the Arctic sea ice (Tjernström et al., 2012). In total, 25 surface O_3 measurement sites are included (Fig. 2.1), of which 6, 8 and 11 sites are characterized as High Arctic, Remote and Terrestrial sites, respectively. A full list of available measurement sites is available in Table A.4.1.

2.2.6 Overview of performed simulations

In total, we perform two simulations. The first WRF simulation (NUDGED) is a run with the setup described in Sect. 2.2.1 and nudged with the synoptic conditions to the ECMWF ERA5 product as described in Sect. 2.2.2. The second simulation (COAREG) includes also includes the adjustments to the O_3 deposition to oceans as described in Sect. 2.2.3 and the O_3 deposition to snow and ice as described in Sect. 2.2.4. Furthermore, we also compare our results with the state-of-the-art CAMS global reanalysis data product (Inness et al., 2019). This product has a temporal resolution of 3 h, a spatial resolution of $0.75^\circ \times 0.75^\circ$ and does not include a mechanistic representation of ocean–atmosphere O_3 exchange. CAMS assimilates satellite observations of O_3 but it does not assimilate O_3 observations from radiosondes or in

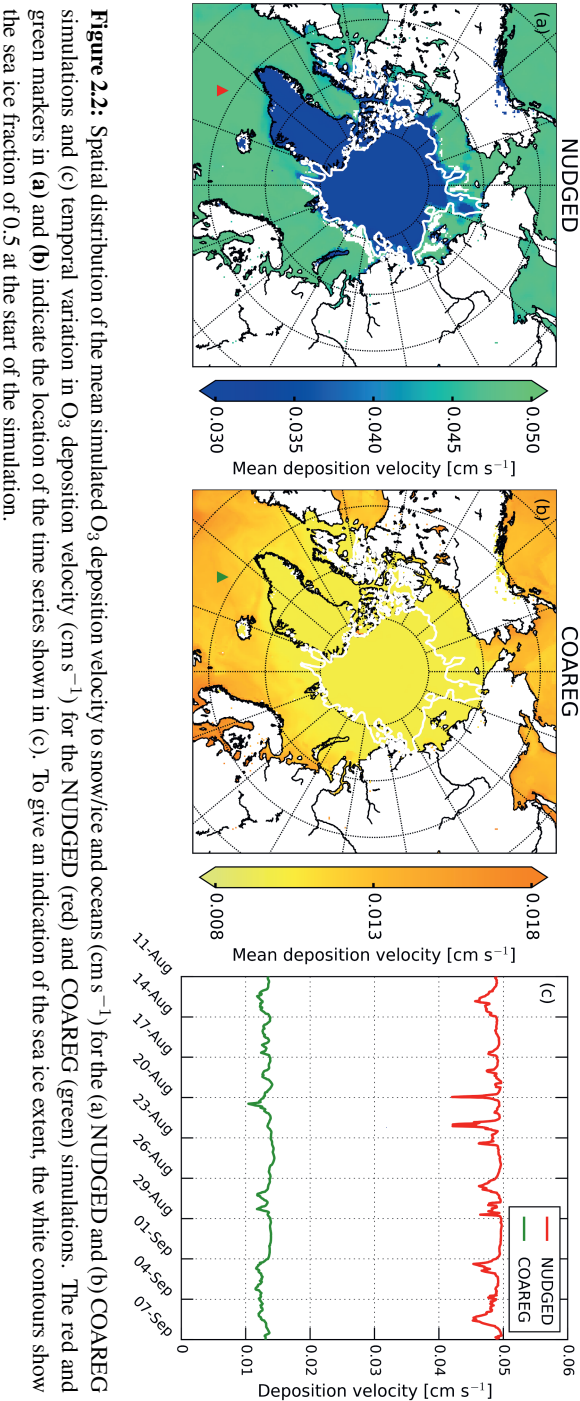
situ measurement sites such as the 25 sites used in the evaluation presented here. This implies that lower-tropospheric O_3 is weakly constrained by observations in this CAMS product making an accurate model representation of the sources and sinks important. We opted to include the CAMS reanalysis data as another tool to study Arctic surface O_3 and to address potential limitations in its model setup. Moreover, CAMS is being widely used for air quality forecasts and assessments but also to constrain regional-scale modeling experiments such as presented in this study. Therefore, an analysis of the performance of the CAMS reanalysis data might also benefit future Arctic air quality assessments.

2.3 Results

2.3.1 Dry-deposition budgets and distribution

Figure 2.2a and b show the mean deposition velocities for the NUDGED and COAREG runs, respectively. As expected, in the NUDGED run (Fig. 2.2a) the mean V_{d,O_3} to oceans is in the order of 0.05 cm s^{-1} . Furthermore, the spatial distribution shows a relatively low heterogeneity and no increase in deposition velocities towards the warmer waters. The COAREG run (Fig. 2.2b) provides a mean V_{d,O_3} in the order of 0.01 cm s^{-1} for the Arctic Ocean $> 70^\circ \text{ N}$ up to 0.018 cm s^{-1} for oceans with high I_{aq}^- concentrations (Fig. A.3.1). Simulated oceanic O_3 deposition is elevated in coastal waters (e.g., Baltic Sea and around the Bering Strait) with I_{aq}^- concentrations reaching up to 130 nM compared to $30\text{--}50 \text{ nM}$ for the open Arctic Ocean waters (Fig. A.3.1). This highlights the sensitivity of the COAREG scheme to chemical enhancement with dissolved iodide.

Figure 2.2c shows the temporal variability in V_{d,O_3} for one of the grid boxes, which is in terms of temporal variability representative of the whole domain. The temporal variability in the NUDGED run is mainly governed by temporal variability in r_a . During episodes with high wind speeds ($> 10 \text{ m s}^{-1}$), r_a becomes so small that it is negligible over the constant surface uptake resistance of 2000 s m^{-1} , corresponding to a maximum V_{d,O_3} of 0.05 cm s^{-1} . During episodes with low wind speeds ($< 5 \text{ m s}^{-1}$), reduced turbulent transport poses some additional restriction on O_3 removal with increasing r_a , which reduces the V_{d,O_3} to $\sim 0.04 \text{ cm s}^{-1}$. In the COAREG run, temporal variability in V_{d,O_3} is also governed by wind speeds that control the waterside turbulent transport of O_3 in seawater besides atmospheric turbulent transport. For high wind speeds, the waterside turbulent transport increases (Fig. A.2.1) and more O_3 is transported through the turbulent layers. For our simulation, we found that the temporal variability in O_3 deposition due to waterside turbulent transport can be up to $\pm 20\%$ around the mean. Only during episodes of very low wind speeds ($< 2.5 \text{ m s}^{-1}$) does the $r_a + r_b$ term pose an additional restriction on O_3 deposition in the COAREG run. Overall, the V_{d,O_3} to oceans in the COAREG



run is reduced by $\sim 60\%$ – 80% compared to the NUDGED run. The mean V_{d,O_3} to snow and ice is reduced by $\sim 66\%$, from $\sim 0.03 \text{ cm s}^{-1}$ in the NUDGED run to $\sim 0.01 \text{ cm s}^{-1}$ in the COAREG run.

The temporal evolution in oceanic O_3 deposition velocities simulated by the COAREG run appears to be on the low side of observed V_{d,O_3} and of that simulated elsewhere (e.g., Chang et al., 2004; Oh et al., 2008; Ganzeveld et al., 2009). Chang et al. (2004) showed that V_{d,O_3} can increase by a factor of 5 with wind speed increasing from 0 to 20 m s^{-1} . Luhar et al. (2017) (their Fig. 7) shows a wide range of observed and simulated sensitivities to wind speed. Observations from the TexAQSO6 summer campaign in the Gulf of Mexico show a large sensitivity to 10 m wind speeds even though the model seems unable to capture these high deposition velocities at high wind speeds (Luhar et al., 2017). However, Luhar et al. (2017) also shows that for the GasEx08 campaign in the cold Southern Ocean the sensitivity of observed and simulated V_{d,O_3} to 10 m wind speeds is very limited. This limited sensitivity is most accurately represented by the modified two-layer reactivity scheme compared to the older one-layer scheme due to a more limited interaction between chemical reactivity and waterside turbulent transport (Luhar et al., 2017). Furthermore, the variability around the mean presented in Table 2.1 ($0.012 \pm 0.002 \text{ cm s}^{-1}$) seems to correspond to the Oh et al. (2008) ($0.016 \pm 0.0015 \text{ cm s}^{-1}$) 1-month simulation including O_3 removal by I_{aq}^- . In this study we show the intra-monthly variability in oceanic O_3 deposition, which is expected to be relatively low compared to the seasonal variability which will also be driven by temporal changes in solubility and reactivity due to the seasonal changes in SST and I_{aq}^- .

By estimating the total deposition flux for the water, snow/ice and land surfaces we can quantify the total simulated O_3 deposition budget (Table 2.1) for the Arctic modeling domain. Land, not covered with snow or ice, is the dominant surface type for this specific domain setup in summer with 48 %. Combined with a relatively high simulated V_{d,O_3} of $\sim 0.45 \text{ cm s}^{-1}$, this is the most important sink, in terms of deposition, of simulated O_3 with $\sim 135 \text{ Tg } O_3 \text{ yr}^{-1}$. The simulated O_3 deposition budget to water bodies, covering 37 % of the total surface area, contributes $\sim 10\%$ in the NUDGED run ($15.4 \text{ Tg } O_3 \text{ yr}^{-1}$) to the total O_3 deposition sink. In the COAREG run, this reduces to only $\sim 3\%$ ($4.6 \text{ Tg } O_3 \text{ yr}^{-1}$) of the total O_3 deposition sink. Simulated O_3 deposition to snow and ice, covering 15 % of the total surface area, is the least important deposition sink removing 4.1 and $1.7 \text{ Tg } O_3 \text{ yr}^{-1}$ in the NUDGED and COAREG runs, respectively.

2.3.2 Simulated and observed monthly mean surface ozone

Figure 2.3 shows the spatial distribution in the simulated mean surface O_3 mixing ratios overlain with the observed mean surface O_3 mixing ratios. In the NUDGED and COAREG runs (Fig. 2.3a and b, respectively) we find similar surface O_3 mixing ratios of ~ 15 – 20 ppb over the Russian,

Table 2.1: Mean simulated O₃ deposition velocity (\pm standard deviation) (cm s^{-1}) and total simulated deposition budget ($\text{Tg O}_3 \text{ yr}^{-1}$) for the NUDGED and COAREG runs to water, snow/ice and land each representing 37 %, 15 % and 48 % of the total surface area, respectively. The standard deviation gives an indication of the spatiotemporal variability in simulated O₃ deposition velocities.

	Water (37 %)	Snow/ice (15 %)	Land (48 %)	Total (100 %)
NUDGED	Deposition velocity (\pm SD) (cm s^{-1})	0.047 (± 0.003)	0.030 (± 0.000)	0.449 (± 0.225)
	Deposition budget ($\text{Tg O}_3 \text{ yr}^{-1}$)	15.4	4.1	133.4
COAREG	Deposition velocity (\pm SD) (cm s^{-1})	0.012 (± 0.002)	0.010 (± 0.000)	0.448 (± 0.251)
	Deposition budget ($\text{Tg O}_3 \text{ yr}^{-1}$)	4.6	1.7	135.8

142.1

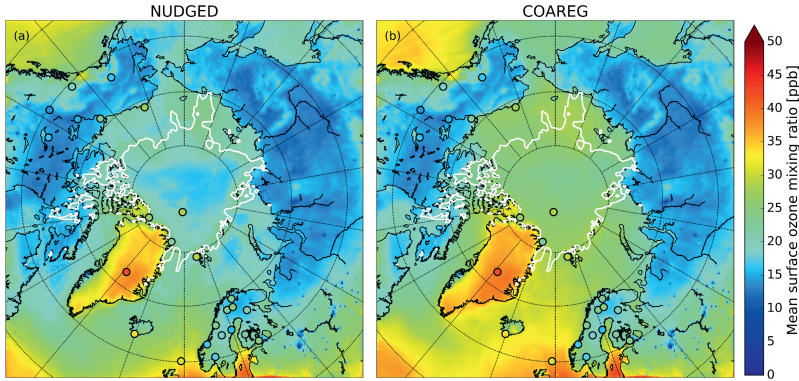


Figure 2.3: Spatial distribution of the simulated mean surface O_3 mixing ratio (ppb) for the (a) NUDGED and (b) COAREG runs. The filled circles indicate the mean observed ozone mixing ratios (ppb) for the simulated period. To indicate the sea ice extent, the white contours show the sea ice fraction of 0.5 at the start of the simulation.

Canadian and Alaskan landmasses. Over Scandinavia, slightly higher surface O_3 mixing ratios of $\sim 20\text{--}25$ ppb are simulated due to more anthropogenic emissions of precursors in the EDGAR emission inventory and advection of O_3 and its precursors from outside the domain. As expected, we find a limited effect of reduced deposition to water and snow/ice to the simulated mean O_3 mixing ratios over land. In general, the model appears to simulate the mean observed surface O_3 mixing ratios for the Remote and Terrestrial sites (all sites $< 70^\circ \text{N}$) generally well without clear positive or negative bias. Due to the altitude effect, relatively high surface O_3 concentrations are simulated over Greenland even though the deposition velocity to snow and the surrounding oceans is of similar magnitude ($\sim 0.01 \text{ cm s}^{-1}$).

The reduced O_3 deposition to water and snow/ice surfaces, comparing the NUDGED and COAREG simulation results (Sect. 2.3.1, Table 2.1), appears to be limited in terms of relative changes in V_{d,O_3} and the total simulated O_3 deposition budget. However, these relatively small changes do substantially affect the simulated spatial distribution of surface O_3 mixing ratios over oceans and sea ice as indicated in Fig. 2.3. We find that the NUDGED run (Fig. 2.3a) systematically underestimates the mean observed surface O_3 mixing ratios for the High Arctic sites (all sites $> 70^\circ \text{N}$) by $\sim 5\text{--}10$ ppb, which appears to be caused by an overestimated deposition to ocean, snow and ice surfaces, also further substantiated by the following analysis of temporal variability in O_3 concentrations (Sect. 2.3.3). Over the Arctic sea ice and oceans the ABL is typically very shallow and atmospheric turbulence is relatively weak. This suppresses vertical mixing and entrainment of O_3 -rich air from the free troposphere. Dry deposition of O_3 to the

ocean or snow/ice surfaces appears to be an important removal mechanism that has a large impact on O_3 concentrations in these shallow ABLs (Clifton et al., 2020b) both in terms of magnitude but also temporal variability (see Sect. 2.3.4). In the COAREG run, surface O_3 mixing ratios over oceans and Arctic sea ice have increased by up to 50 %. Furthermore, the reduced deposition to snow/ice has also clearly affected simulated surface O_3 mixing ratios over Greenland. Most importantly, the negative bias in simulated surface O_3 mixing ratios is reduced in the COAREG run with respect to the NUDGED run (see Sect. 2.3.3).

2.3.3 Simulated and observed hourly surface ozone

In this section we show how the application of the revised deposition scheme improves the model prediction scores of surface O_3 concentrations reflected in a comparison of the simulated and observed hourly surface O_3 mixing ratios at the three site selections (High Arctic, Remote and Terrestrial). To our knowledge, this is the first time such an oceanic O_3 deposition scheme coupled to a meteorology–chemistry model has been evaluated against a large dataset of hourly surface O_3 observations. Figure 2.4 shows a comparison between observed and simulated hourly surface O_3 mixing ratios subdivided into the three site selections: High Arctic, Remote and Terrestrial. As expected, for the High Arctic sites (Fig. 2.4, top row) we find that the NUDGED run is underestimating the observed surface O_3 mixing ratios with a mean bias of -3.8 ppb, which is also consistent with the findings in Fig. 2.3, where the NUDGED run appears to underestimate surface O_3 mixing ratios in the High Arctic region. The COAREG run, having a reduced O_3 deposition sink to oceans and snow/ice appears to better represent the surface O_3 observations with a slight positive bias of 0.3 ppb. The mean absolute error (MAE) in the COAREG run is reduced to 4.7 ppb from 6.4 ppb for the NUDGED run. Furthermore, we find that the CAMS reanalysis data also underestimate surface O_3 in the High Arctic with a bias of -5.0 ppb and an MAE of 6.8 ppb. Note that the performance for the WRF runs and CAMS reanalysis product varies for each observational site, which is further examined in Sect. 2.3.4.

For the Remote sites (Fig. 2.4, middle row), having no clear diurnal cycle in surface O_3 , we again find an improvement by including the mechanistic ocean deposition routine and reduced snow/ice deposition. This improvement appears to be most pronounced for coastal sites like Stórhöfði (63.4° N, 20.3° W) and Inuvik (68.4° N, 133.7° W) with a reduction in the MAE of 32 % and 19 %, respectively (not shown here). Overall, the improvement for the COAREG compared to the NUDGED run in the Remote site selection is not as significant compared to the High Arctic sites, also because of the larger role of O_3 deposition to land and vegetation, which remained unchanged in this study. We find that the CAMS data show the best performance for the Remote sites with no bias and with an MAE of 5.6 ppb.

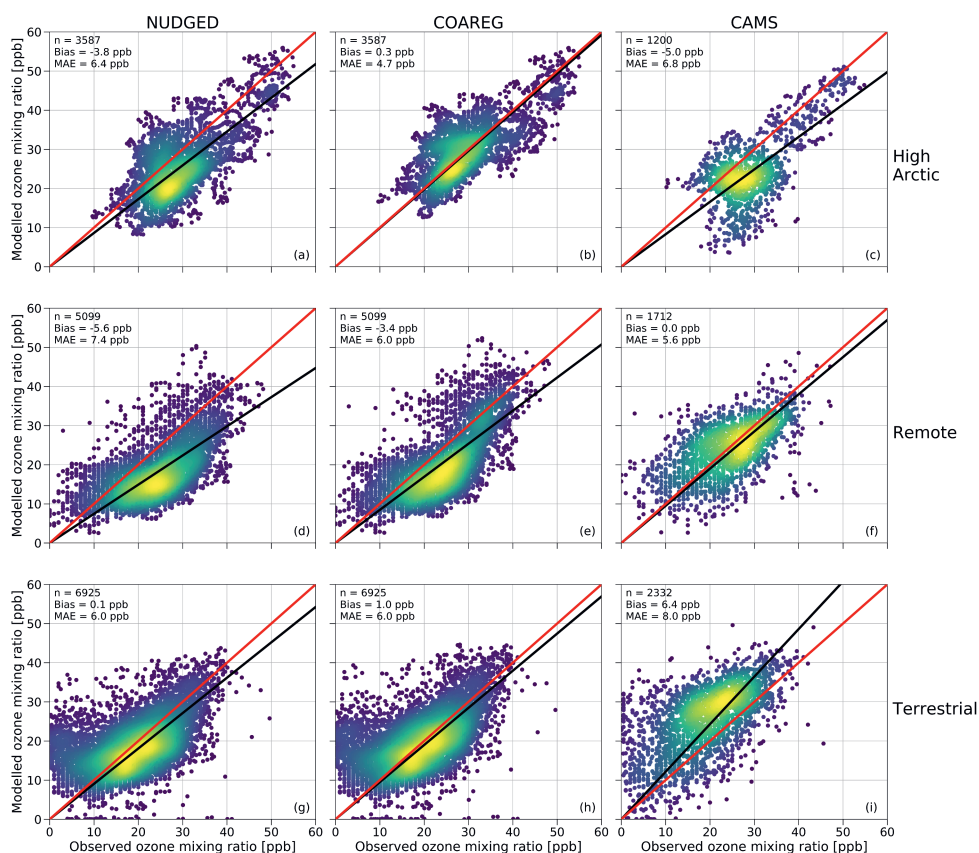


Figure 2.4: Comparison of the hourly observed and simulated ozone mixing ratios (ppb) for the NUDGED (a, d, g) and COAREG (b, e, h) runs and CAMS data (c, f, i) for the High Arctic (a–c), Remote (d–f) and Terrestrial (TE) (g–i) sites. The red line indicates the 1 : 1 line and the black line indicates the ordinary least squares regression line through the origin. The number of data points (n), bias (ppb) and mean absolute error (MAE) (ppb) are shown in the top left corner. The colors represent the multivariate kernel density estimation with yellow colors having a higher density.

For the Terrestrial sites (Fig. 2.4, bottom row), having a clear diurnal cycle in surface O_3 , the WRF runs slightly overestimate the observed surface O_3 mixing ratios with mean biases of 0.1 and 1.0 ppb for the NUDGED and COAREG runs, respectively. Reducing the O_3 deposition to oceans and snow/ice increases the bias, but the MAE of 6.0 ppb remains unchanged. The CAMS reanalysis data appear to perform worst for the Terrestrial sites with a bias of 6.4 ppb and an MAE of 8.0 ppb. This might be explained by the lower spatial and temporal resolution of CAMS specifically at these sites having a relatively strong diurnal cycle in ABL dynamics, O_3 deposition to vegetation and O_3 concentrations. Also a misrepresentation of emissions of precursor emissions and concentrations and the O_3 deposition to vegetation (Michou et al., 2005; Val Martin et al., 2014) might explain some of the differences.

2.3.4 Temporal variability of surface ozone in the High Arctic

In Sect. 2.3.3 we have shown how revising the O_3 deposition scheme to oceans and snow/ice can improve the model's capability to represent the observed hourly surface O_3 mixing ratios, especially for the High Arctic sites. In this section we show how the NUDGED and COAREG runs and CAMS represent the temporal variation in High Arctic surface O_3 observations, focusing on 6 out of the 25 measurement sites. These six High Arctic sites have been selected due to their deposition footprint being dominated by transport over, and deposition to, ocean and sea-ice-covered surfaces. Figure 2.5 shows the observed and simulated surface O_3 time series for ASCOS, Summit, Villum, Zeppelin, Barrow and Alert. Furthermore, Table 2.2 shows the model skill indicators for the High Arctic sites. These skill indicators include the mean absolute error (MAE) that represents the systematic error, the standard deviation of observation minus model prediction σ_{o-p} that represents the random error, and the Pearson R correlation coefficient (R) that represents the degree of correlation.

The observations at ASCOS (Fig. 2.5a) show a sudden increase in surface O_3 mixing ratios from 20 to over 30 ppb around the 17 August due to advection of relatively O_3 -rich air during a synoptically active period (Tjernström et al., 2012). Only the COAREG run appears to be able to simulate a similar increase in surface O_3 , while NUDGED and CAMS show a minor increase in simulated surface O_3 . From the 17 August onwards, the observations show mixing ratios between 25 and 35 ppb. The WRF simulations indicate advection of air over ocean and ice surfaces during this time period (not shown here). In the COAREG simulation, with less deposition to these surfaces, surface O_3 mixing ratios are less depleted. Only the COAREG run is able to represent these observed mixing ratios with a bias of -2.0 ppb, whereas NUDGED and CAMS are clearly biased towards lower mixing ratios.

At Summit (Fig. 2.5b), we find a large temporal variability in observed surface O_3 between 30 and 55 ppb. From the 11 August onwards we find a decreasing trend in observed surface

Table 2.2: MAE (ppb), σ_{o-p} (ppb) and Pearson R correlation coefficient (R) (–) for the NUDGED and COAREG runs and CAMS reanalysis data at the ASCOS, Summit, Villum, Zeppelin, Barrow and Alert observational sites. The lowest model error and highest correlation have been made bold for every site.

	ASCOS			Summit			Villum			Zeppelin			Barrow			Alert		
	MAE	σ_{o-p}	R	MAE	σ_{o-p}	R	MAE	σ_{o-p}	R	MAE	σ_{o-p}	R	MAE	σ_{o-p}	R	MAE	σ_{o-p}	R
NUDGED	9.4	4.3	0.46	7.5	7.0	0.62	5.4	5.7	0.46	7.4	4.8	0.62	5.5	4.6	0.49	4.4	5.1	0.68
COAREG	3.1	3.2	0.67	6.1	5.8	0.67	7.8	4.5	0.6	3.6	4.3	0.69	3.4	4.2	0.6	3.6	4.3	0.74
CAMS	7.5	4.5	0.07	3.9	4.3	0.78	4.5	4.5	0.38	11.1	5.3	0.4	11.1	4.9	0.56	3.0	3.4	0.65

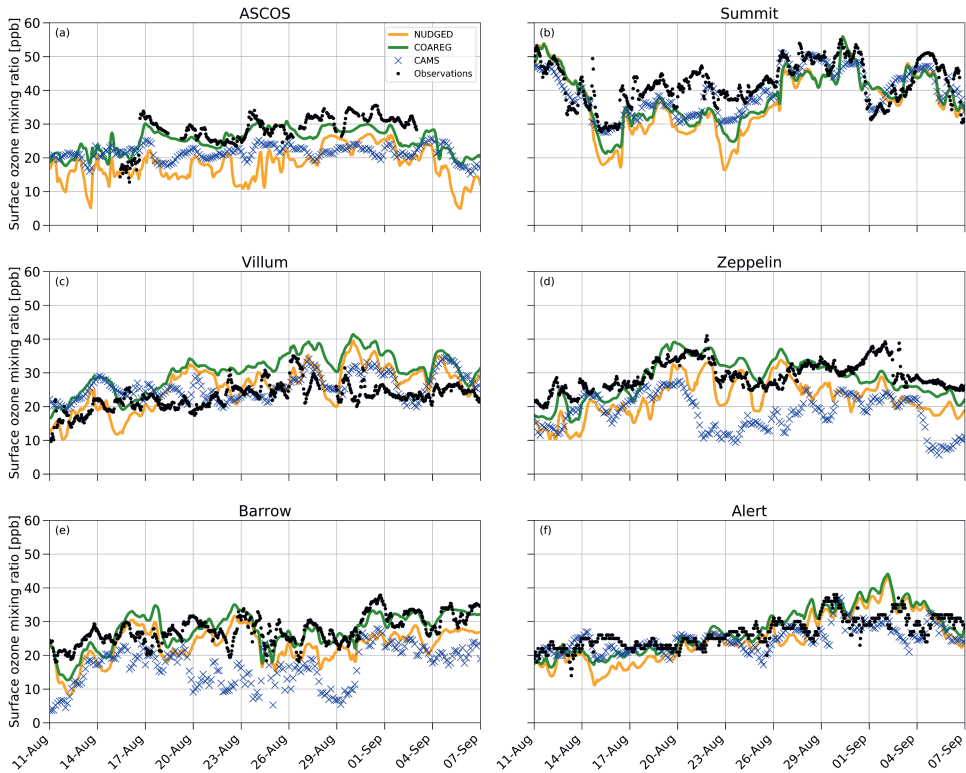


Figure 2.5: Temporal evolution of hourly surface O_3 mixing ratios (ppb) for the NUDGED (yellow) and COAREG (green) runs, CAMS data (blue crosses) and observations (black dots) at ASCOS ($\sim 87.4^\circ$ N, $\sim 6.0^\circ$ W), Summit (72.6° N, 38.5° W), Villum (81.6° N, 16.7° W), Zeppelin (78.9° N, 11.9° E), Barrow (71.3° N, 156.6° W) and Alert (82.5° N, 62.3° W).

O_3 down to 30 ppb before increasing to 40 ppb around the 17 August. All models capture this specific event in terms of temporal variability even though NUDGED and COAREG are still biased at the observed minimum of 30 ppb. Furthermore, we find that the CAMS reanalysis data represent this specific period very well, also in terms of magnitude. At Summit, the increase in surface O_3 in the COAREG run relative to the NUDGED run mostly reflects the reduction in deposition to snow and ice due to the prevailing katabatic wind flow (Gorter et al., 2014). During episodes with low wind speeds the ABL becomes very stable and shallow during which deposition to snow and ice becomes an important process in removing O_3 in the ABL. In the period between the 14 and 26 August this reduction in deposition can increase the surface O_3 mixing ratios of up to 10 ppb (e.g., 23 August). In contrast, during episodes with higher wind speeds and deeper ABLs the reduced O_3 deposition to snow hardly affects the simulated surface O_3 concentrations. Interestingly, we find that the NUDGED and COAREG simulations show a

larger negative bias ($\sim 5\text{--}10$ ppb) during the period with low wind speeds and shallow ABLs. Over the entire simulated period, CAMS performs best at Summit, with an MAE of 3.9 ppb, followed by COAREG, with an MAE of 6.1 ppb.

Villum (Fig. 2.5c) is the only site for which the NUDGED and COAREG runs as well as the CAMS reanalysis data all systematically overestimate the observed mixing ratios, especially later into the simulation. The observations show an increase in O_3 mixing ratios from 10 to 20 ppb in the first 3 d of the simulation, whereafter it remains between 20 and 30 ppb with relatively low temporal variability compared to some of the other sites (e.g., Summit, Barrow). Both the NUDGED and COAREG runs simulate mixing ratios of up to 40 ppb, and CAMS simulates maximum surface O_3 mixing ratios of 35 ppb. In terms of representing the magnitude of surface O_3 mixing ratios CAMS performs best with an MAE of 4.5.

Zeppelin (Fig. 2.5d) and Barrow (Fig. 2.5e) show similar behavior in terms of observation–model comparison. For both locations the CAMS reanalysis data systematically underestimate observed O_3 mixing ratios with a biases > 10 ppb. In the NUDGED run the bias equals -6.9 and -4.6 ppb for Zeppelin and Barrow, respectively. In the COAREG run the bias is reduced to -1.0 and -0.2 ppb for Zeppelin and Barrow, respectively. This reduction in bias is, together with ASCOS, the largest among the six High Arctic sites and shows the large sensitivity to the representation of O_3 deposition. At Barrow, the dominant wind directions during the simulation period are NW–NE reflecting a footprint mostly from the Arctic sea ice and ocean. Especially in the period from the 23 August onward, the COAREG run is very accurate in representing the magnitude as well as the temporal variability in observed surface O_3 . During this period, the NUDGED run simulates surface O_3 mixing ratios of up to 5 ppb lower due to the overestimated deposition to oceans and sea ice. At both sites, the model performance of COAREG is in the same order of magnitude, with an MAE, σ_{o-p} and R of 3.5 ppb, 4.2 ppb and 0.65, respectively.

At Alert (Fig. 2.5f), we find a relatively steady increase in observed surface O_3 from 20 ppb at the start of the simulation to 30 ppb at the end of the simulation. The temporal variability, both in observed and simulated surface O_3 , appears to be lower compared to some of the other High Arctic sites. Again, the statistical parameters such as MAE, σ_{o-p} and R improve in the COAREG run with respect to the NUDGED run. At Alert, we find that CAMS has the lowest MAE and σ_{o-p} of 3.0 and 3.4 ppb, respectively.

The model performance in terms of temporal variability in surface O_3 observations is diagnosed by using the Pearson R correlation coefficient. The model performance improved for all six sites in the COAREG run with respect to the NUDGED run. The COAREG simulation performs best for five out of the six observational sites in terms of Pearson R correlation coefficient and is only outperformed by CAMS at Summit. Overall, we find that coupling the WRF model to the mechanistic COAREG ocean–atmosphere exchange representation decreases the MAE and

σ_{o-p} for all High Arctic sites except for Villum by better representing the magnitude of, but also temporal variability in observed surface O_3 . The CAMS reanalysis data perform well for some locations (e.g., Summit, Alert), while for Zeppelin and Barrow the discrepancy is among the largest we found in the observation–model comparison.

2.4 Discussion

This study demonstrates the impact of a mechanistic representation of ocean–atmosphere O_3 exchange to simulate the magnitude and temporal variability of hourly surface O_3 concentrations in the Arctic at 25 sites. We show that the modeled sensitivity of the surface O_3 concentrations to the representation of O_3 to ocean, ice and snow surfaces is high, even though the total deposition budget is an order of magnitude smaller than the deposition budget to land and vegetation. Using a mechanistic oceanic O_3 deposition representation and reduced O_3 deposition to snow and ice greatly reduced the negative bias in surface O_3 , especially in the High Arctic. Furthermore, the temporal variability in surface O_3 was also better represented by the mechanistic representation of oceanic O_3 deposition also accounting for temporal variations in the driving processes of oceanic O_3 deposition such as waterside turbulent transport. This analysis also shows a discrepancy in the representation of simulated O_3 at sites having a terrestrial footprint (e.g., Norway, Sweden, Finland). However, the model representation of O_3 deposition to vegetation and land, including diurnal and seasonal variability (Lin et al., 2019), is beyond the scope of this study. To find out whether the implementation of a mechanistic representation of oceanic O_3 deposition specifically affects the variability of surface O_3 at certain timescales, we have performed an additional wavelet analysis (Torrence and Compo, 1998). For the six High Arctic sites we found that $\sim 55\%$ – 70% of the simulated and observed signal is present at timescales > 4 d representing the longer timescales and synoptic variability in wind speeds and vertical and horizontal mixing conditions. Interestingly, we found that the observations show more variability compared to the model simulations at timescales of hours, arguably due to the misrepresentation of some sub-grid processes. We do not find any clear indication that the implementation of COAREG significantly affects the variability of surface O_3 at High Arctic sites at a specific timescale.

The COAREG scheme has been developed and validated against eddy-covariance measurements over mostly subtropical waters (Bariteau et al., 2010; Helmig et al., 2012b) and has been applied to study the effects of wind speed and sea state on ocean–atmosphere gas transfer (Blomquist et al., 2017; Bell et al., 2017; Porter et al., 2020). We do expect that these main drivers, i.e., waterside turbulent transfer and chemical enhancement with dissolved iodide, also control oceanic O_3 deposition at high latitudes. Indirect evaluation of oceanic O_3 deposition through a comparison of surface O_3 observations instead of direct oceanic O_3 flux measurements indicates that including this mechanistic representation of O_3 deposition improves both the

modeled magnitude and temporal variability in surface O_3 observations. However, a lack of oceanic O_3 deposition flux measurements hampers the direct model evaluation of the high-latitude O_3 deposition flux. This is expected to be soon resolved by getting access to O_3 flux observations collected in the Multidisciplinary drifting Observatory for the Study of Arctic Climate (MOSAiC) 1-year field campaign.

Furthermore, we have reduced the deposition to snow and ice following Helmig et al. (2007b) and Clifton et al. (2020a). The results of Helmig et al. (2007b) also motivated follow-up observational and modeling studies aiming at the development of more mechanistic representations of O_3 deposition to snow-/ice-covered surfaces. For example, efforts have been made to simulate O_3 dynamics in and above the snowpack using a 1D model setup to explain observations of O_3 and NO_x concentrations measured above and inside the Summit snowpack (van Dam et al., 2015). This 1D modeling study suggested the role of aqueous-phase oxidation of O_3 with formic acid in the snowpack (Murray et al., 2015). Comparable 1D modeling studies focused on assessing the role of catalytic O_3 loss via bromine radical chemistry in the snowpack interstitial air (Thomas et al., 2011; Toyota et al., 2014). However, these studies mainly addressed the role of some of this snowpack chemistry in explaining, partly observed, O_3 concentrations and not so much on snow–atmosphere O_3 fluxes and derived deposition rates that would corroborate the inferred very small O_3 deposition rates by Helmig et al. (2007b). Clifton et al. (2020a) summarized that accurate process-based modeling of O_3 deposition to snow requires a better understanding of the underlying processes and dependencies. An eddy-covariance system that has been deployed as part of the MOSAiC campaign will further enhance our understanding of O_3 deposition in shallow ABLs at high latitudes (Clifton et al., 2020b).

In this study we used the COAREG transfer algorithm version 3.6, which is extended with a two-layer scheme for surface resistance compared to the previous versions (Fairall et al., 2007, 2011) and is similar to Luhar et al. (2018). Our WRF simulations excluded the additional role of chlorophyll, dissolved organic matter (DOM) or other species such as DMS on chemical enhancement of O_3 in surface waters. Experimental studies have shown that DMS, chlorophyll or other reactive organics may enhance the removal of O_3 at the sea surface (Chang et al., 2004; Clifford et al., 2008; Reeser et al., 2009; Martino et al., 2012). The global modeling study by Ganzeveld et al. (2009) included a chlorophyll– O_3 reactivity that increased linearly with chlorophyll concentration as a proxy for the role of DOM in oceanic O_3 deposition. Including this reaction substantially enhances O_3 deposition to coastal waters such that actually observed O_3 deposition to these coastal waters is well reproduced (Ganzeveld et al., 2009). Other studies such as Luhar et al. (2017) and Pound et al. (2019) ignored the potential role of DOM– O_3 chemistry in oceanic O_3 deposition. Luhar et al. (2018), who did not explicitly consider coastal waters, even suggested that including such a reaction deteriorates the comparison with O_3 flux observations above open oceans. To test the sensitivity of our model setup to other

reactants in the surface water we have performed an additional sensitivity analysis including the chlorophyll- O_3 and DMS- O_3 reactions from Ganzeveld et al. (2009). Oceanic chlorophyll concentrations have been retrieved from the 9×9 km resolution MODIS chlorophyll- α dataset available at https://modis.gsfc.nasa.gov/data/dataproduct/chlor_a.php (last access: 14 August 2020). Chlorophyll- α concentrations are typically $< 3 \text{ mg m}^{-3}$ for open oceans and up to 25 mg m^{-3} for coastal waters. For oceanic DMS concentrations, we use the monthly climatology from Lana et al. (2011). The sensitivity study with chlorophyll as an additional reactant indicated a slight increase (up to 5 %) in deposition to coastal waters with chlorophyll concentrations of up to 25 mg m^{-3} . However, the resulting effect on surface O_3 concentrations was not significant due to the large fraction of oceans with very low ($< 3 \text{ mg m}^{-3}$) chlorophyll- α concentrations. Also, the reactions with oceanic DMS appear to be weak due to relatively low DMS concentrations in August/September. These sensitivity studies indicate that I_{aq}^- is the main driver of chemical reactivity of O_3 in the Arctic Ocean in summer. However a potential sensitivity of these reactants on Arctic O_3 deposition could be expected especially in the spring to summer transition following algal blooms (Stefels et al., 2007; Riedel et al., 2008).

We nudged the WRF model to the ECMWF ERA5 reanalysis product to ensure a fair model evaluation with observations due to a better representation of the synoptic conditions. This indicated the important role of the model representation of meteorology, e.g., the advection of polluted air and mixing/entrainment of O_3 in the ABL, in representing the observed surface O_3 concentrations. The model evaluation was set up at a resolution of 30×30 km, which is in the order of the ERA5 reanalysis data ($0.25^\circ \times 0.25^\circ$) used for initial conditions, boundary conditions and nudging. Here, we opted for a 30 km grid spacing because we expect that the main drivers of tropospheric O_3 (chemical production and destruction, stratosphere–troposphere transport, dry deposition, mixing and advection processes) can be sufficiently resolved at this grid spacing especially over the relatively homogeneous ocean, ice and snow surfaces. However, we do realize that such a coarse grid spacing may have hampered representing local air flow phenomena such as katabatic winds (Klein et al., 2001), which could explain some of the mismatch at sites like Villum (Nguyen et al., 2016). Another justification for the 30 km grid spacing was to limit computational time and to have a large enough domain to cover the entire region above 60°N to conduct a large pan-Arctic evaluation while at the same time having all observational sites far enough from the domain boundaries to limit the effect of the imposed meteorological and chemical boundary conditions.

In general, the relatively scarce Arctic observations limit evaluation of modeling studies and extrapolation of these results for the Arctic summer to other seasons and lower latitudes. In this case, this includes the uncertainty in the magnitude and distribution of driving factors of oceanic O_3 deposition such as I_{aq}^- or DOM. New I_{aq}^- measurements at high latitudes, for example those performed during the year-round MOSAiC expedition, will be very useful to better con-

strain the global I_{aq}^- distributions as well as mechanistic oceanic O_3 deposition representations. Measurements of O_3 concentrations and deposition fluxes to the Arctic Ocean can assist us to better constrain these modeling setups in terms of magnitude and temporal variability and can potentially indicate the sensitivity to other environmental factors such as wind speed in waters with low reactivity. Furthermore, including the role of halogen chemistry (Pratt et al., 2013; Thompson et al., 2017) might give an indication of the combined role of halogens and oceanic deposition in removing O_3 and explaining the magnitude and temporal variability of O_3 concentrations in the High Arctic.

2.5 Conclusions

The mesoscale meteorology–chemistry model Polar-WRF-Chem was coupled to the Coupled Ocean–Atmosphere Response Experiment Gas transfer algorithm (COAREG) to allow for a mechanistic representation of ocean–atmosphere exchange of O_3 . This scheme represents the effects of molecular diffusion, solubility, waterside turbulent transfer and chemical enhancement of O_3 uptake through its reactions with dissolved iodide. The COAREG scheme replaces the constant surface uptake resistance approach often applied in ACTMs. Furthermore, we have increased the modeled O_3 surface uptake resistance to snow and ice. In total, two simulations were performed: (1) a default WRF setup nudged to ERA5 synoptic conditions (NUDGED) and (2) a WRF setup with adjustments to O_3 surface uptake resistance as described above (COAREG). Furthermore, the CAMS global reanalysis data product has also been included in the presented evaluation of High Arctic surface O_3 . This CAMS product is widely used in air quality assessments and to constrain regional-scale modeling experiments. This provides additional information on the quality of the CAMS data products but also on potential issues in the representation of O_3 sources and sinks, e.g., oceanic and snow/sea ice deposition, for the High Arctic. The modeling approach was set up for 1 month at the end of summer 2008 and evaluated against hourly surface O_3 at 25 sites for latitudes $> 60^\circ N$ including observations over the Arctic sea ice as part of the ASCOS campaign.

Using the mechanistic representation of ocean–atmosphere exchange, O_3 deposition velocities were simulated in the order of 0.01 cm s^{-1} compared to $\sim 0.05 \text{ cm s}^{-1}$ in the constant surface uptake resistance approach. In the COAREG run, the spatial variability (0.01 to 0.018 cm s^{-1}) in the mean O_3 deposition velocities expressed the sensitivity to chemical enhancement with dissolved iodide. The temporal variability of O_3 deposition velocities (up to $\pm 20\%$ around the mean) is governed by surface wind speeds and expressed differences in waterside turbulent transport. Using the mechanistic representation of ocean–atmosphere exchange reduced the total simulated O_3 deposition budget to water bodies by a factor of 3.3 compared to the default constant ocean uptake rate approach and the increase in surface uptake resistance to snow and

ice reduced the deposition budget by a factor of 2.4.

Despite the fact that O_3 deposition to oceans, snow and ice surfaces only constitutes a small term in the total O_3 deposition budget ($> 90\%$ of the deposition is to land), we find a substantial sensitivity to the simulated surface O_3 mixing ratios. In the COAREG run, the simulated mean monthly surface O_3 mixing ratios have increased by up to 50% in the typically shallow Arctic ABL above the oceans and sea ice relative to the NUDGED run. The mechanistic representation of O_3 deposition to oceans resulted in a substantially improved representation of surface O_3 observations, especially for the High Arctic sites with latitudes $> 70^\circ \text{N}$. The NUDGED run underestimated the observed surface O_3 mixing ratios with a bias of -3.8 ppb, whereas the COAREG run had a bias of 0.3 ppb. The evaluation of the WRF runs at individual High Arctic sites showed that using the mechanistic representation of O_3 deposition to oceans results in a better representation of surface O_3 observations both in terms of magnitude and temporal variability. Similar to the NUDGED run, CAMS underestimated High Arctic observed surface O_3 with a bias of -5.0 ppb indicating that the representation of the deposition removal mechanism to oceans and snow/ice in CAMS might also be overestimated and should be reconsidered.

This study highlights the impact of a mechanistic representation of oceanic O_3 deposition on Arctic surface O_3 concentrations at a high (hourly) temporal resolution. It mostly corroborates the findings of global-scale studies (e.g., Ganzeveld et al., 2009; Luhar et al., 2017; Pound et al., 2019) and recommends that the representation of O_3 deposition to oceans and snow/ice in global- and regional-scale ACTMs should be revised. This revision is needed not only to better quantify the O_3 budget at the global scale, but also to better represent the observed magnitude and temporal variability of surface O_3 at the regional scale. In addition, explicit consideration of the mechanisms involved in O_3 removal by the oceans (and sea ice/snowpack) are essential to also evaluate the role of potentially important feedback mechanisms and future trends in and the role of O_3 in Arctic climate change as a function of declining sea ice cover, increasing emissions and changes in oceanic biogeochemical conditions. On the regional scale, this study also has implications for methods to quantify future trends in Arctic tropospheric O_3 , Arctic air pollution and climate in a period of declining sea ice and increasing local emissions of precursors.

A Appendices

A.1 WRF physical and chemical parameterization schemes.

Table A.1.1: WRF physical and chemical parameterization schemes.

WRF option	Configuration
Physical parameterizations	
Microphysics	WSM5 (Hong et al., 2004)
Long wave radiation	RRTMG (Iacono et al., 2008)
Short wave radiation	RRTMG (Iacono et al., 2008)
Surface layer	Monin-Obukhov (Janjić, 2001)
Land surface	Noah (Chen and Dudhia, 2001)
Boundary layer	MYJ (Janjić, 1994)
Cumulus	Kain-Fritsch (Kain, 2004)
Chemistry	
Gas-phase	CBM-Z (Gery et al., 1989; Zaveri and Peters, 1999)
Photolysis	Fast-J (Wild et al., 2000)
Emissions	
Anthropogenic	EDGAR (Janssens-Maenhout et al., 2019)
Biogenic	MEGAN (Guenther et al., 2012)
Boundary conditions	
Meteorology	ERA5 ($0.25^\circ \times 0.25^\circ$) (Hersbach et al., 2020)
Chemistry	CAMS ($0.75^\circ \times 0.75^\circ$) (Inness et al., 2019)

A.2 Formulation of the air- and waterside resistance terms

The exchange velocity, in this case deposition, of ozone (V_{d,O_3}) [m s^{-1}] is calculated from the waterside resistance (r_w) [s m^{-1}] and air side resistance terms ($r_a + r_b$) [s m^{-1}] as follows:

$$V_{d,O_3} = \frac{1}{\alpha r_w + r_a + r_b}. \quad (\text{A.2.1})$$

Here, α [-] is the dimensionless solubility of O_3 in sea water calculated from SST [K] following Morris (1988) as

$$\alpha = 10^{-0.25-0.013(SST-273.16)} \quad (\text{A.2.2})$$

and the waterside resistance term (r_w) is calculated as

$$r_w = (a \cdot D)^{-1/2} \frac{\Psi K_1(\xi_\delta) \sinh \lambda + K_0(\xi_\delta) \cosh \lambda}{\Psi K_1(\xi_\delta) \cosh \lambda + K_0(\xi_\delta) \sinh \lambda}. \quad (\text{A.2.3})$$

Here, a [s^{-1}] is the chemical reactivity of O_3 with Γ_{aq} calculated with the second order rate coefficient [$\text{M}^{-1} \text{s}^{-1}$] from Magi et al. (1997) and the Γ_{aq} concentrations [M] from Sherwen et al. (2019):

$$a = k \cdot [I_{\text{aq}}^-] = \exp\left(\frac{-8772.2}{SST} + 51.5\right) \cdot [I_{\text{aq}}^-]. \quad (\text{A.2.4})$$

In Eq. A.2.3, D [$\text{m}^2 \text{s}^{-1}$] is the molecular diffusivity of O_3 in ocean water and is calculated from the kinematic viscosity ν [$\text{m}^2 \text{s}^{-1}$] and the waterside Schmidt number (S_{cw}) [-] as

$$D = \frac{\nu}{S_{cw}} = \frac{\mu}{\rho} / [\sqrt{44/48} \cdot \exp(-0.055 \cdot SST + 22.63)] \quad (\text{A.2.5})$$

where μ [$\text{kg m}^{-1} \text{s}^{-1}$] is the dynamic viscosity of seawater and ρ [kg m^{-3}] is the density of seawater. Finally, the air side resistance terms ($r_a + r_b$) [s m^{-1}] of the deposition velocity in Eq. A.2.1 are calculated as

$$r_a + r_b = [C_d^{-1/2} + 13.3 S_c^{1/2} - 5 + \frac{\log(S_c)}{2\kappa}] / u_{*,a} \quad (\text{A.2.6})$$

where C_d [-] is the momentum drag coefficient, S_{ca} [-] is the Schmidt number for ozone in the atmosphere, κ is the Von Karman constant (0.4) and $u_{*,a}$ [m s^{-1}] is the friction velocity in the atmosphere. The $r_a + r_b$ term is typically in the order of 100 s m^{-1} (Fairall et al., 2011).

Compared to COAREG version 3.1 (Fairall et al., 2007, 2011), COAREGv3.6 is extended with a two-layer scheme based on Luhar et al. (2018). This extension is included in the second term of the waterside resistance term (Eq. A.2.3). Here, $\Psi = \sqrt{1 + (\kappa u_{*,w} \delta_m / D)}$, $\xi_\delta = \sqrt{2 a b (\delta_m + b D / 2)}$, and $\lambda = \delta_m \sqrt{a / D}$ with $b = 2 / (\kappa u_{*,w})$. This part of the equation is a function of the chemical reactivity a [s^{-1}] (Eq. A.2.4), the waterside friction velocity $u_{*,w}$ [m s^{-1}], the molecular diffusivity of O_3 in ocean water (Eq. A.2.5) and δ_m [m] representing the depth of the interface between the top water layer and the underlying turbulent layer. In this

study we have applied $\delta_m = c_0 \sqrt{D/a}$ with $c_0 = 0.4$ based on Luhar et al. (2018). $K_0(\xi_\delta)$ and $K_1(\xi_\delta)$ are the modified Bessel functions of the second kind of order 0 and 1, respectively. For more information on the derivation of the formulas please visit Fairall et al. (2007, 2011); Luhar et al. (2018).

Figure A.2.1 shows the sensitivity of the COAREG routine coupled to WRF to the environmental factors wind speed, SST and Iodide concentration. The sensitivity to wind speeds (Fig. A.2.1a) expresses the role of waterside turbulent transport and aerodynamic resistance. For low wind speeds waterside turbulent transport is limited and therefore limits the exchange of O_3 from the atmosphere to the ocean. At high wind speeds, the dry deposition of O_3 is limited by chemical reactivity of O_3 with I_{aq} at typical Arctic SSTs of 5 °C and I_{aq} concentrations of 60 nM (see also Fig. A.3.1). At very low wind speeds ($< 2.5 \text{ m s}^{-1}$) the aerodynamic resistance poses an extra restriction on the ocean-atmosphere exchange of O_3 . The sensitivity to SST (Fig. A.2.1b) mostly represents the role of solubility (Eq. A.2.2) with warmer waters having a lower solubility. In contrast to Luhar et al. (2018), the SST is not used to calculate the I_{aq} concentrations and does therefore not show a positive correlation. The sensitivity to I_{aq} (Fig. A.2.1c) represents the role of chemical enhancement which is stronger than the generally compensating effect of solubility in warmer waters for typical Arctic conditions.

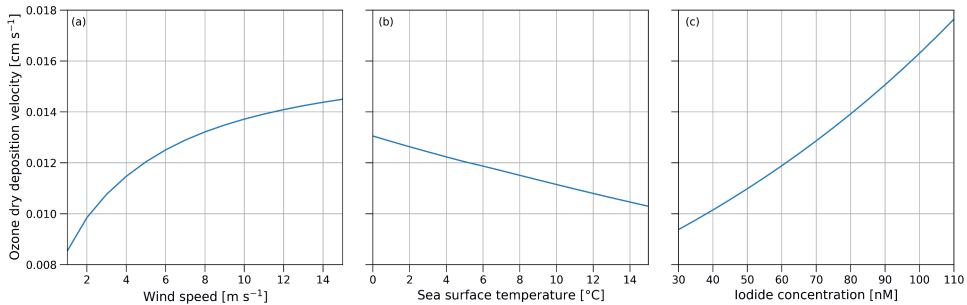


Figure A.2.1: Sensitivity of the ozone dry deposition velocity from COAREG to the environmental factors (a) 10-meter wind speed [m s^{-1}], (b) sea surface temperature [$^{\circ}\text{C}$] and (c) sea surface Iodide concentration [nM] using typical values of 10-meter wind speed, sea surface temperature and Iodide concentration of 5 m s^{-1} , 5°C and 60 nM respectively. Note that the sensitivity to sea surface temperature does not include effects of increasing reactivity but mostly represents the effect of reduced solubility (Eq. A.2.2).

A.3 Spatial distribution of oceanic Iodide

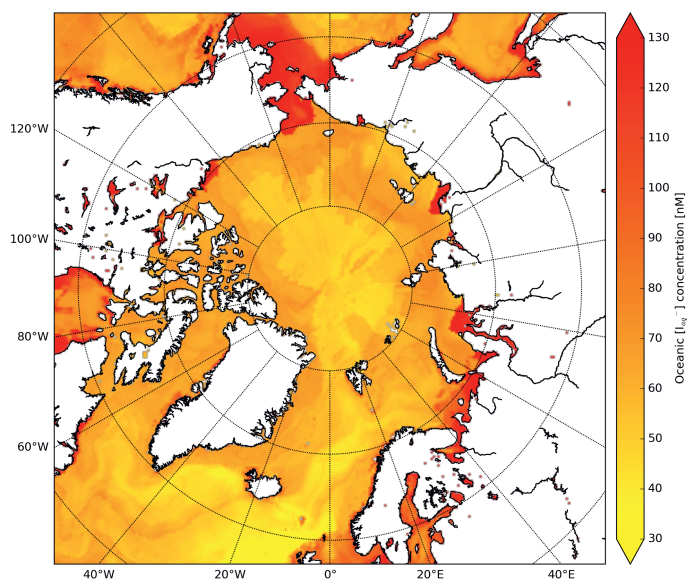


Figure A.3.1: Spatial distribution of Sherwen et al. (2019) oceanic Iodide concentrations [nM] at the start of the simulation.

A.4 Surface ozone measurement sites.

Table A.4.1: Surface ozone measurement sites subdivided in the 'High Arctic', 'Remote' and 'Terrestrial' site selections.

Name	Abbreviation	Group	Latitude [°N]	Longitude [°E]
Alert	ALT	High Arctic	82.5	-62.3
ASCOS	ASC	High Arctic	~ 87.4	~ -6.0
Barrow	BRW	High Arctic	71.3	-156.6
Zeppelin	NYA	High Arctic	78.9	11.9
Summit	SUM	High Arctic	72.6	-38.5
Villum	VIL	High Arctic	81.6	-16.7
Denali NP	DEN	Remote	63.7	-149.0
Esrang	ESR	Remote	67.9	21.1
Karasjok	KAS	Remote	69.5	25.2
Inuvik	INU	Remote	68.4	-133.7
Lerwick	SIS	Remote	60.1	-1.2
Pallas	PAL	Remote	68.0	21.1
Stórhöfði	ICE	Remote	63.4	-20.3
Yellowknife	YEL	Remote	62.5	-114.4
Ähtäri	AHT	Terrestrial	62.6	24.2
Bredkälen	BRE	Terrestrial	63.9	15.3
Fort Liard	FOR	Terrestrial	60.2	-123.5
Hurdal	HUR	Terrestrial	60.4	11.1
Kårvatn	KRV	Terrestrial	62.8	8.9
Norman Wells	NOR	Terrestrial	65.3	-123.8
Oulanka	OUX	Terrestrial	66.3	29.4
Tustervatn	TUV	Terrestrial	65.8	13.9
Vindeln	VDI	Terrestrial	64.3	19.8
Virolahti	VIR	Terrestrial	60.5	27.7
Whitehorse	WHI	Terrestrial	60.7	-135.0

Chapter 3

Low ozone dry deposition rates to sea ice during the MOSAiC field campaign: Implications for the Arctic boundary layer ozone budget



This chapter is based on:

J. G. M. Barten, L. N. Ganzeveld, G.-J. Steeneveld, B. W. Blomquist, H. Angot, S. D. Archer, L. Bariteau, I. Beck, M. Boyer, P. von der Gathen, D. Helmig, D. Howard, J. Hueber, H.-W. Jacobi, T. Jokinen, T. Laurila, K. M. Posman, L. Quéléver, J. Schmale, M. D. Shupe, M.C. Krol (2023). Low ozone dry deposition rates to sea ice during the MOSAiC field campaign: Implications for the Arctic boundary layer ozone budget. *Elementa: Science of the Anthropocene* 11(1). DOI: doi.org/10.1525/elementa.2022.00086

Abstract

Dry deposition to the surface is one of the main removal pathways of tropospheric ozone (O_3). We quantified for the first time the impact of O_3 deposition to the Arctic sea ice on the planetary boundary layer (PBL) O_3 concentration and budget using year-round flux and concentration observations from the Multidisciplinary drifting Observatory for the Study of Arctic Climate (MOSAiC) campaign and simulations with a single-column atmospheric chemistry and meteorological model (SCM). Based on eddy-covariance O_3 surface flux observations, we find a median surface resistance on the order of $20,000 \text{ s m}^{-1}$, resulting in a dry deposition velocity of approximately 0.005 cm s^{-1} . This surface resistance is up to an order of magnitude larger than traditionally used values in many atmospheric chemistry and transport models. The SCM is able to accurately represent the yearly cycle, with maxima above 40 ppb in the winter and minima around 15 ppb at the end of summer. However, the observed springtime ozone depletion events are not captured by the SCM. In winter, the modelled PBL O_3 budget is governed by dry deposition at the surface mostly compensated by downward turbulent transport of O_3 towards the surface. Advection, which is accounted for implicitly by nudging to reanalysis data, poses a substantial, mostly negative, contribution to the simulated PBL O_3 budget in summer. During episodes with low wind speed ($<5 \text{ m s}^{-1}$) and shallow PBL ($<50 \text{ m}$), the 7-day mean dry deposition removal rate can reach up to 1.0 ppb h^{-1} . Our study highlights the importance of an accurate description of dry deposition to Arctic sea ice in models to quantify the current and future O_3 sink in the Arctic, impacting the tropospheric O_3 budget, which has been modified in the last century largely due to anthropogenic activities.

3.1 Introduction

Tropospheric ozone (O_3) acts both as a greenhouse gas and air pollutant negatively affecting human health (Nuvolone et al., 2018) and plant growth (Ainsworth et al., 2012). Furthermore, O_3 plays an important role in atmospheric oxidation chemistry. On the global scale, the main O_3 sources are photochemical production and stratosphere-troposphere exchange. Tropospheric O_3 is removed by dry deposition to the Earth's surface and by photochemical destruction (Lelieveld and Dentener, 2000). Due to its relatively short atmospheric lifetime (3 to 4 weeks) compared to other greenhouse gases, tropospheric O_3 is subject to high spatiotemporal variability, especially close to the Earth's surface. Many local processes determine the evolution of the O_3 concentration in the planetary boundary layer (PBL). These processes include local O_3 precursor emissions, dry deposition to the Earth's surface, advection of different air masses, vertical mixing in the PBL and entrainment of O_3 -rich free tropospheric air as a result of PBL growth (Ganzeveld et al., 2008; Lin et al., 2009; Tang et al., 2017; Lu et al., 2019).

In the Arctic, tropospheric O_3 has been increasing up to the beginning of this century due to increasing emissions of precursors and long-range transport from the mid-latitudes (Cooper et al., 2014). During the last decades (2000 to 2020), the trend in Arctic tropospheric O_3 has been leveling off or even showing some decrease at individual sites (Cooper et al., 2020). Long-term O_3 observations at coastal sites such as Utqiagvik (Alaska, USA), Alert (Canada) and Zeppelin (Norway) have shown a clear seasonality in surface O_3 and a common occurrence of ozone depletion events (ODEs) in springtime. ODEs are often defined as events when the surface O_3 mixing ratio drops below 10 ppb and even down to almost 0 ppb (Simpson et al., 2007; Yang et al., 2020). These ODEs have been attributed to activation of reactive bromine chemistry in the PBL from sea-ice and snow-covered surfaces (Falk and Sinnhuber, 2018; Marelle et al., 2021; Swanson et al., 2022). Recently, Zhou et al. (2020) showed that the ODEs are also sensitive to the background nitrogen oxides (NO_x) concentrations. Local anthropogenic emissions of O_3 precursors are generally absent in the Arctic due to its remote location. Therefore, the O_3 PBL budget is predominantly driven by dry deposition to snow, ice (Helmig et al., 2007b) and the Arctic Ocean (Barten et al., 2021), natural O_3 precursor emissions and halogen chemistry (Yang et al., 2020), atmospheric stability (van Dam et al., 2016), and long-range transport of O_3 and its precursors.

Many previous studies have quantified the O_3 budget and controlling factors for (sub-)urban (Tang et al., 2017; Zhao et al., 2019), rural (Senff et al., 1996; Berkowitz et al., 2000; Hou et al., 2015), forested (Cros et al., 2000; Wolfe et al., 2011; Chen et al., 2018) or marine (Monks et al., 2000; Conley et al., 2011) environments. However, less effort has been spent to understand O_3 dynamics in- and above the Arctic PBL. Compared to the previously mentioned environments, the Arctic PBL is characterized by the occurrence of strong surface inversions (Tjernström et al.,

2019), especially in autumn, winter, and spring (Zhang et al., 2011). These inversions inhibit vertical mixing and PBL growth with consequences for boundary layer O_3 . Previously, Helmig et al. (2007b) and Barten et al. (2021) have shown the important role of O_3 deposition to the snowpack on the composition of the lower troposphere. van Dam et al. (2016) characterized an important role of atmospheric stability on summertime O_3 dynamics over the Arctic tundra. In contrast, the O_3 budget above the Arctic sea ice has not yet been characterized due to limited observational data (Jacobi et al., 2010). The ongoing retreat of the Arctic sea ice as a result of climate change (Stroeve and Notz, 2018; Keen and Blockley, 2018) urges us to improve our understanding of the exchange and further cycling of climate active trace gases, such as O_3 , in the Arctic PBL in current and future climate. Considering that atmospheric chemistry and transport models are still strongly biased with respect to Arctic O_3 observations and showing large model-to-model variability (Whaley et al., 2023), improved process representation is necessary to better constrain Arctic tropospheric O_3 and its radiative effects.

In September 2019, the German research vessel (RV) *Polarstern* was docked within the Arctic sea ice for one year (October 2019–2020) as part of the Multidisciplinary drifting Observatory for the Study of Arctic Climate (MOSAiC) expedition. MOSAiC is centered around the goal to understand the causes and consequences of Arctic sea ice decline from an interdisciplinary perspective. This expedition provided, for the first time, detailed year-round observations of key meteorological and other drivers involved in O_3 dynamics in and above the PBL over sea ice (Shupe et al., 2022). For example, the campaign provided one year of surface O_3 concentration observations, enabling us to study the magnitude and variability of surface O_3 over the entire year. Supporting observations include turbulent O_3 flux observations to quantify the role of O_3 deposition to snow and ice, and O_3 sondes to analyze the vertical structure of O_3 in and above the PBL. The main objectives of this study were 1) to arrive at an improved quantification of Arctic snow/sea-ice O_3 deposition for various meteorological conditions and 2) to evaluate the contribution of dry deposition and other processes to the temporal variability of O_3 concentrations in the Arctic PBL during MOSAiC using a single-column atmospheric chemistry and meteorological model (SCM).

3.2 Methods

To reach the research objectives, we have combined MOSAiC observations with atmospheric modeling. We performed a year-round atmospheric simulation with a single-column atmospheric chemistry and meteorological model and attempted to represent most optimally MOSAiC observed meteorological and chemical conditions. This approach enabled us to use the model as a complementary tool to analyze the observations and to quantify processes that have not been or cannot be observed. We are confident that the behaviour of the SCM is representative for

other 3D atmospheric chemistry and transport models, being applied to study Arctic O₃, in its representation and parameterizations of the meteorological and chemical processes. Applying the SCM, being constrained with reanalysis data, has allowed us to investigate in detail the contribution by all processes that explain the observed O₃ temporal variability.

3.2.1 Single column model

For analysis of in-situ observations, such as those collected during the 1-year MOSAiC field campaign, the SCM has demonstrated its merits in numerous studies (Ganzeveld et al., 2002, 2008; Kuhn et al., 2010; Seok et al., 2013; Barten et al., 2020). The SCM simulates the atmospheric physics and atmospheric chemistry processes in one column for a fixed location or, as in this case, following the track of the RV *Polarstern* in a quasi-Lagrangian mode. The SCM-simulated physics also drive atmospheric chemistry processes, including a selection of natural emissions, gas-phase chemistry, wet and dry deposition, and vertical turbulent and convective tracer transport in an online mode. The result is a feedback between the simulated meteorology and atmospheric chemistry and vice versa. Stratospheric and tropospheric chemistry are represented in this study by the MECCA1 box modeling system (Sander et al., 2005), including an O₃-NO_x-halogen chemistry scheme considering 74 tracers. In addition, the SCM has been coupled to the Coupled Ocean-Atmosphere Response Experiment Gas transfer algorithm (COAREG) (Fairall et al., 2011) for a more explicit representation of ocean-atmosphere fluxes of O₃, as well as carbon dioxide (CO₂), methane (CH₄), and dimethyl sulfide (DMS), all being climate-active trace gases, the fluxes of which were measured during MOSAiC. These fluxes are quantified in the model considering atmospheric- and waterside turbulence and the atmosphere-ocean concentration gradient. Furthermore, the SCM contains a straightforward 2-layer representation of snowpack-atmosphere exchange considering the role of diffusion, wind pumping, sorption, emissions, and gas- and aqueous-phase chemistry on snow-atmosphere exchange of trace gases. This 2-layer representation formed the basis of the development of a more detailed snowpack trace gas exchange model by Murray et al. (2015) that was applied in a study of O₃ and NO_x snow-atmosphere exchange at Summit, Greenland. The simplified 2-layer version applied here mainly makes strong assumptions on the physicochemical representation of the snow layer compared to the extended version by Murray et al. (2015). In this study, we have applied the simplified 2-layer version mainly to study whether this explicit representation of in-snowpack O₃ concentrations might explain short-term events of bidirectional exchange of O₃. We selected an overall snow uptake rate of 0.005 cm s⁻¹ such that the snowpack model reproduced the observation inferred from long-term snowpack uptake resistance (Murray et al., 2015).

Here, the SCM was set up with 60 atmospheric layers having 11 layers in the lowest kilometer, of which 5 layers are in the lowest 100 meters. This layering allows for a relatively detailed

resolution in the PBL and lower free troposphere, which is the focus of this study. The model simulation was initialized with European Centre for Medium-Range Weather Forecasts Reanalysis (ERA5) meteorological (Hersbach et al., 2020) and Copernicus Atmosphere Monitoring Service (CAMS) chemical composition (Inness et al., 2019) reanalysis data and run for the period of October 1, 2019, 00:00 UTC to October 1, 2020, 00:00 UTC at time steps of 60 seconds. We studied model results at a temporal resolution of 1 hour. The SCM also explicitly estimates heat transport through 5 σ -coordinate sea-ice layers with one snow layer on top. The ice-covered fraction of the SCM was initialized with a sea-ice thickness of 1.0 m and a 20-cm-thick snow layer on top based on a preliminary analysis of ice mass balance buoys deployed at the start of MOSAiC (Lei et al., 2021; Nicolaus et al., 2022). Furthermore, the SCM updates the geostrophic and vertical wind speeds, sea-ice fraction, sea surface temperature, and surface pressure from ERA5 throughout the simulation.

We nudged the SCM to the ERA5 and CAMS reanalysis data to consider the role of advection and changes in synoptic conditions. More specifically, we nudged the model to air temperature, u and v winds and liquid water content above the PBL. We did not nudge the SCM to ERA5 for heights below 250 m to avoid a stronger forcing of surface layer variables for very shallow PBLs. Furthermore, we nudged the SCM to mixing ratios of O_3 , NO_x , carbon monoxide (CO) and formaldehyde (HCHO) in and above the PBL to assure that these model simulations optimally consider the role of changes in synoptic conditions and advection regimes in determining local meteorological and chemical conditions. We applied relaxation coefficients of 1 h and 3 h for physical parameters and chemical tracers, respectively. The relaxation coefficient to physical parameters is 6 times larger compared to Sterk et al. (2015), who applied a 1D version of the Weather Research and Forecasting model to simulate clear-sky stable PBLs over snow covering a 2-day period. We have tested a range of relaxation coefficients, and with the relaxation coefficients of 1 h and 3 h, aiming to ensure that the SCM follows the seasonal cycle in meteorology and atmospheric chemistry from the ERA5 and CAMS reanalysis products, but not to nudge too strongly to avoid that these simulations would mainly reflect the quality of the ERA5 and CAMS products. A preliminary analysis showed that additional nudging to specific humidity (q) leads to unrealistically abundant cloud formation in the SCM creating numerical issues associated with differences in the representation of the surface energy balance in the SCM and ERA5 (Ganzeveld et al., 2006). Therefore, no nudging to q has been applied in the SCM simulation to secure a more realistic representation of cloud cover and surface radiation. ERA5 assimilates the radiosondes launched during MOSAiC and the RV *Polarstern* automatic weather station data. Here, we used the same radiosondes to determine the PBL height during MOSAiC that were also used to nudge the SCM above the PBL. However, the SCM still explicitly calculates boundary layer mixing and the PBL height. In Figure B.1.1, we show a direct comparison of SCM-simulated, MOSAiC-observed, and ERA5 reanalysis 2-m air temperature, 10-m wind

speed, and 10-m wind direction. CAMS assimilates observations from several satellites but it does not assimilate O_3 observations from MOSAiC, other in situ measurement sites, or ozone sondes (Inness et al., 2020). In Figure B.1.2, we show a direct comparison of SCM-simulated, MOSAiC-observed, and CAMS reanalysis surface O_3 mixing ratios.

3.2.2 Observations

Meteorological data

To evaluate the SCM-simulated micro-meteorology, we used observations taken at a meteorological tower operated on the sea ice 300 m to 500 m from RV *Polarstern* as part of the MOSAiC Central Observatory (Shupe et al., 2022). Here, we used 1-min observed 2-m air temperature (T_{2m}), 10-m wind speed (V_{10m}), and 10-m wind direction (Cox et al., 2021a) re-sampled to hourly mean observations. Data gaps occurred during periods when the RV *Polarstern* was in transit, i.e., May 10 to June 24 (2020) for the Leg 3 to Leg 4 exchange at Svalbard and July 29 to August 25 (2020), when the original ice floe broke apart and a new Central Observatory was set up around 88°N (Shupe et al., 2022). See Figure 3.1 for an overview of the MOSAiC drift trajectory.

Surface O_3 concentrations and fluxes

Ambient air for the O_3 flux analyzers was drawn from a Teflon inlet at the top of the RV *Polarstern* bow tower. The tower was installed at the end of a horizontal crane extending approximately 5 m in front of the ship's bow (see Shupe et al. (2022)). Inlets were co-located on the tower with a 3D ultrasonic anemometer, approximately 20 m above the ice surface. A heated Teflon inlet line (approximately 1-cm inner diameter, 45-m long) carried sample air to the O_3 flux analyzer located in a below-deck laboratory space at a mean flow of 30 standard liters-per-minute (SLPM). This flow was sub-sampled into the O_3 flux analyzer at a flow of 1.2 SLPM through a Nafion air dryer. See Bariteau et al. (2010) and Boylan et al. (2014) for a detailed description of the fast O_3 flux analyzer.

Synchronization of fast O_3 response with fast wind speed and correction for low-pass filtering effects of the inlet tubing were facilitated by subjecting the sampling system once every hour to a 5-s pulse of pure nitrogen at the inlet tip. See Bariteau et al. (2010) and Blomquist et al. (2010, 2014). The O_3 flux was estimated as the covariance of synchronized dry-air O_3 mole fraction and vertical wind velocity. The flux detection limit was evaluated hourly as the covariance of time-shifted (decorrelated) O_3 mole fraction and vertical velocity. Additional filtering with respect to wind speed ($>1 \text{ m s}^{-1}$) and wind direction ($\pm 90^\circ$) was applied to limit interference from RV *Polarstern* on the eddy-covariance system. Furthermore, non-stationary conditions were filtered out. Finally, we have filtered out the O_3 flux data for boundary layers shallower than 40 m —

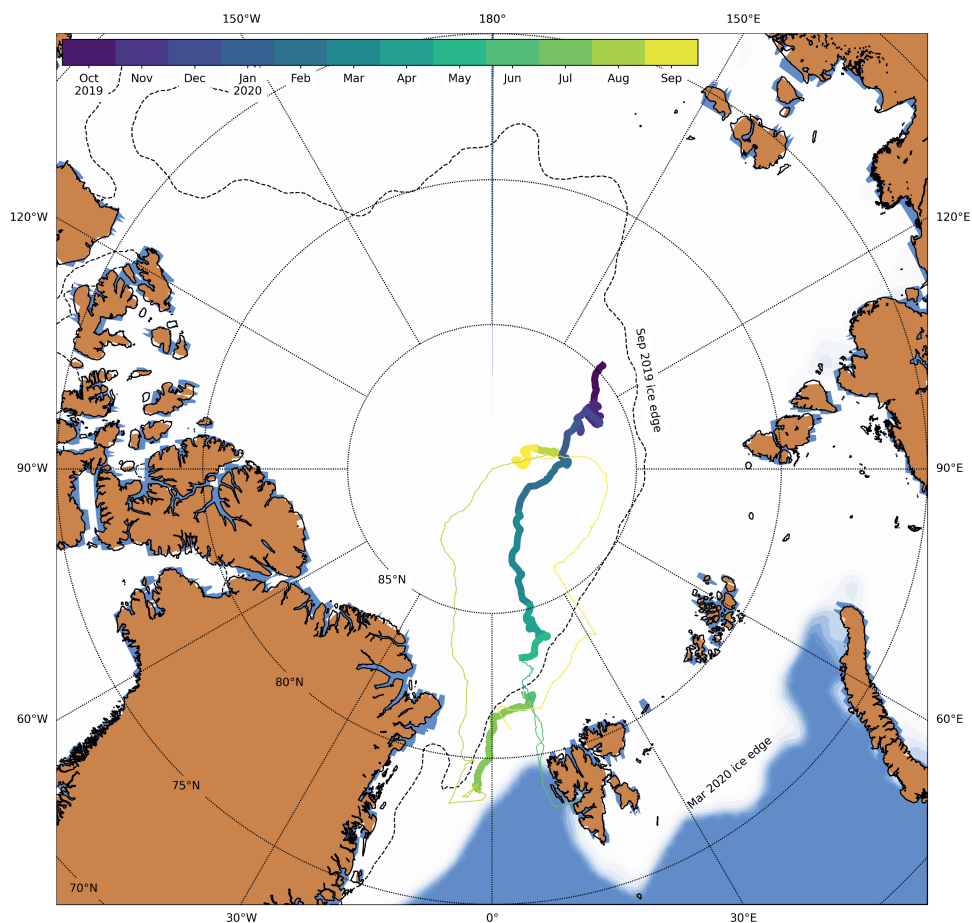


Figure 3.1: Drift trajectory of MOSAiC from October 15, 2019, to September 30, 2020, colored per month. The thick lines indicate the drift trajectory and the thin lines show the path of the RV *Polarstern* when in transit. The white contours in the background indicate the March 2020 sea-ice maximum from ERA5 and the dashed black line indicates the September 2019 sea-ice edge minimum from ERA5 (sea-ice fraction = 0.3).

twice the reference height of the flux observations — based on the SCM-simulated PBL heights. The motivation for this additional filtering was to exclude those O_3 flux observations not deemed being representative for the actual O_3 surface fluxes, but more reflecting the role of entrainment due to presence of a very shallow inversion layer. This filtering resulted overall in removing approximately 12% of the O_3 flux observations. The radiosonde-inferred PBL height was not applied for this filtering due to its high uncertainty in the case of very shallow boundary layers and the limited temporal coverage.

Redundant measurements of ambient air O_3 concentrations were performed in three distinct sea-laboratory containers (Angot et al., 2022d; Beck et al., 2022). Here we used an hourly-averaged merged dataset that combines the cross-evaluated individual O_3 datasets. A detailed description of the set-up and filtering of O_3 flux data, as well as measurements of the CO_2 , CH_4 and DMS fluxes, is planned for an upcoming manuscript.

Observation-derived ozone deposition resistance terms

In state-of-the-art atmospheric chemistry transport models, the deposition process is generally considered by calculation of a deposition velocity following the resistance in series approach first proposed by Wesely (1989). The O_3 deposition velocity V_{d,O_3} ($m\ s^{-1}$) is estimated as

$$V_{d,O_3} = \frac{1}{r_a + r_b + r_c}, \quad (3.1)$$

where r_a is the aerodynamic resistance ($s\ m^{-1}$), r_b is the quasi-laminar sub-layer resistance ($s\ m^{-1}$), and r_c is the surface resistance ($s\ m^{-1}$). Both r_a and r_b , representing turbulent transport and diffusion close to the surface, strongly depend on meteorological conditions. The term r_c represents the efficiency of removal by the surface and is typically two to three orders of magnitude larger than r_a and r_b for simulated O_3 deposition to snow and ice (Helmig et al., 2007b; Hardacre et al., 2015). The simulated O_3 flux $\overline{w'O'_3}$ ($ppb\ m\ s^{-1}$) at the surface is calculated as

$$\overline{w'O'_3} = V_{d,O_3} \cdot [O_3]_{surf}, \quad (3.2)$$

where $[O_3]_{surf}$ is the O_3 mixing ratio at the surface (ppb). Here, we used the observed O_3 deposition fluxes to derive an estimate of r_c as the residual term in explaining the observed flux. Similar to de Jalón et al. (2019), we estimated r_a and r_b from observed meteorological properties according to:

$$r_{a,obs} = \frac{V_z}{u^{*2}} \quad (3.3)$$

and

$$r_{b,obs} = \frac{2}{k \cdot u^*} \cdot \frac{Sc^{2/3}}{Pr}, \quad (3.4)$$

where V_z is the wind speed at height z (m s^{-1}), u^* is the friction velocity (m s^{-1}) from the eddy-covariance system, k is the von Karman constant of 0.4, and $Sc = 1.07$ and $Pr = 0.72$ are the Schmidt number of O_3 and Prandtl number in air, respectively (Hicks et al., 1987). Then, we derived r_c from Equations 3.1 and 3.2 using the observed surface O_3 mixing ratio and flux as

$$r_{c,obs} = \frac{[O_3]_{surf}}{w'O'_{3obs}} - r_{a,obs} - r_{b,obs}. \quad (3.5)$$

A stability correction of r_a is suggested to be significant for very stable conditions under bulk Richardson numbers >0.2 (Toyota et al., 2016) in atmospheric chemistry models. By using the observed wind speed and friction velocity, we accounted for the stability effects in the observation-derived method. Furthermore, this stability correction of r_a is accounted for in the representation of the deposition process in the SCM (Ganzeveld and Lelieveld, 1995).

Radiosondes

We used data from radiosondes launched during MOSAiC (Maturilli et al., 2021) to infer the magnitude and temporal evolution of the PBL Height (PBLH). Radiosondes were launched four times per day (6-hourly) and provide detailed information on the vertical structure of atmospheric temperature, humidity, and horizontal wind speed. We applied the bulk-Richardson-number method, which is a common method to derive the PBLH from radiosondes (e.g., Zilitinkevich and Baklanov, 2002; Zhang et al., 2014). Furthermore, Jozef et al. (2022) found this automated objective method to be most accurate compared to subjective identification of the PBLH during MOSAiC. The bulk Richardson number Ri_B (–) from the surface up to height h (m) is defined as the ratio between the estimated buoyancy and shear production as given in Equation 3.6:

$$Ri_B = \frac{(g/T_{v,0}) \cdot (\theta_v(h) - \theta_v(0)) \cdot h}{u(h)^2 + v(h)^2}. \quad (3.6)$$

Here, g is the gravitational acceleration (m s^{-2}), $T_{v,0}$ is the virtual temperature at the surface (K), $\theta_v(h)$ and $\theta_v(0)$ are the virtual potential temperature (K) at height h and at the surface, respectively, and $u(h)$ and $v(h)$ are u and v wind components (m s^{-1}) at height h . The bulk-Richardson-number method assumes that the PBLH is the height at which the bulk Richardson number reaches the critical bulk Richardson number Ri_{Bc} . When $Ri_B > Ri_{Bc}$, turbulence production by shear is insufficient to compensate for the suppression of turbulence by buoyancy. For this study, we applied a Ri_{Bc} of 0.40 based on a preliminary analysis of a subset of the observed profiles and manual identification of the PBLH based on temperature and humidity gradients at the PBL top. We note that even though a constant Ri_{Bc} is often applied it rather depends on atmospheric stability (Richardson et al., 2013; Basu et al., 2014), with values for Ri_{Bc} typically ranging from 0.1 to 1.0 (Zilitinkevich and Baklanov, 2002). However, a detailed

analysis of appropriate Ri_{Be} for best estimates of PBLH during MOSAiC, e.g., compared with other PBLH estimates from sodar (Brooks et al., 2017), is out of scope for this study. Additional uncertainty arises from the fast ascent of the radiosonde and uncertainty in the GPS-retrieved altitude, especially close to the surface. Therefore, the exact magnitude of the radiosonde-derived PBLH might be subject to a substantial uncertainty. However, we do not focus on the magnitude but rather on the temporal evolution of the PBLH and identification of periods with suppressed mixing relevant for the analysis of surface O_3 concentration and flux observations.

To complement the surface O_3 concentration and flux observations, we used additional observations on the vertical distribution of O_3 using sondes launched during MOSAiC (von der Gathen and Maturilli, 2020, 2022). Approximately one radiosonde per week was equipped with an O_3 sensor, with some periods (e.g., springtime) having a higher temporal coverage. In total, 56 O_3 sondes were launched between October 1, 2019, and September 30, 2020. For better comparison with the SCM, we have regridded the data from the O_3 sondes to 30-m vertical bins to allow for identification of O_3 gradients above the PBL. In this study, we focused on the vertical profiles of O_3 in the PBL and free troposphere and discarded observations of stratospheric O_3 , which have been shown to be highly depleted in the 2020 spring season due to severe chemical loss in a strong and long-lasting polar vortex (Wohltmann et al., 2020; Inness et al., 2020).

3.3 Results

First, we present the model evaluation of meteorological diagnostics essential for the analysis of the PBL budget of O_3 . Second, we compare the simulated and observed O_3 deposition resistance terms as one of the main components of the O_3 budget. Thereafter, we compare the modelled and observed surface O_3 concentrations and quantify the contribution of each process to the O_3 budget in the PBL. Finally, we evaluate the link between surface observations and free tropospheric O_3 by a comparison of SCM simulations and observations on the vertical O_3 distribution.

3.3.1 Evaluation of SCM-simulated meteorology

The SCM shows a good performance with respect to observed T_{2m} (Figure 3.2a and e) with an explained variance R^2 of 0.88. The SCM and observations agree on the seasonal cycle, with a minimum T_{2m} of about -40°C reached at the end of winter and a persistent period of T_{2m} around 0°C in summer due to the melting sea ice (Shupe et al., 2022). Even though the SCM is able to represent most of the temporal variability in observed T_{2m} , the observations show larger variability on hourly timescales, arguably due to the misrepresentation of local processes in the SCM or a misrepresentation of surface properties such as albedo, sea-ice cover and

sea-ice thickness affecting the surface energy balance. The SCM generally simulates warmer conditions than observed with a bias of $+1.0^{\circ}\text{C}$. Most notably, the warm bias increases to $+2.1^{\circ}\text{C}$ for observed $T_{2m} < -25^{\circ}\text{C}$, indicating a potential overestimation of turbulent mixing during very stable conditions (Kral et al., 2021). Note that the SCM-simulated meteorology is strongly affected by nudging the SCM to the ERA5 reanalysis data above the boundary layer. For a direct comparison of SCM-simulated, MOSAiC-observed and ERA5 reanalysis meteorology see Figure B.1.1.

The SCM also shows a relatively good performance with respect to observed V_{10m} (Figure 3.2b and f) with an R^2 of 0.84. The SCM is able to represent the observed maxima and minima in V_{10m} , showing no significant positive or negative bias. Periods with a large positive T_{2m} bias up to $+10^{\circ}\text{C}$ (e.g., around May 1) appear to coincide with a positive V_{10m} bias of 1 to 2 m s^{-1} , related to an underestimation of surface stratification. However, the bias in V_{10m} cannot completely explain the warm bias in T_{2m} , indicating the role of other processes such as energy exchange at the surface or thermal radiation divergence. Similarly to V_{10m} , the wind direction is well represented by the SCM (Figure 3.2c and g) with an R^2 of 0.85. This result indicates that we anticipate a good model representation of the contribution by advection of O_3 and other long-lived precursors with air masses coming from different origins.

Simulated and observed PBLH show large variations, with boundary layer depths ranging from approximately 10 m to 1000 m (Figure 3.2d and h). The 25th and 75th percentiles for the observations and SCM amount to [86, 305] and [57, 241] m, respectively. These values indicate that for this study the Arctic boundary layer was typically shallower than a few hundred meters and boundary layers of a few tens of meters were common. Both the SCM and observations show the largest variation and deepest boundary layers in spring/early summer (March to June). Also during calm conditions with $V_{10m} < 5 \text{ m s}^{-1}$ (e.g., around March 1 and August 1) both the SCM and observations agree well on the presence of boundary layers often shallower than 50 m. In general, the temporal evolution and variability in radiosonde-derived PBLH was captured by the SCM even though biases were more pronounced during certain periods (e.g., May to June). Moreover, a substantial positive bias in PBLH was found around May 1 when the SCM significantly overestimated T_{2m} and V_{10m} . This finding again indicates the presence of excessive turbulent mixing in the SCM during that period.

3.3.2 Ozone deposition resistance terms

The observations show that the aerodynamic resistance (r_a) is typically on the order of 10^2 s m^{-1} , with extremes exceeding 10^3 s m^{-1} during periods with very low wind speeds (Figure 3.3a). For the quasi-laminar sub-layer resistance (r_b), being typically one order of magnitude smaller than r_a , we find a typical magnitude of 10^1 s m^{-1} and peaks exceeding 10^2 s m^{-1} . We find

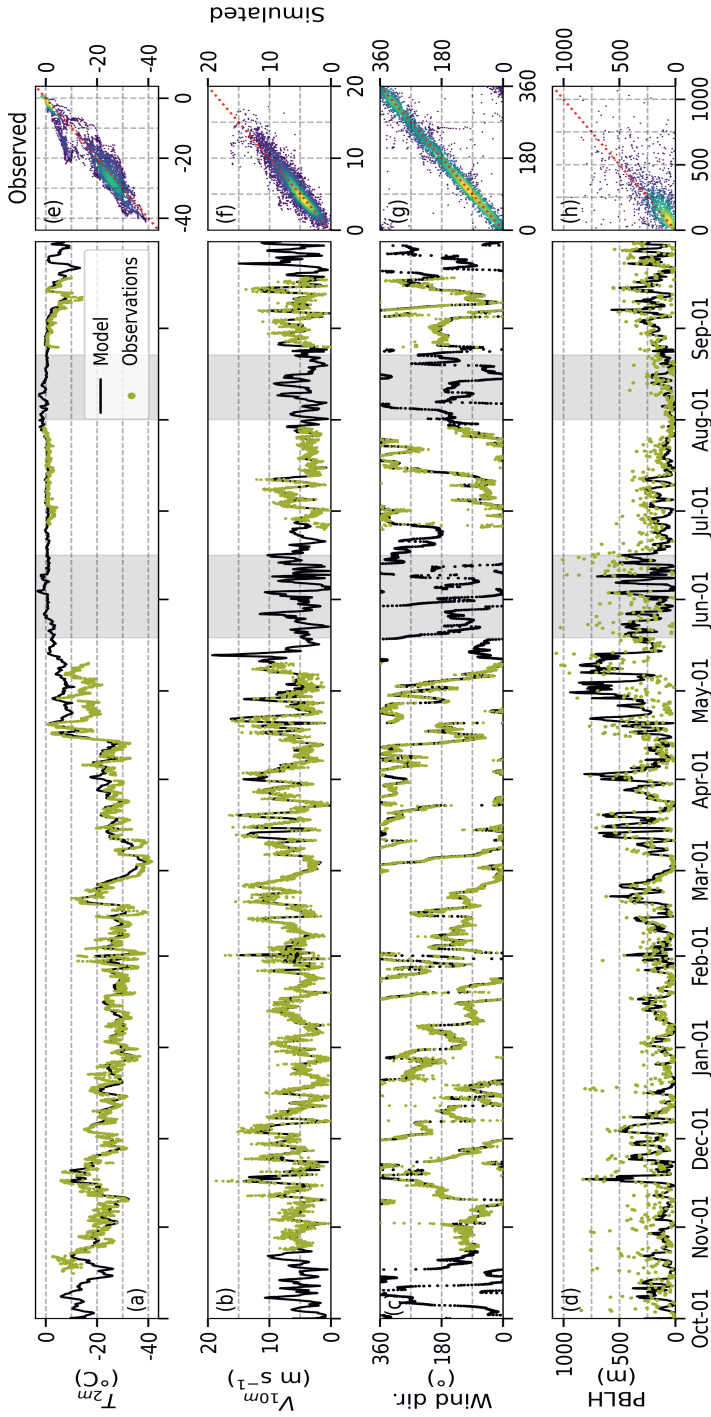


Figure 3.2: Temporal evolution of simulated (black) and observed (olive green) (a) 2-m air temperature ($^{\circ}\text{C}$), (b) 10-m wind speed (m s^{-1}), (c) 10-m wind direction ($^{\circ}$) and (d) planetary boundary layer height (m) and (e-h) corresponding 1:1 scatter plots of observed (x-axis) and simulated (y-axis) variables shown in (a-d). The grey shadings in (a-d) indicate the periods when RV *Polartarn* was in transit. The colors in (e-h) express the kernel density estimation, where brighter colors correspond to a higher point density with (e) $R^2 = 0.88$, (f) $R^2 = 0.85$, (g) $R^2 = 0.35$, and the red line indicates the 1:1 line.

that the SCM simulates generally well the observed magnitude and temporal variability in r_a and r_b both in the timing of the maxima and minima. The co-sampled frequency distributions (Figure 3.3b) show that the SCM slightly underestimates the observed peak in r_a of 10^2 s m^{-1} . Rather, the SCM shows a peak around 80 s m^{-1} . We argue that this discrepancy is related to overestimated surface mixing conditions in the SCM leading to an underestimation in r_a . The SCM resembles rather well the observed frequency distribution of r_b , both peaking at 10^1 s m^{-1} and only exceeding high values of r_b of 10^2 s m^{-1} approximately 4% of the time.

We find a large variability in observed surface resistance (r_c), with minima as small as 10^3 s m^{-1} and maxima up to 10^6 s m^{-1} . The frequency distribution (Figure 3.3b) peaks between 10^4 s m^{-1} and $2 \times 10^4 \text{ s m}^{-1}$. By computing a 7-day running median, we find a r_c of approximately $2 \times 10^4 \text{ s m}^{-1}$ ($V_{d,O_3} \approx 0.005 \text{ cm s}^{-1}$) in winter before dropping below 10^4 s m^{-1} for the months of April and May. This snow-sea ice uptake resistance inferred from these long-term O_3 flux observations is much larger compared to the still commonly applied snow-ice uptake rate of $2 \times 10^3 \text{ s m}^{-1}$, resulting in a dry deposition velocity of 0.05 cm s^{-1} in most atmospheric chemistry and transport models (Simpson et al., 2012; Hardacre et al., 2015; Falk and Søvde Haslerud, 2019). The observation-inferred uptake resistance of $2 \times 10^4 \text{ s m}^{-1}$ is more in line with estimations of $1 \times 10^4 \text{ s m}^{-1}$ by Helmig et al. (2007b) implemented in more recent model experiments (Barten et al., 2021; Herrmann et al., 2021; Marelle et al., 2021). The reduction in observation-derived r_c in spring and summer might potentially be related to a larger open water flux footprint and the reactions between O_3 and ocean water reactants (Loades et al., 2020). At the end of summer, the observed r_c is again on the order of $2 \times 10^4 \text{ s m}^{-1}$. The increase in the summer appears to be insignificant due to the large variability in the observations. The SCM results show less variation compared to observed r_c . This result indicates that the simulated temporal variability in processes considered in the first-order 2-layer snowpack-atmosphere exchange model, e.g., the role of wind pumping, does not explain the observed temporal variability in r_c . However, the model agrees on a rather constant r_c of $2 \times 10^4 \text{ s m}^{-1}$ ($V_{d,O_3} \approx 0.005 \text{ cm s}^{-1}$) in the weekly median from November to April. During August, the SCM-simulated r_c is biased low for a period with significant open water fraction (>0.5 for 2 weeks) in the ERA5 forcing dataset. This bias highlights the sensitivity in the SCM to O_3 deposition to water surfaces that might not be representative for the 7-day median observations with a more local footprint. The r_a and r_b terms, being typically 2 and 3 orders of magnitude smaller than r_c , appear to put no significant constraint on the total resistance term over the entire year. This lack of constraint indicates that the removal rate is dominated by the actual snow/sea-ice uptake efficiency with an insignificant role of turbulent transport to and molecular diffusion near the surface. Therefore, the impact of a misrepresentation of SCM-simulated atmospheric stability on the O_3 deposition flux is limited.

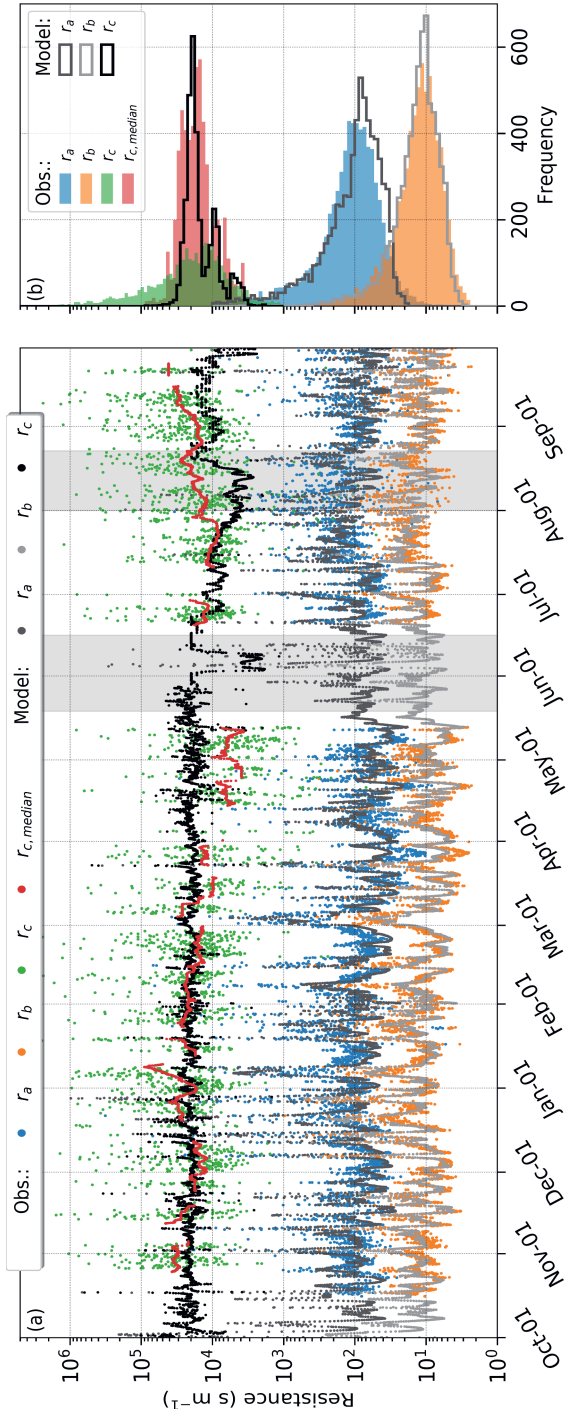


Figure 3.3: (a) Temporal evolution and (b) co-sampled frequency distribution of observation-derived (colors) and simulated (grey scales) aerodynamic resistance (r_a (s m^{-1}); blue, grey), quasi-laminar sub-layer resistance (r_b (s m^{-1}); orange, light grey), surface resistance (r_c (s m^{-1}); green, black) and 7-day running median observed surface resistance ($r_{c,median}$ (s m^{-1}); red). The grey shadings indicate the periods when RV *Polarstern* was in transit.

3.3.3 Surface ozone concentrations and tendencies

The observed evolution in daily mean surface O_3 mixing ratios shows a seasonal cycle with a maximum in winter, followed by ODEs in spring and another minimum at the end of summer (Figure 3.4a). Daily mean O_3 mixing ratios reach 45 ppb in wintertime and 15 to 20 ppb at the end-of-summer minimum. In March, April and May, the observations show clear indications of ODEs with observed O_3 mixing ratios as low as <1 ppb. These ODEs occur on timescales of several hours to days in shallow boundary layers (Figure 3.2d) during episodes with low wind speeds (Figure 3.2b). The recovery of ozone to mixing ratios up to 45 ppb occurs at a similar timescale. The SCM results agree with the seasonal cycle in observed surface O_3 mixing ratios in terms of the winter maximum and end-of-summer minimum. However, the SCM is unable to represent the ODEs in spring due to the fact that we have not considered the halogen emissions in these model experiments. Moreover, the role of halogen chemistry is not considered in the CAMS reanalysis data used for nudging (Figure B.1.2). The SCM and observations also agree on sharp changes in surface O_3 mixing ratios in winter (e.g., around January 1) caused by advection of different air masses in CAMS depicted by a sudden shift in wind direction (Figure 3.2c) and a changing footprint area of the surface O_3 concentration observations. Interestingly, the SCM shows less variability in the daily mean surface O_3 mixing ratios compared to observations, due to a misrepresentation of local processes affecting the surface O_3 concentrations. This reduced variability can be caused by a lower variability in O_3 deposition (Figure 3.3) in the SCM, a misrepresentation of local processes such as snow ridging causing additional surface roughness, or local chemistry caused by halogen emissions from the snowpack which are not included in the SCM. Especially in wintertime, the temporal variability in surface O_3 simulated by the SCM is very low. In wintertime, the model shows no significant positive or negative bias. In springtime, the model is strongly positively biased due to the missing halogen sources and resulting ODEs. From June onwards, the SCM modelled O_3 is slightly negatively biased by 3 to 4 ppb.

The observed and simulated O_3 mixing ratios (Figure 3.4a) are governed by many processes. Ultimately, we want to determine the role of these different processes on the PBL-integrated mixing ratios over the entire year for various meteorological conditions. Therefore, we have estimated the PBL O_3 integrated process tendencies in the SCM. Basically, we have estimated for every time step the contribution by nudging, vertical mixing, dry deposition, chemistry (the net result of all chemical reactions), and entrainment from the free troposphere to the simulated changes in O_3 mixing ratios, as described in Equation 3.7:

$$\frac{d[O_3]}{dt} = \text{Nudging} + \text{Mixing} + \text{Deposition} + \text{Chemistry} + \text{Entrainment}. \quad (3.7)$$

To interpret how temporal changes in observed O_3 mixing ratios are explained by the different processes controlling boundary layer O_3 , the process tendencies are given in ppb h^{-1} . These

values were calculated by integrating the O_3 and air mass over the PBLH accounting for the decreasing density and increasing thickness of layers with altitude. Here, the nudging tendency mainly reflects the contribution by advection if differences between the SCM- and CAMS-simulated processes in the vertical column are small relative to this contribution by advection. Although vertical mixing and entrainment are calculated as different tendencies, both represent mixing of O_3 -rich air from layers aloft to layers in the PBL. The turbulent transport tendency, calculated from the divergence of the fluxes at the interfaces of the SCM model layers representing the boundary layer, mostly reflects the compensating effect by downward transport throughout the boundary layer to the surface to compensate for dry deposition. In contrast, the entrainment tendency solely represents the increase in O_3 concentration due to the increase of the PBLH over time and thus entrainment of free tropospheric air masses enhanced in O_3 using a bulk approach. Because the SCM is unable to capture the high temporal variability in deposition (Figure 3.3) and surface mixing ratios (Figure 3.4a) on hourly timescales, we have applied a 7-day running mean to these tendencies to determine the dominant processes on timescales of days to weeks (Figure 3.4b).

Over the entire year, vertical mixing, representing the redistribution of O_3 towards the surface, always contributes positively to the net O_3 PBL budget. The nudging tendency can be either a positive or a negative contribution. The net effect of chemistry (both positive and negative) and entrainment (only positive) only contribute marginally ($<5\%$) to the simulated 7-day running mean net tendency. In winter, vertical mixing and dry deposition appear to be the processes that dominate the magnitude and temporal variability of PBL O_3 as reflected by their contribution to the net tendency. The removal at the surface by dry deposition is mainly counteracted by the redistribution of O_3 by downward turbulent transport. We expect a larger contribution by chemistry in spring given the ODEs (Figure 3.4a); however, not having considered the potential sources and resulting chemical destruction of O_3 , the tendencies for ODEs do not represent the anticipated on-site observed conditions. While in wintertime dry deposition appears to mainly determine the O_3 sink, compensated for by vertical mixing, nudging also plays a substantial role in the period of June to September. Interestingly, we find a strong negative contribution by dry deposition up to -1.0 ppb h^{-1} in August. Here, both observations and the SCM are characterized by a period of persistent low wind speeds (Figure 3.2b) and shallow boundary layers (Figure 3.2d). Also in wintertime, we find that during periods with relatively shallow boundary layers the role of dry deposition on the O_3 concentrations increases. On the other hand, this finding also implies stronger O_3 gradients from the surface layer to layers aloft, which will ultimately be compensated by turbulent mixing.

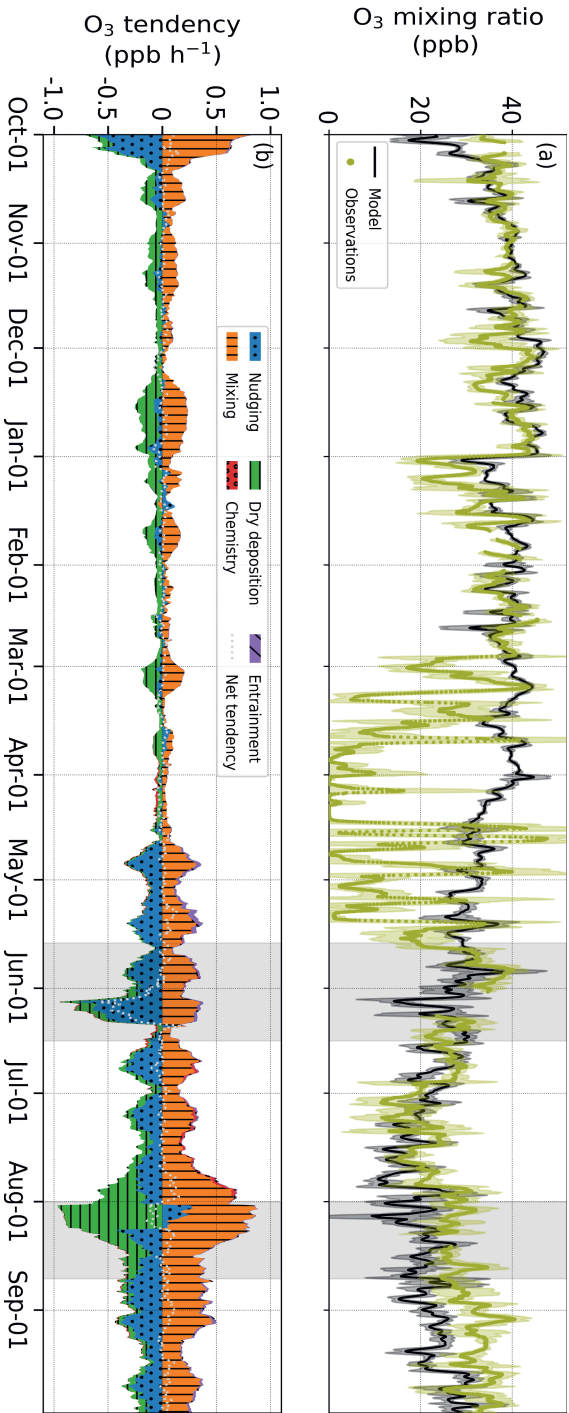


Figure 3.4: Temporal evolution of (a) simulated (black) and observed (olive green) daily running mean surface O_3 mixing ratios ($ppb \pm$ two standard deviations (shadings) and (b) 7-day running means for simulated net (dotted line), nudging (blue, implicitly representing advection), turbulent (orange), dry deposition (green), chemistry (red) and entrainment (purple) O_3 tendencies ($ppb\ h^{-1}$) in the planetary boundary layer. The grey shadings indicate the periods when RV *Polarstern* was in transit.

3.3.4 Vertical distribution of tropospheric ozone

Although we have shown that the SCM is overall very well able to represent the observed seasonal cycle in surface O_3 during MOSAiC, the SCM clearly fails in representing observed springtime surface O_3 concentrations related to ODEs. To further study the dynamics of O_3 in the PBL and in the free troposphere, including its representation in the SCM, we used data from O_3 sondes launched during MOSAiC (Figure 3.5). In wintertime, we find modelled and observed free tropospheric O_3 mixing ratios up to 50 ppb with weak gradients towards the surface. On average, we find a $\Delta O_{3(1500m-surf)}$ of 5.2 and 8.4 ppb in wintertime for the SCM co-sampled with observations and O_3 sondes, respectively. O_3 sonde observations close to the surface have a high uncertainty due to the fast ascent, measurement delay and chaotic rotation of the sonde after launch (Carminati et al., 2019). In springtime, the observations show strong O_3 gradients above the PBL. The vertical extent of the ODEs appears to be confined to the first few hundreds of meters above the estimated PBLH. The observed O_3 mixing ratios above 1000 m are hardly affected by the ODEs in spring, which also indicates a role of entrainment in the recovery of surface O_3 after ODEs. Unfortunately, this entrainment cannot be quantified using the SCM because the ODEs are not represented in these model experiments. Additionally, the temporal coverage of the O_3 sondes is too coarse to allow a quantification of the role of entrainment during ODEs. During springtime, we find a mean $\Delta O_{3(1500m-surf)}$ of 31.2 ppb from the O_3 sondes. Similarly to Figure 3.4a, we find that summertime O_3 is more depleted compared to wintertime, also in the free troposphere (Figure 3.5). During summertime, we find that both model and observations show stronger gradients towards the surface compared to wintertime, with a mean $\Delta O_{3(1500m-surf)}$ of 16.3 and 11.6 ppb in the SCM and O_3 sondes, respectively. However, in summer the SCM produces a negative bias in surface O_3 of 3 to 4 ppb (Figure 3.4a) which explains the stronger gradient in the SCM.

Figure 3.6 confirms that the SCM is most prominently biased in the lowest few hundreds of meters. Including all O_3 sondes results in a positive bias over 10 ppb close to the surface, while excluding the O_3 sondes in springtime still results in a bias of 6 ppb (not shown here). The bias in the free troposphere reduces with increasing altitude and reaches a minimum around 3 km. Above this height, the absolute bias towards the tropopause increases due to elevated O_3 mixing ratios. Most notably, we find a positive bias over the entire troposphere for the October 2019 to February 2020 months with low variability. The bias in May 2020 to September 2020 is smaller, but shows more variability. Again, the fast ascent of the O_3 sonde leads to a high uncertainty in the O_3 observations close to the surface because we do not find a bias of 6 ppb in the surface O_3 observations (Figure 3.4a). This significant bias in the PBL can hint towards an underestimation of the dry deposition sink term, even though we have shown that simulated dry deposition corresponds well with the long-term (weekly mean) observed dry deposition rates (Figure 3.3a). Another reason could be the underestimation of sources of halogens, resulting in

removal of O_3 in the PBL. Furthermore, enhanced turbulent mixing in the SCM (also reflected by overestimated T_{2m} ; Figure 3.2a) might result in an overestimation of entrainment from O_3 -rich air from the free troposphere into the PBL.

3.4 Discussion

This study demonstrates the role of O_3 dry deposition to snow and ice on the year-round O_3 budget in the Arctic PBL using observations as part of the MOSAiC campaign and supported by application of a single-column atmospheric chemistry and meteorological model. By constraining the SCM with the ERA5 meteorological (Hersbach et al., 2020) and CAMS chemical (Inness et al., 2019) reanalysis data, we aim to arrive at the most accurate representation of on-site conditions observed during MOSAiC based on correct process representation. The SCM simulates all of the atmospheric column physical and chemical processes as a function of the explicitly resolved sea-ice/snow and ocean surface source and sink processes. However, application of these reanalysis data to constrain the SCM-simulated processes implies that the simulated meteorology and chemistry also reflects the accuracy of these reanalysis datasets to represent the in-situ meteorological and atmospheric composition observations. Furthermore, the results reflect the average conditions for a domain of $0.25^\circ \times 0.25^\circ$ (ERA5) or $0.75^\circ \times 0.75^\circ$ (CAMS). This resolution suggests that the SCM results, regarding properties that are mostly affected by the role of large-scale synoptic conditions and tracer advection regimes, are more representative for a larger domain compared to the local meteorological and O_3 flux observations. By also forcing the SCM with the ERA5 sea ice fraction, we account for sub-grid scale variability in open water and snow or ice surfaces and a different representation of O_3 dry deposition to these surfaces. However, this $0.25^\circ \times 0.25^\circ$ averaged sea-ice fraction might not be representative for the local footprint of the O_3 flux observations, especially in the marginal ice zone. A detailed footprint analysis of the short-term hourly flux observations would be necessary to distinguish the contribution by ocean and snow/ice-covered surfaces in the marginal ice zone as a function of wind direction. Additionally, the ERA5 forcing data set does not account for leads, melt ponds, and ice ridges, which were commonly observed during spring and summer (Rabe et al., 2022; Nicolaus et al., 2022) and that could lead to potential non-linear effects on surface energy balance and turbulent mixing.

Regarding the SCM-simulated meteorology, our findings confirm many other studies that found that model simulations and reanalysis datasets are typically showing a warm bias over snow-covered surfaces (e.g., Savijärvi, 2014; Sterk et al., 2015; Wang et al., 2019; Tjernström et al., 2021). Most notably, Wang et al. (2019) found that the warm bias of ERA5 increases to $+5.4^\circ\text{C}$ for $T_{2m} < -25^\circ\text{C}$ over the Arctic sea ice. Here, we find an SCM warm bias of $+2.1^\circ\text{C}$ for $T_{2m} < -25^\circ\text{C}$ compared to a mean T_{2m} bias of $+1.0^\circ\text{C}$ for the entire MOSAiC dataset. ERA5 assimilates

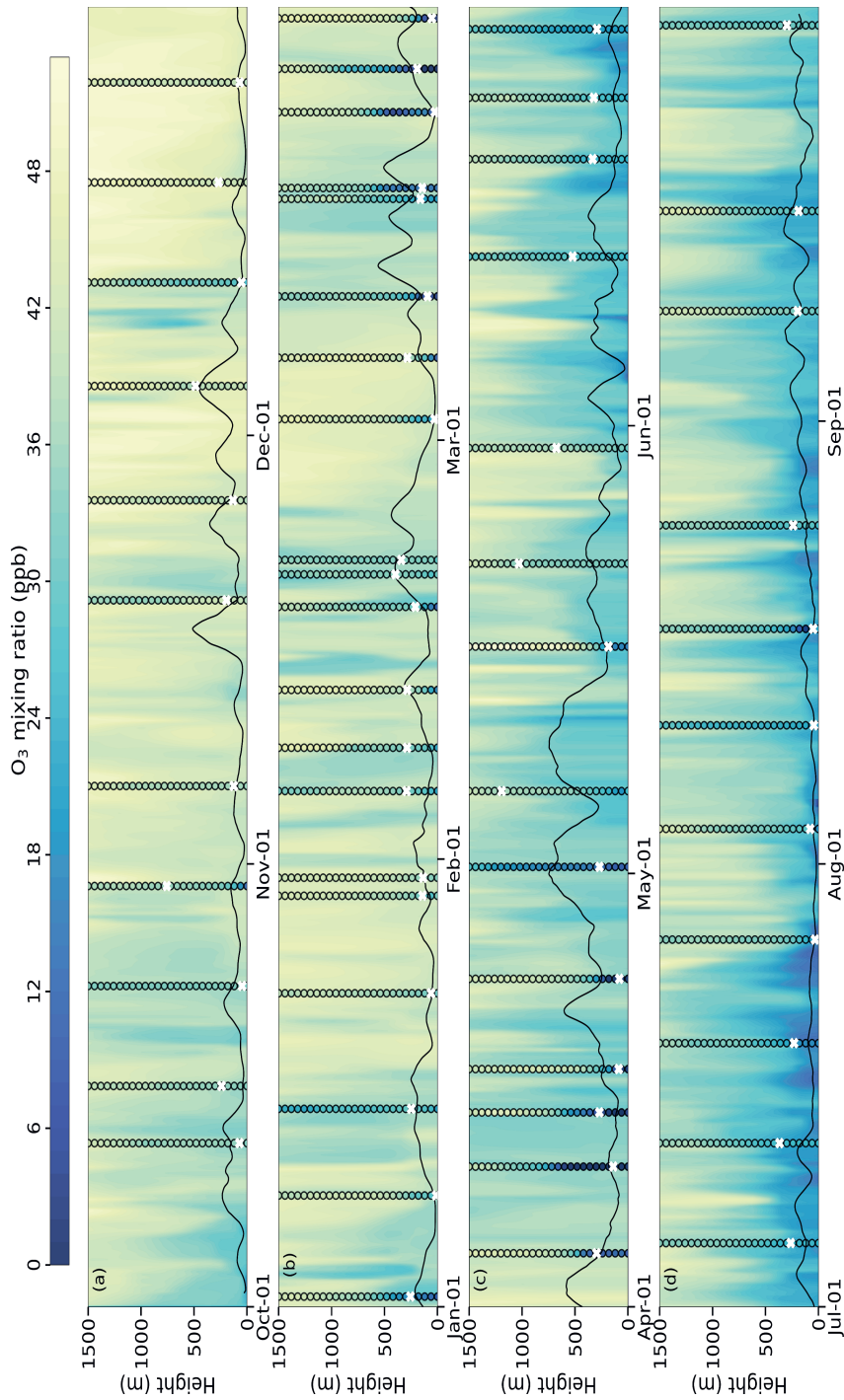


Figure 3.5: Time-height cross section of simulated (background) and observed (filled circles) O₃ mixing ratios (ppb) for (a) October–November–December 2019, (b) January–February–March 2020, (c) April–May–June 2020 and (d) July–August–September 2020. The black line and white crosses represent the simulated and observation-derived planetary boundary layer heights, respectively.

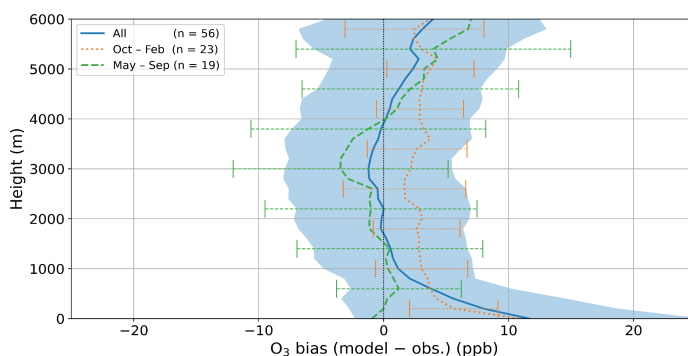


Figure 3.6: Vertical distribution of mean O_3 bias (simulated minus observations) (ppb) for all ozone sondes (blue), October 2019 to February 2020 (orange) and May 2020 to September 2020 (green). The shadings and error bars indicate \pm one standard deviation. Note the extended y-scale with respect to Figure 3.5.

RV *Polarstern* weather station data (not used in this study) and soundings, which might explain a large part of this discrepancy with Wang et al. (2019). Graham et al. (2019a) found that ERA5 performs best among 5 reanalysis products, especially related to the wind fields for a case study in summer. Here, we find that the wind fields (both speed and direction) are well represented by the SCM and arguably also by the role of nudging to ERA5 above the PBL.

Other results further corroborate the representativeness of the SCM for a larger domain compared to the local observations. For example, the surface O_3 observations show more variability on short timescales compared to the SCM (Figure 3.4a). In the SCM, the variability around the mean daily surface O_3 mixing ratio is 2.3 ppb (2σ), whereas the variability in the surface O_3 observations is 5.8 ppb (2σ). Arguably, this difference in variability includes some measurement uncertainty (Angot et al., 2022d) but can also point to missing local processes in the SCM such as snow ridging causing additional surface roughness (Haapala et al., 2013) and mixing, local chemistry caused by halogen emissions from the snowpack (Grannas et al., 2007; Simpson et al., 2007; Morin et al., 2012) and sea ice (Simpson et al., 2005; Jacobi et al., 2006), or missing temporal variability in surface deposition.

The results presented here provide insight on the observed and simulated variability in O_3 deposition, surface O_3 concentrations and the O_3 budget in the PBL. Rinke et al. (2021) has shown that the meteorological conditions during MOSAiC were relatively normal even though anomalous conditions occurred, especially related to more frequent storm events from fall to spring. Furthermore, because the overall shape and the major features in the MOSAiC observed O_3 concentrations are similar to the limited previous O_3 observations over the Arctic Ocean (Jacobi et al., 2010, and references therein), we deem the results presented here to be representative for the baseline state of Arctic surface O_3 .

By analysing for the first time a year-round dataset of eddy-covariance O_3 flux observations over the Arctic sea ice, we have quantified the removal efficiency by the Arctic sea ice and snow surface over the entire year. Previous studies mostly relied on an indirect evaluation of the representation of the dry deposition mechanism in models using surface O_3 observations (Helmig et al., 2007b; Barten et al., 2021). Here, we find a large variability in observation-derived surface resistance (r_c) between 10^3 s m^{-1} and 10^6 s m^{-1} . To what extent this variability can be explained by physical processes, such as wind pumping in snow (Helmig et al., 2007a) as opposed to measurement uncertainty due to missing observations in the snowpack, remains an open question. The SCM, which contains an empirical representation of wind pumping (Toyota et al., 2014; Murray et al., 2015), only shows a weak sensitivity of wind speed on O_3 deposition to snow. Here, we find a median r_c of $20,000 \text{ s m}^{-1}$, resulting in an O_3 deposition velocity (V_{d,O_3}) of 0.005 cm s^{-1} . This result corroborates the findings by Helmig et al. (2007b) who determined that the magnitude and variability in simulated surface O_3 concentrations were best represented using a V_{d,O_3} between 0.00 and 0.01 cm s^{-1} as already implemented by several modeling studies (Barten et al., 2020; Herrmann et al., 2021; Marelle et al., 2021). However, many atmospheric chemistry and transport models still apply by default a surface resistance that is too low by up to an order of magnitude (Simpson et al., 2012; Hardacre et al., 2015; Falk and Søvde Haslerud, 2019; Swanson et al., 2022), resulting in an overestimation of O_3 removal by the surface.

There is uncertainty as to what degree emissions from the RV *Polarstern* being deposited onto the sea-ice surface may have contaminated the snow surface and altered the natural conditions and behaviour of O_3 deposition. From our current understanding of processes controlling O_3 surface uptake (Clifton et al., 2020a), most probably any such contamination effects would have increased the O_3 surface uptake through additional depletion of O_3 with gas and liquid-phase particles in the snowpack interstitial air (Bocquet et al., 2007). Consequently, results from the observations reported here, despite being about the lowest surface O_3 uptake rates ever determined, would most likely represent upper threshold values.

The largest discrepancy between the observed and SCM-simulated O_3 concentrations was found in March to the beginning of May when the observations showed ODEs at the surface (Figure 3.4a) also affecting O_3 concentrations above the estimated PBL height (Figure 3.5b and c). The SCM does not represent these ODEs, given that we have not considered the role of springtime snowpack and sea-ice emissions of halogens and NO_x in this analysis due to missing observations to constrain these events. Therefore, we deem the results of the SCM PBL O_3 budget as not representative of the spring ODEs for which we would expect a larger contribution by chemistry and recovery of O_3 from turbulent mixing and entrainment of O_3 -rich air. An analysis of the multi-year (2003–2021) CAMS O_3 data used to nudge the SCM above the PBL indicates that CAMS also does not show ODEs in spring. Therefore, constraining the SCM with overestimated O_3 concentrations does not provide a realistic representation of the conditions of relevance for the

simulation of these ODEs, even if the surface halogen sources would be represented accurately. A detailed analysis of the ODEs and relevant halogen sources should rely on a high resolution regional 3D model simulation, including reactive halogen production due to blowing snow, sea salt aerosols and other sources (Marelle et al., 2021). Alternatively, ODEs could be further assessed with halogen-O₃ chemistry box model experiments being constrained with MOSAiC meteorological and tracer observations.

This study arrives for the first time at a quantification of the PBL O₃ budget over Arctic sea ice and specifically the role of dry deposition in the PBL O₃ budget. We show that dry deposition can strongly affect O₃ concentration in the PBL, especially during events with a shallow boundary layer, even though the O₃ dry deposition velocity to the Arctic sea ice is small compared to any other natural surface (Hardacre et al., 2015). A detailed analysis of the O₃ flux observations, including the potential role of bi-directional exchange and a comparison with other flux observations of CO₂, CH₄ and DMS, is planned for a future manuscript. Such an analysis of flux observations and footprints in combination with ocean water iodide observations might provide insight on the contribution of O₃ deposition to the ocean surface during MOSAiC. However, such an analysis will be limited to individual events when the footprint is dominantly over open ocean and is not expected to influence the results of this study. Furthermore, presence of fresh meltwater on top of the saline ocean (Rabe et al., 2022) during spring and summer might limit the atmosphere-ocean exchange of trace gases. Given the findings that dry deposition to the Arctic sea ice is an important removal mechanism of PBL O₃, a reconsideration of the dry deposition routines and corresponding surface resistance in global and regional atmospheric chemistry and transport models or reanalysis datasets is recommended. This study now confirms based on this one-year O₃ flux dataset that these models overestimate O₃ deposition to snow and ice (Simpson et al., 2012; Hardacre et al., 2015; Falk and Søvde Haslerud, 2019; Barten et al., 2021), likely resulting in an underestimation of Arctic surface and PBL O₃ concentrations. For example, Barten et al. (2021) found a mean underestimation of 5.0 ppb for the CAMS reanalysis product at 6 High Arctic sites (>70°N) for an end-of-summer case, indicating a potential overestimation of the surface removal in shallow boundary layers. Furthermore, the anticipated increase of local air pollution (Law et al., 2017; Schmale et al., 2018) and shipping emissions (Aliabadi et al., 2015; Stephenson et al., 2018) calls for continuing efforts to enhance our understanding of current estimates of O₃ radiative forcing and the fate of O₃ in the Arctic PBL.

3.5 Conclusion

This study highlights the role of dry deposition in the O₃ budget of the Planetary Boundary Layer (PBL) over the Arctic sea ice. We quantified the removal of O₃ by dry deposition to sea-ice

and snow-covered surfaces using, for the first time, year-round O_3 flux observations in the High Arctic as part of MOSAiC campaign. By combining this information with model simulations using a single-column atmospheric chemistry and meteorological model, we quantified the role of deposition and other processes in determining the O_3 concentration in the PBL.

The SCM-simulated meteorology shows a good resemblance with observations, having an R^2 of 0.88, 0.84 and 0.85 for 2-m air temperature (T_{2m}), 10-m wind speed (V_{10m}) and 10-m wind direction, respectively. On average, the SCM is unbiased with respect to wind direction and V_{10m} . However, the SCM shows a warm bias for T_{2m} , being on average $+1.0^\circ\text{C}$ and increasing to $+2.1^\circ\text{C}$ for $T_{2m} < -25^\circ\text{C}$, related to an underestimation of the stable stratification at the surface. The SCM-simulated meteorology is also strongly affected by nudging to ERA5 above the boundary layer. The SCM-simulated PBL Height (PBLH) agrees well with radiosonde-derived PBLH in terms of temporal variability and identification of extended periods, with shallow boundary layers and limited mixing during calm conditions essential for the fate of O_3 in the PBL.

From the eddy-covariance O_3 flux observations we infer the O_3 deposition surface resistance (r_c) as a residual term by calculating the aerodynamic resistance (r_a) and quasi-laminar sub-layer resistance (r_b) based on the stability of the atmosphere. We find that r_a , representing turbulent transport to the surface, is on the order of 10^2 s m^{-1} . Diffusion close to the surface, reflected by r_b , is typically one order of magnitude smaller (10^1 s m^{-1}) than r_a . A high temporal variability in observation-derived r_c was found, ranging between 10^3 s m^{-1} and 10^6 s m^{-1} . Applying a 7-day running median to derive the long-term r_c relevant for the PBL O_3 budget results in an r_c of $20,000 \text{ s m}^{-1}$ ($V_{d,\text{O}_3} \approx 0.005 \text{ cm s}^{-1}$). This value is among the lowest surface O_3 uptake ever determined and most likely represents upper threshold values, given potential contamination effects. Over the whole year, the total removal rate of O_3 to the surface is determined by the uptake efficiency of the snow and ice surface, because turbulent transport to the surface and diffusion close to the surface are seldom a limiting factor for O_3 deposition in this study.

The SCM is able to represent the yearly cycle in observed surface O_3 related to the wintertime maximum of >40 ppb and the end-of-summer minimum of approximately 15 ppb. However, the SCM is unable to reproduce the ODEs in spring due to missing halogen sources in the model and in the CAMS reanalysis dataset that was used to nudge the model. In wintertime, the PBL O_3 budget is governed mainly by removal of O_3 at the surface by dry deposition compensated by downward turbulent transport, with weekly mean tendencies up to 0.25 ppb h^{-1} . In summer, advection, which is accounted for implicitly by nudging to CAMS, also poses a significant mostly negative contribution to the PBL O_3 budget that is typically larger than the removal of O_3 by dry deposition. The contribution by dry deposition strongly depends on the depth of the PBL. During extended periods with low wind speeds ($V_{10m} < 5 \text{ m s}^{-1}$) and shallow boundary layers ($<50 \text{ m}$), the weekly mean removal tendency of O_3 by dry deposition can reach up to -1.0

ppb h⁻¹. Entrainment and the net effect of chemistry only contribute marginally (<5%) to the total simulated PBL O₃ budget.

By including vertical O₃ concentration profiles collected by 56 O₃ sondes, we gain insight on the vertical structure of PBL and free tropospheric O₃. In wintertime, we find weak O₃ gradients from the surface to the free troposphere. In springtime, the observed profiles indicate that depleted O₃ concentrations caused by the ODEs are limited to a few hundreds of meters above the PBL, resulting in very sharp vertical O₃ gradients. In the end-of-summer period, strong vertical O₃ gradients are caused by depleted O₃ concentrations in the PBL and limited entrainment of free tropospheric air with enhanced O₃ concentrations.

Results of this study strongly motivate a revision of the representation of sea ice and snow deposition of O₃ in global and regional atmospheric chemistry models, especially because many models still use surface resistances for snow and ice surfaces up to an order of magnitude smaller than presented here. Improved representations of deposition will yield better simulations of Arctic air quality, especially during calm conditions with very shallow PBLs when dry deposition strongly affects boundary layer O₃ concentrations. They also provide improved constraints on the removal role of snow and ice in the total tropospheric O₃ budget and O₃ burden in current and future climate.

B Appendices

B.1 A comparison of ERA5 and CAMS reanalysis data used for nudging

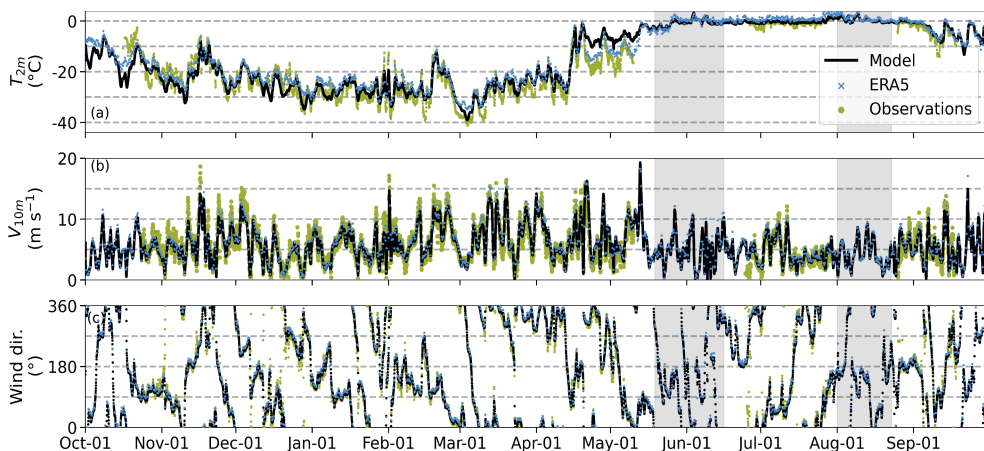


Figure B.1.1: Temporal evolution of simulated (black), ERA5 reanalysis (blue) and observed (olive green) (a) 2-m air temperature ($^{\circ}\text{C}$), (b) 10-m wind speed (m s^{-1}) and (c) 10-m wind direction ($^{\circ}$). The grey shadings in (a-c) indicate the periods when RV *Polarstern* was in transit. The SCM strongly resembles ERA5 in terms of wind speed and direction, while the temporal variation in temperature indicates differences with respect to ERA5, e.g., due to a different representation of the surface energy balance.

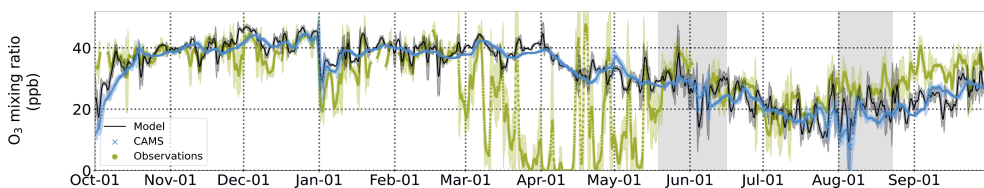
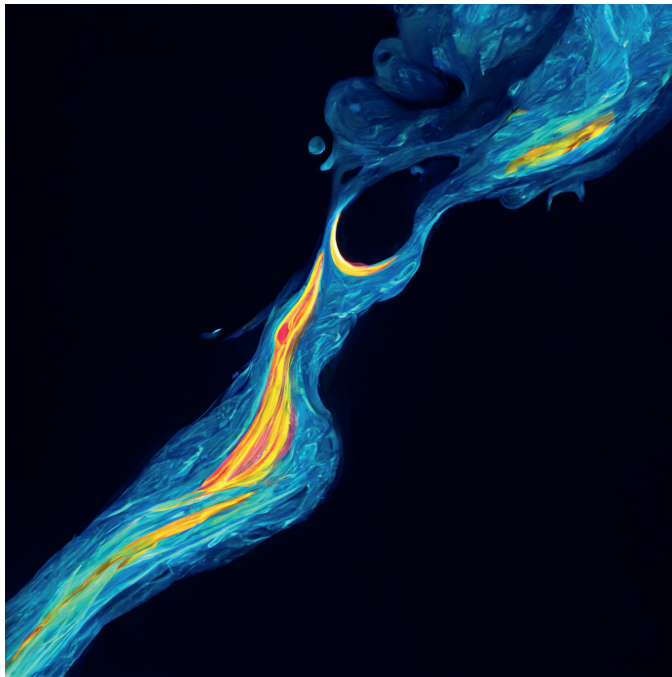


Figure B.1.2: Temporal evolution of simulated (black), CAMS reanalysis and observed (olive green) daily running mean surface O_3 mixing ratios (ppb) \pm two standard deviations (shadings). The grey shadings indicate the periods when RV *Polarstern* was in transit. The SCM follows the seasonal trend in CAMS O_3 due to nudging of the SCM to CAMS.

Chapter 4

Simulations of long-range transport of trace gases by a warm intrusion event observed during the MOSAiC field campaign



Abstract

Synoptic scale warm air intrusions provide anomalous amounts of heat and moisture to the Arctic. This enhanced transport can also bring elevated concentrations of aerosols and trace gases to the Central Arctic, where local emissions are generally absent. Even though atmospheric models are often used to study these warm air intrusions, there is limited focus on the transport of trace gases into the Central Arctic using atmospheric chemistry and transport models for such synoptic events. This is despite the expected increase in frequencies and duration of warm air intrusions in future climate. Here, we set up the Polar-WRF-Chem (WRF) model, in a case study focusing on simulations of an Arctic warm air intrusion event in April 2020. This specific warm air intrusion was observed during the MOSAiC campaign in two episodes, both with a strong increase in temperature and humidity but also showing distinct differences in observed tracer concentrations. Furthermore, we have evaluated the sensitivity of WRF simulated meteorology and trace gas concentrations to horizontal model resolution and planetary boundary layer scheme. Additionally, we show the additional benefit of running highly-resolved coupled meteorology-chemistry simulations compared to using atmospheric composition reanalysis products.

WRF is able to accurately represent MOSAiC observed meteorology during the warm air intrusions. The first episode of the warm air intrusion is dominated by southeasterly wind coming from the Eurasian mainland, with elevated mixing ratios of CO (150 ppb) and NO₂ (200 ppt). The second episode is dominated by southerly wind, coming from the Atlantic Ocean. At that time, WRF simulates lower mixing ratios of CO (125 ppb) and NO₂ (50 ppt), but elevated mixing ratios of O₃ (50 ppb). The distinct differences in tracer footprints for the two warm air intrusion events is further supported by MOSAiC observations, which generally agree well with WRF during the warm air intrusion. We find some improvement of model performance on horizontal model resolution (3 km versus 27 km) and no clear preference for planetary boundary layer scheme, even though performance strongly varies across the different selected variables. We do find that WRF performs better in terms of simulated mixing ratios of trace gases with respect to the CAMS reanalysis data. Results in this study provide insight in the role of long-range transport of trace gases during Arctic warm air intrusion events. We show that simulations and observations of atmospheric trace gases can help identify source regions and the transport pathway during Arctic warm air intrusions. In future climate, this event-driven transport might become a more significant source of trace gases in the Arctic atmosphere if these intrusions increase in frequency and intensity.

4.1 Introduction

The Arctic is warming at nearly four times the rate of the global average (Rantanen et al., 2022). This phenomenon is often referred to as Arctic Amplification (Serreze and Barry, 2011; Cohen et al., 2014). The rapid warming has caused a major decline of Arctic sea ice and snow cover (Cavalieri and Parkinson, 2012; Simmonds, 2015), at faster rates than predicted by global climate models (Derksen and Brown, 2012; Blanchard-Wrigglesworth et al., 2015). Arctic Amplification likely follows from a multitude of mechanisms and feedbacks, of which the importance of each individual component is repeatedly debated (Serreze and Francis, 2006; Dai et al., 2019; Previdi et al., 2021). These mechanisms include the snow- and ice-albedo feedback (Curry et al., 1995), increased downwelling longwave radiation due to enhanced water vapor and cloud cover (Graversen and Wang, 2009; Ghatak and Miller, 2013), local radiative effects associated with enhanced greenhouse gas concentrations (Gillett et al., 2008), and the deposition of black carbon on snow (Dou and Xiao, 2016; Kang et al., 2020).

These local effects are accompanied by an increase in poleward energy transport in the atmosphere (Alexeev and Jackson, 2013; Roe et al., 2015) and ocean (Jungclauss et al., 2014; Marshall et al., 2015). On shorter timescales, low pressure systems can enhance the transport of energy from lower latitudes to the Arctic, providing a significant source of heat and moisture to the Central Arctic atmosphere (Kim et al., 2017; Pithan et al., 2018; Rydsaa et al., 2021; You et al., 2021). These synoptic scale warm air intrusions strongly alter the exchange of energy and momentum (You et al., 2022) and local sea-ice retreat (Boisvert et al., 2016; Graham et al., 2019b). Especially in winter, warm air intrusions are occurring at increasing frequencies and duration (Graham et al., 2019b), which is expected to continue in future climate (Henderson et al., 2021). This enhanced transport also brings enhanced trace gas and aerosol concentrations from the mid-latitudes into the Central Arctic (Bossioli et al., 2021; Dada et al., 2022), where local emissions are generally absent. This will strongly alter the composition of the Arctic troposphere, which may further enhance local warming through effects on radiation and clouds.

Observations of Arctic surface trace gases often rely on site-specific analysis of observations over land (Barten et al., 2020; Yang et al., 2020; Whaley et al., 2023). However, these intrusions of warm air masses with enhanced trace gas and aerosol concentrations can also be transported over the Arctic sea ice, where observations are generally absent. Additionally, these trace gases and aerosols are anticipated to have a long lifetime due to the reduced (photo-)chemical destruction, stratified atmosphere and low surface removal rates. From October 2019 to September 2020 the German icebreaker *RV Polarstern* docked into the Arctic sea ice as part of the Multidisciplinary drifting Observatory for the Study of Arctic Climate (MOSAiC) expedition. The main goal of the MOSAiC expedition is to better understand the causes and consequences of Arctic climate change. For the full year of the MOSAiC expedition there have been detailed observations of

the Arctic atmosphere (Shupe et al., 2022), sea ice (Nicolaus et al., 2022), ocean (Rabe et al., 2022), biogeochemistry and ecology. In April 2020, a warm air intrusion brought relatively warm and moist air in two episodes to the central observatory of MOSAiC (Männel et al., 2021), generating a brief episode of surface ice melt (Cox et al., 2021b). In fact, this warm air intrusion resulted in record high observations of near surface air temperature and surface downwelling longwave radiation, with respect to 40 years of European Centre for Medium-Range Weather Forecasts (ECMWF) Reanalysis v5 (ERA5) data (Rinke et al., 2021). Furthermore, enhanced concentrations of cloud condensation nuclei and aerosols, such as black carbon and ammonium, were observed (Dada et al., 2022).

Even though these warm air intrusions bring about large changes in the composition of the Arctic atmosphere, dedicated 3D mesoscale modeling studies, focused on the transport and cycling of trace gases, have not yet been performed. Additionally, observational studies often strongly rely on back trajectories from products such as FLEXible PARTicle dispersion model (FLEXPART) (Brioude et al., 2013; Pissot et al., 2019) or Hybrid Single-Particle Lagrangian Integrated Trajectory (HYSPPLIT) (Draxler and Rolph, 2010), to understand the sources of enhanced concentrations of trace gases or aerosols. By tracing the air back in time, these back trajectory models approximate the footprint area of the observations. However, these back trajectories are often driven by reanalysis data on a relatively coarse grid spacing of $\geq 0.25^\circ \times 0.25^\circ$, resulting in a large uncertainty in the estimates for specific cases (Dacre et al., 2016). Especially for the prevailing conditions in the Arctic, with a generally strongly stratified atmosphere, the accuracy of the estimates decreases with coarser resolution model simulations (Su et al., 2015).

Here, we evaluate simulations of the warm air intrusion using the Weather Research and Forecasting (WRF) model (Skamarock et al., 2019). We focus on the transport and further cycling of the trace gases carbon monoxide (CO), nitrogen oxides ($\text{NO}_x = \text{NO} + \text{NO}_2$) and ozone (O_3), and compare these model simulations with observations performed at the MOSAiC central observatory over the Arctic sea ice. Additionally, we show how additional information of simulations and observations of atmospheric trace gases can help identify source regions and the transport pathway during Arctic warm air intrusions. The main objectives of this study are 1) to evaluate the WRF model performance with respect to concentrations of trace gases and other relevant properties such as atmospheric transport, stability and mixing and 2) to address the sensitivity to model resolution and the choice of parameterization schemes.

4.2 Methods

4.2.1 Model setup

Here, we use the WRF model version 4.1.1 (Skamarock et al., 2019) optimized for Polar regions (Hines and Bromwich, 2008; Hines et al., 2015) coupled with Chemistry (Grell et al., 2005) (Polar-WRF-Chem, hereafter: WRF). WRF is a non-hydrostatic, state-of-the-art, fully coupled meteorology and atmospheric chemistry model, often used for air quality studies over many different regions (Kukkonen et al., 2012; Baklanov et al., 2014; Bocquet et al., 2015). Our model domain is centered at 84.3 °N and 14.5 °E, approximately the location of *RV Polarstern* at the start of the simulation. We set up three domains with 250×250 grid cells each, and a grid spacing of 27 km, 9 km and 3 km, respectively. Here, we use 61 vertical levels from the surface up to 100 hPa. The setup of the three domains can be seen in Fig. 4.1. We initialize the model with meteorological reanalysis data from ERA5 (Hersbach et al., 2020) ($0.25^\circ \times 0.25^\circ$) and chemical reanalysis data from the Copernicus Atmosphere Monitoring Service (CAMS) (Inness et al., 2019) ($0.75^\circ \times 0.75^\circ$). These products also provide the boundary conditions for the simulations at the edge of the domain, which are updated every three hours. Furthermore, we update the sea surface temperature and sea ice fraction from ERA5, to allow for the retreat of sea ice during the simulation. We nudge the outermost domain every three hours to ERA5 specific humidity, temperature and wind speeds in the free troposphere, with nudging coefficients of $1 \times 10^{-5} \text{ s}^{-1}$, $3 \times 10^{-4} \text{ s}^{-1}$ and $3 \times 10^{-4} \text{ s}^{-1}$, respectively (Barten et al., 2021). The simulation starts the 5th of April, 2020, 00:00 UTC and ends the 22nd of April, 2020, 00:00 UTC. This allows for more than one week of spin-up before the warm air intrusion arrives at MOSAiC around the 16th of April. This ensures that the simulated conditions during the warm air intrusion events are to a lesser extent determined by the quality of the initial conditions.

The physical and chemical parameterization schemes used in this study are listed in Tab. C.1.1 in Appendix C.1. We specifically opted for the double-moment Thompson micro-physics scheme (Thompson et al., 2016), due to its most accurate representation of cloud cover in this specific case study, based on preliminary model simulations. Other micro-physics parameterization schemes, especially single-moment schemes, simulated too abundant cloud cover with resulting effects on the radiation and energy budget, and surface temperatures. Furthermore, we use the previously applied representation of atmospheric chemistry processes, including the oceanic O₃ deposition parameterization and reduced snow-ice O₃ uptake rate as implemented Barten et al. (2021). This scheme accounts for the process-based removal of O₃ in the surface water based on oceanic iodide (I⁻) and waterside turbulent transport, and replaces the default constant dry deposition velocity approach by Wesely (1989). This generally results in a much lower removal of O₃ by the Arctic ocean surface (Barten et al., 2021).



Figure 4.1: Setup of the three WRF domains (d01, d02, d03) including sea ice cover from ERA5 interpolated to the WRF grid at the start of the simulation. The drifting path of the MOSAiC campaign during the simulation is indicated with the black line at the center of the domains.

4.2.2 Observations

We compare the model results to observations collected at the MOSAiC central observatory. Surface observations of O_3 were performed in three dedicated containers, of which a merged product is compiled. This product is minute-averaged and de-spiked to filter the role of local air pollution (Angot et al., 2022a). Similar to O_3 , observations of CO were performed in two containers and are de-spiked and minute-averaged (Angot et al., 2022f). Observations of NO_2 were sampled from the bow-crane and analyzed in the Colorado University container. We have re-sampled all observations of trace gas concentrations to hourly values and compare these to the hourly model output.

Furthermore, we use meteorological data from a tower, operated on the sea ice, approximately 500 m from *RV Polarstern* (Cox et al., 2021a). This tower is complemented by an automatic surface flux station, measuring all four surface radiation components and surface energy fluxes at a height of 3.8 m. Additionally we compare the model output to radiosondes launched every six hours (Maturilli et al., 2021). These radiosondes are also used to infer the Planetary Boundary Layer Height (PBLH) using the bulk-Richardson method and a critical bulk-Richardson number of 0.40. See (Jozef et al., 2022; Barten et al., 2023) for a detailed description of the method to derive the PBLH from the radiosondes. It is important to note that the automatic weather

station data aboard the *RV Polarstern*, and the meteorological radiosondes have been assimilated into ERA5 implying that the use of these meteorological observations do not provide a fully independent source of data for model evaluation. The other meteorological observations provide an independent dataset for model evaluation.

4.2.3 Reanalysis data

Additionally, we compare the WRF model results to the ERA5 (Hersbach et al., 2020) and CAMS (Inness et al., 2019) reanalysis data of meteorology and atmospheric chemistry, respectively. Even though we initialize the WRF model simulations with the same reanalysis datasets, and we use these datasets as boundary conditions throughout the simulations, we aim with this study to evaluate the potential benefit of running a higher resolution model setup. Given that the *RV Polarstern* is located in the center of the domain, and the model boundaries are located > 3000 km away from the ship, we are confident that the properties simulated by WRF can be analyzed independently from these reanalysis products.

4.3 Results

First, we present the WRF simulated synoptic meteorology during the warm air intrusion events and evaluate simulated surface-layer meteorological variables at the MOSAiC location. We will also evaluate the simulated vertical atmospheric structure using some selected representative radiosonde observations. Thereafter, we will present the synoptic-scale spatial distribution of the selected trace gases NO_x , CO and O_3 during the warm air intrusion events and compare these with locally observed concentrations observed during MOSAiC. Finally, we will present the model sensitivity to model resolution and choice of PBL parameterization scheme on selected meteorological and chemical variables. In this analysis, we also include reanalysis data to indicate the potential benefit of the high-resolution WRF model in analyzing this warm air intrusion case.

4.3.1 WRF simulated synoptic conditions and comparison with observed meteorology

During the first wave of the warm air intrusion, around the 16th of April 2020, WRF simulates a low pressure system above northwestern Russia with a core pressure of about 977 hPa (Fig. 4.2a). This low pressure system generates a cyclonic flow, transporting warm and moist air from eastern Europe into the Arctic. A well developed high pressure system above Laptev sea and a smaller low pressure system just off the coast of northeast Greenland cause strong southeasterly winds towards the MOSAiC location. The transport of relatively warm air (~ -5 to 0°C near the

surface) reaches up to the geographic North Pole and is in clear contrast to colder temperatures above northeastern Russia and the Canadian High Arctic.

During the second wave of the warm air intrusion, around the 19th of April 2020, a high pressure system with a central pressure of about 1032 hPa developed off the coast of Norway (Fig. 4.2b). This high pressure system generates an anticyclonic flow transporting warm and moist air from the North Atlantic Ocean and western Europe towards the Arctic. This air is transported further north due to a low pressure system just off the coast of northeast Greenland creating southerly winds through the Fram strait towards the MOSAiC location. While the first episode of the warm air intrusion event created a strong flow off the Eurasian mainland, the second episode is much more dominated by maritime footprint with further consequences for the composition of the atmosphere during the two episodes.

These transport pathways of the two episodes of the warm air intrusion event are further supported by FLEXPART Lagrangian back-trajectory model simulations, which uses ERA5 as meteorological input. In Fig. C.2.1, Appendix C.2 we show back-trajectories for the air masses arriving at the MOSAiC location at 100 m and 3000 m height for the two warm intrusion episodes. For both episodes, we find that the back-trajectories agree with WRF model simulated footprints. Additionally, we do not find a strong spread in the geographical footprint region between the two simulated heights. This indicates that the composition of the boundary layer and free troposphere is dominated by approximately the same mid-latitude source region.

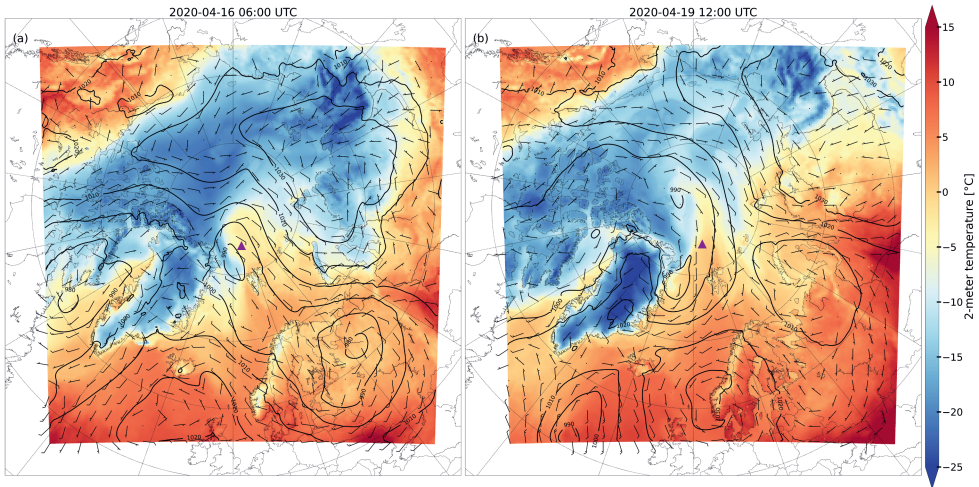


Figure 4.2: Simulated 2-meter air temperature [°C] (colors), sea level pressure [hPa] (contours) and 10-meter wind speed and direction (wind barbs) at (a) 2020-04-16 06:00 UTC and (b) 2020-04-16 12:00 UTC. The purple triangle corresponds to the position of the *RV Polarstern*.

Both episodes of the warm air intrusion feature a decrease in sea level pressure and increase in 10-meter wind speed, 2-meter air temperature and 2-meter relative humidity (Fig. 4.3). Both episodes of the warm air intrusion are relatively similar in terms of 10-meter wind speed (10 to 15 m s⁻¹), 2-meter temperature (-5 to 0 °C) and relative humidity (90 to 100 %). Observed wind direction is south-southeast during the first episode, while the wind direction is south during the second episode. Observed 2-meter air temperatures feature a continuous increase from -26 °C on the 14th of April onward, to reach a maximum of -2 °C on the 16th of April around noon. After the first episode we find a sharp decrease in air temperature (about -15 °C in a few hours), accompanied by a sharp decrease in wind speed (from 12 to 5 m s⁻¹) and relative humidity (from 97 to 80 %). The second episode of the warm air intrusion is more persistent, having > 24 hours of air temperatures > -5 °C. Additionally, we find a notable decrease in wind speed and shift in wind direction at the end of the episode due to the passage of the center of the low pressure system. The days prior to the warm air intrusion are relatively cold (down to -30 °C) and dry (70 to 80 % relative humidity). Observations of surface short- and long-wave radiation show mostly cloud free conditions up to the 14th of April (Fig. 4.3f) represented by low values of incoming long-wave radiation and a clear diurnal cycle in incoming short-wave radiation. From this day onward, cloudy conditions persist up to the end of the second episode of the warm air intrusion, with one exception. The 17th of April, between the two warm air intrusion episodes, shows cloud free conditions which makes the air close to the surface able to cool down rapidly for one day (Fig. 4.3c).

The WRF model is able to accurately simulate sea level pressure, wind speed and wind direction prior to, and during the warm air intrusion episodes. A quantification of the quality of the WRF model simulation with respect to MOSAiC observed meteorology is provided in Sect. 4.3.3. In terms of air temperature, WRF is able to simulate the maxima during the warm air intrusion episodes, as well as the rapid cooling in between. However, WRF shows a clear warm bias during the days prior to the warm air intrusion, potentially indicating a misrepresentation of near-surface stability. In terms of relative humidity, the WRF model is able to represent the dry conditions (70 to 80 % relative humidity) prior to the warm air intrusion. However, the WRF model simulates a drying of the atmosphere after the two episodes, which is too fast compared to observations. WRF simulates completely cloud free conditions prior to the warm air intrusion, even though observations show some presence of clouds (e.g. the 9th of April). The WRF model agrees generally well on the cloud free to cloudy transition prior to the warm air intrusion episodes (Fig. 4.3f), as well as the cloud free conditions on the 17th of April. In Appendix C.3 we show and discuss a comparison between the WRF simulation and selected radiosondes, prior to and during the warm air intrusion.

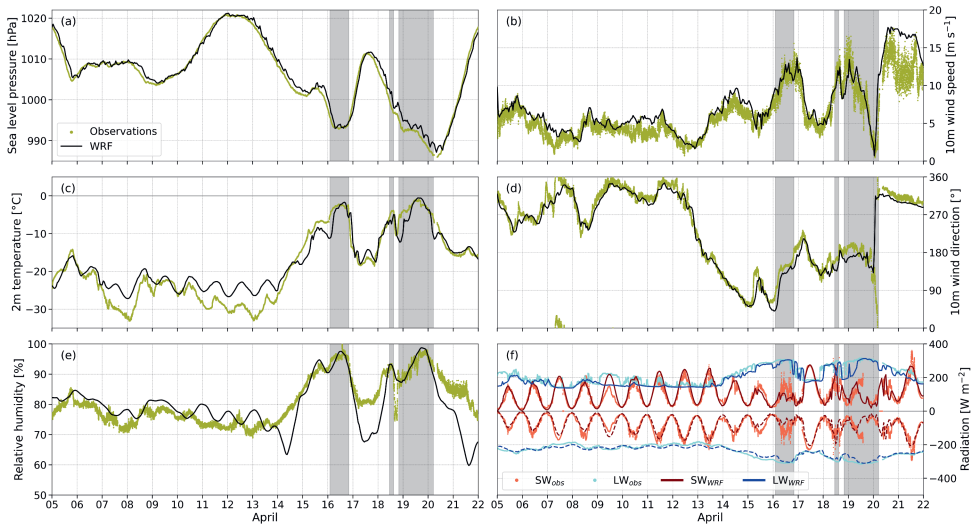


Figure 4.3: Temporal evolution of observed (olive green) and simulated (black) (a) sea level pressure [hPa], (b) 10–meter wind speed [m s^{-1}], (c) 2–meter air temperature [$^{\circ}\text{C}$], (d) 10–meter wind direction [$^{\circ}$], 2–meter relative humidity [%] and (f) all four surface radiation components [W m^{-2}]. In (f) positive values indicate the incoming radiation components and negative values represent the outgoing radiation components. The grey boxes indicate observed 2–meter air temperature $> -5^{\circ}\text{C}$, representing the warm air intrusion events.

4.3.2 Distribution and evolution of NO_x , CO and O_3 during the warm air intrusion

Figure 4.4 shows the spatial distribution of WRF simulated NO_x , CO and O_3 during the two episodes of the warm air intrusion also depicted in Fig. 4.2. During the first episode of the warm air intrusion we find elevated mixing ratios of NO_x (Fig. 4.4a) and CO (Fig. 4.4c), transported from northeastern Europe towards the MOSAiC location. Especially for CO, we find a relatively narrow band of transport across the Barentz sea. Elevated mixing ratios can be partially attributed to anthropogenic sources, well visible in the maps of NO_x and CO. We also find a substantial contribution of CO transported across the model boundaries reflecting the important role of long-range transport and the imposed boundary conditions using the CAMS reanalysis data. WRF simulates relatively depleted O_3 mixing ratios for the first warm air intrusion episode (Fig. 4.4f), which is likely a remnant of the O_3 titration caused by high NO_x emissions in eastern Europe.

For the second warm air intrusion episode, WRF simulates much lower mixing ratios of NO_x (Fig. 4.4b) and CO (Fig. 4.4d), reflecting a more maritime footprint. On the other hand, WRF simulates elevated O_3 mixing ratios across the North Atlantic Ocean and Greenland (Fig. 4.4f), which are now transported to the MOSAiC location. Again, we find a strong role of CO

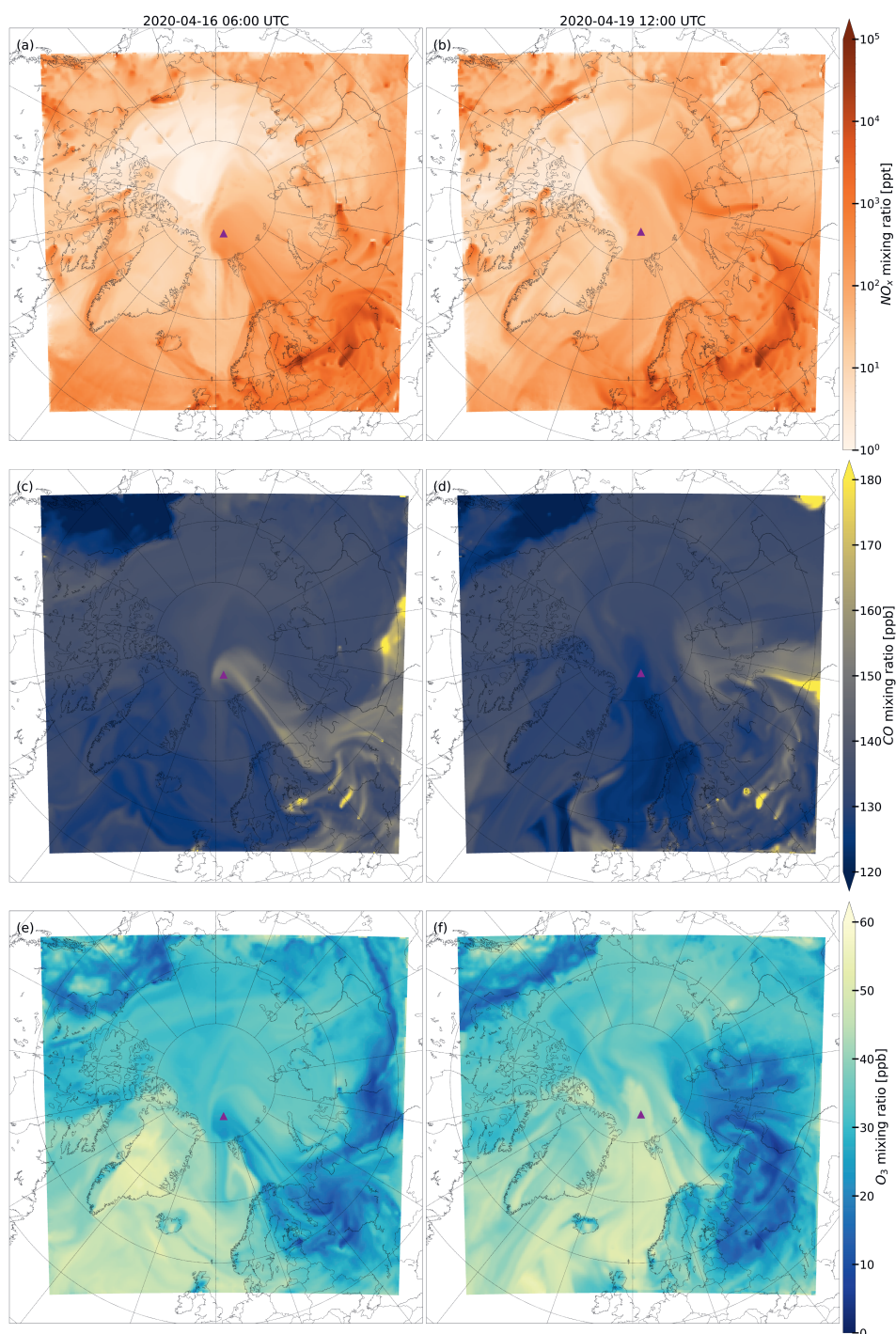


Figure 4.4: Simulated surface mixing ratios of (a,b) nitrogen dioxide [ppt], (c,d) carbon monoxide [ppb] and (e,f) ozone [ppb] at (left) 2020-04-16 06:00 UTC and (right) 2020-04-19 12:00 UTC. The purple triangle corresponds to the position of the RV *Polarstern*.

advection over the model boundaries which is more pronounced compared to NO_x and O_3 , due to the longer lifetime. This implies that the WRF model results for the MOSAiC location are to some degree impacted by the quality of the CAMS reanalysis dataset.

MOSAiC observed NO_2 and CO also indicate strongly enhanced mixing ratios during the first warm air intrusion episode, with observed mixing ratios up to 150 ppt and 150 ppb, respectively. (Fig. 4.5a,b). These observations confirm the role of long-range transport of air pollutants, partially originating from anthropogenic emissions at lower latitudes, during the first episode of the warm air intrusion event. Additionally, the WRF model agrees with lower observed mixing ratios of NO_2 and CO, during the second episode. Especially in terms of CO, observations show mixing ratios about 25 ppb lower than background conditions in April. Observations of CO confirm the role of advection of air masses over maritime areas, where local emissions are mostly absent. In Appendix C.4 (Fig. C.4.1) we show WRF simulated vertical wind speed and CO mixing ratios up to 8000 m height for the entire WRF simulation. We find that WRF simulates strong upward motions at the start of the first warm air intrusion episode. This coincides with enhanced mixing ratios of CO over the entire troposphere. For the second episode, WRF simulates very dynamic conditions of both strong upward and downward motions. Here, we also find depleted CO mixing ratios over the entire troposphere, indicating a strong role of vertical transport during the warm air intrusion.

In terms of O_3 (Fig. 4.5c), WRF simulated mixing ratios during the two episodes of the warm air intrusion event do not fully agree with MOSAiC observed mixing ratios. Rather, O_3 observations show mixing ratios up to 50 ppb for both episodes, with WRF showing O_3 mixing ratios less than 35 ppb during the first wave of the warm air intrusion. This indicates a potential overestimation of O_3 titration at lower latitude source regions with NO emissions, or an underestimation of O_3 production during transport of the air masses over the Arctic Ocean. For the second episode, the WRF model is able to accurately represent observed O_3 mixing ratios of 45 to 50 ppb. Additional model simulations (not shown here) indicate the role of O_3 deposition to the Arctic Ocean and sea ice. In this WRF simulation we have strongly reduced O_3 deposition to oceans and sea ice based on Barten et al. (2021), compared to the commonly used Wesely (1989) approach. Especially for the second episode, having a more maritime footprint, this enhances simulated O_3 mixing ratios up to 10 ppb. What is clear from Fig. 4.5c is that the observations indicate very low O_3 mixing ratios in the period before and between the warm air intrusions. We speculate that this is to a large extent caused by halogen chemistry that is currently not included in our model simulations. While O_3 depletion events appear to be dominant for the period preceding the warm air intrusion, recovery of an O_3 depletion event up to mixing ratios of 50 ppb can occur in less than 24 hours (Fig. 4.5c).

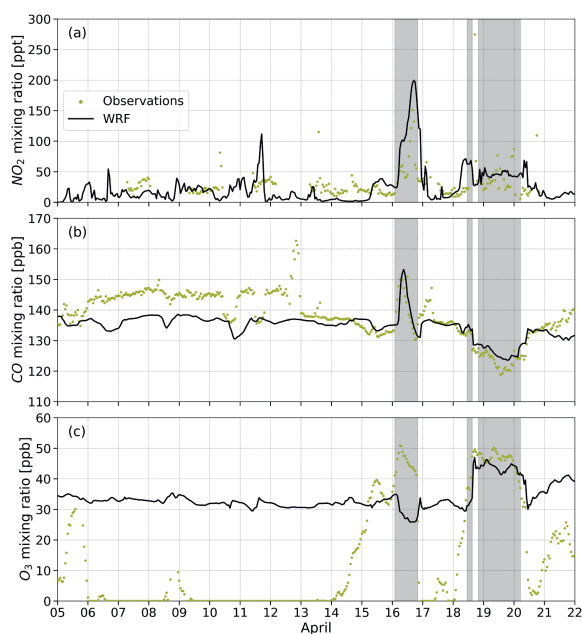


Figure 4.5: Temporal evolution of observed (olive green) and simulated (black) mixing ratios of (a) nitrogen dioxide [ppt], (b) carbon monoxide [ppb] and (c) ozone [ppb]. The grey boxes indicate observed 2-meter air temperature $> -5^{\circ}\text{C}$, representing the warm air intrusion events.

4.3.3 Model sensitivity to resolution and planetary boundary layer scheme

In Sect. 4.3.1 and Sect. 4.3.2 we have shown a comparison of WRF simulated and MOSAiC observed properties, for the WRF model simulation at a resolution of 3×3 km. Here, we will show the sensitivity of the WRF model simulations to the horizontal model resolution, by also including the results of a model simulation at a resolution of 27×27 km. Additionally, we will show the results of a WRF simulation using the YSU PBL scheme compared to the MYJ PBL scheme in the reference simulation. YSU is a non-local, first-order closure PBL scheme where vertical mixing is calculated based on the eddy diffusivity profiles of momentum, heat and moisture (Hong et al., 2006). MYJ is a local, 1.5 order closure PBL scheme where vertical mixing is calculated based on simulated turbulent kinetic energy and buoyancy (Janjić, 1994). Additionally, we include statistics for the ERA5 and CAMS reanalysis data. Figure 4.6 shows skill indicators for six selected variables for the WRF simulations and the ERA5/CAMS reanalysis data. These skill indicators include the explained variance R^2 which represents the degree of correlation, the mean absolute error (MAE) which represents the systematic error, and the standard deviation of observation minus model prediction σ_{o-p} which represents the random error.

In terms of relative humidity the MYJ_{27km} simulation remains too dry during the warm air intrusion and does not simulate a completely saturated PBL as we found in the observations and MYJ_{3km} simulation (Fig. C.3.1f,j). Additionally, the MYJ_{3km} simulation shows the lowest MAE among all simulations for 2-meter temperature (Fig. C.3.1c) and outperforms the MYJ_{27km} for wind speed (Fig. C.3.1b) and wind direction (not shown here). In most cases we find symmetry between the MAE and σ_{o-p} skill indicators. However, for 2-meter temperature we find the lowest MAE and the highest σ_{o-p} for the MYJ_{3km} simulation (Fig. C.3.1c). This indicates that even though the prediction for 2-meter temperatures is on average better, there is a larger spread around the mean bias. This can be related to local exchange processes at the surface, which are better represented at a higher resolution, causing additional variability in surface stability and resulting temperature variability.

For each WRF simulation we calculate the boundary layer height based on the bulk-Richardson method, similar to the calculation radiosonde derived PBL height (Barten et al., 2023) (Fig. 4.6). Because every PBL scheme has its own method to calculate the PBL height, the aforementioned method is needed to allow for a fair comparison between the different PBL schemes. We find that the 1.5 order closure MYJ PBL scheme is able to better represent observation derived PBL heights, compared to the first-order YSU PBL scheme. Typically, YSU simulates increased mixing and a deeper PBL compared to MYJ. Additionally, the surface-layer inversions are weaker in YSU, with respect to MYJ. Interestingly, YSU outperforms MYJ in other variables such as CO mixing ratio and relative humidity. These results indicate that some increase in model

performance from a higher model resolution can be achieved. However, no clear improvement can be found by changing the WRF PBL parameterization scheme for this warm air intrusion event. Rather, the specific model setup depends strongly on the variable of interest.

For both sea level pressure and 10-meter wind speed, ERA5 outperforms the WRF simulations. This is partially because the data from the *RV Polarstern* automatic weather station data is assimilated in ERA5, which is located approximately 500 meters away from the meteorological tower. Additionally, ERA5 results show a good correlation ($R^2 = 0.76$) with observed relative humidity. In contrast, all WRF simulations outperform CAMS in terms of simulated mixing ratios of CO (Fig. 4.6e) and NO₂ (not shown here). This indicates the benefit of running highly-resolved coupled meteorology-chemistry model simulations to study the transport of air pollutants for Arctic warm air intrusions, regarding the composition of the atmosphere.

4.4 Discussion

This study highlights the role of long-range transport of trace gases during an Arctic warm air intrusion event in April 2020 using observational data from MOSAiC, WRF simulations and reanalysis data. Here, we opted for a mesoscale 3D coupled meteorology and atmospheric chemistry transport model to fully resolve the emissions and transport of trace gases from the mid-latitudes. Additionally, 1D model simulations from Barten et al. (2023) show that 1D models lack appropriate constraints during synoptically driven events, when large-scale processes dominate over local processes. These 1D model simulations typically rely on the use of reanalysis data as boundary conditions, to account for advection of temperature, humidity and trace gases. Here, we show that WRF outperforms CAMS reanalysis data, in representing MOSAiC observed trace gas concentrations. Additionally, WRF shows a lower MAE with respect to ERA5 2-meter temperature. This motivates to explore the potential of using mesoscale 3D model simulations as boundary conditions in 1D model experiments, to study local exchange processes during large-scale driven events.

Here, we found some improvement of the WRF model by increasing the horizontal model grid spacing from 27 km to 3 km. However, this improvement is not consistent across all selected parameters. This is in contrast to many previous studies who found a clear improvement of the WRF model for increasing horizontal model grid spacing (e.g., Gustafson et al., 2011; Ma et al., 2014; Weigum et al., 2016; Crippa et al., 2017). For example, Crippa et al. (2017) showed improved model performance for all meteorological variables and trace gas concentrations over North America, at a resolution of 12 km compared to 60 km. Most of the studies assessing the role of model resolution on model performance focus on mid-latitude regions, with a large variability in surface characteristics, surface emissions and orography. For these cases, enhanced resolution

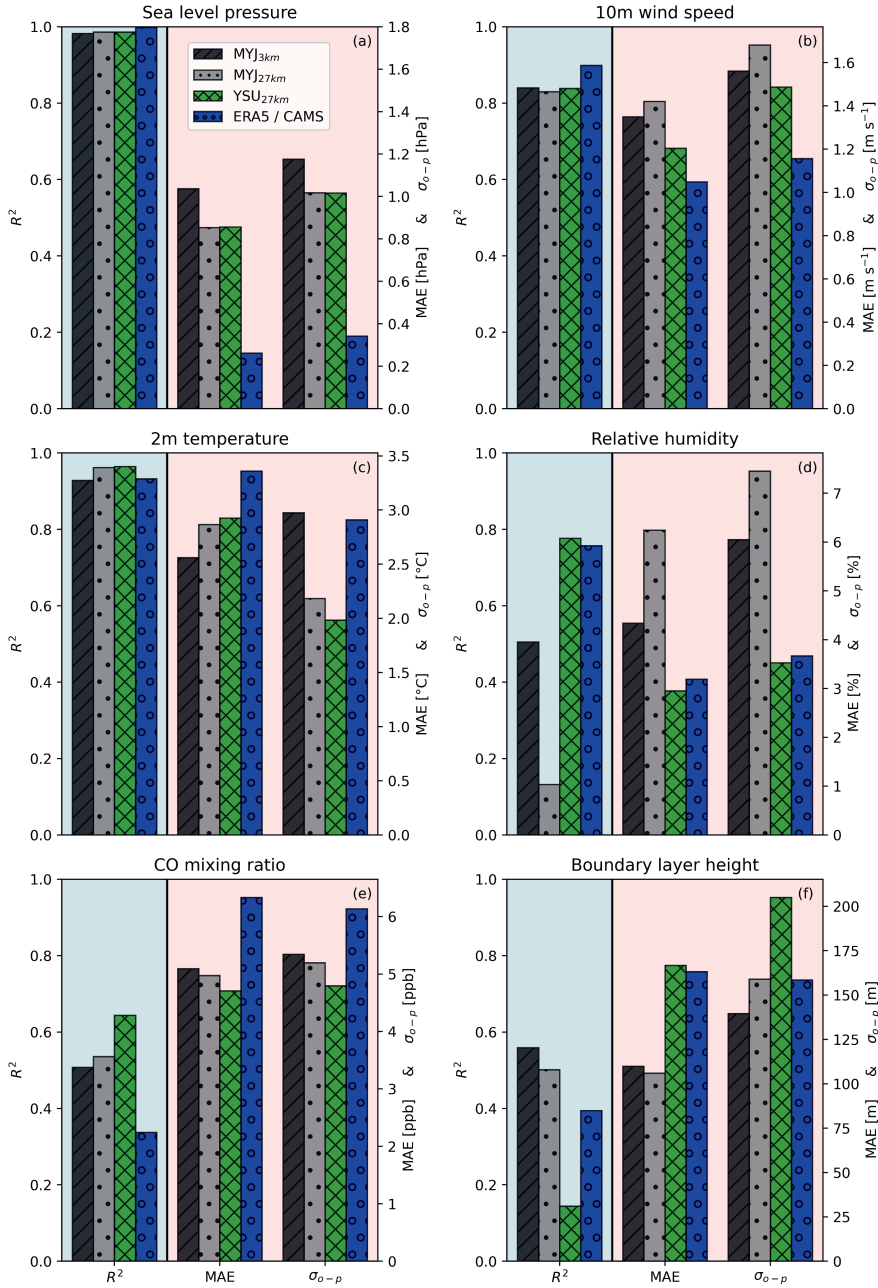


Figure 4.6: Skill indicators of three different WRF simulations and the ERA5/CAMS data for (a) sea level pressure, (b) 10-meter wind speed, (c) 2-meter air temperature, (d) 2-meter relative humidity, (e) carbon monoxide mixing ratio and (f) boundary layer height. Note that R^2 is represented on the left y-axis and the mean absolute error (MAE) and standard deviation of observation minus prediction (σ_{o-p}) are represented on the right y-axis.

inherently implies higher resolution surface boundary conditions, emissions and other surface characteristics. In our study, the main benefit of running higher resolution simulations would arise from resolving the physical and chemical processes, such as surface-atmosphere exchange, boundary layer mixing, advection and (photo-)chemistry at smaller scales. For example, even though the sea ice fraction and sea surface temperature is updated for the higher-resolution grid, it still relies on the ERA5 boundary conditions which are at a resolution of $0.25^\circ \times 0.25^\circ$. Furthermore, WRF does not consider heterogeneity in the sea ice surface such as leads and ridges. We argue that enhanced model resolution is mostly beneficial for cases with high surface heterogeneity, also being available in a consistent dataset of boundary conditions for both the physical and chemical processes to be resolved by the model.

By changing the PBL parameterization scheme from the local MYJ scheme to the non-local YSU scheme, we did not find a clear improvement in model skill score across all selected parameters. This is supported by Marelle et al. (2021), who evaluated the MYJ and YSU schemes, in addition to the Mellor-Yamada Nakanishi and Niino (MYNN2.5) scheme (Nakanishi and Niino, 2006), with surface and radiosonde observations at Utqiavik, Alaska. Generally, non-local schemes perform better for unstably stratified conditions, while local schemes perform better for stable conditions (Jia and Zhang, 2020). The main reason is that non-local closure schemes will produce stronger turbulent mixing due to non-local effects (Hu et al., 2010). Even though the Arctic is generally strongly stably stratified, deep PBLs and strong turbulent mixing is apparent in WRF and the observations, during the warm intrusion (e.g. Fig. C.3.1 and C.4.1). We indeed do find that YSU simulates deeper and warmer PBLs compared to MYJ, which is in line with many other studies (e.g. Hu et al., 2012, 2013; Cuchiara et al., 2014).

Arctic warm air intrusions are a commonly studied phenomenon across many disciplines. For example, warm air intrusions strongly affect the Arctic aerosol loading (Dada et al., 2022), cloud properties (Bossioli et al., 2021) and resulting energy budget of the sea ice (You et al., 2022). Arctic warm air intrusions are mainly driven by quasi-stationary high pressure systems (You et al., 2021), which block eastward propagation of cyclones. This behaviour is also found in the April 2020 warm air intrusions investigated in this case study. Here, we have shown that simulations and observations of atmospheric trace gases can help identify source regions and the transport pathway during Arctic warm air intrusions. Blocking events have shown increasing trends in recent years and are expected to increase in a warming climate (Henderson et al., 2021). Therefore, this might also increase poleward transport of mid-latitude anthropogenic, biogenic and biomass burning emissions, with further consequences on atmospheric composition and local warming through effects on radiation and clouds.

4.5 Conclusions

This study highlights the role of long-range transport of trace gases during an Arctic warm air intrusion event in April 2020. This warm air intrusion was observed during MOSAiC and shows two distinct episodes. We have set up the Polar-WRF-Chem (WRF) model to simulate the warm air intrusion, and have compared the model results to observations performed during MOSAiC. We have tested the sensitivity of WRF simulated meteorology and trace gas concentrations to horizontal model resolution and planetary boundary layer scheme. Additionally, we include the ERA5 (meteorological) and CAMS (chemical) reanalysis data in the evaluation.

WRF simulated meteorology shows a good resemblance with MOSAiC observed meteorology, both in and above the planetary boundary layer. Both episode are characterized by very high temperatures (up to 0 °C), relative humidity (90–100%) and wind speed (10–15 m s⁻¹). However, inclusion and evaluation of both simulated and observed trace gas concentrations allows to further corroborate that there are distinctly different long-range transport and footprint area of the air that is arriving at the MOSAiC location.

During the first episode, a depression above western Russia and a blocking high over the Laptev sea create southeasterly winds coming from the Eurasian mainland. During the second episode, only 2 to 3 days later, a high pressure area off the coast of Norway and a depression off the coast of Greenland creates southerly winds to the MOSAiC location. While the first episode can be considered as a terrestrial footprint, the second episode is much more dominated by a maritime footprint from the Atlantic Ocean. This transport and footprints are further supported by simulated back-trajectories using the Lagrangian FLEXPART back-trajectory model.

The first episode brings elevated mixing ratios of CO (150 ppb) and NO₂ (200 ppt) to the MOSAiC location, reflecting the transport of air masses affected by anthropogenic emissions from the mid-latitudes. During the second episode, WRF simulates lower mixing ratios of CO (125 ppb) and NO₂ (50 ppt), but elevated concentrations of O₃ (50 ppb). This transport of trace gases is further supported by MOSAiC observations, which generally agree well with WRF during the warm air intrusion. Furthermore, WRF shows that this long-range transport is not limited to the lower troposphere. Elevated concentrations of CO are found over the entire troposphere, linked to strong vertical mixing during the warm air intrusion.

We have tested the sensitivity of WRF to horizontal model grid spacing of 3 km and 27 km. Additionally, we have performed simulations with the local MYJ and non-local YSU schemes. We found some improvement with respect to enhanced resolution. Most notably in terms of 2-meter temperature and relative humidity. We did not find a clear preference with respect to applied planetary boundary layer scheme. It has to be noted that performance of the different settings strongly depends on the variable of interest. For a specific focus, this might lead to

a preference of one of the PBL schemes over the other. Additionally, we show that WRF model simulations, both at high and coarse resolution, outperform CAMS reanalysis data for simulations of trace gas concentrations during the warm air intrusion.

Results in this study show that WRF can be a useful tool to further diagnose long-range transport of trace gases, into remote areas such as the Arctic with limited observations, during synoptically driven events. This event-driven transport might become a more significant source of Arctic trace gases in future climate if these intrusions increase in frequency and intensity.

C Appendices

C.1 Overview of physical and chemical parameterization schemes used in the WRF model simulations

Table C.1.1: Physical and chemical parameterization schemes used in the WRF model simulations.

WRF option	Configuration
Physical parameterizations	
Microphysics	Thompson (Thompson et al., 2016)
Long wave radiation	RRTMG (Iacono et al., 2008)
Short wave radiation	RRTMG (Iacono et al., 2008)
Surface layer	Monin-Obukhov (Janjić, 2001)
Land surface	Noah (Chen and Dudhia, 2001)
Boundary layer	MYJ (Janjić, 1994)
Cumulus	Kain-Fritsch (Kain, 2004)
Chemistry	
Gas-phase	CBM-Z (Gery et al., 1989; Zaveri and Peters, 1999)
Photolysis	Fast-J (Wild et al., 2000)
Emissions	
Anthropogenic	ECLIPSE (Stohl et al., 2015)
Biogenic	MEGAN (Guenther et al., 2012)
Boundary conditions	
Meteorology	ERA5 ($0.25^{\circ} \times 0.25^{\circ}$) (Hersbach et al., 2020)
Chemistry	CAMS ($0.75^{\circ} \times 0.75^{\circ}$) (Inness et al., 2019)

C.2 FLEXPART backtrajectories

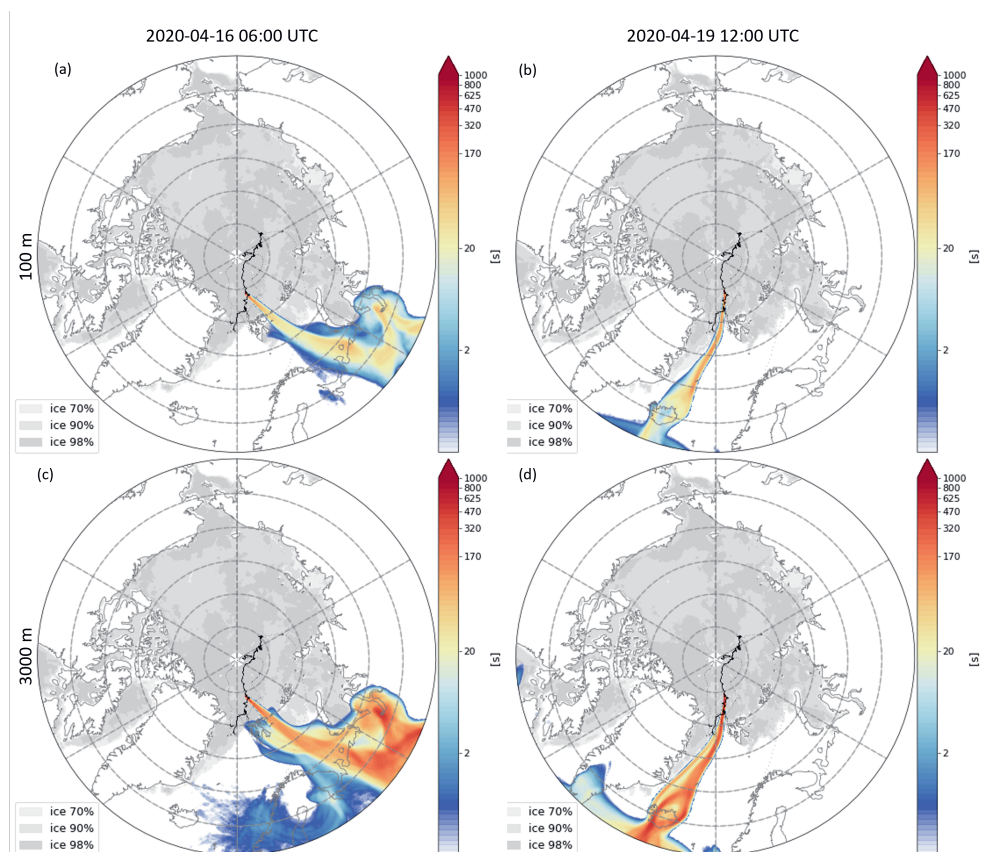


Figure C.2.1: FLEXPART 7-day back-trajectories for the air at (a,b) 100 m and (c,d) 3000 m height arriving at the MOSAiC location at (a,c) 2020-04-16 06:00 UTC and (b,d) 2020-04-19 12:00 UTC. The colors indicate the relative footprint contribution of the air arriving at MOSAiC. Trajectory analysis from the FLEXPART model simulations, performed by the FLEXPART group at the University of Vienna.

C.3 Observed and simulated vertical profiles

Figure C.3.1 shows a comparison between WRF simulated and radiosonde observed vertical profiles of potential temperature, relative humidity, wind direction and wind speed prior to and during the warm air intrusion event. Prior to the warm air intrusion (Fig. C.3.1, top panels) we typically find shallow PBLs in the order of 50 to 200 m with a strong temperature inversion at the PBL top. Additionally, several profiles indicate the presence of a second inversion layer indicating the presence of residual layers and suppressed mixing conditions. During both episodes of the warm air intrusion (Fig. C.3.1, middle and bottom panels) we find deeper PBLs in the order of 500 to 1000 m with well developed temperature inversions at the PBL top. Additionally, observations show strong gradients in relative humidity at the PBL top. The WRF model simulations agree generally well on the saturated conditions during the warm air intrusion in the PBL and the location of the PBL top.

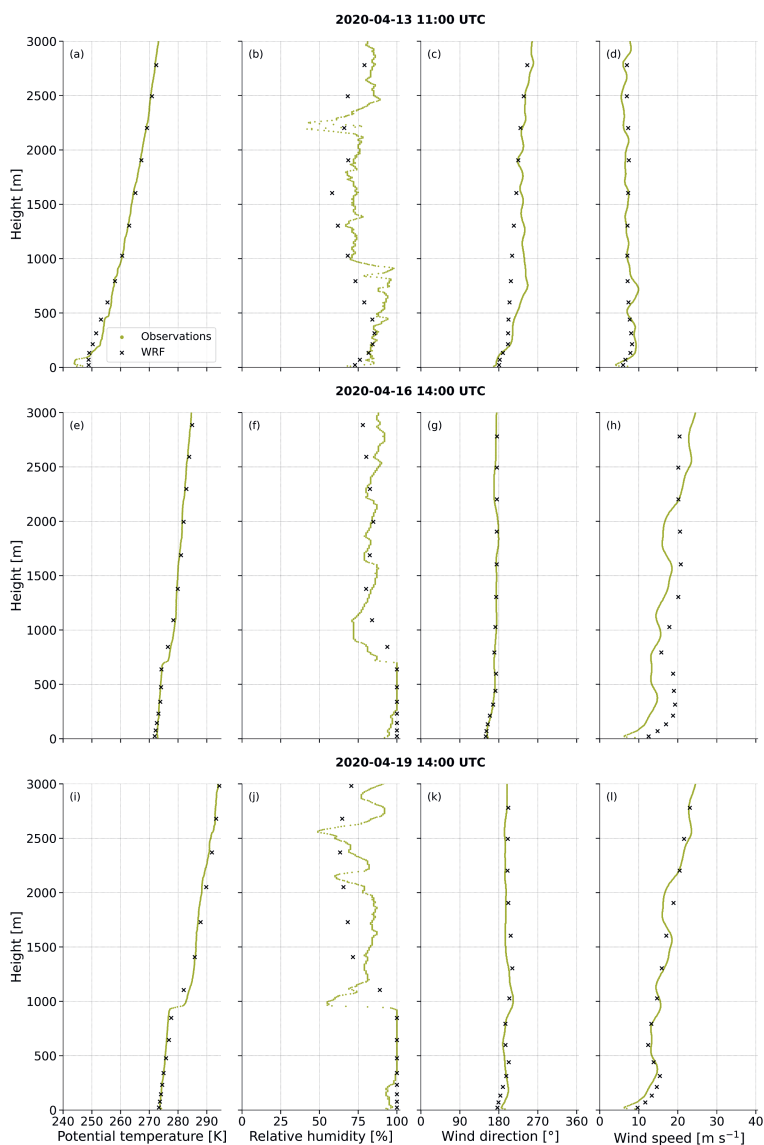


Figure C.3.1: Vertical profiles of observed (olive green) and simulated (black) (a,e,i) potential temperature [K], (b,f,j) relative humidity [%], (c,g,k) wind direction [°] and (d,h,l) wind speed [m s^{-1}] at (top) 2020-04-13 11:00 UTC, (middle) 2020-04-16 14:00 UTC and (bottom) 2020-04-19 14:00 UTC. Note that the top profiles are prior to the warm air intrusion events, the middle profiles are during the first warm air intrusion and the bottom profiles are during the last warm air intrusion event.

C.4 Simulated vertical wind speed and vertical distribution of carbon monoxide

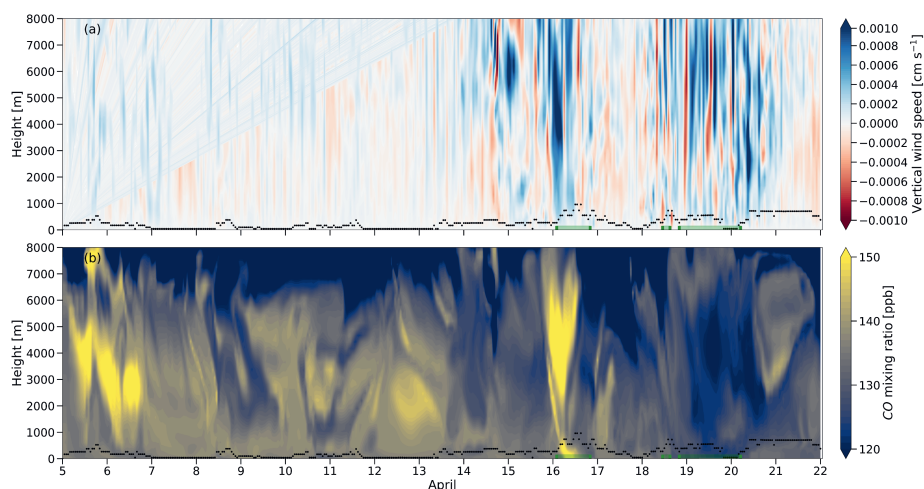
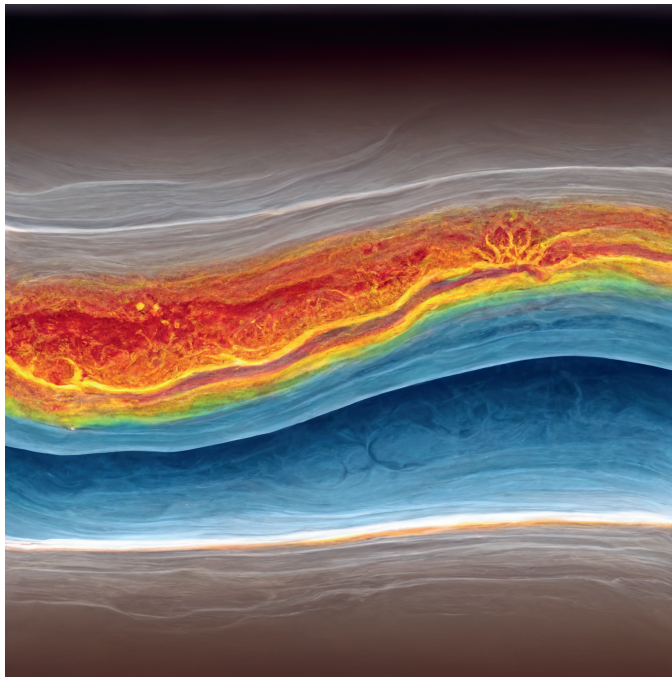


Figure C.4.1: Temporal evolution of the vertical distribution of simulated (a) vertical wind speed [cm s^{-1}] and (b) carbon monoxide mixing ratio [ppb]. The black dots represent the simulated boundary layer height and the green markers indicate observed 2-meter air temperature $> -5^\circ\text{C}$, representing the warm air intrusion events.

Chapter 5

Near-surface atmospheric composition during the MOSAiC field campaign: A long-term comparison with 18 years of reanalysis product



Abstract

During the last decades, Arctic atmospheric concentrations of the main greenhouse gases have been increasing. While concentrations of greenhouse gases are expected to further increase in the future due to world-wide sources, also local greenhouse gas emissions are expected to increase due to further exploitation of the Arctic. These global and local sources are expected to further impact the composition of the Arctic atmosphere for the upcoming decades in terms of greenhouse gases, and air pollutants. Given the observed past concentrations and anticipated future emission projections, it raises the question what the current state of Arctic atmospheric composition is, and how representative reanalysis products are with respect to in-situ observations, which are normally restricted to the Arctic land-surface. Here, we use 18-years (2003–2021) reanalysis data from the Copernicus Atmosphere Monitoring Service (CAMS) and compare these to surface continuous and flask observations of the central Arctic atmosphere from The Multidisciplinary drifting Observatory for the Study of Arctic Climate (MOSAiC) campaign. Our analysis includes the trace gases carbon dioxide (CO_2), methane (CH_4), nitrous oxide (N_2O), ozone (O_3), carbon monoxide (CO), dimethylsulfide (DMS), sulphur dioxide (SO_2) and propane (C_3H_8). Additionally, we study the annual cycle of observed surface fluxes of CO_2 and CH_4 and their representation in the CAMS reanalysis product.

CAMS indicates an upward trend of Arctic atmospheric greenhouse gas concentrations for CO_2 , CH_4 and N_2O of 2.04 ppm yr^{-1} , 4.78 ppb yr^{-1} and 0.93 ppb yr^{-1} , respectively. In contrast, both CO and C_3H_8 show a downward trend of $-1.03 \text{ ppb yr}^{-1}$ and $-1.28 \text{ ppt yr}^{-1}$, respectively. A comparison of CAMS with MOSAiC observations highlighted a number of notable aspects. In summer, CAMS overestimates surface CO_2 mixing ratios, but underestimates CH_4 mixing ratios. Additionally, CAMS underestimates surface CO mixing ratios, especially during winter. For DMS, the MOSAiC observed mixing ratios are lower, and fall mostly outside of the range of the 18-years CAMS climatology. For C_3H_8 , observed mixing ratios in winter, up to 1100 ppt, are much higher than $\sim 150 \text{ ppt}$ predicted by CAMS. Conditions observed during MOSAiC mostly fall within the climatology. However, a number of dynamic weather events in winter with enhanced mixing ratios of CO_2 , O_3 , CO and SO_2 were observed. Yearly averaged surface fluxes of CO_2 and CH_4 amount to $-0.13 \pm 3.31 (1\sigma) \text{ mmol m}^{-2} \text{ d}^{-1}$ and $1.03 \pm 19.77 (1\sigma) \text{ } \mu\text{mol m}^{-2} \text{ d}^{-1}$, representing an uptake and emission flux respectively. In August, we find a significant increase in surface CO_2 -uptake, related to a decrease in sea ice cover, which does not correlate with enhanced surface emissions of CH_4 . This hints to a strong sub-saturation of CO_2 in the Arctic ocean during the ice melt period.

These results provide, for the first time, insight in the full seasonal cycle of atmospheric greenhouse gases and other relevant trace gases in the near-surface atmosphere over the Arctic sea ice, constrained by continuous and flask observations. We highlight the strengths and weaknesses

of chemical reanalysis data in representing these observations. Our results should be considered in trend analyses on Arctic atmospheric composition based on reanalysis data, or while using reanalysis data as boundary conditions for local or regional scale modeling studies.

5.1 Introduction

The Multidisciplinary drifting Observatory for the Study of Arctic Climate (MOSAiC) expedition (Shupe et al., 2020) was the most extensive Arctic expedition in history that took place from October 2019 to September 2020. For a full year, the German icebreaker *RV Polarstern* was docked in the Arctic sea ice with the overarching goal to better understand the causes and consequences of Arctic climate change. MOSAiC was a large, interdisciplinary campaign centered around the themes atmosphere (Shupe et al., 2022), ocean (Rabe et al., 2022), sea ice and snow (Nicolaus et al., 2022), ecology, and biogeochemistry. This expedition has brought forward a plethora of new observations of quantities that have never been observed, or never been observed over a full seasonal cycle before. As part of MOSAiC, observations of many different air pollutants, climate active trace gases and aerosol precursors have been collected. Normally, these observations rely on dedicated land surface stations around the Arctic, of which the coverage is very sparse compared to other regions in the world such as Europe, North America and East Asia (Sofen et al., 2016; Schultz et al., 2017; Chang et al., 2017).

Since the industrial era, global mean atmospheric concentrations of greenhouse gases have been increasing. Due to the long lifetimes of these gases, this increase is also observed at Arctic surface stations (Morimoto et al., 2021). At the same time, local Arctic air pollution can become a significant problem for the upcoming decades (Schmale et al., 2018; Yu et al., 2019; Kirdyanov et al., 2020) especially given the anticipated opening of shipping lanes resulting in increased cargo transport across the Arctic (Marelle et al., 2016). Furthermore, increasing prevalence and intensities of forest fires in boreal forests are predicted in future climate (Flannigan et al., 2009; de Groot et al., 2013; Shvidenko and Schepaschenko, 2013) further affecting the composition of the Arctic atmosphere. All these factors raise the question how representative the observations performed during MOSAiC are for Arctic climate with respect to the composition of the Arctic atmosphere.

In terms of meteorological conditions, Rinke et al. (2021) concluded that the MOSAiC observations appear to be quite representative for the conditions prevailing the 4 past decades. However, some anomalous episodes related to synoptic events were observed (Rinke et al., 2021). For example, an extreme case of a moist and warm air intrusion was observed in April 2020 (Dada et al., 2022) which brought the warmest air with respect to 40 years of reanalysis data (Rinke et al., 2021). Interestingly, the 2019 – 2020 Arctic winter was characterized by an exceptionally strong and cold polar vortex causing extreme stratospheric ozone (O_3) loss (Lawrence et al., 2020; Manney et al., 2020; Wohltmann et al., 2020; Dameris et al., 2021) as been observed during MOSAiC. Furthermore, signatures of Siberian wildfire smokes were observed in the Arctic stratosphere up to 12 km height (Ohneiser et al., 2021; Ansmann et al., 2022). However, so far studies characterizing the normalcy and anomalies in the Arctic near-surface composition

during MOSAiC are lacking.

Here, we will compare the year-round trace gas observations during MOSAiC, with the Copernicus Atmosphere Monitoring Service (CAMS) (Inness et al., 2019) reanalysis data of the past 18 years (2003–2021). We specifically choose for CAMS because it is the most complete source of information on large-scale atmospheric composition in terms of number of gases and temporal coverage (Ryu and Min, 2021). Also, it has been shown to be more accurate compared to previous versions such as the Monitoring Atmospheric Composition and Climate (MACC) and the CAMS Interim Reanalysis (CIRA) reanalysis datasets (Wang et al., 2020; Ramonet et al., 2021). The CAMS reanalysis data is often used for risk assessment (Falk et al., 2021) and studies of local air quality (Ukhov et al., 2020; Becker et al., 2021) and trends therein (Chutia et al., 2022; Gui et al., 2022). Furthermore, CAMS is often used as boundary conditions to drive regional scale air quality and atmospheric chemistry models (Visser et al., 2019; Barten et al., 2020). This motivates our quality assessment of these reanalysis datasets and to compare them to independent observations, also for regions with limited coverage of observations such as the Arctic. Here, we aim to fill this knowledge gap.

The main research objectives are 1) to address the representativeness of the CAMS reanalysis dataset with respect to independent observations from MOSAiC and 2) to put year-round observations of trace gases during MOSAiC in the context of inter-annual variability and extremes within the past 18 years. We will investigate whether the atmospheric composition, as observed by MOSAiC is representative for the long-term mean and whether anomalous conditions have occurred. Additionally, we will present the carbon dioxide (CO₂) and methane (CH₄) fluxes observed during MOSAiC and compare these fluxes to the climatological CAMS surface fluxes.

5.2 Methods

First, we will describe the continuous surface and flask observations performed during the MOSAiC campaign used in this study. Thereafter, we describe which CAMS reanalysis products are included and show an overview table of all observational and reanalysis data. Furthermore, we describe the pre-processing algorithm to arrive at a fair comparison between MOSAiC observed trace gas concentrations and the CAMS reanalysis data.

5.2.1 MOSAiC observations

Here, we use observations of gases collected on the deck *RV Polarstern* during the MOSAiC expedition. Ambient air O₃ was collected in the University of Colorado (CU), Atmospheric Radiation Measurement user facility (ARM) and École Polytechnique Fédérale de Lausanne

(Swiss) containers. These observations were de-spiked and minute averaged to arrive at an hourly mean merged product (Angot et al., 2022e). Carbon monoxide (CO) was collected in the ARM and Swiss containers. These observations were de-spiked, minute averaged and cross-calibrated with flask observations to arrive at a minute averaged merged product (Angot et al., 2022f). Sulphur dioxide (SO₂) observations were performed in the Swiss container and cross-calibrated against a certified SO₂ standard post-cruise (Angot et al., 2022c). These observations were minute-averaged, de-spiked and filtered for local air pollution following Beck et al. (2022). CO₂, CH₄, dimethylsulfide (DMS) and a selection of Volatile Organic Compounds (VOCs), including propane C₃H₈, were analyzed in the CU container and collected on the bow crane using an approximately 50 m long Teflon tube to allow sampling forward of the vessel. CH₄ and CO₂ observations (Blomquist et al., 2022a,c) were minute averaged cross-calibrated against independent observations collected on a tower set up on the sea ice (Cox et al., 2021a; Blomquist et al., 2022b,d). DMS (Blomquist et al., 2022e) and VOC (Angot et al., 2022b) observations are available at a temporal resolution of 1 minute and ~ 3 hours, respectively. Nitrous oxide (N₂O) observations were performed in the ARM container and are available at a temporal resolution of 1 second. N₂O mixing ratios have been corrected for water vapor interference (Zeller, 2000; Lebegue et al., 2016).

The inlets of the trace gas observations were variable for each sensor and container, but were typically located 18–25 m above the ice surface (Angot et al., 2022d). Here, we have applied an additional hourly averaging to allow for a better comparison with the CAMS reanalysis data. This averaging was only applied if $> 50\%$ of the raw data was available. Because of the lower temporal resolution of the VOCs, we have not applied further averaging to this data.

Additional ambient air was collected in 2.5 L borosilicate flasks upwind of local air pollution. These flasks were analyzed post-cruise in the National Oceanic and Atmospheric Administration–Global Monitoring Laboratory (NOAA–GML) facility (Dlugokencky et al., 2022). Trace gases analyzed in the flask samples include CO₂, CH₄, N₂O, CO and C₃H₈, which we include in this comparison. Flask samples were collected in duplicate. In this analysis, we include the mean of the duplicate samples. For more detail on the collection and analysis of these flasks see Angot et al. (2022d).

Turbulent fluxes of CO₂ ($\overline{w'CO_2'}$) and CH₄ ($\overline{w'CH_4'}$) were collected on the bow crane using an eddy-covariance system (Blomquist et al., 2022f) at a frequency of 10 Hz. Instantaneous fluxes were averaged over a time window of 13.5 min. These 13.5 min fluxes were filtered for wind direction ($\pm 90^\circ$) and wind speed ($> 2 \text{ m s}^{-1}$) to limit flow and emission interference from *RV Polarstern*. Additionally, non-stationary conditions were removed. Thereafter, the fluxes are averaged to a time window of 3 h with a minimum of 5 valid segments per 3 h period. The 3 h

Detection Limit (DL) [$\text{moles m}^{-2} \text{ s}^{-1}$] is defined as

$$DL_{3h} = \frac{\overline{DL_{13min}}}{\sqrt{N}}; (5 \leq N \leq 24) \quad (5.1)$$

where $\overline{DL_{13min}}$ is the detection limit of the 13.5 min flux measurements [$\text{moles m}^{-2} \text{ s}^{-1}$] and N is the number of valid segments. For more details on the measurements of trace gas fluxes using eddy-covariance, refer to Sect. 1.3.1.

The previously described observational data provide a full annual cycle of relevant climate active trace gases and air pollutants. Additionally, we include an additional constraint by the flask observations. This coherent dataset of year-round observations provides a unique dataset to evaluate the representativity of atmospheric composition reanalysis datasets, such as the CAMS product.

5.2.2 CAMS reanalysis data

In this study, we use three different sources of CAMS reanalysis data. The European Centre for Medium-Range Weather Forecasts (ECMWF) Atmospheric Composition Reanalysis version 4 (EAC4) is used for all short-lived gases (< 1 year). Here, we include O_3 , CO , DMS , SO_2 and C_3H_8 . We also study CO_2 and CH_4 and their respective surface fluxes (F_{CO_2} and F_{CH_4}), from the CAMS Global Greenhouse gas reanalysis 4 (EGG4) dataset for long-lived greenhouse gases. Additionally, we use the CAMS global inversion-optimised greenhouse gas fluxes and concentrations dataset for N_2O . These datasets can be downloaded through the Atmosphere Data Store (ADS) using the following link: ads.atmosphere.copernicus.eu (last access: 04 January 2023).

We have used the reanalysis datasets at a temporal resolution of 3 hours and a spatial resolution of $0.75^\circ \times 0.75^\circ$. We have opted for the highest resolution temporal and spatial data available for a fair comparison with the local and higher temporal resolution MOSAiC observational data. The CAMS reanalysis data is available at 60 model levels. Due to the assimilation system in CAMS and sparse observational networks, the data is available from 2003 onwards only. We analyze data from the 01st of January 2003 to the 30th of June 2021 for the short-lived gases and from the 01st of January 2003 to the 31st of December 2020 for the long-lived gases. N_2O data is only available up to the 31st of December 2019. Table 5.1 shows a comprehensive overview of the CAMS reanalysis data and observations used in this study. CAMS uses the ECMWF Integrated Forecast System (IFS) and a 4D Variational Data Assimilation system (4D-Var) with 12 hour assimilation windows. More details about the CAMS reanalysis system can be found in Inness et al. (2019) or the data documentation on the website. CAMS mostly assimilates satellite observations from various instruments including, but not limited to, the

Ozone Monitoring Instrument (OMI) (Krotkov et al., 2017), Measurement of Pollution in the Troposphere (MOPITT) (Deeter et al., 2003) and Global Ozone Monitoring Experiment–2 (GOME–2) (Munro et al., 2016). No surface observations or radiosondes are assimilated in the CAMS system which makes this analysis an independent evaluation of the CAMS reanalysis data.

5.2.3 Pre-processing algorithm

Here, we will define the steps taken to arrive at a fair comparison of MOSAiC observations with the climatology from CAMS. It has to be noted that the temporal coverage used in this study, namely 18 years, does not fit the classical definition of climatology being 30 years (Solomon et al., 2007). However, for the sake of this study and clarity of the text, we will take the liberty to use the terminology climatology, to define the 18 year mean state, throughout.

First, we have defined the MOSAiC master track (Rex, 2020; Haas, 2020; Kanzow, 2020; Rex, 2021a,b) from 01 October 2019 to 30 September 2020. Then, we have extracted for every 3 hours, the 4 closest grid cells in CAMS and have applied a bilinear interpolation to the CAMS data. The motivation for this bilinear interpolation is to avoid large concentration differences in gases with a high spatial variability when the MOSAiC track moves from one grid cell to another. Additionally, we have applied a vertical linear interpolation of the 60-layer (L60) CAMS data to an altitude of 20 m, the approximate height of the trace gas sensors (Angot et al., 2022a). This interpolation involves the reference heights of the first and second CAMS model levels which are located approximately 10 m and 35 m above the surface. Finally, this same master track and interpolation is then applied to all preceding and subsequent dates to ensure that the climatology defined across the years is over the same geographic path.

It is important to note that because the gas analyzers used in this study are located on the deck of *RV Polarstern* we include both the ship’s passive drift and the active sailing time. This includes two major transit periods. The first transit to and from Svalbard is from 10 May 2020 to 24 June 2020. The second transit is from 29 July 2020 to 25 August 2020, when the original ice floe broke apart and a new Central Observatory was set up around 88 °N (Shupe et al., 2022). The first transit period covers major parts of presence of the *RV Polarstern* on the open ocean, and being docked in the harbor of Svalbard. We have indicated these periods in the figures throughout this chapter.

5.3 Results and discussion

Firstly, we will present the multi-year trends and variability in trace gases from the CAMS reanalysis data. Thereafter, we will focus on the seasonal cycle of trace gases in the CAMS re-

Table 5.1: Overview of observations and CAMS reanalysis data used in this study.

	Trace gas	Temporal Resolution	Time span (YYYY-MM-DD)	Reference or hyperlink
Continuous observations	O ₃	1h	2019/10/01–2020/09/30	Angot et al. (2022e)
	CO	1min	2019/10/01–2020/09/30	Angot et al. (2022f)
	DMS	1min	2020/07/13–2020/09/30	Blomquist et al. (2022e)
	SO ₂	1min	2019/10/01–2020/09/30	Angot et al. (2022c)
	C ₃ H ₈	~ 3h	2019/10/01–2020/09/30	Angot et al. (2022d)
	CO ₂	1min	2019/10/01–2020/09/30	Blomquist et al. (2022c)
	CH ₄	1min	2019/10/01–2020/09/30	Blomquist et al. (2022a)
	N ₂ O	1s	2019/10/01–2020/09/30	Angot et al. (2022d)
Flasks	$\overline{wCO_2}, \overline{wCH_4}$	3h	2019/10/01–2020/09/30	Blomquist et al. (2022f)
	CO ₂ , CH ₄ , N ₂ O, CO, C ₃ H ₈	~ 7d	2019/10/27–2020/09/25	Dlugokencky et al. (2022)
CAMS	O ₃ , CO, DMS, SO ₂ , C ₃ H ₈	3h	2003/01/01–2021/06/30	ads.atmosphere.copernicus.eu/cdsapp#!/dataset/cams-global-reanalysis-eac4
	CO ₂ , CH ₄ , F _{CO₂} , F _{CH₄}	3h	2003/01/01–2020/12/31	ads.atmosphere.copernicus.eu/cdsapp#!/dataset/cams-global-ghg-reanalysis-egg4
	N ₂ O	3h	2003/01/01–2019/12/31	ads.atmosphere.copernicus.eu/cdsapp#!/dataset/cams-global-greenhouse-gas-inversion

analysis data and MOSAiC observations, studying both the climatological seasonal cycle and the 2019–2020 seasonal cycle during the MOSAiC expedition, to study the representativeness of the MOSAiC campaign in terms of surface trace gas concentrations for the long-term average. Additionally, we will directly compare the co-sampled CAMS reanalysis data with the observations to study the most prominent similarities and biases between CAMS and the observations.

5.3.1 Multi-year trends and variability in trace gases from the CAMS reanalysis data

Figure 5.1 shows the temporal evolution of CO_2 , CH_4 , N_2O , O_3 , CO , DMS , SO_2 and C_3H_8 from 2003–2021 in the CAMS reanalysis data including a 1-year moving average to indicate multi-year trends. The three greenhouse gases CO_2 (Fig. 5.1a), CH_4 (Fig. 5.1b) and N_2O (Fig. 5.1c) show clear upward trends over the past two decades, consistent with global observations (e.g., Friedlingstein et al., 2022). Applying a linear regression to the 1-year moving average results in a significant increase of atmospheric CO_2 of 2.04 ppm yr^{-1} ($R^2 = 0.99$) corresponding to an increased burden of 4.33 GtC yr^{-1} using $1 \text{ ppm} = 2.124 \text{ GtC}$ as a conversion factor (Ballantyne et al., 2012). For N_2O , the increase corresponds to 0.93 ppb yr^{-1} ($R^2 = 0.99$). For CH_4 , the overall trend equals 4.78 ppb yr^{-1} ($R^2 = 0.90$). However, the trend in CH_4 shows two clear phases, with distinctly different trends in CH_4 . Since industrial times the concentration of CH_4 has been increasing due to increasing emissions from agriculture and fossil fuels. From 1999 to 2006 the concentrations of atmospheric CH_4 reached a plateau, whereafter increase resumed after 2006 (Schaefer, 2019). Possible causes mentioned are reduced emissions from tropical wetlands, livestock, fossil fuels and biomass burning (Turner et al., 2019) and an increasing sink from the hydroxyl radical (OH) (Rigby et al., 2017). Calculating the upward trend in CH_4 from 2006 onward, results in an increase of 5.64 ppb yr^{-1} ($R^2 = 0.93$).

No significant trends in O_3 (Fig. 5.1d), DMS (Fig. 5.1f) and SO_2 (Fig. 5.1g) are found. For O_3 we find background mixing ratios of $\sim 30\text{--}35 \text{ ppb}$ while the total range equals $\sim 10\text{--}60 \text{ ppb}$. Unusually high surface O_3 up to 60 ppb is suggested by CAMS at the end of winter 2013. No clear explanation for this feature could be found in literature. It could be related to enhanced stratosphere-troposphere exchange, affecting also O_3 concentrations at the surface (Zhang et al., 2017). Another potential explanation is horizontal transport of O_3 rich air from the mid-latitudes, during the end-of-winter-maximum. This horizontal transport could be accompanied by accumulation of VOCs and the restart of photo-chemical activity at the onset of Polar day (Monks, 2000). Both DMS and SO_2 show a seasonal variability, peaking in summer and winter respectively, which will be discussed later. Due to this high variability, no clear trends in the multi-year mean or multi-year maximum (e.g. trends in the 95th percentile) could be determined.

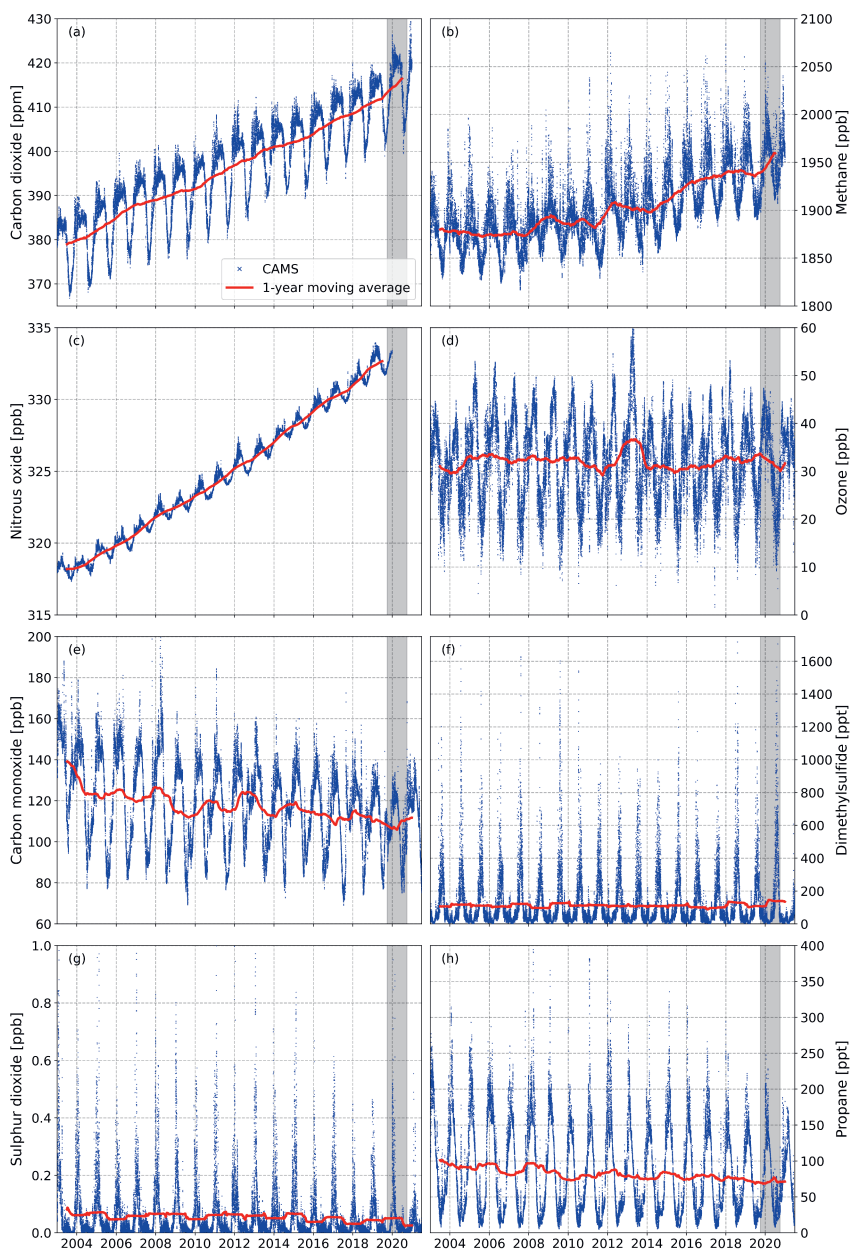


Figure 5.1: Temporal evolution of (a) carbon dioxide [ppm], (b) methane [ppb], (c) nitrous oxide [ppb], (d) ozone [ppb], (e) carbon monoxide [ppb], (f) dimethylsulfide [ppt], (g) sulphur dioxide [ppb] and (h) propane [ppt] in the CAMS reanalysis data (blue). The red line indicates the 1-year moving average. The grey box indicates the MOSAiC expedition from October 2019–September 2020.

Both CO (Fig. 5.1e) and C₃H₈ (Fig. 5.1h) show a negative trend in the analyzed CAMS data from 2003–2021. For CO, this trend equals $-1.03 \text{ ppb yr}^{-1}$ ($R^2 = 0.68$). For C₃H₈, this trend equals $-1.28 \text{ ppt yr}^{-1}$ ($R^2 = 0.67$). For both CO and C₃H₈, this downward trend appears to be mostly dominated by a downward trend in the winter maximum, while the summer minimum remains rather constant. As an example, the winter maximum of CO in the early 2000s easily reached 160 and sometimes up to 180 ppb, while the winter maximum in 2020 and 2021 does not exceed 140 ppb. The decline in atmospheric CO follows from a decrease in anthropogenic and biomass burning CO emissions, that overcompensates for the increasing chemical production of CO in the atmosphere (Zheng et al., 2019). This decrease in CO is occurring despite increasing wildfire activity in the Siberian Arctic in 2010–2020 with respect to 2000–2010 (Kharuk et al., 2022). Regarding C₃H₈, the downward trend in CAMS is in contrast with Helmig et al. (2016) and Angot et al. (2021). In these studies, a positive trend in C₃H₈ and ethane (C₂H₆) from 2009–2014 was observed across the Northern Hemisphere (Helmig et al., 2016) and at Arctic sites (Angot et al., 2021). This positive trend reversed in the period between 2015–2018, before experiencing another upturn from 2019 onwards. The increase in Non Methane Hydrocarbons (NMHCs) is attributed to an increase in oil and natural gas production in North America (Angot et al., 2021). Given the relatively short lifetime of C₃H₈ (~ 13 days), the observed trends in Northern Hemispheric C₃H₈ over land might not be representative for trends in central Arctic C₃H₈. The representation of the C₃H₈ sources and sinks in CAMS is further discussed in Sect. 5.3.2.

5.3.2 Seasonal cycle of trace gases from the CAMS reanalysis data and observed during MOSAiC

Figure 5.2 shows the mean seasonal cycle and 2019–2020 seasonal cycle of CO₂, CH₄, N₂O, O₃, CO, DMS, SO₂ and C₃H₈ in the CAMS reanalysis data and the observed seasonal cycle from MOSAiC. Figure 5.3 shows the frequency distributions of the climatology and 2019–2020 season in CAMS, and the MOSAiC observations. The 2019–2020 CAMS season is co-sampled to allow for a direct comparison between the MOSAiC observations and CAMS reanalysis data.

From the start of the MOSAiC campaign (October 2019), the CAMS CO₂ reanalysis data follows the increasing trend in MOSAiC observations, as a result of a decrease in the CO₂ uptake by the land-surface vegetation in Northern Hemisphere fall (Fig. 5.2a). The observed winter and spring maximum of ~ 420 ppm is apparent in both continuous and flask observations and CAMS reanalysis data. However, CAMS appears to underestimate the decrease of observed CO₂ during summer by ~ 4 ppm. Interestingly, this overestimation of CO₂ in CAMS correlates with an underestimation of CH₄ in CAMS during summer (Fig. 5.2b). Additionally, the CAMS reanalysis data appears to overestimate the magnitude of the seasonal cycle in CH₄ for the 2019–

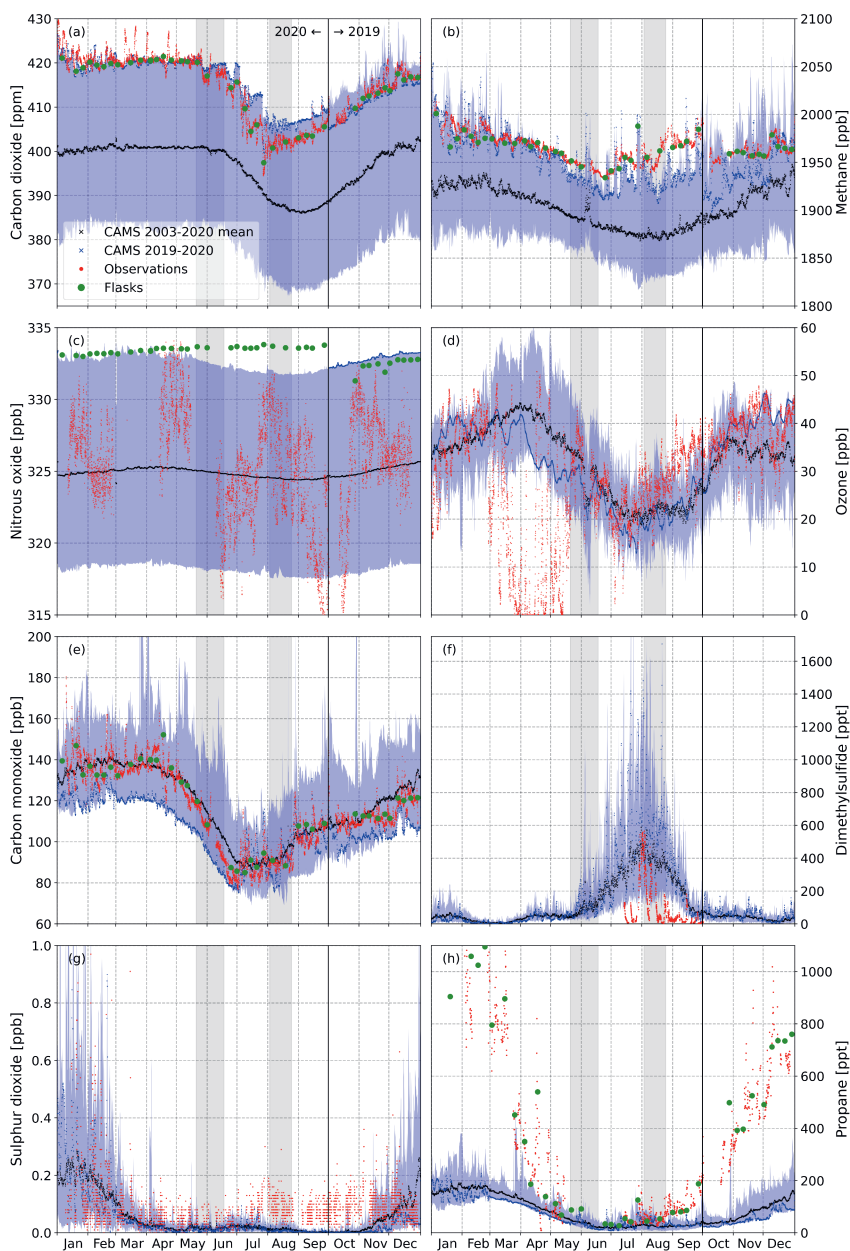


Figure 5.2: Seasonal cycle of (a) carbon dioxide [ppm], (b) methane [ppb], (c) nitrous oxide [ppb], (d) ozone [ppb], (e) carbon monoxide [ppb], (f) dimethylsulfide [ppt], (g) sulphur dioxide [ppb] and (h) propane [ppb] of the CAMS mean (black), CAMS 2019–2020 season (blue) and MOSAiC 2019–2020 continuous (red) and flask (green) observations. The grey boxes indicate the periods when *RV Polarstern* was in transit and the blue shading indicates the CAMS 18-year min/max range.

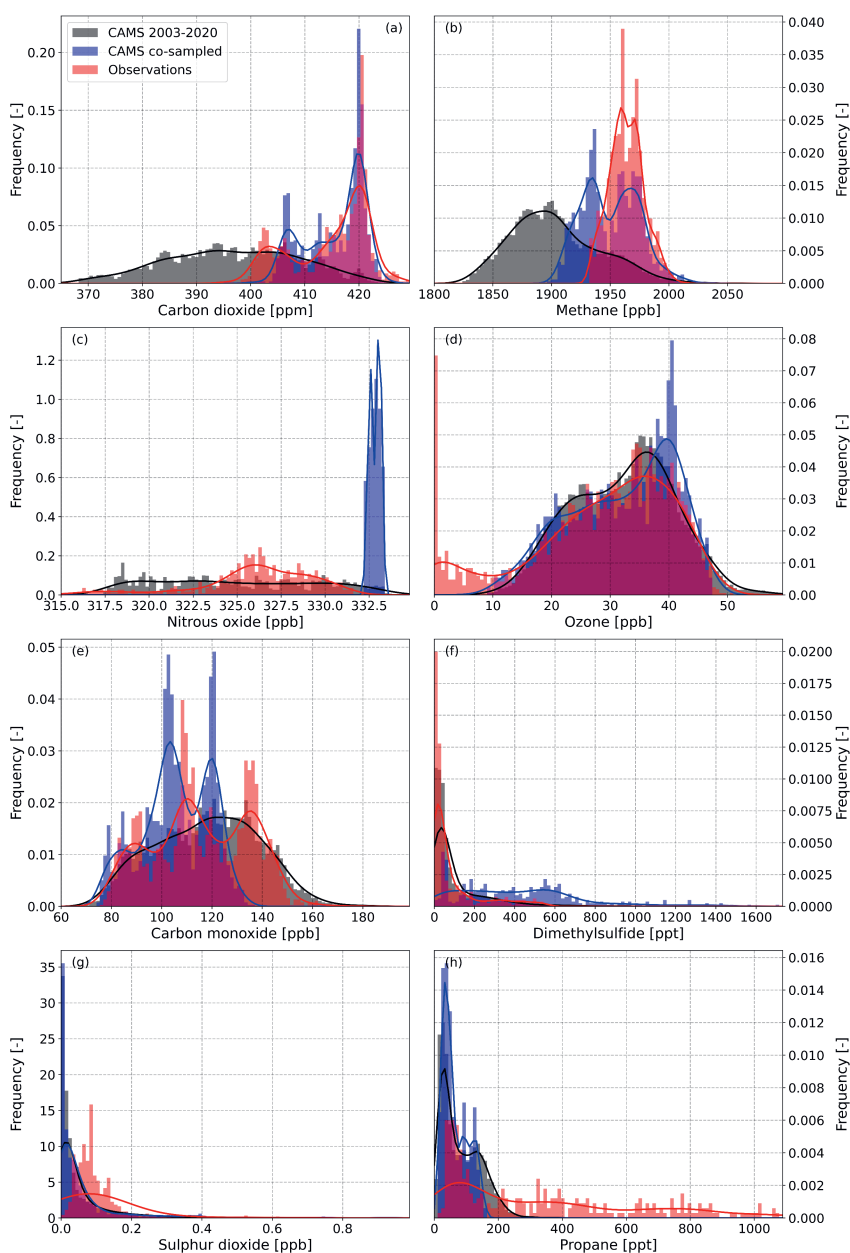


Figure 5.3: Relative frequency distributions of (a) carbon dioxide [ppm], (b) methane [ppb], (c) nitrous oxide [ppb], (d) ozone [ppb], (e) carbon monoxide [ppb], (f) dimethylsulphide [ppt], (g) sulphur dioxide [ppb] and (h) propane [ppb] of the CAMS mean (black), CAMS co-sampled with observations (blue) and continuous MOSAiC 2019–2020 observations (red). The solid lines indicate the kernel density estimate of the respective frequency distributions.

2020 season. For a large part of the summer, both continuous and flask observed CH₄ mixing ratios exceed the range of the CAMS seasonal cycle. Elevated observed CH₄ concentrations are found despite the reduction in global anthropogenic CH₄ emissions as a result of the COVID-19 outbreak (Forster et al., 2020). In fact, increased wetland CH₄ emissions (Peng et al., 2022) and a reduction of CH₄ removal by OH, following from a decrease in NO_x emissions (Stevenson et al., 2021), resulted in an unexpected increase in the background atmospheric CH₄ growth rate in 2020.

Due to the constraints on the temporal coverage of the CAMS N₂O data, the seasonal cycle for 2019–2020 is incomplete (Fig. 5.2c). Following the multi-year trend in N₂O (Fig. 5.1c), the CAMS 2019 season shows the highest Arctic N₂O mixing ratios. Furthermore, the seasonal cycle in N₂O is much lower compared to CO₂ and CH₄ due to the long lifetime and less active interaction with the biosphere and ocean and atmospheric chemistry, respectively. Similar to CO₂ and CH₄, the concentrations of N₂O in the atmosphere and ocean are comparable due to small source and sink contributions, relative to the atmospheric and oceanic burden. This results in occurrence of bi-directional exchange of N₂O (Rees et al., 2022). The supplementary performed flask observations of N₂O highlight the large uncertainty and bias in the continuous surface N₂O observations. The estimated uncertainty of the flask observations is ± 0.157 ppb which deems the continuous surface N₂O observations unreliable.

For CO₂, CH₄ and N₂O, the distribution in the 2019–2020 season falls at the upper end of the distribution of the 18-year climatology. By accounting for the multi-year trend (not shown here), the distribution of these three greenhouse gases fall within 2σ of the climatological mean. Only for CH₄, some episodes of anomalous high mixing ratios are found in the CAMS data (Fig. 5.2b). Observations agree on a bi-modal distribution in CO₂ with one peak at 420 ppm. However, the distribution in observations is wider, compared to the CAMS 2019–2020 distribution, at the lower end. Interestingly, the observed frequency distribution in CH₄ is narrower indicating an overestimation of the seasonal cycle in CAMS.

For O₃ (Fig. 5.2d), both observations and CAMS show a seasonal cycle with an end-of-winter maximum and summer minimum. Observations also show clear O₃ depletion events during March, April and May. The release of halogens and the resulting breakdown of O₃ from halogen chemistry is not included in CAMS. In November and December, both observations and CAMS show enhanced O₃ mixing ratios up to 10 ppb higher than the climatological mean. In summer, CAMS appears to underestimate observed surface O₃ potentially related to an overestimation of the removal by O₃ deposition to the ocean, snow and ice surfaces (Barten et al., 2021). The frequency distribution of O₃ in the CAMS 2019–2020 season falls mostly within the distribution of the CAMS climatology (Fig. 5.3d). However, more episodes of O₃ rich air (> 40 ppb) were estimated in 2019–2020.

The seasonal cycle in climatological mean CO in CAMS follows the continuous and flask observed CO mixing ratios (Fig. 5.2e). However, the CAMS reanalysis data for 2019–2020 consistently underestimates surface CO mixing ratios up to ~ 20 ppb. This bias is especially apparent during winter. Interestingly, the frequency distribution in CO observed during MOSAiC corresponds well with the 18-year climatology from CAMS (Fig. 5.3d). The CAMS 2019–2020 frequency distribution is biased low with respect to the observations, especially for the winter maximum.

Regarding DMS, the CAMS climatological mean shows background DMS mixing ratios in winter of < 100 ppt and a summer maximum of ~ 500 ppt (Fig. 5.2f, Fig. 5.3f). This is despite the enhanced role of DMS oxidation with OH in summer decreasing its lifetime (Edtbauer et al., 2020). The lifetime of DMS in the atmosphere is ~ 1.3 d and therefore strongly dependent on local emissions from the ocean (Albu et al., 2006). In summer, oceanic DMS emissions peak due to enhanced production from phytoplankton (Kloster et al., 2006; Hayashida et al., 2020). The observations show generally low background mixing ratios of < 100 ppt in summer. Maximum observed DMS mixing ratios are ~ 570 ppt in August while CAMS 2019–2020 often estimates mixing ratios > 1000 ppt. This indicates an overestimation of local DMS emissions in CAMS. Whether this is related to an overestimation of the oceanic DMS concentration climatology (Lana et al., 2011) or the ocean-atmosphere exchange velocity (Bell et al., 2017) can not be assessed due to the limited number of DMS flux observations during MOSAiC. Moreover, due to the coarse resolution of CAMS compared to the local MOSAiC observations, the observed DMS emissions might not be representative for the $0.75^\circ \times 0.75^\circ$ grid in CAMS.

Both SO₂ (Fig. 5.2g) and C₃H₈ (Fig. 5.2h) show a seasonal cycle with high mixing ratios in winter and low mixing ratios in summer, in both CAMS and the observations. Especially in January and February, a high variability in SO₂ is observed. This correlates with variability in CO and most probably relates to dynamic weather events (Rinke et al., 2021) because local sources of CO and SO₂ are absent in winter. Regarding C₃H₈, the observations agree with the summer minimum of approximately 50–100 ppt. However, both continuous and flask observations show a sharp increase in C₃H₈ mixing ratios in winter, with observed C₃H₈ peaks around 1100 ppt. This is in sharp contrast with the estimates of CAMS of ~ 150 ppt potentially related to an underestimation of oil and natural gas production over land and removal in the atmosphere. Because this overestimation is not limited to single events, but persistent over the whole winter period, a misrepresentation of long-range transport from remote point sources can be ruled out. Enhanced levels of C₃H₈ in winter might also explain additional local O₃ formation (Hodnebrog et al., 2018). Especially for C₃H₈, the observed frequency distribution clearly falls outside the range of both the CAMS climatology and the 2019–2020 season indicating a clear misrepresentation of the atmospheric C₃H₈ burden in CAMS (Fig. 5.3h).

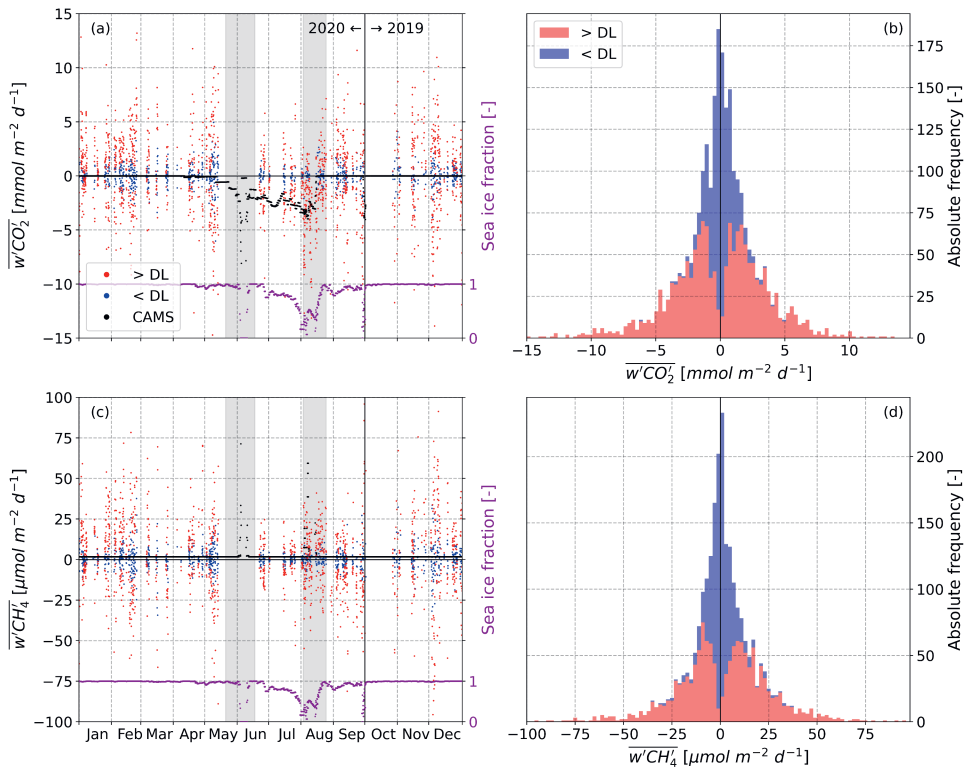


Figure 5.4: (a) Temporal evolution and (b) frequency distribution of surface fluxes of carbon dioxide ($\overline{w'CO_2}$) [$\text{mmol m}^{-2} \text{d}^{-1}$] and (c,d) methane ($\overline{w'CH_4}$) [$\mu\text{mol m}^{-2} \text{d}^{-1}$] observed above the detection limit (red) and below the detection limit (blue) and the CAMS reanalysis data (black). The grey boxes indicate the periods when RV Polarstern was in transit and the purple markers indicate the sea ice fraction [-] from ERA5 (right-side y-axis).

5.3.3 Surface fluxes of CO₂ and CH₄

Figure 5.4 shows the temporal evolution and frequency distribution of the observed surface fluxes of CO₂ ($\overline{w'CO_2'}$) and CH₄ ($\overline{w'CH_4'}$). The yearly averaged observed $\overline{w'CO_2'}$ amounts to -0.13 ± 3.31 (1σ) $mmol\ m^{-2}\ d^{-1}$ (Fig. 5.4b), indicating a very small uptake of CO₂ by the Arctic sea ice and ocean. By only accounting for observations above the detection limit ($\overline{w'CO_2'_{>DL}}$), the mean amounts to -0.22 ± 4.10 (1σ) $mmol\ m^{-2}\ d^{-1}$. MOSAiC observed average surface fluxes of CO₂ are about a factor of two smaller compared to those reported by Yasunaka et al. (2016) for the ice-covered Arctic Ocean. Our maximum observed CO₂-uptake fluxes of $\sim -0.17\ \mu mol\ m^{-2}\ s^{-1}$ ($= -15\ mmol\ m^{-2}\ d^{-1}$) are lower compared to those observed by Zemmeling et al. (2006) ($-0.8\ \mu mol\ m^{-2}\ s^{-1}$), Semiletov et al. (2007) ($-0.3\ \mu mol\ m^{-2}\ s^{-1}$) and Papakyriakou and Miller (2011) ($-3.0\ \mu mol\ m^{-2}\ s^{-1}$) for other sea ice covered regions. By co-sampling CAMS with MOSAiC observations we find a mean Arctic ocean CO₂ flux of $-0.48\ mmol\ m^{-2}\ d^{-1}$ in CAMS, indicating a slightly higher uptake, which is still well within 1σ of the observed surface fluxes. CAMS uses the Takahashi et al. (2009) net sea-air CO₂ flux climatology multiplied by the open water fraction, using a minimum open water fraction of 10%. CAMS shows a constant small uptake of CO₂, which increases for lower sea ice fractions (Fig. 5.4a).

Regarding the observed $\overline{w'CH_4'}$, the yearly average amounts to 1.03 ± 19.77 (1σ) $\mu mol\ m^{-2}\ d^{-1}$ (Fig. 5.4d). By only accounting for observations above the detection limit ($\overline{w'CH_4'_{>DL}}$), the mean amounts to 1.56 ± 25.40 (1σ) $\mu mol\ m^{-2}\ d^{-1}$. Both indicate a slight emission of CH₄ from the Arctic sea ice and ocean, with a large variability. Mean co-sampled emissions of CH₄ in CAMS amount to $1.69\ \mu mol\ m^{-2}\ d^{-1}$, which is well within the variability of MOSAiC observations. CAMS uses a constant emission rate of CH₄ in the Arctic ocean, independent of the sea ice fraction (Fig. 5.4c). Our averaged observed surface fluxes of CH₄ ($0.19\ ng\ m^{-2}\ s^{-1}$) are comparable to those reported by Thornton et al. (2020) for the ice-covered Chukchi sea ($0.39\ ng\ m^{-2}\ s^{-1}$). However, the estimates by Thornton et al. (2020) for the central Arctic Ocean, or other ice-covered seas, exceed the observed flux by more than one order of magnitude.

No clear seasonal trend in $\overline{w'CO_2'}$ or $\overline{w'CH_4'}$ can be observed, as the presence of sea ice mostly limits the surface exchange between the open ocean and the atmosphere (Fig. 5.4a,c). However, $\overline{w'CO_2'}$ shows a significantly higher uptake in August (-1.52 ± 3.24 (1σ) $mmol\ m^{-2}\ d^{-1}$; p -value = 0.01) compared to the rest of the year, using a Welch t -test. This increase in CO₂-uptake corresponds to low sea ice fractions (Fig. 5.4a) in the marginal ice zone, under-saturation of CO₂ in the Arctic Ocean, and thus increased CO₂-exchange. For $\overline{w'CH_4'}$, there is no significant change (p -value = 0.84) in August, compared to the rest of the year. This might indicate that the surface waters of the central Arctic Ocean are less super-saturated in CH₄ compared to the other Arctic seas such as the Laptev, East Siberian and Chukchi seas (Thornton et al., 2016,

2020). This is further supported by the increased uptake of CO_2 in August, indicating that there is no significant physical constraint on the ocean-atmosphere exchange. Additionally, enhanced atmospheric concentrations of CH_4 in summer (Fig. 5.2b) could have played a role in limiting the surface exchange in the marginal ice zone. Here, we did not conduct a detailed footprint analysis for the flux observations. Especially in the the marginal ice zone, the observed footprint area of the eddy-covariance system can be highly variable dependent on the stability and prevailing wind direction. This will affect whether an ice-covered, ice-free or mixed surface type is observed. This might result in an underestimation of the ocean-atmosphere exchange as observed during MOSAiC. A detailed footprint analysis is recommended to distinguish between flux observations of the Arctic sea ice, Arctic ocean and melt ponds to arrive at an accurate estimation of the surface fluxes for these different surface types.

5.4 Conclusions

In this study, we presented an analysis of the climatology of the Arctic atmospheric composition. We used 18 years (2003–2021) of reanalysis data from CAMS (Inness et al., 2019) and year-round (October 2019 – September 2020) surface continuous and flask trace gas observations from MOSAiC. We study the trace gases CO_2 , CH_4 , N_2O , O_3 , CO , DMS , SO_2 and C_3H_8 . We mainly focused on 1) the representativeness of the CAMS reanalysis dataset with respect to independent observations from MOSAiC and 2) the context of the year-round observations of trace gases during MOSAiC with respect to interannual variability and extremes within the past 18 years. Additionally, we study surface flux observations of CO_2 and CH_4 and focus on the magnitude and variability of these fluxes.

For the three greenhouse gases CO_2 , CH_4 and N_2O we found clear, statistically significant, positive trends in the CAMS reanalysis data with increases of 2.04 ppm yr^{-1} , 4.78 ppb yr^{-1} and 0.93 ppb yr^{-1} , respectively. Both CO and C_3H_8 indicated a negative trend of $-1.03 \text{ ppb yr}^{-1}$ and $-1.28 \text{ ppt yr}^{-1}$, respectively. No significant upward or downward trends have been found in 18-years reanalysis data of O_3 , DMS and SO_2 .

A comparison of the CAMS reanalysis data with MOSAiC observations highlighted a few notable aspects. Firstly, CAMS overestimates surface CO_2 and underestimates surface CH_4 from May to September. Observed CH_4 during MOSAiC summer exceeds the 18-year reanalysis data by up to 40 ppb. Additionally, CAMS systematically underestimates observed CO mixing ratios by $\sim 20 \text{ ppb}$ during winter. A number of dynamic events in winter with enhanced mixing ratios of CO_2 , O_3 , CO and SO_2 were observed, which can be attributed to anomalous counts and intensity of cyclones (Rinke et al., 2021).

The most prominent biases between CAMS and MOSAiC are related to DMS and C_3H_8 . For

DMS, the CAMS seasonal cycle clearly overestimates MOSAiC observed mixing ratios. Even though the maximum observed DMS mixing ratio of ~ 570 ppt corresponds to the mean seasonal cycle, the observed background summer mixing ratios of < 100 ppt are much smaller than the range of the CAMS DMS climatology. It has to be noted that locally observed DMS emissions from MOSAiC might not be representative for the $0.75^\circ \times 0.75^\circ$ emissions in CAMS. Regarding C_3H_8 , the CAMS summer minimum (50–100 ppt) corresponds well with MOSAiC observations. However, observations show a sharp increase in C_3H_8 mixing ratios in winter which peak around 1100 ppt. This is in sharp contrast with the estimates of CAMS of ~ 150 ppt. This might be related to an underestimation of NMHC emissions from oil and natural gas production in CAMS. Additionally, other observations of C_3H_8 and C_2H_6 at sites across the Northern Hemisphere and Arctic do not show this downward trend in C_3H_8 (Helmig et al., 2016; Angot et al., 2021), which is found in CAMS.

Finally, we presented observations of the surface fluxes of CO_2 and CH_4 . On average, we find, on average, a very small uptake of CO_2 of -0.13 ± 3.31 (1σ) $mmol\ m^{-2}\ d^{-1}$ (Fig. 5.4a,b) over one year. For CH_4 , we find, on average, a very small release of 1.03 ± 19.77 (1σ) $\mu mol\ m^{-2}\ d^{-1}$ (Fig. 5.4c,d). Both for CO_2 and CH_4 , our eddy-correlation observations indicate among the lowest ice-atmosphere and ocean-atmosphere fluxes compared to previous literature (e.g., Zemmelen et al., 2006; Semiletov et al., 2007; Papakyriakou and Miller, 2011; Thornton et al., 2016, 2020). We find a significant increase in CO_2 -uptake in August related to a decrease in sea ice fraction. Interestingly, this does not correlate to an increase in CH_4 emissions. We argue that the super-saturation of CH_4 in the central Arctic Ocean might be limited because we do not find a clear indication of a physical constraint on the ocean-atmosphere exchange reflected by the increase in CO_2 -uptake.

We have highlighted the strengths and weaknesses of chemical reanalysis products in representing the full seasonal cycle of near-surface continuous, and complementary flask observations of atmospheric greenhouse gases and other relevant trace gases. Results from this study should be considered when using reanalysis data to study trends in Arctic atmospheric composition and air quality, or as boundary conditions for local or regional scale modeling studies. It also motivates to improve model representation of trace gases in the Arctic atmosphere through improved understanding of the sources and sinks, or other relevant processes such as transport and (photo-)chemistry.

Chapter 6

General Discussion and Outlook



6.1 Findings of this thesis

This thesis focused on understanding the surface exchange of climate-active trace gases, and further cycling in the Arctic atmosphere, using a combination of novel in-situ observations and a variety of state-of-the-art models and reanalysis datasets. Specifically, this thesis investigated the role of local- versus long-range controls on the composition of the Arctic atmosphere, on a broad range of spatial and temporal scales. This thesis contains four chapters reporting research results, each of them having specific research questions, which will be addressed below. After summarizing the results of the individual chapters, the overall findings of this thesis are placed into context of the general research objectives, and recommendations on future research directions are provided.

6.1.1 Chapter 2: Role of oceanic ozone deposition in explaining temporal variability in surface ozone at High Arctic sites

In Chapter 2 I focused on the role of the O_3 dry deposition process to the open and sea-ice covered Arctic ocean, and its implications for determining pan-Arctic surface O_3 concentrations. To this end, I coupled a process-based model representation of the oceanic O_3 dry deposition process to the regional Polar-WRF-Chem model. This process-based representation includes the physical and biogeochemical drivers of oceanic O_3 deposition, such as waterside turbulent transport and the reaction of O_3 with dissolved iodide in the ocean mixing layer. In addition, I also applied a strongly reduced O_3 dry deposition rate to sea ice and snow covered surfaces based on past studies. By conducting a number of WRF experiments, I addressed the following research questions:

How well does a commonly applied (constant resistance) parameterization compare to the results of a process-based model representation of oceanic O_3 dry deposition?

I compared results of model simulations with this process-based representation to simulations with a commonly applied constant resistance approach. The constant resistance approach resulted in a mean O_3 dry deposition velocity of 0.05 cm s^{-1} , without spatial variability and limited temporal variability based on environmental drivers such as near-surface wind speed. The process-based representation resulted in a mean O_3 dry deposition velocity of about 0.01 to 0.018 cm s^{-1} . The spatial variability in the process-based approach expresses the sensitivity to chemical enhancement with dissolved iodide, whereas the temporal variability ($\pm 20\%$ around the mean) expresses mainly differences in waterside turbulent transport.

What is the role of oceanic ozone dry deposition in explaining the magnitude and temporal variability of pan-Arctic surface O_3 ?

I evaluated the 30×30 km Polar-WRF-Chem model simulation results against hourly surface O_3 concentration observations at 25 individual sites (latitudes $> 60^\circ$ N). A comparison between the model simulations and observations showed that including a process-based approach of oceanic O_3 deposition results in a substantial improvement of the model performance at High Arctic sites ($> 70^\circ$ N) and sites largely influenced by an oceanic footprint. Surface O_3 concentrations were generally underestimated in the constant resistance approach. This bias was significantly reduced by the reduction in oceanic O_3 deposition in the process-based approach. Additionally, a main interesting finding has been that the process-based approach resulted in a better representation of the temporal variability at the observational sites, by including the spatial and temporal variability in the physical and biogeochemical drivers of oceanic O_3 deposition. To conclude, a process-based representation of oceanic O_3 deposition in atmospheric chemistry and transport models is recommended to improve simulations of Arctic surface O_3 in current and future climate.

6.1.2 Chapter 3: Low ozone dry deposition rates to sea ice during the MOSAiC field campaign: Implications for the Arctic boundary layer ozone budget

Chapter 3 centers around the O_3 dry deposition process to the Arctic sea ice and snow, and its role in the boundary layer budget of O_3 . Chapter 2 indirectly evaluated simulated O_3 fluxes by using pan-Arctic surface O_3 concentrations. Chapter 3 uses, for the first time, year-round eddy-covariance O_3 surface flux observations over the Arctic sea ice, as part of the MOSAiC campaign. These O_3 flux observations are complemented by supporting observations from a meteorological tower, radiosondes and O_3 sondes. Additionally, I have performed simulations with a 1D coupled meteorology-atmospheric chemistry model to quantify all physical and chemical processes ultimately determining O_3 concentrations in the Arctic boundary layer. The 1D modelling experiments and MOSAiC observational data were applied to address the following research questions:

Can I quantify the removal of O_3 by dry deposition the Arctic sea ice?

Based on the eddy-covariance O_3 flux observations I found a median surface resistance on the order of $2 \cdot 10^4 \text{ s m}^{-1}$, resulting in a dry deposition velocity of approximately 0.005 cm s^{-1} . Additionally, I found that the aerodynamic resistance and the quasi-laminar boundary layer resistance, both determined by the stability of the atmosphere, do not play a significant role in determining the magnitude of the O_3 deposition flux. Despite the fact that the Arctic atmosphere is typically very stable, resulting in very large aerodynamic resistances, the very low surface uptake rate is still the main limiting factor in the overall O_3 deposition rate.

What is the contribution of O_3 dry deposition and other processes to the observed temporal variability of O_3 over the Arctic sea ice?

Only the atmospheric O_3 concentrations, and the O_3 deposition flux were observed during MOSAiC. However, many other processes are at play in ultimately determining the O_3 concentrations in the Arctic PBL. Therefore, I have estimated the budget contribution of advection (implicitly accounted for by nudging), vertical turbulent mixing, dry deposition, chemistry and entrainment in the 1D model. It appears that in winter, the modelled PBL O_3 budget is governed by dry deposition at the surface, mostly compensated for by downward turbulent transport of O_3 towards the surface. In summer, advection posed a substantial, mostly negative, contribution to the simulated PBL O_3 budget. This hints that advection generally seems to result in transport of air masses that are relatively depleted in O_3 compared to the air masses present along the MOSAiC drift trajectory. Entrainment, and the net result of all chemical reactions, only contributed marginally ($< 5\%$) to the total PBL O_3 budget. Especially during periods with low wind speeds ($< 5 \text{ m s}^{-1}$) and shallow boundary layers ($< 50 \text{ m}$), the weekly mean removal tendency by O_3 dry deposition reached up to -1.0 ppb h^{-1} .

To conclude, the observed mean O_3 dry deposition velocity of 0.005 cm s^{-1} is much smaller than typically used in atmospheric chemistry and transport models. Additionally, I have shown that O_3 dry deposition to the Arctic sea ice and snow surface is an important process in determining the concentration of O_3 in the Arctic PBL. This motivates a more accurate description of the O_3 dry deposition process to snow and ice in models, to quantify the current and future O_3 sink in the Arctic.

6.1.3 Chapter 4: Simulations of long-range transport of trace gases by a warm intrusion event observed during the MOSAiC field campaign

Chapter 3 focused mostly on local drivers of the O_3 PBL budget over the entire year. From that study it became clear that 1D models lack appropriate constraints during synoptically driven events, such as warm air intrusions, when large-scale processes dominate over local processes. In Chapter 4 I studied long-range transport of O_3 and other trace gases, as a result of an Arctic warm air intrusion event in April 2020 during the MOSAiC campaign. This specific event brought warm and moist air masses to the Central Arctic in two episodes. Besides providing anomalous amounts of heat and moisture to the Arctic, these warm air intrusions can enhance transport of aerosols and trace gases to the Central Arctic, where local emissions are generally absent. In Chapter 4 I set up the Polar-WRF-Chem model to study this warm air intrusion event assessing the following research questions:

How well does a 3D atmospheric chemistry and transport model represent a central Arctic warm air intrusion considering the role of local– versus large–scale processes controlling Arctic O_3 ?

I found that WRF was able to accurately represent the observed meteorology in the PBL during

the warm air intrusion. During the first episode of the warm air intrusion, a dominating southeasterly transport coming from the Eurasian mainland was found. This southeasterly transport brought elevated mixing ratios of CO (maximum hourly observed value of 150 ppb) and NO₂ (maximum hourly observed value of 200 ppt) to the Central Arctic. The second episode was dominated by southerly transport, coming from the Atlantic Ocean. At that time, WRF simulated lower mixing ratios of CO (125 ppb) and NO₂ (50 ppt), but elevated mixing ratios of O₃ (50 ppb). This transport of trace gases in two episodes was further supported by FLEXPART back-trajectories and MOSAiC observations, which generally agreed well with WRF during the warm air intrusion. Additionally, I showed additional benefit of running a highly-resolved 3D coupled meteorology and atmospheric chemistry model such as WRF, over the use of readily available reanalysis datasets such as CAMS.

What is the sensitivity of model simulated meteorology and trace gas concentrations to horizontal spatial resolution and selected PBL parameterization schemes?

I have run the WRF model in various setups to analyse the effect of horizontal spatial resolution and PBL schemes. Specifically, I have run WRF at a horizontal grid spacing of 3 km versus 27 km, and with non-local (YSU) and local (MYJ) turbulence closure PBL schemes. I found some improvement of model performance resulting from an increased horizontal model resolution. However, this improvement was not consistent over the included variables, and is not as prominent as in many other studies investigating the role of horizontal model resolution on model performance. I argued that enhanced model resolution only needs to be considered for cases with high surface heterogeneity, which can also be resolved by the model. Additionally, no clear preference for PBL scheme was found. For example, the local MYJ scheme performed best for near-surface stability and PBL heights, while the non-local YSU scheme performed best for relative humidity and trace gas mixing ratios.

6.1.4 Chapter 5: Near-surface atmospheric composition during the MOSAiC field campaign: A long-term comparison with 18 years of reanalysis product

Chapters 2 to 4 mostly concerned local- and large-scale forcings on the composition of the Arctic atmosphere, on hourly to monthly timescales, using observations and modelling. I aimed to connect the previously used observations and modelling techniques to timescales relevant for Arctic climate. This is considering the increasing environmental and socio-economic pressure on the Arctic region, with unknown consequences for the exchange of climate-active trace gases and composition of the Arctic atmosphere. The goal of Chapter 5 was to place the year-round observations during MOSAiC in the context of Arctic climate and composition of the Arctic atmosphere, thus considering the longer timescales (years). To that extent, I answered the following research questions in Chapter 5:

Are MOSAiC observed trace gas concentrations representative for the past 18 years?

Here, our analysis comprised surface continuous and flask observations taken during the MOSAiC campaign of the following 8 trace gases: CO₂, CH₄, N₂O, O₃, CO, DMS, SO₂ and C₃H₈. These observations were compared with the re-analysis product from CAMS. Observations during MOSAiC mostly fell within the expected climatology when accounting for upward trends in the greenhouse gases CO₂, CH₄, N₂O. A number of dynamic events in winter with enhanced mixing ratios of CO₂, O₃, CO and SO₂ were observed, which could be attributed to anomalous counts and intensity of cyclones. Additionally, surface observations of C₃H₈ highlighted elevated mixing ratios up to 1000 ppt, which had to be explained by long-range transport of C₃H₈ from oil and natural gas production.

How well do reanalysis datasets represent trace gas concentrations observed during MOSAiC?

I have compared the state-of-the-art CAMS reanalysis dataset to the MOSAiC observations. During summer, CAMS overestimated surface CO₂ and DMS, and underestimated surface CH₄ observations. Additionally, CAMS systematically underestimated observed CO mixing ratios by ~ 20 ppb during winter. Especially surface C₃H₈ mixing ratios were underestimated in CAMS, which raises the question whether the downward trend in atmospheric C₃H₈ in CAMS can be valued as a reliable indicator of the long-term trend in Arctic air quality.

What is the magnitude and variability in surface CO₂ and CH₄ fluxes during MOSAiC?

For the first time, year-round measurements were performed of CO₂ and CH₄ fluxes over the Arctic sea ice during the MOSAiC campaign. These observations showed a clear bi-directional exchange of CO₂ and CH₄, with a large temporal variability. Over the entire year, I found a small uptake of CO₂, and a small emission of CH₄, over the Arctic sea ice. The uptake rate of CO₂ increased for diminishing sea ice cover, while I did not find a significant increase in the exchange of CH₄. These eddy-correlation observations indicate among the lowest surface-atmosphere fluxes compared to previous literature.

6.2 Outlook

6.2.1 Disentangling flux observations over a heterogeneous surface

For the first time, year-round flux observations of the climate-active trace gases O₃, CO₂, CH₄ and DMS over the Arctic sea ice were performed. Previously, assessment of model performance for the surface exchange of trace gases relied on an indirect evaluation using a large network of surface trace gas concentration observations (e.g. Chapter 2). In Chapter 3 I have, for the first time, performed a direct comparison of the simulated and observed O₃ surface exchange.

However, this raises the question to what extent these surface flux observations are actually a representation of the Arctic sea ice/snow covered surface and to what extent surface heterogeneity should be taken into account in atmospheric chemistry and transport models.

The Arctic sea ice is often perceived as a homogeneous surface. This is especially true in the context of climate modelling. Many local processes such as the deformation of the sea ice, leading to ridging and opening of leads are often not considered in climate models (Hunke et al., 2010). However, ridges can strongly influence the turbulent structure of the atmosphere (Garbrecht et al., 1999), and leads might enhance the surface exchange of trace gases. Additionally, melt ponds provide auxiliary surface heterogeneity during summer.

In Chapter 3 I have assumed that the observed surface fluxes are a representation of the Arctic sea ice/snow surface, not accounting for these local structures of the sea ice. Figure 6.1 shows an example of a flux footprint calculation, using the Kljun et al. (2015) method, overlaying an $\sim 4 \times 4$ km area of surface temperature measurements by an infrared camera deployed during helicopter flights. First of all, the figure shows that the Arctic sea ice is very heterogeneous at a resolution which is much smaller than the typical size of a grid cell in weather ($\sim 5 \times 5$ km) and climate ($\sim 27 \times 27$ km) models. In the infrared image, many open leads (depicted by the red colors) and recently refrozen leads (depicted by the green colors) can be observed. The contrast in surface temperature between these openings in the sea ice and thicker ridges can be up to 40 °C in winter. The effective footprint of the eddy-covariance system, in this case described as the surface area that accounts for 80% of the total area, extends up to 2000 m from the *RV Polarstern* and covers a surface area of about 3 to 4 km². I found that these values are fairly typical for the prevailing stable wintertime conditions from an analysis of multiple flux footprint calculations.

An attempt has been made to disentangle the climate-active trace gas flux observations for the different types of surfaces: sea ice, snow, melt ponds and open ocean using a combination of flux footprint calculations and visible and infrared imagery. No clear connection between surface type and magnitude of the fluxes could be observed. The explanation for this is twofold. Firstly, the often limited area of open ocean or leads in the effective flux footprint, combined with an already high variability of the flux observations (e.g. Fig. 3.3 and 5.4) is reflected in differences in fluxes that are not statistically significant. Secondly, the open Arctic ocean surface water within the footprint area, or more distant vicinity of the central observatory, is often extremely stably stratified due to the input of fresh melt water from the sea ice and snow surface (Perovich et al., 2021). These stably stratified melt water layers can be up to 1.0 m thick in open leads as observed during MOSAiC (Nomura et al., 2023). Additionally, under-ice melt water and false bottoms can provide an additional source of ocean stratification during the melt season (Smith et al., 2022). This fresh melt water constrains physical and biogeochemical processes (Carmack

et al., 2016). All these factors contribute to potentially limiting the effective exchange between the atmosphere and ocean for many climate relevant trace gases.

The state of Arctic sea ice will shift towards more permeable sea ice favoring the ocean-atmosphere exchange of gases (Angelopoulos et al., 2022), and increasing light penetration in the ocean water initiates an earlier onset of primary production (Lannuzel et al., 2020). At the same time, increased freshwater input from rivers, glacial melt and precipitation will enhance freshwater stratification in the Arctic ocean in future climate (Nummelin et al., 2016), with disruptive effects on ocean biogeochemistry (Fu et al., 2020). This raises the question to what extent the opening of the Arctic sea ice will actually affect the surface exchange of trace gases. To tackle this open question, an interdisciplinary approach is required integrating all relevant disciplines. Specifically, dedicated flux observations over open leads, with and without strong surface stratification, melt ponds and the open ocean are required. These flux observations should be supported by relevant in-situ observations in the Arctic ocean, sea ice and atmosphere focusing on understanding and quantifying processes which could affect the exchange of trace gases in current and future climate. Examples include sea ice permeability, ocean surface stratification and primary productivity. As such, these observations can be used to develop new, or extend current gas-transfer algorithms with process-based representations of factors limiting trace gas exchange. At a later stage, these process-based implementations should be incorporated in larger scale climate and earth system models, to quantify the main factors limiting surface trace gas exchange in future Arctic climate.

6.2.2 The way forward in modelling the Arctic atmosphere

Towards observing and modelling halogen chemistry

A shortcoming of many state-of-the-art atmospheric chemistry and climate models is the inability to reproduce Ozone Depletion Events (ODEs) in Arctic spring (e.g. Chapters 3 & 5). These ODEs, following from emissions of halogens from the Arctic sea ice and snow pack, are a prominent feature in the seasonal cycle of Arctic surface O_3 and observed at many sites across the Arctic (Halfacre et al., 2014). However, the underlying mechanics and horizontal and vertical extent of these ODEs are not well understood. Models often do not include halogen chemistry at all, and if they do, they typically use a highly empirical formulation of the halogen emissions from the snowpack (Falk and Sinnhuber, 2018). Recent attempts to include halogen emissions and chemistry in regional atmospheric chemistry models are promising, and show that surface O_3 observations and satellite observed BrO can be reasonably reproduced by these models (Marelle et al., 2021; Ahmed et al., 2023; Cao et al., 2023). They also indicate a potentially large role of heterogeneous reactions on sea salt aerosols emitted through blowing snow (Yang et al., 2008).

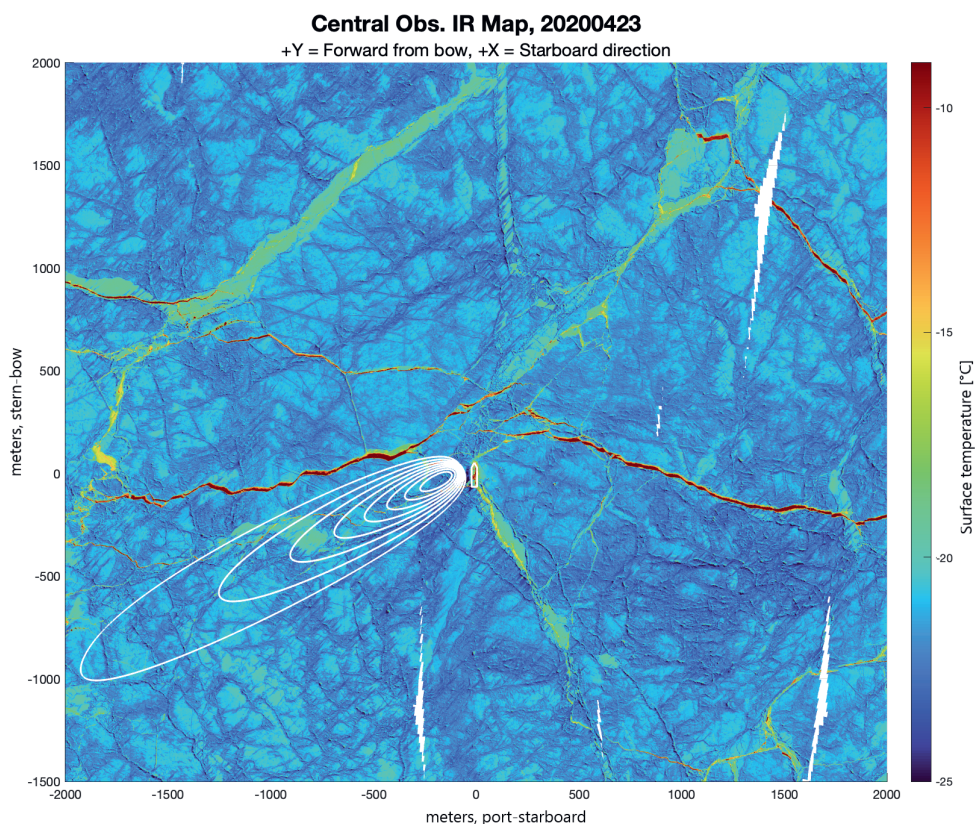


Figure 6.1: Example of a flux footprint calculation on 23-Apr-2020, using the eddy-covariance system equipped to the bow crane. The white contours indicate the flux footprint in increments of 10%, up to a maximum of 80%. The colors in the background represent the surface temperature derived from an infrared camera, deployed during helicopter flights (Thielke et al., 2022).

A logical next step would be to understand turbulent mixing and cycling of halogens and O_3 in the Arctic PBL. Currently it is unknown as to what vertical extent these ODEs occur, and what drives the recovery of these ODEs back to the normal state of $\sim 30\text{--}40$ ppb O_3 . Here, the previously developed regional 3D model simulations (e.g., Marelle et al., 2021; Ahmed et al., 2023; Cao et al., 2023) can serve as boundary conditions for more local 1D or Large Eddy Simulation models. Also because reanalysis data, which are typically used as boundary conditions, do not include these ODEs at all (e.g., Chapter 6). Still, these model simulations rely on accurate estimates of halogen production in- and emissions from the snowpack (Ahmed et al., 2022) and might require a fully coupled snow model to accurately represent these emissions. These proposed higher resolution model simulations have the potential to elucidate the vertical extent of ODEs, and the role of entrainment of O_3 rich air from the free troposphere in the

recovery of the ODE. These model simulations can be supported by relevant observations from MOSAiC such as the radiosondes and tethered balloon observations during spring. Additionally, GOME-2 (Theys et al., 2011) or TROPOMI (Seo et al., 2019) satellite observations have the potential to provide an approximation of BrO concentrations in the Arctic PBL.

Nevertheless, a significant drawback of the MOSAiC campaign is the limited availability of comprehensive observations of halogens within and above the snowpack. This gap hampers the quantification and understanding of the fundamental processes governing halogen production in the snowpack and their subsequent emission into the atmosphere. Addressing this challenge is crucial to bridging the existing knowledge gap and advancing the representation of Arctic tropospheric halogen chemistry in atmospheric models. Enhancing our understanding of Arctic halogen chemistry within atmospheric models is expected to be crucial due to its implications for atmospheric composition and air quality. By incorporating more accurate halogen chemistry representations and leveraging high-resolution simulations, we can gain deeper insights into ODEs and broader atmospheric processes in the Arctic region.

Wintertime surface energy balance & boundary layer dynamics

For a long time, understanding of Arctic boundary layer dynamics were bounded, partly due to scarce observations. The Surface Heat Budget of the Arctic (SHEBA) campaign in 1997–1998 provided for the first time year-round observations of radiation and energy fluxes and cloud characteristics over the Arctic sea ice (Perovich et al., 1999). Results from SHEBA highlighted many shortcomings in weather and climate models to represent the Arctic near-surface atmosphere and clouds (e.g., Curry and Lynch, 2002; Inoue et al., 2006; Rinke et al., 2006; Wyser et al., 2008). Specifically, simulation errors due to surface fluxes and cloud effects were identified as the most important drivers for the warm bias in weather and climate models (Inoue et al., 2006). Needless to say, this motivated efforts to improve the representation of cloud radiative effects and the surface energy balance in weather and climate models by modelling studies and an additional series of coordinated international field campaigns (e.g., Leck et al., 1996, 2001; Tjernström, 2005; Tjernström et al., 2012; Granskog et al., 2016; Heinemann et al., 2021; Shupe et al., 2022; Geerts et al., 2022).

Many years, and multiple field experiments later since SHEBA, global and regional climate models still face the same biases as decades ago (Sedlar et al., 2020; Solomon et al., 2023). This is despite the development of fully coupled regional earth system models with increasing spatial resolution (Giorgi, 2019). Biases in the surface energy balance are allocated to the treatment of clouds and cloud radiative effects in models (Sedlar et al., 2020). Specifically, the wintertime Arctic boundary layer is poorly represented due to the misrepresentation of Arctic mix-phase clouds (Pithan and Mauritsen, 2014).

Some of these biases have also become apparent in this thesis (Chapters 3 & 4), and provide and additional uncertainty in model assessments, related to the exchange, and further cycling of climate-active trace gases in- and above the atmospheric boundary layer. As an example, I show in Figure 6.2 the distribution of net surface longwave radiation ($LW_{net} = LW_{in} - LW_{out}$) observed during MOSAiC and simulated with the single-column atmospheric chemistry and meteorological model (SCM) (see Chapter 3). A large negative LW_{net} can be interpreted as a clear atmosphere since the LW_{out} from the relatively warm surface ($LW \propto \sigma T^4$) is higher than that of the atmosphere. A LW_{net} around 0 W m^{-2} can be interpreted as a cloudy atmosphere since the temperature of the low clouds is approximately equal to the surface temperature. Effects of variable emissivity of the clouds and surface are not taken into account here. In wintertime (Fig. 6.2a), MOSAiC observations show a clear bi-modal state of alternating clear and cloudy conditions. The SCM shows a clear preference for a clear wintertime Arctic atmosphere, similar to many other regional climate models. These models typically have an issue in developing and maintaining thin Arctic clouds at very low temperatures (Solomon et al., 2023). The summertime bi-modal state of LW_{net} is much better represented in the SCM (Fig. 6.2b) and other climate models (Luo et al., 2023).

Looking ahead, addressing the persistent biases in representing the Arctic atmosphere in weather and climate models requires a comprehensive and multi-scale approach (e.g. 1.5). While significant progress has been made over the years, biases in surface energy balance, cloud representation, and cloud radiative effects continue to exist, despite the increasing spatial resolution of coupled regional earth system models (Giorgi, 2019). The limitations in simulating the wintertime Arctic boundary layer, as highlighted by the misrepresentation of mix-phase clouds (Pithan and Mauritsen, 2014), underline the need for a shift in modeling strategies. One way to improve our understanding and improving model performance involves using a diverse ensemble of models that span the entire spectrum of spatial scales. Integrating these models, ranging from large-scale global models to fine-scale regional, Large Eddy Simulations, Direct Numerical Simulations and single-column models, can offer a more holistic perspective. These models can provide complementary insights into the mechanisms behind cloud formation, radiative effects, and their impact on the surface energy balance. Performing multi-scale model ensembles, and integrating the strengths of each individual model, can help identify common biases and collectively contribute to a more accurate representation of the Arctic atmosphere. Additionally, these efforts should focus on process-based understanding and identifying the mechanisms responsible for the biases. Finally, collaboration and data sharing remains crucial. Open access to observational data and to model output fosters cross-validation and facilitates a more robust assessment of model performance.

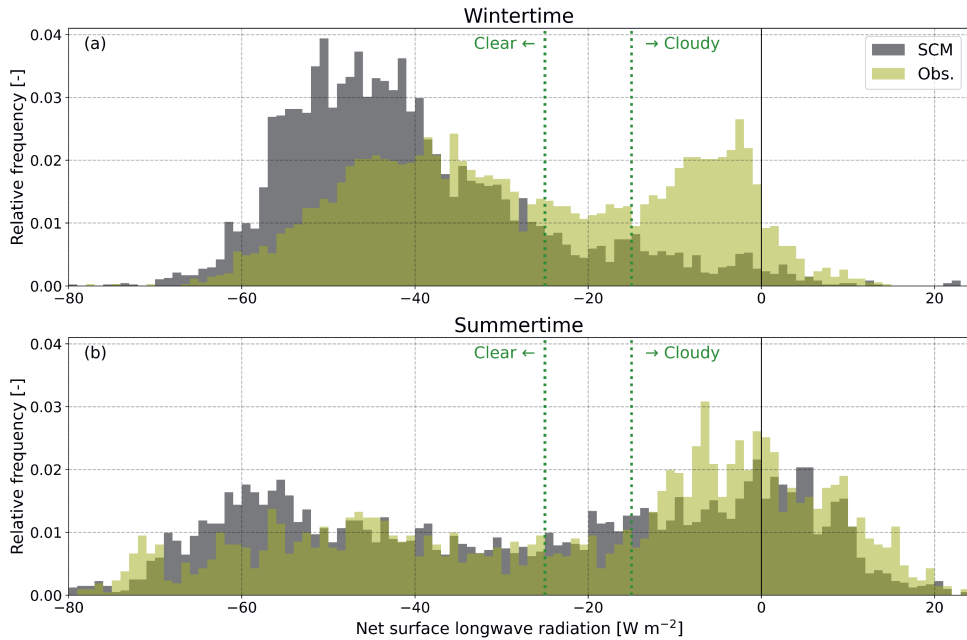


Figure 6.2: Frequency distribution of net surface longwave radiation (incoming longwave radiation minus outgoing longwave radiation) for (a) wintertime (incoming shortwave radiation $< 5 \text{ W m}^{-2}$) and (b) summertime (incoming shortwave radiation $\geq 5 \text{ W m}^{-2}$), observed during MOSAiC (olive green) and simulated with the single-column atmospheric chemistry and meteorological model (SCM).

6.2.3 Arctic climate change across disciplines, domains and scales

The Arctic is characterized many intricate connections across scientific disciplines (Arnold et al., 2016; Petrov et al., 2016; Vincent et al., 2023). Some of which have been addressed in this thesis such as the physical and biogeochemical connections in the ocean–sea ice–atmosphere continuum (Fig. 1.3). However, implications of Arctic climate change and pollution go far beyond melting sea ice and increasing temperatures. These changes have far-fetched implications for, e.g., ecology (Falardeau and Bennett, 2019), bird migration (Amélineau et al., 2019; Clairbaux et al., 2019), local indigenous communities (Vogel and Bullock, 2021) and economic activities (Vincent, 2020). Additionally, it has become evident that the Arctic is tele-connected to the mid-latitudes, and vice-versa, through various feedback mechanisms (Macias-Fauria et al., 2012; Handorf et al., 2015; Siew et al., 2020). The reduction in meridional temperature gradient promotes a weaker and wavier mid-latitude circulation, leading to prolonged extreme weather events (Francis and Vavrus, 2012). For example, the decline in sea ice appears to promote cold and snowy winters over large parts of North America, Europe and East Asia (Liu et al., 2012). At the same time, the weakened meridional temperature gradient leads to more persistent hot–dry

extremes in the mid-latitudes (Coumou et al., 2018).

To understand and quantify these intricate connections across disciplines and scales, a more holistic approach to open scientific questions need to be taken. This not only requires trans-disciplinary cooperation but also requires more effective Arctic science diplomacy and research agenda. Even though large international expeditions like MOSAiC are excellent benchmarks for decades to come, many researchers will already move on to new experimental expeditions because funding has run out. These large international and interdisciplinary expeditions provide such vast amounts of data, which should be exploited to its maximum potential. In my opinion, funding agencies should consider prioritizing, where possible, exploiting these current datasets in combination with modelling tools and other readily available observations such as satellite data.

It is evident that the Arctic will face unprecedented changes in the coming decades. We can not rely on global politics and big international companies to carry responsibility for changes in the Arctic, or anywhere else in the world for that matter. It remains key to address short- and long-term threats to the Arctic through work of scientific working groups, such as those part of the Arctic Council. At the same time, adequate political decision making based on scientific expertise, and additional conservation measures need to be taken to preserve the Arctic where possible. Arctic diplomacy could learn from successful predecessors such as the Antarctic Treaty (Hanessian, 1960; Dudeney and Walton, 2012), and should not shy away from making more drastic and binding agreements between member states.

In summary, this thesis provides one of many fundamental scientific contributions, to a whole chain of necessary activities to assess, and potentially mitigate Arctic and global climate change. The complexity of the consequences of Arctic climate change require collaborative efforts in both the scientific and political domains. Fostering synergy between scientific disciplines, leveraging existing data, and embracing cooperative international initiatives are key to comprehend and address the intricate challenges posed by Arctic climate change.

References

- S. Ahmed, J. L. Thomas, K. Tuite, J. Stutz, F. Flocke, J. J. Orlando, R. S. Hornbrook, E. C. Apel, L. K. Emmons, D. Helmig, P. Boylan, L. G. Huey, S. R. Hall, K. Ullmann, C. A. Cantrell, and A. Fried. The role of snow in controlling halogen chemistry and boundary layer oxidation during Arctic spring: A 1D modeling case study. *Journal of Geophysical Research: Atmospheres*, 127(5):e2021JD036140, 2022.
- S. Ahmed, J. L. Thomas, H. Angot, A. Dommergue, S. D. Archer, L. Bariteau, I. Beck, N. Benavent, A.-M. Blechschmidt, B. Blomquist, M. Boyer, J. H. Christensen, S. Dahlke, A. Dastoor, D. Helmig, D. Howard, H.-W. Jacobi, T. Jokinen, R. Lapere, T. Laurila, L. L. J. Quéléver, A. Richter, A. Ryjkov, A. S. Mahajan, L. Marelle, K. A. Pfaffhuber, K. Posman, A. Rinke, A. Saiz-Lopez, J. Schmale, H. Skov, A. Steffen, G. Stupple, J. Stutz, O. Travnikov, and B. Zilker. Modelling the coupled mercury-halogen-ozone cycle in the central Arctic during spring. *Elem Sci Anth*, 11(1):00129, 2023.
- E. A. Ainsworth, C. R. Yendrek, S. Sitch, W. J. Collins, and L. D. Emberson. The effects of tropospheric ozone on net primary productivity and implications for climate change. *Annual Review of Plant Biology*, 63:637–661, 2012.
- M. Albu, I. Barnes, K. H. Becker, I. Patroescu-Klotz, R. Mocanu, and T. Benter. Rate coefficients for the gas-phase reaction of OH radicals with dimethyl sulfide: temperature and O₂ partial pressure dependence. *Physical Chemistry Chemical Physics*, 8(6):728–736, 2006.
- V. A. Alexeev and C. H. Jackson. Polar amplification: is atmospheric heat transport important? *Climate dynamics*, 41(2):533–547, 2013.
- V. A. Alexeev, I. Esau, I. V. Polyakov, S. J. Byam, and S. Sorokina. Vertical structure of recent Arctic warming from observed data and reanalysis products. *Climatic Change*, 111(2):215–239, 2012.
- A. A. Aliabadi, R. M. Staebler, and S. Sharma. Air quality monitoring in communities of the Canadian Arctic during the high shipping season with a focus on local and marine pollution. *Atmospheric Chemistry and Physics*, 15(5):2651–2673, 2015.
- AMAP (Arctic Monitoring and Assessment Programme). Impacts of short-lived climate forcers on Arctic climate, air quality, and human health. *AMAP*, 2021a.
- AMAP (Arctic Monitoring and Assessment Programme). AMAP Arctic Climate Change Update 2021: Key Trends and Impacts. *AMAP*, 2021b.
- F. Amélineau, D. Grénillet, A. M. Harding, W. Walkusz, R. Choquet, and J. Fort. Arctic climate change and pollution impact little auk foraging and fitness across a decade. *Scientific reports*, 9(1):1014, 2019.
- M. Angelopoulos, E. Damm, P. Simões Pereira, K. Abrahamsson, D. Bauch, J. Bowman, G. Castellani, J. Creamean, D. V. Divine, A. Dumitrascu, S. W. Fons, M. A. Granskog, N. Kolabutin, T. Krumpfen, C. Marsay, M. Nicolaus, M. Oggier, A. Rinke, T. Sachs, E. Shimanchuk, J. Stefels, M. Stephens, A. Ulfsbo, J. Verdugo, L. Wang,

- L. Zhan, and C. Haas. Deciphering the properties of different arctic ice types during the growth phase of MOSAiC: Implications for future studies on gas pathways. *Frontiers in Earth Science*, 10:864523, 2022.
- H. Angot, C. Davel, C. Wiedinmyer, G. Pétron, J. Chopra, J. Hueber, B. Blanchard, I. Bourgeois, I. Vimont, S. A. Montzka, B. R. Miller, J. W. Elkins, and D. Helmig. Temporary pause in the growth of atmospheric ethane and propane in 2015–2018. *Atmospheric Chemistry and Physics*, 21(19):15153–15170, 2021.
- H. Angot, S. Archer, L. Bariteau, B. Blomquist, D. Helmig, D. Howard, J. Hueber, H.-W. Jacobi, and K. Posman. Ambient air ozone mole fractions measured in the University of Colorado container during the 2019-2020 MOSAiC (Multidisciplinary drifting Observatory for the Study of Arctic Climate) expedition. Arctic Data Center, 2022a. doi: 10.1594/PANGAEA.944393.
- H. Angot, S. Archer, L. Bariteau, B. Blomquist, D. Helmig, D. Howard, J. Hueber, H.-W. Jacobi, and K. Posman. Ambient air mole fractions of selected volatile organic compounds measured in the University of Colorado container during the 2019-2020 MOSAiC (Multidisciplinary drifting Observatory for the Study of Arctic Climate) expedition, 2022b. doi: 10.18739/A21R6N241.
- H. Angot, I. Beck, T. Jokinen, T. Laurila, L. Quéléver, and J. Schmale. Ambient air sulfur dioxide mole fractions measured in the Swiss container during MOSAiC 2019/2020, 2022c. doi: 10.1594/PANGAEA.944270.
- H. Angot, B. Blomquist, D. Howard, S. Archer, L. Bariteau, I. Beck, M. Boyer, M. Crotwell, D. Helmig, J. Hueber, H.-W. Jacobi, T. Jokinen, M. Kulmala, X. Lan, T. Laurila, M. Madronich, D. Neff, T. Petäjä, K. Posman, L. Quéléver, M. D. Shupe, I. Vimont, and J. Schmale. Year-round trace gas measurements in the central Arctic during the MOSAiC expedition. *Scientific Data*, 9(1):1–19, 2022d.
- H. Angot, B. Blomquist, D. Howard, S. Archer, L. Bariteau, I. Beck, D. Helmig, J. Hueber, H.-W. Jacobi, T. Jokinen, T. Laurila, K. Posman, L. Quéléver, M. D. Shupe, J. Schmale, and M. Boyer. Ozone dry air mole fractions measured during MOSAiC 2019/2020 (merged dataset), 2022e. doi: 10.1594/PANGAEA.944393.
- H. Angot, B. Blomquist, D. Howard, S. Archer, L. Bariteau, I. Beck, D. Helmig, J. Hueber, H.-W. Jacobi, T. Jokinen, L. Xin, T. Laurila, M. Madronich, K. Posman, L. Quéléver, M. D. Shupe, J. Schmale, and M. Boyer. Carbon monoxide dry air mole fractions measured during MOSAiC 2019/2020 (merged dataset), 2022f. doi: 10.1594/PANGAEA.944389.
- A. Ansmann, K. Ohneiser, A. Chudnovsky, D. A. Knopf, E. W. Eloranta, D. Villanueva, P. Seifert, M. Radenz, B. Barja, F. Zamorano, C. Jimenez, R. Engelmann, H. Baars, H. Griesche, J. Hofer, D. Althausen, and U. Wandinger. Ozone depletion in the Arctic and Antarctic stratosphere induced by wildfire smoke. *Atmospheric Chemistry and Physics*, 22(17):11701–11726, 2022.
- S. R. Arnold, K. S. Law, C. A. Brock, J. L. Thomas, S. M. Starkweather, K. von Salzen, A. Stohl, S. Sharma, M. T. Lund, M. G. Flanner, T. Petäjä, H. Tanimoto, J. Gamble, J. E. Dibb, M. Melamed, N. Johnson, M. Fidel, V.-P. Tynkkynen, A. Baklanov, S. Eckhardt, S. A. Monks, J. Browse, and H. Bozem. Arctic air pollution: Challenges and opportunities for the next decade. *Elementa: Science of the Anthropocene*, 2016.
- K. R. Arrigo and G. L. van Dijken. Secular trends in Arctic Ocean net primary production. *Journal of Geophysical Research: Oceans*, 116(C9), 2011.
- K. R. Arrigo, S. Pabi, G. L. van Dijken, and W. Maslowski. Air-sea flux of CO₂ in the Arctic Ocean, 1998–2003. *Journal of Geophysical Research: Biogeosciences*, 115(G4), 2010.
- M. Årthun, B. Bogstad, U. Daewel, N. S. Keenlyside, A. B. Sandø, C. Schrum, and G. Ottersen. Climate based multi-year predictions of the Barents Sea cod stock. *PloS one*, 13(10):e0206319, 2018.
- A. Baklanov, K. Schlünzen, P. Suppan, J. Baldasano, D. Brunner, S. Aksoyoglu, G. Carmichael, J. Douros,

- J. Flemming, R. Forkel, S. Galmarini, M. Gauss, G. Grell, M. Hirtl, S. Joffre, O. Jorba, E. Kaas, M. Kaasik, G. Kallos, X. Kong, U. Korsholm, A. Kurganskiy, J. Kushta, U. Lohmann, A. Mahura, A. Manders-Groot, A. Maurizi, N. Moussiopoulos, S. T. Rao, N. Savage, C. Seigneur, R. S. Sokhi, E. Solazzo, S. Solomos, B. Sørensen, G. Tsegas, E. Vignati, B. Vogel, and Y. Zhang. Online coupled regional meteorology chemistry models in Europe: current status and prospects. *Atmospheric Chemistry and Physics*, 14(1):317–398, 2014.
- A. P. Ballantyne, C. B. Alden, J. B. Miller, P. P. Tans, and J. W. C. White. Increase in observed net carbon dioxide uptake by land and oceans during the past 50 years. *Nature*, 488(7409):70–72, 2012.
- R. F. Banks, J. Tiana-Alsina, J. M. Baldasano, F. Rocadenbosch, A. Papayannis, S. Solomos, and C. G. Tzanis. Sensitivity of boundary-layer variables to PBL schemes in the WRF model based on surface meteorological observations, lidar, and radiosondes during the HygrA-CD campaign. *Atmospheric Research*, 176:185–201, 2016.
- L. Bariteau, D. Helmig, C. W. Fairall, J. E. Hare, J. Hueber, and E. K. Lang. Determination of oceanic ozone deposition by ship-borne eddy covariance flux measurements. *Atmospheric Measurement Techniques*, 3(2): 441–455, 2010.
- L. Barrie, J. Bottenheim, R. Schnell, P. Crutzen, and R. Rasmussen. Ozone destruction and photochemical reactions at polar sunrise in the lower Arctic atmosphere. *Nature*, 334(6178):138–141, 1988.
- J. G. M. Barten, L. N. Ganzeveld, A. J. Visser, R. Jiménez, and M. C. Krol. Evaluation of nitrogen oxides (NO_x) sources and sinks and ozone production in Colombia and surrounding areas. *Atmospheric Chemistry and Physics*, 20(15):9441–9458, 2020.
- J. G. M. Barten, L. N. Ganzeveld, G.-J. Steeneveld, and M. C. Krol. Role of oceanic ozone deposition in explaining temporal variability in surface ozone at High Arctic sites. *Atmospheric Chemistry and Physics*, 21(13):10229–10248, 2021.
- J. G. M. Barten, L. N. Ganzeveld, G.-J. Steeneveld, B. W. Blomquist, H. Angot, S. D. Archer, L. Bariteau, I. Beck, M. Boyer, P. von der Gathen, D. Helmig, D. Howard, J. Hueber, H.-W. Jacobi, T. Jokinen, T. Laurila, K. M. Posman, L. Quéléver, J. Schmale, M. D. Shupe, and M. C. Krol. Low ozone dry deposition rates to sea ice during the MOSAiC field campaign: Implications for the Arctic boundary layer ozone budget. *Elementa: Science of the Anthropocene*, 11(1), 02 2023. ISSN 2325-1026.
- S. Basu, A. A. M. Holtslag, L. Caporaso, A. Riccio, and G. Steeneveld. Observational support for the stability dependence of the bulk Richardson number across the stable boundary layer. *Boundary-Layer Meteorology*, 150 (3):515–523, 2014.
- N. R. Bates, W.-J. Cai, and J. T. Mathis. The ocean carbon cycle in the western Arctic Ocean: Distributions and air-sea fluxes of carbon dioxide. *Oceanography*, 24(3):186–201, 2011.
- I. Beck, H. Angot, A. Baccarini, L. Dada, L. Quéléver, T. Jokinen, T. Laurila, M. Lampimäki, N. Bukowiecki, M. Boyer, X. Gong, M. Gysel-Beer, T. Petäjä, J. Wang, and J. Schmale. Automated identification of local contamination in remote atmospheric composition time series. *Atmospheric Measurement Techniques*, 15(14): 4195–4224, 2022.
- S. Becker, R. P. Sapkota, B. Pokharel, L. Adhikari, R. P. Pokhrel, S. Khanal, and B. Giri. Particulate matter variability in Kathmandu based on in-situ measurements, remote sensing, and reanalysis data. *Atmospheric Research*, 258:105623, 2021.
- T. G. Bell, S. Landwehr, S. D. Miller, W. J. de Bruyn, A. H. Callaghan, B. Scanlon, B. Ward, M. Yang, and E. S. Saltzman. Estimation of bubble-mediated air-sea gas exchange from concurrent DMS and CO_2 transfer

- velocities at intermediate-high wind speeds. *Atmospheric Chemistry and Physics*, 17(14):9019–9033, 2017.
- N. Benavent, A. S. Mahajan, Q. Li, C. A. Cuevas, J. Schmale, H. Angot, T. Jokinen, L. L. Quéléver, A.-M. Blechschmidt, B. Zilker, A. Richter, J. A. Serna, D. Garcia-Nieto, R. P. Fernandez, H. Skov, A. Dumitrascu, P. Simões Pereira, K. Abrahamsson, S. Bucci, M. Duetsch, A. Stohl, I. Beck, T. Laurila, B. Blomquist, D. Howard, S. D. Archer, L. Bariteau, D. Helmig, J. Hueber, H.-W. Jacobi, K. Posman, L. Dada, K. R. Daellenbach, and A. Saiz-Lopez. Substantial contribution of iodine to Arctic ozone destruction. *Nature Geoscience*, 15(10): 770–773, 2022.
- C. M. Berkowitz, J. D. Fast, and R. C. Easter. Boundary layer vertical exchange processes and the mass budget of ozone: Observations and model results. *Journal of Geophysical Research: Atmospheres*, 105(D11):14789–14805, 2000.
- E. Blanchard-Wrigglesworth, S. L. Farrell, T. Newman, and C. M. Bitz. Snow cover on Arctic sea ice in observations and an Earth System Model. *Geophysical Research Letters*, 42(23):10–342, 2015.
- B. Blomquist, H. Angot, S. Archer, L. Bariteau, D. Helmig, D. Howard, J. Hueber, H.-W. Jacobi, and K. Posman. Minute-averaged methane dry air mole fractions measured in the University of Colorado container during the 2019-2020 MOSAiC (Multidisciplinary drifting Observatory for the Study of Arctic Climate) expedition, 2022a. doi: 10.18739/A2GF0MX7X.
- B. Blomquist, H. Angot, S. Archer, L. Bariteau, D. Helmig, D. Howard, J. Hueber, H.-W. Jacobi, and K. Posman. Minute-averaged methane dry air mole fractions measured at Met City during the 2019-2020 MOSAiC (Multidisciplinary drifting Observatory for the Study of Arctic Climate) expedition, 2022b. doi: 10.18739/A20G3H05R.
- B. Blomquist, H. Angot, S. Archer, L. Bariteau, D. Helmig, D. Howard, J. Hueber, H.-W. Jacobi, and K. Posman. Minute-averaged carbon dioxide dry air mole fractions measured in the University of Colorado container during the 2019-2020 MOSAiC (Multidisciplinary drifting Observatory for the Study of Arctic Climate) expedition, 2022c. doi: 10.18739/A2M61BR25.
- B. Blomquist, H. Angot, S. Archer, L. Bariteau, D. Helmig, D. Howard, J. Hueber, H.-W. Jacobi, and K. Posman. Minute-averaged carbon dioxide dry air mole fractions measured at Met City during the 2019-2020 MOSAiC (Multidisciplinary drifting Observatory for the Study of Arctic Climate) expedition, 2022d. doi: 10.18739/A2VQ2SC0C.
- B. Blomquist, H. Angot, S. Archer, L. Bariteau, D. Helmig, D. Howard, J. Hueber, H.-W. Jacobi, and K. Posman. Minute-averaged dimethylsulfide dry air mole fractions measured in the University of Colorado container during the 2019-2020 MOSAiC (Multidisciplinary drifting Observatory for the Study of Arctic Climate) expedition, 2022e. doi: 10.18739/A2QZ22J60.
- B. W. Blomquist, B. J. Huebert, C. W. Fairall, and I. C. Faloona. Determining the sea-air flux of dimethylsulfide by eddy correlation using mass spectrometry. *Atmospheric Measurement Techniques*, 3(1):1–20, 2010.
- B. W. Blomquist, B. J. Huebert, C. W. Fairall, L. Bariteau, J. B. Edson, J. E. Hare, and W. R. McGillis. Advances in air-sea CO₂ flux measurement by eddy correlation. *Boundary-Layer Meteorology*, 152(3):245–276, 2014.
- B. W. Blomquist, S. E. Brumer, C. W. Fairall, B. J. Huebert, C. J. Zappa, I. M. Brooks, M. Yang, L. Bariteau, J. Prytherch, J. E. Hare, H. Czerski, A. Matei, and R. W. Pascal. Wind speed and sea state dependencies of air-sea gas transfer: Results from the high wind speed gas exchange study (HiWinGS). *Journal of Geophysical Research: Oceans*, 122(10):8034–8062, 2017.
- B. W. Blomquist, D. Helmig, S. D. Archer, L. N. Ganzeveld, D. Howard, H. Angot, L. Bariteau, H. Jacobi, K. M. Posman, and J. Hueber. Trace gas and wind velocities at 10 Hertz from Research Vessel Polarstern bow tower

- during the MOSAiC Arctic drift campaign, 2019–2020, 2022f. doi: 10.18739/A2NC5SD71.
- F. Bocquet, D. Helmig, and S. J. Oltmans. Ozone in interstitial air of the mid-latitude, seasonal snowpack at Niwot Ridge, Colorado. *Arctic, Antarctic, and Alpine Research*, 39(3):375–387, 2007.
- M. Bocquet, H. Elbern, H. Eskes, M. Hirtl, R. Žabkar, G. R. Carmichael, J. Flemming, A. Inness, M. Pagowski, J. L. Pérez Camañó, P. E. Saide, R. San Jose, M. Sofiev, J. Vira, A. Baklanov, C. Carnevale, G. Grell, and C. Seigneur. Data assimilation in atmospheric chemistry models: current status and future prospects for coupled chemistry meteorology models. *Atmospheric chemistry and physics*, 15(10):5325–5358, 2015.
- K. F. Boersma, H. J. Eskes, A. Richter, I. de Smedt, A. Lorente, S. Beirle, J. H. G. M. van Geffen, M. Zara, E. Peters, M. van Roozendael, T. Wagner, J. D. Maasakkers, R. J. van der A, J. Nightingale, A. de Rudder, H. Irie, G. Pinardi, J.-C. Lambert, and S. C. Compernelle. Improving algorithms and uncertainty estimates for satellite NO₂ retrievals: results from the quality assurance for the essential climate variables (QA4ECV) project. *Atmospheric Measurement Techniques*, 11(12):6651–6678, 2018.
- L. N. Boisvert, A. A. Petty, and J. C. Stroeve. The impact of the extreme winter 2015/16 Arctic cyclone on the Barents–Kara Seas. *Monthly Weather Review*, 144(11):4279–4287, 2016.
- E. Bossioli, G. Sotiropoulou, G. Methymaki, and M. Tombrou. Modeling Extreme Warm-Air Advection in the Arctic During Summer: The Effect of Mid-Latitude Pollution Inflow on Cloud Properties. *Journal of Geophysical Research: Atmospheres*, 126(7):e2020JD033291, 2021.
- P. Boylan, D. Helmig, and J.-H. Park. Characterization and mitigation of water vapor effects in the measurement of ozone by chemiluminescence with nitric oxide. *Atmospheric Measurement Techniques*, 7(5):1231–1244, 2014.
- J. Brioude, D. Arnold, A. Stohl, M. Cassiani, D. Morton, P. Seibert, W. Angevine, S. Evan, A. Dingwell, J. D. Fast, R. C. Easter, I. Pizzo, J. Burkhardt, and G. Wotawa. The Lagrangian particle dispersion model FLEXPART-WRF version 3.1. *Geoscientific Model Development*, 6(6):1889–1904, 2013.
- D. H. Bromwich, F. O. Otieno, K. M. Hines, K. W. Manning, and E. Shilo. Comprehensive evaluation of polar weather research and forecasting model performance in the Antarctic. *Journal of Geophysical Research: Atmospheres*, 118(2):274–292, 2013.
- D. H. Bromwich, A. B. Wilson, L. Bai, Z. Liu, M. Barlage, C.-F. Shih, S. Maldonado, K. M. Hines, S.-H. Wang, J. Woollen, B. Kuo, H.-C. Lin, T.-K. Wee, M. C. Serreze, and J. E. Walsh. The arctic system reanalysis, version 2. *Bulletin of the American Meteorological Society*, 99(4):805–828, 2018.
- I. M. Brooks, M. Tjernström, P. O. G. Persson, M. D. Shupe, R. A. Atkinson, G. Canut, C. E. Birch, T. Mauritsen, J. Sedlar, and B. J. Brooks. The turbulent structure of the Arctic summer boundary layer during the Arctic Summer Cloud-Ocean Study. *Journal of Geophysical Research: Atmospheres*, 122(18):9685–9704, 2017.
- CAFF (Conservation of Arctic Flora and Fauna). Arctic biodiversity assessment. *Arctic Council*, 2013.
- W.-J. Cai, L. Chen, B. Chen, Z. Gao, S. H. Lee, J. Chen, D. Pierrot, K. Sullivan, Y. Wang, X. Hu, W.-J. Huang, Y. Zhang, S. Xu, A. Murata, J. M. Grebmeier, E. P. Jones, and H. Zhang. Decrease in the CO₂ uptake capacity in an ice-free Arctic Ocean basin. *Science*, 329(5991):556–559, 2010.
- L. Cao, U. Platt, and E. Guthelil. Role of the boundary layer in the occurrence and termination of the tropospheric ozone depletion events in polar spring. *Atmospheric Environment*, 132:98–110, 2016.
- L. Cao, S. Li, Y. Gu, and Y. Luo. A three-dimensional simulation and process analysis of tropospheric ozone depletion events (ODEs) during the springtime in the Arctic using CMAQ (Community Multiscale Air Quality Modeling System). *Atmospheric Chemistry and Physics*, 23(5):3363–3382, 2023.

- E. C. Carmack, M. Yamamoto-Kawai, T. W. N. Haine, S. Bacon, B. A. Bluhm, C. Lique, H. Melling, I. V. Polyakov, F. Straneo, M.-L. Timmermans, and W. J. Williams. Freshwater and its role in the Arctic Marine System: Sources, disposition, storage, export, and physical and biogeochemical consequences in the Arctic and global oceans. *Journal of Geophysical Research: Biogeosciences*, 121(3):675–717, 2016.
- F. Carminati, S. Migliorini, B. Ingleby, W. Bell, H. Lawrence, S. Newman, J. Hocking, and A. Smith. Using reference radiosondes to characterise NWP model uncertainty for improved satellite calibration and validation. *Atmospheric Measurement Techniques*, 12(1):83–106, 2019.
- L. J. Carpenter, S. D. Archer, and R. Beale. Ocean-atmosphere trace gas exchange. *Chemical Society Reviews*, 41(19):6473–6506, 2012.
- D. J. Cavalieri and C. L. Parkinson. Arctic sea ice variability and trends, 1979–2010. *The Cryosphere*, 6(4):881–889, 2012.
- R. Chance, A. R. Baker, L. Carpenter, and T. D. Jickells. The distribution of iodide at the sea surface. *Environmental Science: Processes & Impacts*, 16(8):1841–1859, 2014.
- K.-L. Chang, I. Petropavlovskikh, O. R. Cooper, M. G. Schultz, and T. Wang. Regional trend analysis of surface ozone observations from monitoring networks in eastern North America, Europe and East Asia. *Elementa: Science of the Anthropocene*, 5, 2017.
- W. Chang, B. G. Heikes, and M. Lee. Ozone deposition to the sea surface: chemical enhancement and wind speed dependence. *Atmospheric Environment*, 38(7):1053–1059, 2004.
- R. Checa-Garcia, M. I. Hegglin, D. Kinnison, D. A. Plummer, and K. P. Shine. Historical tropospheric and stratospheric ozone radiative forcing using the CMIP6 database. *Geophysical Research Letters*, 45(7):3264–3273, 2018.
- F. Chen and J. Dudhia. Coupling an advanced land surface–hydrology model with the Penn State–NCAR MM5 modeling system. Part I: Model implementation and sensitivity. *Monthly weather review*, 129(4):569–585, 2001.
- X. Chen, L. L. J. Quéléver, P. L. Fung, J. Kesti, M. P. Rissanen, J. Bäck, P. Keronen, H. Junninen, T. Petäjä, V.-M. Kerminen, and M. Kulmala. Observations of ozone depletion events in a Finnish boreal forest. *Atmospheric Chemistry and Physics*, 18(1):49–63, 2018.
- L. Chutia, N. Ojha, I. Girach, B. Pathak, L. K. Sahu, C. Sarangi, J. Flemming, A. da Silva, and P. K. Bhuyan. Trends in sulfur dioxide over the Indian subcontinent during 2003–2019. *Atmospheric Environment*, page 119189, 2022.
- M. Clairbaux, J. Fort, P. Mathewson, W. Porter, H. Strøm, and D. Grémillet. Climate change could overturn bird migration: Transarctic flights and high-latitude residency in a sea ice free Arctic. *Scientific Reports*, 9(1):17767, 2019.
- D. Clifford, D. Donaldson, M. Brigante, B. D’Anna, and C. George. Reactive uptake of ozone by chlorophyll at aqueous surfaces. *Environmental science & technology*, 42(4):1138–1143, 2008.
- O. E. Clifton, A. M. Fiore, W. J. Massman, C. B. Baublitz, M. Coyle, L. Emberson, S. Fares, D. K. Farmer, P. Gentine, G. Gerosa, A. B. Guenther, D. Helmig, D. L. Lombardozi, J. W. Munger, E. G. Patton, S. E. Pusede, D. B. Schwede, S. J. Silva, M. Sörgel, A. L. Steiner, and A. P. K. Tai. Dry deposition of ozone over land: processes, measurement, and modeling. *Reviews of Geophysics*, 58(1):e2019RG000670, 2020a.
- O. E. Clifton, F. Paulot, A. M. Fiore, L. W. Horowitz, G. Correa, C. B. Baublitz, S. Fares, I. Goded, A. H. Goldstein, C. Gruening, A. J. Hogg, B. Loubet, I. Mammarella, J. W. Munger, L. Neil, P. Stella, J. Uddling, T. Vesala, and E. Weng. Influence of dynamic ozone dry deposition on ozone pollution. *Journal of Geophysical Research: Atmospheres*, 125(8):e2020JD032398, 2020b.

- J. Cohen, J. A. Screen, J. C. Furtado, M. Barlow, D. Whittleston, D. Coumou, J. Francis, K. Dethloff, D. Entekhabi, J. Overland, and J. Jones. Recent Arctic amplification and extreme mid-latitude weather. *Nature geoscience*, 7(9):627–637, 2014.
- J. C. Comiso and D. K. Hall. Climate trends in the Arctic as observed from space. *Wiley Interdisciplinary Reviews: Climate Change*, 5(3):389–409, 2014.
- J. C. Comiso, C. L. Parkinson, R. Gersten, and L. Stock. Accelerated decline in the Arctic sea ice cover. *Geophysical research letters*, 35(1), 2008.
- S. A. Conley, I. C. Faloona, D. H. Lenschow, T. Campos, C. Heizer, A. Weinheimer, C. A. Cantrell, R. L. Mauldin, R. S. Hornbrook, I. Pollack, and A. Bandy. A complete dynamical ozone budget measured in the tropical marine boundary layer during PASE. *Journal of Atmospheric Chemistry*, 68(1):55–70, 2011.
- O. R. Cooper, D. D. Parrish, J. Ziemke, N. V. Balashov, M. Cupeiro, I. E. Galbally, S. Gilge, L. Horowitz, N. R. Jensen, J.-F. Lamarque, V. Naik, S. J. Oltmans, J. Schwab, D. T. Shindell, A. M. Thompson, V. Thouret, Y. Wang, and R. M. Zbinden. Global distribution and trends of tropospheric ozone: An observation-based review. *Elementa: Science of the Anthropocene*, 2:000029, 07 2014.
- O. R. Cooper, M. G. Schultz, S. Schröder, K.-L. Chang, A. Gaudel, G. Carbajal-Benítez, E. Cuevas, M. Fröhlich, I. E. Galbally, S. Molloy, D. Kubistin, X. Lu, A. McClure-Begley, P. Nédélec, J. O’Brien, S. J. Oltmans, I. Petropavlovskikh, L. Ries, I. Senik, K. Sjöberg, S. Solberg, G. T. Spain, W. Spangl, M. Steinbacher, D. Tarasick, V. Thouret, and X. Xu. Multi-decadal surface ozone trends at globally distributed remote locations. *Elementa: Science of the Anthropocene*, 8:23, 06 2020.
- J. J. Corbett, D. A. Lack, J. J. Winebrake, S. Harder, J. A. Silberman, and M. Gold. Arctic shipping emissions inventories and future scenarios. *Atmospheric Chemistry and Physics*, 10(19):9689–9704, 2010.
- D. Coumou, G. Di Capua, S. Vavrus, L. Wang, and S. Wang. The influence of Arctic amplification on mid-latitude summer circulation. *Nature Communications*, 9(1):2959, 2018.
- C. Cox, M. Gallagher, M. Shupe, O. Persson, A. Solomon, T. Ayers, D. Costa, J. Hutchings, J. Leach, S. Morris, J. Osborn, S. Pezoa, and T. Uttal. Atmospheric Surface Flux Station #30 measurements (Level 1 Raw), Multidisciplinary Drifting Observatory for the Study of Arctic Climate (MOSAIC), central Arctic, October 2019–September 2020, 2021a. doi: 10.18739/A20C4SM1J.
- C. Cox, O. Persson, M. Shupe, A. Solomon, M. Gallagher, Z. Lawrence, and D. Perovich. Driving mechanisms for the onset of the summer melt season at MOSAiC. In *AGU Fall Meeting Abstracts*, volume 2021, pages C55C–0603, 2021b.
- P. Crippa, R. C. Sullivan, A. Thota, and S. C. Pryor. The impact of resolution on meteorological, chemical and aerosol properties in regional simulations with WRF-Chem. *Atmospheric Chemistry and Physics*, 17(2): 1511–1528, 2017.
- B. Cros, C. Delon, C. Affre, T. Marion, A. Druilhet, P. E. Perros, and A. Lopez. Sources and sinks of ozone in savanna and forest areas during EXPRESSO: Airborne turbulent flux measurements. *Journal of Geophysical Research: Atmospheres*, 105(D24):29347–29358, 2000.
- G. C. Cuchiara, X. Li, J. Carvalho, and B. Rappenglück. Intercomparison of planetary boundary layer parameterization and its impacts on surface ozone concentration in the WRF/Chem model for a case study in Houston/Texas. *Atmospheric Environment*, 96:175–185, 2014.
- J. A. Curry and A. H. Lynch. Comparing arctic regional climate model. *Eos, Transactions American Geophysical Union*, 83(9):87–87, 2002.

- J. A. Curry, J. L. Schramm, and E. E. Ebert. Sea ice-albedo climate feedback mechanism. *Journal of Climate*, 8 (2):240–247, 1995.
- H. F. Dacre, N. J. Harvey, P. W. Webley, and D. Morton. How accurate are volcanic ash simulations of the 2010 Eyjafjallajökull eruption? *Journal of Geophysical Research: Atmospheres*, 121(7):3534–3547, 2016.
- L. Dada, H. Angot, I. Beck, A. Baccarini, L. L. Quéléver, M. Boyer, T. Laurila, Z. Brasseur, G. Jozef, G. de Boer, M. D. Shupe, S. Henning, S. Bucci, M. Dütsch, A. Stohl, T. Petäjä, K. R. Daellenbach, and J. Schmale. A central arctic extreme aerosol event triggered by a warm air-mass intrusion. *Nature communications*, 13(1):1–15, 2022.
- A. Dai, D. Luo, M. Song, and J. Liu. Arctic amplification is caused by sea-ice loss under increasing CO₂. *Nature communications*, 10(1):1–13, 2019.
- M. Dameris, D. G. Loyola, M. Nützel, M. Coldewey-Egbers, C. Lerot, F. Romahn, and M. van Roozendael. Record low ozone values over the Arctic in boreal spring 2020. *Atmospheric Chemistry and Physics*, 21(2):617–633, 2021.
- E. Damm, E. Helmke, S. Thoms, U. Schauer, E. Nöthig, K. Bakker, and R. Kiene. Methane production in aerobic oligotrophic surface water in the central Arctic Ocean. *Biogeosciences*, 7(3):1099–1108, 2010.
- W. J. de Groot, M. D. Flannigan, and A. S. Cantin. Climate change impacts on future boreal fire regimes. *Forest Ecology and Management*, 294:35–44, 2013.
- S. G. de Jalón, P. J. Burgess, J. Curiel Yuste, G. Moreno, A. Graves, J. H. N. Palma, J. Crous-Duran, S. Kay, and A. Chiabai. Dry deposition of air pollutants on trees at regional scale: A case study in the Basque Country. *Agricultural and Forest Meteorology*, 278:107648, 2019.
- M. N. Deeter, L. K. Emmons, G. L. Francis, D. P. Edwards, J. C. Gille, J. X. Warner, B. Khattatov, D. Ziskin, J.-F. Lamarque, S.-P. Ho, V. Yudin, J.-L. Attié, D. Packman, J. Chen, D. Mao, and J. R. Drummond. Operational carbon monoxide retrieval algorithm and selected results for the MOPITT instrument. *Journal of Geophysical Research: Atmospheres*, 108(D14), 2003.
- O. Demir, J. T. Johnson, K. C. Jezek, M. J. Andrews, K. Ayotte, G. Spreen, S. Hendricks, L. Kaleschke, M. Oggier, M. A. Granskog, A. Fong, M. Hoppmann, I. Matero, and D. Scholz. Measurements of 540–1740 MHz brightness temperatures of sea ice during the winter of the MOSAiC campaign. *IEEE Transactions on Geoscience and Remote Sensing*, 60:1–11, 2021.
- C. Derksen and R. Brown. Spring snow cover extent reductions in the 2008–2012 period exceeding climate model projections. *Geophysical Research Letters*, 39(19), 2012.
- R. G. Derwent, D. D. Parrish, I. E. Galbally, D. S. Stevenson, R. M. Doherty, V. Naik, and P. J. Young. Uncertainties in models of tropospheric ozone based on Monte Carlo analysis: Tropospheric ozone burdens, atmospheric lifetimes and surface distributions. *Atmospheric Environment*, 180:93–102, 2018.
- F. X. Diebold and G. D. Rudebusch. Probability assessments of an ice-free Arctic: Comparing statistical and climate model projections. *Journal of Econometrics*, 2021.
- E. Dlugokencky, X. Lan, S. Michel, G. Pétron, I. Vimont, M. Crotwell, M. Madronich, A. Crotwell, D. Neff, S. Wolter, E. Moglia, and J. Mund. NOAA GML & INSTAAR SIL measurements of Greenhouse Gases and Related Tracers from the MOSAiC project (Version 2022.05.23) [Data set], 2022. doi: 10.25925/AYBV-YZ43.
- T.-F. Dou and C.-D. Xiao. An overview of black carbon deposition and its radiative forcing over the Arctic. *Advances in Climate Change Research*, 7(3):115–122, 2016.
- R. R. Draxler and G. D. Rolph. HYSPLIT (HYbrid Single-Particle Lagrangian Integrated Trajectory) model access

- via NOAA ARL READY website (<http://ready.arl.noaa.gov/HYSPLIT.php>), NOAA Air Resources Laboratory, 2010.
- J. R. Dudeney and D. W. H. Walton. Leadership in politics and science within the Antarctic Treaty. *Polar Research*, 31(1):11075, 2012.
- A. Edtbauer, C. Stönnner, E. Y. Pfannerstill, M. Berasategui, D. Walter, J. N. Crowley, J. Lelieveld, and J. Williams. A new marine biogenic emission: methane sulfonamide (MSAM), dimethyl sulfide (DMS), and dimethyl sulfone (DMSO₂) measured in air over the Arabian Sea. *Atmospheric Chemistry and Physics*, 20(10):6081–6094, 2020.
- L. Emberson. Effects of ozone on agriculture, forests and grasslands. *Philosophical Transactions of the Royal Society A*, 378(2183):20190327, 2020.
- I. Esau and S. Sorokina. Climatology of the arctic planetary boundary layer. *Atmospheric Turbulence, Meteorological Modeling and Aerodynamics*, pages 3–58, 2009.
- C. Fairall, D. Helmig, L. Ganzeveld, and J. Hare. Water-side turbulence enhancement of ozone deposition to the ocean. *Atmospheric Chemistry and Physics*, 2007(7):443–451, 2007.
- C. W. Fairall, E. F. Bradley, D. P. Rogers, J. B. Edson, and G. S. Young. Bulk parameterization of air-sea fluxes for tropical ocean-global atmosphere coupled-ocean atmosphere response experiment. *Journal of Geophysical Research: Oceans*, 101(C2):3747–3764, 1996.
- C. W. Fairall, M. Yang, L. Bariteau, J. B. Edson, D. Helmig, W. McGillis, S. Pezoa, J. E. Hare, B. Huebert, and B. Blomquist. Implementation of the Coupled Ocean-Atmosphere Response Experiment flux algorithm with CO₂, dimethyl sulfide, and O₃. *Journal of Geophysical Research: Oceans*, 116(C4):C00F09, 2011.
- M. Falardeau and E. M. Bennett. Towards integrated knowledge of climate change in Arctic marine systems: A systematic literature review of multidisciplinary research. *Arctic Science*, 6(1):1–23, 2019.
- S. Falk and B.-M. Sinnhuber. Polar boundary layer bromine explosion and ozone depletion events in the chemistry–climate model EMAC v2.52: implementation and evaluation of AirSnow algorithm. *Geoscientific Model Development*, 11(3):1115–1131, 2018.
- S. Falk and A. Søyde Haslerud. Update and evaluation of the ozone dry deposition in Oslo CTM3 v1.0. *Geoscientific Model Development*, 12(11):4705–4728, 2019.
- S. Falk, A. V. Vollsnes, A. B. Eriksen, F. Stordal, and T. Koren Berntsen. Quality assessment of ozone reanalysis products and gap-filling over subarctic Europe for vegetation risk mapping. *Atmospheric Chemistry and Physics*, 21(20):15647–15661, 2021.
- Z. Fang and J. M. Wallace. Arctic sea ice variability on a timescale of weeks and its relation to atmospheric forcing. *Journal of Climate*, 7(12):1897–1914, 1994.
- M. Flannigan, B. Stocks, M. Turetsky, and M. Wotton. Impacts of climate change on fire activity and fire management in the circumboreal forest. *Global change biology*, 15(3):549–560, 2009.
- Z. L. Fleming, R. M. Doherty, E. von Schneidmesser, C. S. Malley, O. R. Cooper, J. P. Pinto, A. Colette, X. Xu, D. Simpson, M. G. Schultz, A. S. Lefohn, S. Hamad, R. Moolla, S. Solberg, and Z. Feng. Tropospheric Ozone Assessment Report: Present-day ozone distribution and trends relevant to human health. *Elementa: Science of the Anthropocene*, 6, 2018.
- P. M. Forster, H. I. Forster, M. J. Evans, M. J. Gidden, C. D. Jones, C. A. Keller, R. D. Lamboll, C. L. Quéré, J. Rogelj, D. Rosen, C.-F. Schleussner, T. B. Richardson, C. J. Smith, and S. T. Turnock. Current and future global climate impacts resulting from COVID-19. *Nature Climate Change*, 10(10):913–919, 2020.

- R. R. Forster, D. G. Long, K. C. Jezek, S. D. Drobot, and M. R. Anderson. The onset of Arctic sea-ice snowmelt as detected with passive-and active-microwave remote sensing. *Annals of Glaciology*, 33:85–93, 2001.
- J. A. Francis and S. J. Vavrus. Evidence linking Arctic amplification to extreme weather in mid-latitudes. *Geophysical research letters*, 39(6), 2012.
- P. Friedlingstein, M. O’Sullivan, M. W. Jones, R. M. Andrew, L. Gregor, J. Hauck, C. Le Quéré, I. T. Luijkx, A. Olsen, G. P. Peters, W. Peters, J. Pongratz, C. Schwingshackl, S. Sitch, J. G. Canadell, P. Ciais, R. B. Jackson, S. R. Alin, R. Alkama, A. Arneth, V. K. Arora, N. R. Bates, M. Becker, N. Bellouin, H. C. Bittig, L. Bopp, F. Chevallier, L. P. Chini, M. Cronin, W. Evans, S. Falk, R. A. Feely, T. Gasser, M. Gehlen, T. Gkritzalis, L. Gloege, G. Grassi, N. Gruber, O. Gürses, I. Harris, M. Hefner, R. A. Houghton, G. C. Hurtt, Y. Iida, T. Ilyina, A. K. Jain, A. Jersild, K. Kadono, E. Kato, D. Kennedy, K. Klein Goldewijk, J. Knauer, J. I. Korsbakken, P. Landschützer, N. Lefèvre, K. Lindsay, J. Liu, Z. Liu, G. Marland, N. Mayot, M. J. McGrath, N. Metz, N. M. Monacci, D. R. Munro, S.-I. Nakaoka, Y. Niwa, K. O’Brien, T. Ono, P. I. Palmer, N. Pan, D. Pierrot, K. Pocock, B. Poulter, L. Resplandy, E. Robertson, C. Rödenbeck, C. Rodriguez, T. M. Rosan, J. Schwinger, R. Séférian, J. D. Shutler, I. Skjelvan, T. Steinhoff, Q. Sun, A. J. Sutton, C. Sweeney, S. Takao, T. Tanhua, P. P. Tans, X. Tian, H. Tian, B. Tilbrook, H. Tsujino, F. Tubiello, G. R. van der Werf, A. P. Walker, R. Wanninkhof, C. Whitehead, A. Willstrand Wranne, R. Wright, W. Yuan, C. Yue, X. Yue, S. Zaehle, J. Zeng, and B. Zheng. Global carbon budget 2022. *Earth System Science Data*, 14(11):4811–4900, 2022.
- W. Fu, J. K. Moore, F. W. Primeau, K. Lindsay, and J. T. Randerson. A growing freshwater lens in the Arctic Ocean with sustained climate warming disrupts marine ecosystem function. *Journal of Geophysical Research: Biogeosciences*, 125(12):e2020JG005693, 2020.
- M. Gallagher, K. Beswick, and H. Coe. Ozone deposition to coastal waters. *Quarterly Journal of the Royal Meteorological Society*, 127(572):539–558, 2001.
- L. Ganzeveld, D. Helmig, C. W. Fairall, J. Hare, and A. Pozzer. Atmosphere-ocean ozone exchange: A global modeling study of biogeochemical, atmospheric, and waterside turbulence dependencies. *Global Biogeochemical Cycles*, 23(4), 2009.
- L. N. Ganzeveld and J. Lelieveld. Dry deposition parameterization in a chemistry general circulation model and its influence on the distribution of reactive trace gases. *Journal of Geophysical Research: Atmospheres*, 100(D10): 20999–21012, 1995.
- L. N. Ganzeveld, J. Lelieveld, F. J. Dentener, M. C. Krol, and G.-J. Roelofs. Atmosphere-biosphere trace gas exchanges simulated with a single-column model. *Journal of Geophysical Research: Atmospheres*, 107(D16): ACH–8, 2002.
- L. N. Ganzeveld, O. Klemm, B. Rappenglück, and J. Valverde-Canossa. Evaluation of meteorological parameters over a coniferous forest in a single-column chemistry-climate model. *Atmospheric Environment*, 40:21–27, 2006.
- L. N. Ganzeveld, G. Eerdekens, G. Feig, H. Fischer, H. Harder, R. Königstedt, D. Kubistin, M. Martinez, F. X. Meixner, H. A. Scheeren, V. Sinha, D. Taraborrelli, J. Williams, J. Vilà-Guerau de Arellano, and J. Lelieveld. Surface and boundary layer exchanges of volatile organic compounds, nitrogen oxides and ozone during the GABRIEL campaign. *Atmospheric Chemistry and Physics*, 8(20):6223–6243, 2008.
- T. Garbrecht, C. Lüpkes, E. Augstein, and C. Wamser. Influence of a sea ice ridge on low-level airflow. *Journal of Geophysical Research: Atmospheres*, 104(D20):24499–24507, 1999.
- A. Gaudel, O. R. Cooper, K.-L. Chang, I. Bourgeois, J. R. Ziemke, S. A. Strode, L. D. Oman, P. Sellitto, P. Nédélec, R. Blot, V. Thouret, and C. Granier. Aircraft observations since the 1990s reveal increases of tropospheric ozone

- at multiple locations across the Northern Hemisphere. *Science Advances*, 6(34):eaba8272, 2020.
- B. Geerts, S. E. Giangrande, G. M. McFarquhar, L. Xue, S. J. Abel, J. M. Comstock, S. Crewell, P. J. DeMott, K. Ebell, P. Field, T. C. J. Hill, A. Hunzinger, M. P. Jensen, K. L. Johnson, T. W. Juliano, P. Kollias, B. Kosovic, C. Lackner, E. Luke, C. Lüpkes, A. A. Matthews, R. Neggers, M. Ovchinnikov, H. Powers, M. D. Shupe, T. Spengler, B. E. Swanson, M. Tjernström, A. K. Theisen, N. A. Wales, Y. Wang, M. Wendisch, and P. Wu. The comble campaign: A study of marine boundary layer clouds in arctic cold-air outbreaks. *Bulletin of the American Meteorological Society*, 103(5):E1371–E1389, 2022.
- M. W. Gery, G. Z. Whitten, J. P. Killus, and M. C. Dodge. A photochemical kinetics mechanism for urban and regional scale computer modeling. *Journal of Geophysical Research: Atmospheres*, 94(D10):12925–12956, 1989.
- D. Ghatak and J. Miller. Implications for Arctic amplification of changes in the strength of the water vapor feedback. *Journal of Geophysical Research: Atmospheres*, 118(14):7569–7578, 2013.
- R. Gierens, S. Kneifel, M. D. Shupe, K. Ebell, M. Maturilli, and U. Löhnert. Low-level mixed-phase clouds in a complex Arctic environment. *Atmospheric Chemistry and Physics*, 20(6):3459–3481, 2020.
- N. P. Gillett, D. A. Stone, P. A. Stott, T. Nozawa, A. Y. Karpechko, G. C. Hegerl, M. F. Wehner, and P. D. Jones. Attribution of polar warming to human influence. *Nature Geoscience*, 1(11):750–754, 2008.
- F. Giorgi. Thirty years of regional climate modeling: where are we and where are we going next? *Journal of Geophysical Research: Atmospheres*, 124(11):5696–5723, 2019.
- V. Gorshelev, A. Serdyuchenko, M. Weber, W. Chehade, and J. Burrows. High spectral resolution ozone absorption cross-sections—Part 1: Measurements, data analysis and comparison with previous measurements around 293 K. *Atmospheric Measurement Techniques*, 7(2):609–624, 2014.
- W. Gortler, J. H. van Angelen, J. T. M. Lenaerts, and M. R. van den Broeke. Present and future near-surface wind climate of Greenland from high resolution regional climate modelling. *Climate dynamics*, 42(5-6):1595–1611, 2014.
- R. M. Graham, L. Cohen, N. Ritzhaupt, B. Segger, R. G. Graversen, A. Rinke, V. P. Walden, M. A. Granskog, and S. R. Hudson. Evaluation of six atmospheric reanalyses over Arctic sea ice from winter to early summer. *Journal of Climate*, 32(14):4121–4143, 2019a.
- R. M. Graham, P. Itkin, A. Meyer, A. Sundfjord, G. Spreen, L. H. Smedsrud, G. E. Liston, B. Cheng, L. Cohen, D. Divine, I. Fer, A. Fransson, S. Gerland, J. Haapala, S. R. Hudson, A. M. Johansson, J. King, I. Merkouriadi, A. K. Peterson, C. Provost, A. Randelhoff, A. Rinke, A. Rösel, N. Sennéchaël, V. P. Walden, P. Duarte, P. Assmy, H. Steen, and M. A. Granskog. Winter storms accelerate the demise of sea ice in the Atlantic sector of the Arctic Ocean. *Scientific Reports*, 9(1):1–16, 2019b.
- C. Granier, U. Niemeier, J. H. Jungclaus, L. Emmons, P. Hess, J.-F. Lamarque, S. Walters, and G. P. Brasseur. Ozone pollution from future ship traffic in the Arctic northern passages. *Geophysical Research Letters*, 33(13), 2006.
- A. M. Grannas, A. E. Jones, J. Dibb, M. Ammann, C. Anastasio, H. Beine, M. Bergin, J. Bottenheim, C. Boxe, G. Carver, G. Chen, J. H. Crawford, F. Dominé, M. M. Frey, M. I. Guzmán, D. E. Heard, D. Helmig, M. R. Hoffmann, R. E. Honrath, L. G. Huey, M. Hutterli, H. W. Jacobi, P. Klán, B. Lefer, J. McConnell, J. Plane, R. Sander, J. Savarino, P. B. Shepson, W. R. Simpson, J. R. Sodeau, R. von Glasow, R. Weller, E. W. Wolff, and T. Zhu. An overview of snow photochemistry: evidence, mechanisms and impacts. *Atmospheric Chemistry and Physics*, 7(16):4329–4373, 2007.

- M. A. Granskog, P. Assmy, S. Gerland, G. Spreen, H. Steen, and L. H. Smedsrud. Arctic research on thin ice: Consequences of Arctic sea ice loss. *Eos Trans. AGU*, 97(5):22–26, 2016.
- R. G. Graversen and M. Wang. Polar amplification in a coupled climate model with locked albedo. *Climate Dynamics*, 33(5):629–643, 2009.
- G. A. Grell, S. E. Peckham, R. Schmitz, S. A. McKeen, G. Frost, W. C. Skamarock, and B. Eder. Fully coupled “online” chemistry within the WRF model. *Atmospheric Environment*, 39(37):6957–6975, 2005.
- A. Guenther, X. Jiang, C. Heald, T. Sakulyanontvittaya, T. Duhl, L. Emmons, and X. Wang. The Model of Emissions of Gases and Aerosols from Nature version 2.1 (MEGAN2. 1): an extended and updated framework for modeling biogenic emissions. *Geoscientific Model Development*, 5(6):1471–1492, 2012.
- K. Gui, H. Che, L. Li, Y. Zheng, L. Zhang, H. Zhao, J. Zhong, W. Yao, Y. Liang, Y. Wang, and X. Zhang. The significant contribution of small-sized and spherical aerosol particles to the decreasing trend in total aerosol optical depth over land from 2003 to 2018. *Engineering*, 16:82–92, 2022.
- W. I. Gustafson, Y. Qian, and J. D. Fast. Downscaling aerosols and the impact of neglected subgrid processes on direct aerosol radiative forcing for a representative global climate model grid spacing. *Journal of Geophysical Research: Atmospheres*, 116(D13), 2011.
- J. Haapala, M. Lensu, M. Dumont, A. H. H. Renner, M. A. Granskog, and S. Gerland. Small-scale horizontal variability of snow, sea-ice thickness and freeboard in the first-year ice region north of Svalbard. *Annals of Glaciology*, 54(62):261–266, 2013.
- C. Haas. Master track of POLARSTERN cruise PS122/2 in 1 sec resolution (zipped, 36.7 MB), 2020. doi: 10.1594/PANGAEA.924672.
- J. W. Halfacre, T. N. Knepp, P. B. Shepson, C. R. Thompson, K. A. Pratt, B. Li, P. K. Peterson, S. J. Walsh, W. R. Simpson, P. A. Matrai, J. W. Bottenheim, S. Netcheva, D. K. Perovich, and A. Richter. Temporal and spatial characteristics of ozone depletion events from measurements in the Arctic. *Atmospheric Chemistry and Physics*, 14(10):4875, 2014.
- J. Hamilton, G. de Boer, A. Doddi, and D. A. Lawrence. The DataHawk2 uncrewed aircraft system for atmospheric research. *Atmospheric Measurement Techniques*, 15(22):6789–6806, 2022.
- D. Handorf, R. Jaiser, K. Dethloff, A. Rinke, and J. Cohen. Impacts of Arctic sea ice and continental snow cover changes on atmospheric winter teleconnections. *Geophysical Research Letters*, 42(7):2367–2377, 2015.
- J. Hanessian. The Antarctic Treaty 1959. *International & Comparative Law Quarterly*, 9(3):436–480, 1960.
- C. Hardacre, O. Wild, and L. Emberson. An evaluation of ozone dry deposition in global scale chemistry climate models. *Atmospheric Chemistry and Physics*, 15(11):6419–6436, 2015.
- H. Hayashida, G. Carnat, M. Galí, A. H. Monahan, E. Mortenson, T. Sou, and N. S. Steiner. Spatiotemporal variability in modeled bottom ice and sea surface dimethylsulfide concentrations and fluxes in the Arctic during 1979–2015. *Global Biogeochemical Cycles*, 34(10):e2019GB006456, 2020.
- G. Heinemann, S. Willmes, L. Schefczyk, A. Makshtas, V. Kustov, and I. Makhotina. Observations and simulations of meteorological conditions over Arctic thick sea ice in late winter during the Transarktika 2019 expedition. *Atmosphere*, 12(2):174, 2021.
- D. Helmig, F. Bocquet, L. Cohen, and S. J. Oltmans. Ozone uptake to the polar snowpack at Summit, Greenland. *Atmospheric Environment*, 41(24):5061–5076, 2007a.
- D. Helmig, L. Ganzeveld, T. Butler, and S. J. Oltmans. The role of ozone atmosphere-snow gas exchange on polar,

- boundary-layer tropospheric ozone—a review and sensitivity analysis. *Atmospheric Chemistry and Physics*, 7(1): 15–30, 2007b.
- D. Helmig, S. J. Oltmans, D. Carlson, J. Lamarque, A. Jones, C. Labuschagne, K. Anlauf, and K. Hayden. A review of surface ozone in the polar regions. *Atmospheric Environment*, 41(24):5138–5161, 2007c.
- D. Helmig, L. D. Cohen, F. Bocquet, S. Oltmans, A. Grachev, and W. Neff. Spring and summertime diurnal surface ozone fluxes over the polar snow at Summit, Greenland. *Geophysical research letters*, 36(8), 2009.
- D. Helmig, P. Boylan, B. Johnson, S. Oltmans, C. Fairall, R. Staebler, A. Weinheimer, J. Orlando, D. J. Knapp, D. D. Montzka, F. Flocke, U. Frieß, H. Sihler, and P. B. Shepson. Ozone dynamics and snow-atmosphere exchanges during ozone depletion events at Barrow, Alaska. *Journal of Geophysical Research: Atmospheres*, 117(D20), 2012a.
- D. Helmig, E. Lang, L. Bariteau, P. Boylan, C. Fairall, L. Ganzeveld, J. Hare, J. Hueber, and M. Pallandt. Atmosphere-ocean ozone fluxes during the TexAQS 2006, STRATUS 2006, GOMECC 2007, GasEx 2008, and AMMA 2008 cruises. *Journal of Geophysical Research: Atmospheres*, 117(D4), 2012b.
- D. Helmig, S. Rossabi, J. Hueber, P. Tans, S. A. Montzka, K. Masarie, K. Thoning, C. Plass-Duelmer, A. Claude, L. J. Carpenter, A. C. Lewis, S. Punjabi, S. Reimann, M. K. Vollmer, R. Steinbrecher, J. W. Hannigan, L. K. Emmons, E. Mahieu, B. Franco, D. Smale, and A. Pozzer. Reversal of global atmospheric ethane and propane trends largely due to US oil and natural gas production. *Nature Geoscience*, 9(7):490–495, 2016.
- G. R. Henderson, B. S. Barrett, L. J. Wachowicz, K. S. Mattingly, J. R. Preece, and T. L. Mote. Local and remote atmospheric circulation drivers of Arctic change: a review. *Frontiers in Earth Science*, 9:549, 2021.
- A. Herber, S. Becker, H. J. Belter, J. Brauchle, A. Ehrlich, M. Klingebiel, T. Krumpfen, C. Lüpkes, M. Mech, M. Moser, and M. Wendisch. MOSAiC Expedition: Airborne Surveys with Research Aircraft POLAR 5 and POLAR 6 in 2020. *Berichte zur Polar-und Meeresforschung= Reports on polar and marine research*, 754, 2021.
- M. Herrmann, H. Sihler, U. Frieß, T. Wagner, U. Platt, and E. Gutheil. Time-dependent 3D simulations of tropospheric ozone depletion events in the Arctic spring using the Weather Research and Forecasting model coupled with Chemistry (WRF-Chem). *Atmospheric Chemistry and Physics*, 21(10):7611–7638, 2021.
- H. Hersbach, B. Bell, P. Berrisford, S. Hirahara, A. Horányi, J. Muñoz-Sabater, J. Nicolas, C. Peubey, R. Radu, D. Schepers, A. Simmons, C. Soci, S. Abdalla, X. Abellan, G. Balsamo, P. Bechtold, G. Biavati, J. Bidlot, M. Bonavita, G. de Chiara, P. Dahlgren, D. Dee, M. Diamantakis, R. Dragani, J. Flemming, R. Forbes, M. Fuentes, A. Geer, L. Haimberger, S. Healy, R. J. Hogan, E. Hólm, M. Janisková, S. Keeley, P. Laloyaux, P. Lopez, C. Lupu, G. Radnoti, P. de Rosnay, I. Rozum, F. Vamborg, S. Villaume, and J.-N. Thépaut. The ERA5 global reanalysis. *Quarterly Journal of the Royal Meteorological Society*, 146(730):1999–2049, 2020.
- B. B. Hicks, D. D. Baldocchi, T. P. Meyers, R. P. Hosker, and D. R. Matt. A preliminary multiple resistance routine for deriving dry deposition velocities from measured quantities. *Water, Air, and Soil Pollution*, 36(3-4):311–330, 1987.
- K. M. Hines and D. H. Bromwich. Development and testing of Polar Weather Research and Forecasting (WRF) model. Part I: Greenland ice sheet meteorology. *Monthly Weather Review*, 136(6):1971–1989, 2008.
- K. M. Hines, D. H. Bromwich, L. Bai, C. M. Bitz, J. G. Powers, and K. W. Manning. Sea ice enhancements to Polar WRF. *Monthly Weather Review*, 143(6):2363–2385, 2015.
- Ø. Hodnebrog, S. B. Dalsøren, and G. Myhre. Lifetimes, direct and indirect radiative forcing, and global warming potentials of ethane (C₂H₆), propane (C₃H₈), and butane (C₄H₁₀). *Atmospheric Science Letters*, 19(2):e804, 2018.

- A. A. M. Holtslag, G. Svensson, P. Baas, S. Basu, B. Beare, A. C. M. Beljaars, F. C. Bosveld, J. Cuxart, J. Lindvall, G. J. Steeneveld, M. Tjernström, and B. J. H. van de Wiel. Stable atmospheric boundary layers and diurnal cycles: challenges for weather and climate models. *Bulletin of the American Meteorological Society*, 94(11): 1691–1706, 2013.
- S.-Y. Hong, J. Dudhia, and S.-H. Chen. A revised approach to ice microphysical processes for the bulk parameterization of clouds and precipitation. *Monthly weather review*, 132(1):103–120, 2004.
- S.-Y. Hong, Y. Noh, and J. Dudhia. A new vertical diffusion package with an explicit treatment of entrainment processes. *Monthly weather review*, 134(9):2318–2341, 2006.
- M. Hoppmann, I. Kuznetsov, Y.-C. Fang, and B. Rabe. Mesoscale observations of temperature and salinity in the Arctic Transpolar Drift: a high-resolution dataset from the MOSAiC Distributed Network. *Earth System Science Data*, 14(11):4901–4921, 2022.
- X. Hou, B. Zhu, D. Fei, and D. Wang. The impacts of summer monsoons on the ozone budget of the atmospheric boundary layer of the Asia-Pacific region. *Science of the Total Environment*, 502:641–649, 2015.
- X.-M. Hu, J. W. Nielsen-Gammon, and F. Zhang. Evaluation of three planetary boundary layer schemes in the WRF model. *Journal of Applied Meteorology and Climatology*, 49(9):1831–1844, 2010.
- X.-M. Hu, D. C. Doughty, K. J. Sanchez, E. Joseph, and J. D. Fuentes. Ozone variability in the atmospheric boundary layer in Maryland and its implications for vertical transport model. *Atmospheric Environment*, 46: 354–364, 2012.
- X.-M. Hu, P. M. Klein, and M. Xue. Evaluation of the updated YSU planetary boundary layer scheme within WRF for wind resource and air quality assessments. *Journal of Geophysical Research: Atmospheres*, 118(18): 10–490, 2013.
- Y. Huang, X. Dong, D. A. Bailey, M. M. Holland, B. Xi, A. K. DuVivier, J. E. Kay, L. L. Landrum, and Y. Deng. Thicker clouds and accelerated Arctic sea ice decline: The atmosphere-sea ice interactions in spring. *Geophysical Research Letters*, 46(12):6980–6989, 2019.
- E. C. Hunke, W. H. Lipscomb, and A. K. Turner. Sea-ice models for climate study: retrospective and new directions. *Journal of Glaciology*, 56(200):1162–1172, 2010.
- M. J. Iacono, J. S. Delamere, E. J. Mlawer, M. W. Shephard, S. A. Clough, and W. D. Collins. Radiative forcing by long-lived greenhouse gases: Calculations with the AER radiative transfer models. *Journal of Geophysical Research: Atmospheres*, 113(D13), 2008.
- A. Inness, M. Ades, A. Agustí-Panareda, J. Barré, A. Benedictow, A.-M. Blechschmidt, J. J. Dominguez, R. Engelen, H. Eskes, J. Flemming, V. Huijnen, L. Jones, Z. Kipling, S. Massart, M. Parrington, V.-H. Peuch, M. Razinger, S. Remy, M. Schulz, and M. Suttie. The CAMS reanalysis of atmospheric composition. *Atmospheric Chemistry and Physics*, 19(6):3515–3556, 2019.
- A. Inness, S. Chabrillat, J. Flemming, V. Huijnen, B. Langenrock, J. Nicolas, I. Polichtchouk, and M. Razinger. Exceptionally low Arctic stratospheric ozone in spring 2020 as seen in the CAMS reanalysis. *Journal of Geophysical Research: Atmospheres*, 125(23):e2020JD033563, 2020.
- J. Inoue, J. Liu, J. O. Pinto, and J. A. Curry. Intercomparison of Arctic regional climate models: Modeling clouds and radiation for SHEBA in May 1998. *Journal of Climate*, 19(17):4167–4178, 2006.
- D. J. Jacob. Heterogeneous chemistry and tropospheric ozone. *Atmospheric Environment*, 34(12-14):2131–2159, 2000.

- D. J. Jacob, J. H. Crawford, H. Maring, A. D. Clarke, J. E. Dibb, L. K. Emmons, R. A. Ferrare, C. A. Hostetler, P. B. Russell, H. B. Singh, A. M. Thompson, G. E. Shaw, E. McCauley, J. R. Pederson, and J. A. Fisher. The Arctic Research of the Composition of the Troposphere from Aircraft and Satellites (ARCTAS) mission: design, execution, and first results. *Atmospheric Chemistry and Physics*, 10(11):5191–5212, 2010.
- H. Jacobi, L. Kaleschke, A. Richter, A. Rozanov, and J. P. Burrows. Observation of a fast ozone loss in the marginal ice zone of the Arctic Ocean. *Journal of Geophysical Research: Atmospheres*, 111(D15):D15309, 2006.
- H. Jacobi, S. Morin, and J. W. Bottenheim. Observation of widespread depletion of ozone in the springtime boundary layer of the central Arctic linked to mesoscale synoptic conditions. *Journal of Geophysical Research: Atmospheres*, 115(D17):D17302, 2010.
- C. Jacques, C. J. Sapart, F. Fripiat, G. Carnat, J. Zhou, B. Delille, T. Röckmann, C. van der Veen, H. Niemann, T. Haskell, and J.-L. Tison. Sources and sinks of methane in sea ice: Insights from stable isotopes. *Elem Sci Anth*, 9(1):00167, 2021.
- Z. I. Janjić. The step-mountain eta coordinate model: Further developments of the convection, viscous sublayer, and turbulence closure schemes. *Monthly weather review*, 122(5):927–945, 1994.
- Z. I. Janjić. Nonsingular implementation of the Mellor-Yamada level 2.5 scheme in the NCEP Meso model, 2001.
- G. Janssens-Maenhout, M. Crippa, D. Guizzardi, M. Muntean, E. Schaaf, F. Dentener, P. Bergamaschi, V. Pagliari, J. G. J. Olivier, J. A. H. W. Peters, J. A. van Aardenne, S. Monni, U. Doering, A. M. R. Petrescu, E. Solazzo, and G. D. Oreggioni. EDGAR v4.3.2 Global Atlas of the three major Greenhouse Gas Emissions for the period 1970–2012. *Earth System Science Data*, 11(3):959–1002, 2019.
- W. Jia and X. Zhang. The role of the planetary boundary layer parameterization schemes on the meteorological and aerosol pollution simulations: A review. *Atmospheric Research*, 239:104890, 2020.
- P. Jöckel, H. Tost, A. Pozzer, C. Brühl, J. Buchholz, L. Ganzeveld, P. Hoor, A. Kerkweg, M. G. Lawrence, R. Sander, B. Steil, G. Stiller, M. Tanarhte, D. Taraborrelli, J. van Aardenne, and J. Lelieveld. The atmospheric chemistry general circulation model ECHAM5/MESSy1: consistent simulation of ozone from the surface to the mesosphere. *Atmospheric Chemistry and Physics*, 6(12):5067–5104, 2006.
- G. Jozef, J. Cassano, S. Dahlke, and G. de Boer. Testing the efficacy of atmospheric boundary layer height detection algorithms using uncrewed aircraft system data from MOSAiC. *Atmospheric Measurement Techniques*, 15(13):4001–4022, 2022.
- J. H. Jungclauss, K. Lohmann, and D. Zanchettin. Enhanced 20th-century heat transfer to the Arctic simulated in the context of climate variations over the last millennium. *Climate of the Past*, 10(6):2201–2213, 2014.
- L. Jungsberg, E. Turunen, T. Heleniak, S. Wang, J. Ramage, and J. Roto. Atlas of population, society and economy in the Arctic, 2019.
- J. S. Kain. The Kain–Fritsch convective parameterization: an update. *Journal of applied meteorology*, 43(1):170–181, 2004.
- S. Kang, Y. Zhang, Y. Qian, and H. Wang. A review of black carbon in snow and ice and its impact on the cryosphere. *Earth-science reviews*, 210:103346, 2020.
- T. Kanzow. Master track of POLARSTERN cruise PS122/3 in 1 sec resolution (zipped, 52 MB), 2020. doi: 10.1594/PANGAEA.924678.
- J. E. Kay, T. L’Ecuyer, H. Chepfer, N. Loeb, A. Morrison, and G. Cesana. Recent advances in Arctic cloud and climate research. *Current Climate Change Reports*, 2(4):159–169, 2016.

- A. Keen and E. Blockley. Investigating future changes in the volume budget of the Arctic sea ice in a coupled climate model. *The Cryosphere*, 12(9):2855–2868, 2018.
- K. Keil. The Arctic: A new region of conflict? The case of oil and gas. *Cooperation and conflict*, 49(2):162–190, 2014.
- V. I. Kharuk, M. L. Dvinskaya, S. T. Im, A. S. Golyukov, and K. T. Smith. Wildfires in the Siberian Arctic. *Fire*, 5(4):106, 2022.
- B.-M. Kim, J.-Y. Hong, S.-Y. Jun, X. Zhang, H. Kwon, S.-J. Kim, J.-H. Kim, S.-W. Kim, and H.-K. Kim. Major cause of unprecedented Arctic warming in January 2016: Critical role of an Atlantic windstorm. *Scientific Reports*, 7(1):1–9, 2017.
- A. V. Kirdyanov, P. J. Krusic, V. V. Shishov, E. A. Vaganov, A. I. Fertikov, V. S. Myglan, V. V. Barinov, J. Browse, J. Esper, V. A. Ilyin, A. A. Knorre, M. A. Korets, V. V. Kukarskikh, D. A. Mashukov, A. A. Onuchin, A. Piermattei, A. V. Pimenov, A. S. Prokushkin, V. A. Ryzhkova, A. S. Shishikin, K. T. Smith, A. V. Taynik, M. Wild, E. Zorita, and U. Büntgen. Ecological and conceptual consequences of Arctic pollution. *Ecology Letters*, 23(12):1827–1837, 2020.
- T. Klein, G. Heinemann, D. H. Bromwich, J. J. Cassano, and K. M. Hines. Mesoscale modeling of katabatic winds over Greenland and comparisons with AWS and aircraft data. *Meteorology and Atmospheric Physics*, 78(1-2): 115–132, 2001.
- N. Kljun, P. Calanca, M. Rotach, and H. P. Schmid. A simple two-dimensional parameterisation for Flux Footprint Prediction (FFP). *Geoscientific Model Development*, 8(11):3695–3713, 2015.
- S. Kloster, J. Feichter, E. Maier-Reimer, K. D. Six, P. Stier, and P. Wetzol. DMS cycle in the marine ocean-atmosphere system—a global model study. *Biogeosciences*, 3(1):29–51, 2006.
- C. Knote, D. Brunner, H. Vogel, J. Allan, A. Asmi, M. Äijälä, S. Carbone, H. D. van der Gon, J. L. Jimenez, A. Kiendler-Scharr, C. Mohr, L. Poulain, A. S. H. Prévôt, E. Swietlicki, and B. Vogel. Towards an online-coupled chemistry-climate model: evaluation of COSMO-ART. *Geoscientific Model Development Discussions*, 4(3): 1809–1874, 2011.
- U. S. Korsholm, A. Baklanov, A. Gross, A. Mahura, B. H. Sass, and E. Kaas. Online coupled chemical weather forecasting based on HIRLAM—overview and prospective of Enviro-HIRLAM. *HIRLAM newsletter*, 54:151–168, 2008.
- E. A. Kort, S. C. Wofsy, B. C. Daube, M. Diao, J. W. Elkins, R. S. Gao, E. J. Hints, D. F. Hurst, R. Jimenez, F. L. Moore, J. R. Spackman, and M. A. Zondlo. Atmospheric observations of Arctic Ocean methane emissions up to 82 north. *Nature Geoscience*, 5(5):318–321, 2012.
- M. Kotovitch, S. Moreau, J. Zhou, M. Vancoppenolle, G. S. Dieckmann, K.-U. Evers, F. van der Linden, D. N. Thomas, J.-L. Tison, and B. Delille. Air-ice carbon pathways inferred from a sea ice tank experiment Air-ice carbon pathways. *Elementa: Science of the Anthropocene*, 4, 2016.
- S. T. Kral, J. Reuder, T. Vihma, I. Suomi, K. F. Hualand, G. H. Urbancic, B. R. Greene, G. Steeneveld, T. Lorenz, B. Maronga, M. O. Jonassen, H. Ajosennpää, L. Bäserud, P. B. Chilson, A. A. M. Holtslag, A. D. Jenkins, R. Kouznetsov, S. Mayer, E. A. Pillar-Little, A. Rautenberg, J. Schwenkel, A. W. Seidl, and B. Wrenger. The innovative strategies for observations in the Arctic Atmospheric Boundary Layer Project (ISOBAR): Unique finescale observations under stable and very stable conditions. *Bulletin of the American Meteorological Society*, 102(2):E218–E243, 2021.
- N. A. Krotkov, L. N. Lamsal, E. A. Celarier, W. H. Swartz, S. V. Marchenko, E. J. Bucsela, K. L. Chan, M. Wenig, and

- M. Zara. The version 3 OMI NO₂ standard product. *Atmospheric Measurement Techniques*, 10(9):3133–3149, 2017.
- T. Krumpfen, L. von Albedyll, H. F. Goessling, S. Hendricks, B. Juhls, G. Spreen, S. Willmes, H. J. Belter, K. Dethloff, C. Haas, L. Kaleschke, C. Katlein, X. Tian-Kunze, R. Ricker, P. Rostosky, J. Rückert, S. Singha, and J. Sokolova. MOSAiC drift expedition from October 2019 to July 2020: Sea ice conditions from space and comparison with previous years. *The Cryosphere*, 15(8):3897–3920, 2021.
- U. Kuhn, L. Ganzeveld, A. Thielmann, T. Dindorf, G. Schebeske, M. Welling, J. Sciare, G. Roberts, F. X. Meixner, J. Kesselmeier, J. Lelieveld, O. Kolle, P. Ciccioli, J. Lloyd, J. Trentmann, P. Artaxo, and M. O. Andreae. Impact of Manaus City on the Amazon Green Ocean atmosphere: ozone production, precursor sensitivity and aerosol load. *Atmospheric Chemistry and Physics*, 10(19):9251–9282, 2010.
- J. Kukkonen, T. Olsson, D. M. Schultz, A. Baklanov, T. Klein, A. I. Miranda, A. Monteiro, M. Hirtl, V. Tarvainen, M. Boy, V.-H. Peuch, A. Poupkou, I. Kioutsioukis, S. Finardi, M. Sofiev, R. Sokhi, K. E. J. Lehtinen, K. Karatzas, R. San José, M. Astitha, G. Kallos, M. Schaap, E. Reimer, H. Jakobs, and K. Eben. A review of operational, regional-scale, chemical weather forecasting models in Europe. *Atmospheric Chemistry and Physics*, 12(1): 1–87, 2012.
- P. Kupiszewski, C. Leck, M. Tjernström, S. Sjogren, J. Sedlar, M. Graus, M. Müller, B. Brooks, E. Swietlicki, S. Norris, and A. Hansel. Vertical profiling of aerosol particles and trace gases over the central Arctic Ocean during summer. *Atmospheric Chemistry and Physics*, 13(24):12405–12431, 2013.
- A. Lana, T. G. Bell, R. Simó, S. M. Vallina, J. Ballabrera-Poy, A. J. Kettle, J. Dachs, L. Bopp, E. S. Saltzman, J. Stefels, J. E. Johnson, and P. S. Liss. An updated climatology of surface dimethylsulfide concentrations and emission fluxes in the global ocean. *Global Biogeochemical Cycles*, 25(1), 2011.
- D. Lannuzel, L. Tedesco, M. van Leeuwe, K. Campbell, H. Flores, B. Delille, L. Miller, J. Stefels, P. Assmy, J. Bowman, K. Brown, G. Castellani, M. Chierici, O. Crabeck, E. Damm, B. Else, A. Fransson, F. Fripiat, N.-X. Geilfus, C. Jacques, E. Jones, H. Kaartokallio, M. Kotovitch, K. Meiners, S. Moreau, D. Nomura, I. Peeken, J.-M. Rintala, N. Steiner, J.-L. Tison, M. Vancoppenolle, F. van der Linden, M. Vichi, and P. Wongpan. The future of Arctic sea-ice biogeochemistry and ice-associated ecosystems. *Nature Climate Change*, 10(11):983–992, 2020.
- K. S. Law, A. Stohl, P. K. Quinn, C. A. Brock, J. F. Burkhart, J.-D. Paris, G. Ancellet, H. B. Singh, A. Roiger, H. Schlager, J. Dibb, D. J. Jacob, S. R. Arnold, J. Pelon, and J. L. Thomas. Arctic air pollution: New insights from POLARCAT-IPY. *Bulletin of the American Meteorological Society*, 95(12):1873–1895, 2014.
- K. S. Law, A. Roiger, J. L. Thomas, L. Marelle, J. Raut, S. Dalsøren, J. Fuglestad, P. Tuccella, B. Weinzierl, and H. Schlager. Local Arctic air pollution: Sources and impacts. *Ambio*, 46(S3):453–463, 2017.
- Z. D. Lawrence, J. Perlwitz, A. H. Butler, G. L. Manney, P. A. Newman, S. H. Lee, and E. R. Nash. The remarkably strong Arctic stratospheric polar vortex of winter 2020: Links to record-breaking Arctic oscillation and ozone loss. *Journal of Geophysical Research: Atmospheres*, 125(22):e2020JD033271, 2020.
- B. Lebegue, M. Schmidt, M. Ramonet, B. Wastine, C. Yver Kwok, O. Laurent, S. Belviso, A. Guemri, C. Philippon, J. Smith, and S. Conil. Comparison of nitrous oxide (N₂O) analyzers for high-precision measurements of atmospheric mole fractions. *Atmospheric Measurement Techniques*, 9(3):1221–1238, 2016.
- C. Leck, E. K. Bigg, D. S. Covert, J. Heintzenberg, W. Maenhaut, E. D. Nilsson, and A. Wiedensohler. Overview of the atmospheric research program during the International Arctic Ocean Expedition of 1991 (IAOE-91) and its scientific results. *Tellus B*, 48(2):136–155, 1996.
- C. Leck, E. D. Nilsson, E. K. Bigg, and L. Bäcklin. Atmospheric program on the Arctic Ocean Expedition 1996

- (AOE-96): An overview of scientific goals, experimental approach, and instruments. *Journal of Geophysical Research: Atmospheres*, 106(D23):32051–32067, 2001.
- R. Lei, B. Cheng, M. Hoppmann, and G. Zuo. Snow depth and sea ice thickness derived from the measurements of SIMBA buoy 2019T69, 2021. doi: 10.1594/PANGAEA.938235.
- J. Lelieveld and F. J. Dentener. What controls tropospheric ozone? *Journal of Geophysical Research: Atmospheres*, 105(D3):3531–3551, 2000.
- H. Levy, L. W. Horowitz, M. D. Schwarzkopf, Y. Ming, J.-C. Golaz, V. Naik, and V. Ramaswamy. The roles of aerosol direct and indirect effects in past and future climate change. *Journal of Geophysical Research: Atmospheres*, 118(10):4521–4532, 2013.
- X. Li, S. K. Krueger, C. Strong, G. G. Mace, and S. Benson. Midwinter Arctic leads form and dissipate low clouds. *Nature Communications*, 11(1):1–8, 2020.
- J.-T. Lin, D. Youn, X.-Z. Liang, and D. J. Wuebbles. Global model simulation of summertime US ozone diurnal cycle and its sensitivity to PBL mixing, spatial resolution, and emissions. *Atmospheric Environment*, 42(36):8470–8483, 2008.
- M. Lin, T. Holloway, T. Oki, D. G. Streets, and A. Richter. Multi-scale model analysis of boundary layer ozone over East Asia. *Atmospheric Chemistry and Physics*, 9(10):3277–3301, 2009.
- M. Lin, L. W. Horowitz, R. Payton, A. M. Fiore, and G. Tonnesen. US surface ozone trends and extremes from 1980 to 2014: quantifying the roles of rising Asian emissions, domestic controls, wildfires, and climate. *Atmospheric Chemistry and Physics*, 17(4):2943–2970, 2017.
- M. Lin, S. Malyshev, E. Shevliakova, F. Paulot, L. W. Horowitz, S. Fares, T. N. Mikkelsen, and L. Zhang. Sensitivity of ozone dry deposition to ecosystem-atmosphere interactions: A critical appraisal of observations and simulations. *Global Biogeochemical Cycles*, 33(10):1264–1288, 2019.
- R. Lindsay, M. Wensnahan, A. Schweiger, and J. Zhang. Evaluation of seven different atmospheric reanalysis products in the Arctic. *Journal of Climate*, 27(7):2588–2606, 2014.
- J. Liu, J. A. Curry, H. Wang, M. Song, and R. M. Horton. Impact of declining Arctic sea ice on winter snowfall. *Proceedings of the National Academy of Sciences*, 109(11):4074–4079, 2012.
- Y. Liu and J. R. Key. Assessment of Arctic cloud cover anomalies in atmospheric reanalysis products using satellite data. *Journal of Climate*, 29(17):6065–6083, 2016.
- D. C. Loades, M. Yang, T. G. Bell, A. R. Vaughan, R. J. Pound, S. Metzger, J. D. Lee, and L. J. Carpenter. Ozone deposition to a coastal sea: comparison of eddy covariance observations with reactive air–sea exchange models. *Atmospheric Measurement Techniques*, 13(12):6915–6931, 2020.
- M. Lonardi, C. Pilz, E. F. Akansu, S. Dahlke, U. Egerer, A. Ehrlich, H. Griesche, A. J. Heymsfield, B. Kirbus, C. G. Schmitt, M. D. Shupe, H. Siebert, B. Wehner, and M. Wendisch. Tethered balloon-borne profile measurements of atmospheric properties in the cloudy atmospheric boundary layer over the Arctic sea ice during MOSAiC: Overview and first results. *Elem Sci Anth*, 10(1):000120, 2022.
- X. Lu, L. Zhang, and L. Shen. Meteorology and climate influences on tropospheric ozone: a review of natural sources, chemistry, and transport patterns. *Current Pollution Reports*, 5(4):238–260, 2019.
- R. M. Lucas, A. J. McMichael, B. K. Armstrong, and W. T. Smith. Estimating the global disease burden due to ultraviolet radiation exposure. *International journal of epidemiology*, 37(3):654–667, 2008.
- A. K. Luhr, I. E. Galbally, M. T. Woodhouse, and M. Thatcher. An improved parameterisation of ozone dry

- deposition to the ocean and its impact in a global climate-chemistry model. *Atmospheric Chemistry and Physics*, 17(5):3749, 2017.
- A. K. Luhar, M. T. Woodhouse, and I. E. Galbally. A revised global ozone dry deposition estimate based on a new two-layer parameterisation for air-sea exchange and the multi-year MACC composition reanalysis. *Atmospheric Chemistry & Physics*, 18(6), 2018.
- R. Luo, Q. Ding, I. Baxter, X. Chen, Z. Wu, M. Bushuk, and H. Wang. Uncertain role of clouds in shaping summertime atmosphere-sea ice connections in reanalyses and CMIP6 models. *Climate Dynamics*, pages 1–22, 2023.
- P.-L. Ma, P. J. Rasch, J. D. Fast, R. C. Easter, W. I. Gustafson, X. Liu, S. J. Ghan, and B. Singh. Assessing the CAM5 physics suite in the WRF-Chem model: Implementation, resolution sensitivity, and a first evaluation for a regional case study. *Geoscientific Model Development*, 7(3):755–778, 2014.
- S. M. MacDonald, J. C. Gómez Martín, R. Chance, S. Warriner, A. Saiz-Lopez, L. J. Carpenter, and J. M. C. Plane. A laboratory characterisation of inorganic iodine emissions from the sea surface: dependence on oceanic variables and parameterisation for global modelling. *Atmospheric Chemistry and Physics*, 14(11):5841–5852, 2014.
- M. Macias-Fauria, B. C. Forbes, P. Zetterberg, and T. Kumpula. Eurasian Arctic greening reveals teleconnections and the potential for structurally novel ecosystems. *Nature climate change*, 2(8):613–618, 2012.
- L. Magi, F. Schweitzer, C. Pallares, S. Cherif, P. Mirabel, and C. George. Investigation of the uptake rate of ozone and methyl hydroperoxide by water surfaces. *The Journal of Physical Chemistry A*, 101(27):4943–4949, 1997.
- B. Männel, F. Zus, G. Dick, S. Glaser, M. Semmling, K. Balidakis, J. Wickert, M. Maturilli, S. Dahlke, and H. Schuh. GNSS-based water vapor estimation and validation during the MOSAiC expedition. *Atmospheric Measurement Techniques*, 14(7):5127–5138, 2021.
- G. L. Manney, N. J. Livesey, M. L. Santee, L. Froidevaux, A. Lambert, Z. D. Lawrence, L. F. Millán, J. L. Neu, W. G. Read, M. J. Schwartz, and R. A. Fuller. Record-low Arctic stratospheric ozone in 2020: MLS observations of chemical processes and comparisons with previous extreme winters. *Geophysical Research Letters*, 47(16):e2020GL089063, 2020.
- L. Marelle, J. L. Thomas, J.-C. Raut, K. S. Law, J.-P. Jalkanen, L. Johansson, A. Roiger, H. Schlager, J. Kim, A. Reiter, and B. Weinzierl. Air quality and radiative impacts of Arctic shipping emissions in the summertime in northern Norway: from the local to the regional scale. *Atmospheric Chemistry and Physics*, 16(4):2359–2379, 2016.
- L. Marelle, J. L. Thomas, S. Ahmed, K. Tuite, J. Stutz, A. Dommergue, W. R. Simpson, M. M. Frey, and F. Baladima. Implementation and impacts of surface and blowing snow sources of Arctic bromine activation within WRF-Chem 4.1.1. *Journal of Advances in Modeling Earth Systems*, 13(8):e2020MS002391, 2021.
- G. J. Marshall, S. Kivinen, K. Jylhä, R. M. Vignols, and W. G. Rees. The accuracy of climate variability and trends across Arctic Fennoscandia in four reanalyses. *International Journal of Climatology*, 38(10):3878–3895, 2018.
- J. Marshall, J. R. Scott, K. C. Armour, J.-M. Campin, M. Kelley, and A. Romanou. The ocean’s role in the transient response of climate to abrupt greenhouse gas forcing. *Climate Dynamics*, 44(7):2287–2299, 2015.
- M. Martino, B. Lézé, A. R. Baker, and P. S. Liss. Chemical controls on ozone deposition to water. *Geophysical research letters*, 39(5), 2012.
- M. Maturilli, D. J. Holdridge, S. Dahlke, J. Graeser, A. Sommerfeld, R. Jaiser, H. Deckelmann, and A. Schulz. Initial radiosonde data from 2019-10 to 2020-09 during project MOSAiC, 2021. doi: 10.1594/PANGAEA.928656.

- M. Mauder, T. Foken, M. Aubinet, and A. Ibrom. Eddy-covariance measurements. In *Springer Handbook of Atmospheric Measurements*, pages 1485–1515. Springer, 2021.
- A. D. McGuire, L. G. Anderson, T. R. Christensen, S. Dallimore, L. Guo, D. J. Hayes, M. Heimann, T. D. Lorenson, R. W. Macdonald, and N. Roulet. Sensitivity of the carbon cycle in the Arctic to climate change. *Ecological Monographs*, 79(4):523–555, 2009.
- C. Melsheimer, G. Spreen, Y. Ye, and M. Shokr. Antarctic sea ice types from active and passive microwave remote sensing. *The Cryosphere Discussions*, pages 1–23, 2022.
- M. Michou, P. Laville, D. Serça, A. Fotiadis, P. Bouchou, and V.-H. Peuch. Measured and modeled dry deposition velocities over the ESCOMPTE area. *Atmospheric Research*, 74(1-4):89–116, 2005.
- U. Mikolajewicz, D. V. Sein, D. Jacob, T. König, R. Podzun, and T. Semmler. Simulating Arctic sea ice variability with a coupled regional atmosphere-ocean-sea ice model. *Meteorologische Zeitschrift*, 14(6):793–800, 2005.
- P. S. Monks. A review of the observations and origins of the spring ozone maximum. *Atmospheric environment*, 34(21):3545–3561, 2000.
- P. S. Monks, G. Salisbury, G. Holland, S. A. Penkett, and G. P. Ayers. A seasonal comparison of ozone photochemistry in the remote marine boundary layer. *Atmospheric Environment*, 34(16):2547–2561, 2000.
- A. M. Moore and H. B. Gordon. An investigation of climate drift in a coupled atmosphere-ocean-sea ice model. *Climate dynamics*, 10(1):81–95, 1994.
- S. Morimoto, D. Goto, S. Murayama, R. Fujita, Y. Tohjima, S. Ishidoya, T. Machida, Y. Inai, P. K. Patra, S. Maksyutov, A. Ito, and S. Aoki. Spatio-temporal variations of the atmospheric greenhouse gases and their sources and sinks in the Arctic region. *Polar Science*, 27:100553, 2021.
- S. Morin, J. Erbland, J. Savarino, F. Domine, J. Bock, U. Friess, H.-W. Jacobi, H. Sihler, and J. M. F. Martins. An isotopic view on the connection between photolytic emissions of NO_x from the Arctic snowpack and its oxidation by reactive halogens. *Journal of Geophysical Research: Atmospheres*, 117(D14):D00R08, 2012.
- J. Morris. The aqueous solubility of ozone—A review. *Ozone news*, 1:14–16, 1988.
- J. B. A. Muller, J. R. Dorsey, M. Flynn, M. W. Gallagher, C. J. Percival, D. E. Shallcross, A. Archibald, H. K. Roscoe, R. W. Obbard, H. M. Atkinson, J. D. Lee, S. J. Moller, and L. J. Carpenter. Energy and ozone fluxes over sea ice. *Atmospheric environment*, 47:218–225, 2012.
- R. Munro, R. Lang, D. Klaes, G. Poli, C. Retscher, R. Lindstrot, R. Huckle, A. Lacan, M. Grzegorski, A. Holdak, A. Kokhanovsky, J. Livschitz, and M. Eisinger. The GOME-2 instrument on the Metop series of satellites: instrument design, calibration, and level 1 data processing—an overview. *Atmospheric Measurement Techniques*, 9(3):1279–1301, 2016.
- K. A. Murray, L. J. Kramer, P. V. Doskey, L. Ganzeveld, B. Seok, B. van Dam, and D. Helmig. Dynamics of ozone and nitrogen oxides at Summit, Greenland. II. Simulating snowpack chemistry during a spring high ozone event with a 1-D process-scale model. *Atmospheric Environment*, 117:110–123, 2015.
- M. Nakanishi and H. Niino. An improved Mellor–Yamada level-3 model: Its numerical stability and application to a regional prediction of advection fog. *Boundary-Layer Meteorology*, 119:397–407, 2006.
- Q. T. Nguyen, M. Glasius, L. L. Sørensen, B. Jensen, H. Skov, W. Birmili, A. Wiedensohler, A. Kristensson, J. K. Nøjgaard, and A. Massling. Seasonal variation of atmospheric particle number concentrations, new particle formation and atmospheric oxidation capacity at the high Arctic site Villum Research Station, Station Nord. *Atmospheric Chemistry and Physics*, 16(17):11319–11336, 2016.

- M. Nicolaus, D. K. Perovich, G. Spreen, M. A. Granskog, L. von Albedyll, M. Angelopoulos, P. Anhaus, S. Arndt, H. J. Belter, V. Bessonov, G. Birnbaum, J. Brauchle, R. Calmer, E. Cardellach, B. Cheng, D. Clemens-Sewall, R. Dadic, E. Damm, G. de Boer, O. Demir, K. Dethloff, D. V. Divine, A. A. Fong, S. Fons, M. M. Frey, N. Fuchs, C. Gabarró, S. Gerland, H. F. Goessling, R. Gradinger, J. Haapala, C. Haas, J. Hamilton, H.-R. Hannula, S. Hendricks, A. Herber, C. Heuzé, M. Hoppmann, K. V. Høyland, M. Huntemann, J. K. Hutchings, B. Hwang, P. Itkin, H.-W. Jacobi, M. Jaggi, A. Jutila, L. Kaleschke, C. Katlein, N. Kolabutin, D. Krampe, S. S. Kristensen, T. Krumpfen, N. Kurtz, A. Lampert, B. A. Lange, R. Lei, B. Light, F. Linhardt, G. E. Liston, B. Loose, A. R. Macfarlane, M. Mahmud, I. O. Matero, S. Maus, A. Morgenstern, R. Naderpour, V. Nandan, A. Niubom, M. Oggier, N. Oppelt, F. Pätzold, C. Perron, T. Petrovsky, R. Pirazzini, C. Polashenski, B. Rabe, I. A. Raphael, J. Regnery, M. Rex, R. Ricker, K. Riemann-Campe, A. Rinke, J. Rohde, E. Salganik, R. K. Scharien, M. Schiller, M. Schneebeli, M. Semmling, E. Shimanchuk, M. D. Shupe, M. M. Smith, V. Smolyanitsky, V. Sokolov, T. Stanton, J. Stroeve, L. Thielke, A. Timofeeva, R. T. Tonboe, A. Tavri, M. Tsamados, D. N. Wagner, D. Watkins, M. Webster, and M. Wendisch. Overview of the MOSAiC expedition: Snow and sea ice. *Elementa: Science of the Anthropocene*, 10(1):000046, 02 2022.
- D. Nomura, Y. Kawaguchi, A. L. Webb, Y. Li, M. Dall’osto, K. Schmidt, E. S. Droste, E. J. Chamberlain, N. Kolabutin, E. Shimanchuk, M. Hoppmann, M. R. Gallagher, H. Meyer, M. Mellat, D. Bauch, C. Gabarró, M. M. Smith, J. Inoue, E. Damm, and B. Delille. Meltwater layer dynamics in a central Arctic lead: Effects of lead width, re-freezing, and mixing during late summer. *Elementa: Science of the Anthropocene*, 11(1), 2023.
- D. Notz. Arctic sea ice in CMIP6. *Geophysical Research Letters*, 47(10):e2019GL086749, 2020.
- A. Nummelin, M. Ilicak, C. Li, and L. H. Smedsrud. Consequences of future increased Arctic runoff on Arctic Ocean stratification, circulation, and sea ice cover. *Journal of Geophysical Research: Oceans*, 121(1):617–637, 2016.
- M. Nuttall. *Protecting the Arctic: Indigenous peoples and cultural survival*. Routledge, 2005.
- D. Nuvolone, D. Petri, and F. Voller. The effects of ozone on human health. *Environmental Science and Pollution Research*, 25(9):8074–8088, 2018.
- F. Ogawa, N. Keenlyside, Y. Gao, T. Koenigk, S. Yang, L. Suo, T. Wang, G. Gastineau, T. Nakamura, H. N. Cheung, N.-E. Omrani, J. Ukita, and V. Semenov. Evaluating impacts of recent Arctic sea ice loss on the northern hemisphere winter climate change. *Geophysical Research Letters*, 45(7):3255–3263, 2018.
- I.-B. Oh, D. W. Byun, H.-C. Kim, S. Kim, and B. Cameron. Modeling the effect of iodide distribution on ozone deposition to seawater surface. *Atmospheric Environment*, 42(19):4453–4466, 2008.
- K. Ohneiser, A. Ansmann, A. Chudnovsky, R. Engelmann, C. Ritter, I. Veselovskii, H. Baars, H. Gebauer, H. Griesche, M. Radenz, J. Hofer, D. Althausen, S. Dahlke, and M. Maturilli. The unexpected smoke layer in the High Arctic winter stratosphere during MOSAiC 2019–2020. *Atmospheric Chemistry and Physics*, 21(20):15783–15808, 2021.
- S. J. Oltmans, A. S. Lefohn, D. Shadwick, J. M. Harris, H. E. Scheel, I. Galbally, D. W. Tarasick, B. J. Johnson, E.-G. Brunke, H. Claude, G. Zeng, S. Nichol, F. Schmidlin, J. Davies, E. Cuevas, A. Redondas, H. Naoe, T. Nakano, and T. Kawasato. Recent tropospheric ozone changes—A pattern dominated by slow or no growth. *Atmospheric Environment*, 67:331–351, 2013.
- C. Orbe, P. A. Newman, D. W. Waugh, M. Holzer, L. D. Oman, F. Li, and L. M. Polvani. Airmass origin in the Arctic. Part I: Seasonality. *Journal of Climate*, 28(12):4997–5014, 2015.
- J. Paatero, P. Vaattovaara, M. Vestenius, O. Meinander, U. Makkonen, R. Kivi, A. Hyvärinen, E. Asmi, M. Tjernström, and C. Leck. Finnish contribution to the arctic summer cloud ocean study (ASCOS) expedition, Arctic

- Ocean 2008. *Geophysica*, 45(1-2):119–146, 2009.
- J. Padro. Summary of ozone dry deposition velocity measurements and model estimates over vineyard, cotton, grass and deciduous forest in summer. *Atmospheric Environment*, 30(13):2363–2369, 1996.
- T. Papakyriakou and L. Miller. Springtime CO₂ exchange over seasonal sea ice in the Canadian Arctic Archipelago. *Annals of Glaciology*, 52(57):215–224, 2011.
- J.-D. Paris, A. Stohl, P. Nédélec, M. Y. Arshinov, M. Panchenko, V. Shmargunov, K. S. Law, B. Belan, and P. Ciais. Wildfire smoke in the Siberian Arctic in summer: source characterization and plume evolution from airborne measurements. *Atmospheric Chemistry and Physics*, 9(23):9315–9327, 2009.
- F.-J. W. Parmentier, T. R. Christensen, L. L. Sørensen, S. Rysgaard, A. D. McGuire, P. A. Miller, and D. A. Walker. The impact of lower sea-ice extent on Arctic greenhouse-gas exchange. *Nature climate change*, 3(3):195–202, 2013.
- F. Pausata, L. Pozzoli, E. Vignati, and F. Dentener. North Atlantic Oscillation and tropospheric ozone variability in Europe: model analysis and measurements intercomparison. *Atmospheric Chemistry & Physics*, 12(14), 2012.
- F. Pedregosa, G. Varoquaux, A. Gramfort, V. Michel, B. Thirion, O. Grisel, M. Blondel, P. Prettenhofer, R. Weiss, V. Dubourg, J. Vanderplas, A. Passos, D. Cournapeau, M. Brucher, M. Perrot, and É. Duchesnay. Scikit-learn: Machine learning in Python. *the Journal of machine Learning research*, 12:2825–2830, 2011.
- S. Peng, X. Lin, R. L. Thompson, Y. Xi, G. Liu, D. Hauglustaine, X. Lan, B. Poulter, M. Ramonet, M. Sauniois, Y. Yin, Z. Zhang, B. Zheng, and P. Ciais. Wetland emission and atmospheric sink changes explain methane growth in 2020. *Nature*, 612(7940):477–482, 2022.
- D. Perovich, M. Smith, B. Light, and M. Webster. Meltwater sources and sinks for multiyear Arctic sea ice in summer. *The Cryosphere*, 15(9):4517–4525, 2021.
- D. K. Perovich and J. A. Richter-Menge. Loss of sea ice in the Arctic. *Annual review of marine science*, 1(1): 417–441, 2009.
- D. K. Perovich, E. L. Andreas, J. A. Curry, H. Eiken, C. W. Fairall, T. C. Grenfell, P. S. Guest, J. Intrieri, D. Kadko, R. W. Lindsay, M. G. McPhee, J. Morison, R. E. Moritz, C. A. Paulson, W. S. Pegau, P. Persson, R. Pinkel, J. A. Richter-Menge, T. Stanton, H. Stern, M. Sturm, W. B. Tucker III, and T. Uttal. Year on ice gives climate insights. *Eos, Transactions American Geophysical Union*, 80(41):481–486, 1999.
- P. O. G. Persson, C. W. Fairall, E. L. Andreas, P. S. Guest, and D. K. Perovich. Measurements near the Atmospheric Surface Flux Group tower at SHEBA: Near-surface conditions and surface energy budget. *Journal of Geophysical Research: Oceans*, 107(C10):SHE–21, 2002.
- A. N. Petrov, S. BurnSilver, F. S. Chapin III, G. Fondahl, J. Graybill, K. Keil, A. E. Nilsson, R. Riedlsperger, and P. Schweitzer. Arctic sustainability research: Toward a new agenda. *Polar Geography*, 39(3):165–178, 2016.
- I. Pissò, E. Sollum, H. Grythe, N. I. Kristiansen, M. Cassiani, S. Eckhardt, D. Arnold, D. Morton, R. L. Thompson, C. D. Groot Zwaartink, N. Evangelio, H. Sodemann, L. Haimberger, S. Henne, D. Brunner, J. F. Burkhart, A. Fouilloux, J. Brioude, A. Philipp, P. Seibert, and A. Stohl. The Lagrangian particle dispersion model FLEXPART version 10.4. *Geoscientific Model Development*, 12(12):4955–4997, 2019.
- F. Pithan and T. Mauritsen. Arctic amplification dominated by temperature feedbacks in contemporary climate models. *Nature geoscience*, 7(3):181–184, 2014.
- F. Pithan, G. Svensson, R. Caballero, D. Chechin, T. W. Cronin, A. M. Ekman, R. Neggers, M. D. Shupe, A. Solomon, M. Tjernström, and M. Wendisch. Role of air-mass transformations in exchange between the Arctic

- and mid-latitudes. *Nature Geoscience*, 11(11):805–812, 2018.
- F. Pithan, M. Athanase, S. Dahlke, A. Sánchez-Benítez, M. D. Shupe, A. Sledd, J. Streffing, G. Svensson, and T. Jung. Nudging allows direct evaluation of coupled climate models with in situ observations: a case study from the MOSAiC expedition. *Geoscientific Model Development*, 16(7):1857–1873, 2023.
- J. G. Porter, W. de Bruyn, S. D. Miller, and E. S. Saltzman. Air/sea transfer of highly soluble gases over coastal waters. *Geophysical Research Letters*, 47(4):no–no, 2020.
- R. J. Pound, T. Sherwen, D. Helmig, L. J. Carpenter, and M. J. Evans. Influences of oceanic ozone deposition on tropospheric photochemistry. *Atmospheric Chemistry and Physics Discussions*, pages 1–25, 2019.
- C. Prados-Roman, C. A. Cuevas, R. P. Fernandez, D. E. Kinnison, J.-F. Lamarque, and A. Saiz-Lopez. A negative feedback between anthropogenic ozone pollution and enhanced ocean emissions of iodine. *Atmospheric Chemistry and Physics*, 15(4):2215–2224, 2015.
- K. A. Pratt. Tropospheric Halogen Photochemistry in the Rapidly Changing Arctic. *Trends in Chemistry*, 1(6): 545–548, 2019.
- K. A. Pratt, K. D. Custard, P. B. Shepson, T. A. Douglas, D. Pöhler, S. General, J. Zielcke, W. R. Simpson, U. Platt, D. J. Tanner, L. G. Huey, M. Carlsen, and B. H. Stirm. Photochemical production of molecular bromine in Arctic surface snowpacks. *Nature Geoscience*, 6(5):351–356, 2013.
- M. Previdi, K. L. Smith, and L. M. Polvani. Arctic amplification of climate change: a review of underlying mechanisms. *Environmental Research Letters*, 16(9):093003, 2021.
- M. Qu, X. Pang, X. Zhao, J. Zhang, Q. Ji, and P. Fan. Estimation of turbulent heat flux over leads using satellite thermal images. *The Cryosphere*, 13(6):1565–1582, 2019.
- B. Rabe, C. Heuzé, J. Regnery, Y. Aksenov, J. Allerholt, M. Athanase, Y. Bai, C. Basque, D. Bauch, T. M. Baumann, D. Chen, S. T. Cole, L. Craw, A. Davies, E. Damm, K. Dethloff, D. V. Divine, F. Doglioni, F. Ebert, Y.-C. Fang, I. Fer, A. A. Fong, R. Gradinger, M. A. Granskog, R. Graupner, C. Haas, H. He, Y. He, M. Hoppmann, M. Janout, D. Kadko, T. Kanow, S. Karam, Y. Kawaguchi, Z. Koenig, B. Kong, R. A. Krishfield, T. Krumpen, D. Kuhlmei, I. Kuznetsov, M. Lan, G. Laukert, R. Lei, T. Li, S. Torres-Valdés, L. Lin, L. Lin, H. Liu, N. Liu, B. Loose, X. Ma, R. McKay, M. Mallet, R. D. C. Mallett, W. Maslowski, C. Mertens, V. Mohrholz, M. Muilwijk, M. Nicolaus, J. K. O’Brien, D. Perovich, J. Ren, M. Rex, N. Ribeiro, A. Rinke, J. Schaffer, I. Schuffenhauer, K. Schulz, M. D. Shupe, W. Shaw, V. Sokolov, A. Sommerfeld, G. Spreen, T. Stanton, M. Stephens, J. Su, N. Sukhikh, A. Sundfjord, K. Thomisch, S. Tippenhauer, J. M. Toole, M. Vredenburg, M. Walter, H. Wang, L. Wang, Y. Wang, M. Wendisch, J. Zhao, M. Zhou, and J. Zhu. Overview of the MOSAiC expedition: Physical oceanography. *Elementa: Science of the Anthropocene*, 10(1):00062, 02 2022.
- M. Ramonet, B. Langerock, T. Warneke, and H. J. Eskes. Validation report for the CAMS greenhouse gas global reanalysis, years 2003–2016, 2021. doi: 10.24380/y034-7672.
- M. Rantanen, A. Y. Karpechko, A. Lipponen, K. Nordling, O. Hyvärinen, K. Ruosteenoja, T. Vihma, and A. Laaksonen. The Arctic has warmed nearly four times faster than the globe since 1979. *Communications Earth & Environment*, 3(1):1–10, 2022.
- A. P. Rees, H. W. Bange, D. L. Arévalo-Martínez, Y. Artioli, D. M. Ashby, I. Brown, H. I. Campen, D. R. Clark, V. Kitidis, G. Lessin, G. A. Tarran, and C. Turley. Nitrous oxide and methane in a changing Arctic Ocean. *Ambio*, 51(2):398–410, 2022.
- D. I. Reeser, A. Jammoul, D. Clifford, M. Brigante, B. D’Anna, C. George, and D. Donaldson. Photoenhanced reaction of ozone with chlorophyll at the seawater surface. *The Journal of Physical Chemistry C*, 113(6):

- 2071–2077, 2009.
- S. Ren, X. Liang, Q. Sun, H. Yu, L. B. Tremblay, B. Lin, X. Mai, F. Zhao, M. Li, N. Liu, Z. Chen, and Y. Zhang. A fully coupled Arctic sea-ice–ocean–atmosphere model (ArcIOAM v1. 0) based on C-Coupler2: model description and preliminary results. *Geoscientific Model Development*, 14(2):1101–1124, 2021.
- M. Rex. Master track of POLARSTERN cruise PS122/1 in 1 sec resolution (zipped, 43.3 MB), 2020. doi: 10.1594/PANGAEA.924669.
- M. Rex. Master track of POLARSTERN cruise PS122/4 in 1 sec resolution (zipped, 36 MB), 2021a. doi: 10.1594/PANGAEA.926830.
- M. Rex. Master track of POLARSTERN cruise PS122/5 in 1 sec resolution (zipped, 34 MB), 2021b. doi: 10.1594/PANGAEA.926911.
- H. Richardson, S. Basu, and A. A. M. Holtslag. Improving stable boundary-layer height estimation using a stability-dependent critical bulk Richardson number. *Boundary-Layer Meteorology*, 148(1):93–109, 2013.
- A. Riedel, C. Michel, M. Gosselin, and B. LeBlanc. Winter–spring dynamics in sea-ice carbon cycling in the coastal Arctic Ocean. *Journal of Marine Systems*, 74(3-4):918–932, 2008.
- M. Rigby, S. A. Montzka, R. G. Prinn, J. W. C. White, D. Young, S. O’Doherty, M. F. Lunt, A. L. Ganesan, A. J. Manning, P. G. Simmonds, P. K. Salameh, C. M. Harth, J. Mühle, R. F. Weiss, P. J. Fraser, L. P. Steele, P. B. Krummel, A. McCulloch, and S. Park. Role of atmospheric oxidation in recent methane growth. *Proceedings of the National Academy of Sciences*, 114(21):5373–5377, 2017.
- A. Rinke, K. Dethloff, J. J. Cassano, J. H. Christensen, J. A. Curry, P. Du, E. Girard, J.-E. Haugen, D. Jacob, C. G. Jones, M. Koltzow, R. Laprise, A. H. Lynch, S. Pfeifer, M. C. Serreze, M. J. Shaw, M. Tjernström, K. Wyser, and M. Žagar. Evaluation of an ensemble of Arctic regional climate models: spatiotemporal fields during the SHEBA year. *Climate dynamics*, 26:459–472, 2006.
- A. Rinke, J. J. Cassano, E. N. Cassano, R. Jaiser, and D. Handorf. Meteorological conditions during the MOSAiC expedition: Normal or anomalous? *Elementa: Science of the Anthropocene*, 9(1):00023, 2021.
- M. J. Roberts, A. Baker, E. W. Blockley, D. Calvert, A. Coward, H. T. Hewitt, L. C. Jackson, T. Kuhlbrodt, P. Mathiot, C. D. Roberts, R. Schiemann, J. Seddon, B. Vannière, and P. L. Vidale. Description of the resolution hierarchy of the global coupled HadGEM3-GC3. 1 model as used in CMIP6 HighResMIP experiments. *Geoscientific Model Development*, 12(12):4999–5028, 2019.
- G. H. Roe, N. Feldl, K. C. Armour, Y.-T. Hwang, and D. M. W. Frierson. The remote impacts of climate feedbacks on regional climate predictability. *Nature Geoscience*, 8(2):135–139, 2015.
- V. E. Romanovsky, D. S. Drozdov, N. G. Oberman, G. V. Malkova, A. L. Kholodov, S. S. Marchenko, N. G. Moskalenko, D. O. Sergeev, N. G. Ukraintseva, A. A. Abramov, D. A. Gilichinsky, and A. A. Vasiliev. Thermal state of permafrost in Russia. *Permafrost and Periglacial Processes*, 21(2):136–155, 2010.
- J. H. Rydsaa, R. G. Graverson, T. I. H. Heiskanen, and P. J. Stoll. Changes in atmospheric latent energy transport into the Arctic: Planetary versus synoptic scales. *Quarterly Journal of the Royal Meteorological Society*, 147(737):2281–2292, 2021.
- Y.-H. Ryu and S.-K. Min. Long-term evaluation of atmospheric composition reanalyses from CAMS, TCR-2, and MERRA-2 over South Korea: Insights into applications, implications, and limitations. *Atmospheric Environment*, 246:118062, 2021.
- R. Sander, A. Kerkweg, P. Jöckel, and J. Lelieveld. The new comprehensive atmospheric chemistry module

- MECCA. *Atmospheric Chemistry and Physics*, 5(2):445–450, 2005.
- I. Sandu, A. Beljaars, P. Bechtold, T. Mauritsen, and G. Balsamo. Why is it so difficult to represent stably stratified conditions in numerical weather prediction (NWP) models? *Journal of Advances in Modeling Earth Systems*, 5(2):117–133, 2013.
- G. Sarwar, D. Kang, K. Foley, D. Schwede, B. Gantt, and R. Mathur. Examining ozone deposition over seawater. *Atmospheric Environment*, 141:255–262, 2016.
- H. Savijärvi. High-resolution simulations of the night-time stable boundary layer over snow. *Quarterly Journal of the Royal Meteorological Society*, 140(680):1121–1128, 2014.
- M. Schaap, R. M. Timmermans, M. Roemer, G. Boersen, P. Builtjes, F. Sauter, G. Velders, and J. Beck. The LOTOS–EUROS model: description, validation and latest developments. *International Journal of Environment and Pollution*, 32(2):270–290, 2008.
- H. Schaefer. On the causes and consequences of recent trends in atmospheric methane. *Current Climate Change Reports*, 5(4):259–274, 2019.
- J. Schmale, S. R. Arnold, K. S. Law, T. Thorp, S. Anenberg, W. R. Simpson, J. Mao, and K. A. Pratt. Local Arctic air pollution: A neglected but serious problem. *Earth’s Future*, 6(10):1385–1412, 2018.
- M. G. Schultz, S. Schröder, O. Lyapina, O. R. Cooper, I. Galbally, I. Petropavlovskikh, E. von Schneidmesser, H. Tanimoto, Y. Elshorbany, M. Naja, R. J. Seguel, U. Dauert, P. Eckhardt, S. Feigenspan, M. Fiebig, A.-G. Hjellbrekke, Y.-D. Hong, P. C. Kjeld, H. Koide, G. Lear, D. Tarasick, M. Ueno, M. Wallasch, D. Baumgardner, M.-T. Chuang, R. Gillett, M. Lee, S. Molloy, R. Moolla, T. Wang, K. Sharps, J. A. Adame, G. Ancellet, F. Apadula, P. Artaxo, M. E. Barlasina, M. Bogucka, P. Bonasoni, L. Chang, A. Colomb, E. Cuevas-Agulló, M. Cupeiro, A. Degorska, A. Ding, M. Fröhlich, M. Frolova, H. Gadhavi, F. Gheusi, S. Gilge, M. Y. Gonzalez, V. Gros, S. H. Hamad, D. Helmig, D. Henriques, O. Hermansen, R. Holla, J. Hueber, U. Im, D. A. Jaffe, N. Komala, D. Kubistin, K.-S. Lam, T. Laurila, H. Lee, I. Levy, C. Mazzoleni, L. R. Mazzoleni, A. McClure-Begley, M. Mohamad, M. Murovec, M. Navarro-Comas, F. Nicodim, D. Parrish, K. A. Read, N. Reid, L. Ries, P. Saxena, J. J. Schwab, Y. Scorgie, I. Senik, P. Simmonds, V. Sinha, A. I. Skorokhod, G. Spain, W. Spangl, R. Spoor, S. R. Springston, K. Steer, M. Steinbacher, E. Suharguniyawan, P. Torre, T. Trickl, L. Weili, R. Weller, X. Xiaobin, L. Xue, and M. Zhiqiang. Tropospheric Ozone Assessment Report: Database and metrics data of global surface ozone observations. *Elementa: Science of the Anthropocene*, 5, 2017.
- J. Sedlar, M. Tjernström, A. Rinke, A. Orr, J. Cassano, X. Fettweis, G. Heinemann, M. Seefeldt, A. Solomon, H. Matthes, T. Phillips, and S. Webster. Confronting Arctic troposphere, clouds, and surface energy budget representations in regional climate models with observations. *Journal of Geophysical Research: Atmospheres*, 125(6):e2019JD031783, 2020.
- I. P. Semiletov, I. I. Pipko, I. Repina, and N. E. Shakhova. Carbonate chemistry dynamics and carbon dioxide fluxes across the atmosphere–ice–water interfaces in the Arctic Ocean: Pacific sector of the Arctic. *Journal of Marine Systems*, 66(1-4):204–226, 2007.
- C. Senff, J. Bösenberg, G. Peters, and T. Schaberl. Remote sensing of turbulent ozone fluxes and the ozone budget in the convective boundary layer with DIAL and radar-RASS: a case study. *Contributions to Atmospheric Physics*, 69:161–176, 1996.
- S. Seo, A. Richter, A.-M. Blechschmidt, I. Bougoudis, and J. P. Burrows. First high-resolution BrO column retrievals from TROPOMI. *Atmospheric Measurement Techniques*, 12(5):2913–2932, 2019.
- B. Seok, D. Helmig, L. Ganzeveld, M. W. Williams, and C. S. Vogel. Dynamics of nitrogen oxides and ozone

- above and within a mixed hardwood forest in northern Michigan. *Atmospheric Chemistry and Physics*, 13(15): 7301–7320, 2013.
- M. C. Serreze and R. G. Barry. Processes and impacts of Arctic amplification: A research synthesis. *Global and planetary change*, 77(1-2):85–96, 2011.
- M. C. Serreze and J. A. Francis. The Arctic amplification debate. *Climatic change*, 76(3):241–264, 2006.
- W. R. Sessions, H. E. Fuelberg, R. A. Kahn, and D. M. Winker. An investigation of methods for injecting emissions from boreal wildfires using WRF-Chem during ARCTAS. *Atmospheric Chemistry and Physics*, 11(12):5719–5744, 2011.
- J. Shen and Z. Gao. Ozone removal on building material surface: A literature review. *Building and Environment*, 134:205–217, 2018.
- T. G. Shepherd. Effects of a warming Arctic. *Science*, 353(6303):989–990, 2016.
- T. Sherwen, R. J. Chance, L. Tinel, D. Ellis, M. J. Evans, and L. J. Carpenter. A machine learning based global sea-surface iodide distribution. *Earth System Science Data Discussions*, pages 1–40, 2019.
- M. D. Shupe and J. M. Intrieri. Cloud radiative forcing of the Arctic surface: The influence of cloud properties, surface albedo, and solar zenith angle. *Journal of climate*, 17(3):616–628, 2004.
- M. D. Shupe, V. P. Walden, E. Eloranta, T. Uttal, J. R. Campbell, S. M. Starkweather, and M. Shiobara. Clouds at Arctic atmospheric observatories. Part I: Occurrence and macrophysical properties. *Journal of Applied Meteorology and Climatology*, 50(3):626–644, 2011.
- M. D. Shupe, M. Rex, K. Dethloff, E. Damm, A. A. Fong, R. Gradingner, C. Heuzé, B. Loose, A. Makarov, W. Maslowski, M. Nicolaus, D. Perovich, B. Rabe, A. Rinke, V. Sokolov, and A. Sommerfeld. Arctic Report Card 2020: The MOSAiC expedition: A year drifting with the Arctic sea ice, 2020. doi: 10.25923/9g3v-xh92.
- M. D. Shupe, M. Rex, B. Blomquist, P. O. G. Persson, J. Schmale, T. Uttal, D. Althausen, H. Angot, S. Archer, L. Bariteau, I. Beck, J. Bilberry, S. Bucci, C. Buck, M. Boyer, Z. Brasseur, I. M. Brooks, R. Calmer, J. Cassano, V. Castro, D. Chu, D. Costa, C. J. Cox, J. Creamean, S. Crewell, S. Dahlke, E. Damm, G. de Boer, H. Deckelmann, K. Dethloff, M. Dütsch, K. Ebell, A. Ehrlich, J. Ellis, R. Engelmann, A. A. Fong, M. M. Frey, M. R. Gallagher, L. Ganzeveld, R. Gradingner, J. Graeser, V. Greenamyre, H. Griesche, S. Griffiths, J. Hamilton, G. Heinemann, D. Helmig, A. Herber, C. Heuzé, J. Hofer, T. Houchens, D. Howard, J. Inoue, H.-W. Jacobi, R. Jaiser, T. Jokinen, O. Jourdan, G. Jozef, W. King, A. Kirchgaessner, M. Klingebiel, M. Krassovski, T. Krumpfen, A. Lampert, W. Landing, T. Laurila, D. Lawrence, M. Lonardi, B. Loose, C. Lüpkes, M. Maahn, A. Macke, W. Maslowski, C. Marsay, M. Maturilli, M. Mech, S. Morris, M. Moser, M. Nicolaus, P. Ortega, J. Osborn, F. Pätzold, D. K. Perovich, T. Petäjä, C. Pilz, R. Pirazzini, K. Posman, H. Powers, K. A. Pratt, A. Preußner, L. Quéléver, M. Radenz, B. Rabe, A. Rinke, T. Sachs, A. Schulz, H. Siebert, T. Silva, A. Solomon, A. Sommerfeld, G. Spreen, M. Stephens, A. Stohl, G. Svensson, J. Uin, J. Viegas, C. Voigt, P. von der Gathen, B. Wehner, J. M. Welker, M. Wendisch, M. Werner, Z. Xie, and F. Yue. Overview of the MOSAiC expedition: Atmosphere. *Elementa: Science of the Anthropocene*, 10(1):00060, 02 2022.
- A. Z. Shvidenko and D. G. Schepaschenko. Climate change and wildfires in Russia. *Contemporary Problems of Ecology*, 6(7):683–692, 2013.
- P. Y. F. Siew, C. Li, S. P. Sobolowski, and M. P. King. Intermittency of Arctic–mid-latitude teleconnections: stratospheric pathway between autumn sea ice and the winter North Atlantic Oscillation. *Weather and Climate Dynamics*, 1(1):261–275, 2020.
- I. Silber and M. D. Shupe. Insights on sources and formation mechanisms of liquid-bearing clouds over MOSAiC

- examined from a Lagrangian framework. *Elem Sci Anth*, 10(1):000071, 2022.
- I. Simmonds. Comparing and contrasting the behaviour of Arctic and Antarctic sea ice over the 35 year period 1979–2013. *Annals of Glaciology*, 56(69):18–28, 2015.
- D. Simpson, A. Benedictow, H. Berge, R. Bergström, L. D. Emberson, H. Fagerli, C. R. Flechard, G. D. Hayman, M. Gauss, J. E. Jonson, M. E. Jenkin, A. Nyíri, C. Richter, V. S. Semeena, S. Tsyro, J. Tuovinen, Á. Valdebenito, and P. Wind. The EMEP MSC-W chemical transport model – technical description. *Atmospheric Chemistry and Physics*, 12(16):7825–7865, 2012.
- W. R. Simpson, L. Alvarez-Aviles, T. A. Douglas, M. Sturm, and F. Domine. Halogens in the coastal snow pack near Barrow, Alaska: Evidence for active bromine air-snow chemistry during springtime. *Geophysical Research Letters*, 32(4):L04811, 2005.
- W. R. Simpson, R. von Glasow, K. Riedel, P. Anderson, P. Ariya, J. Bottenheim, J. Burrows, L. J. Carpenter, U. Frieß, M. E. Goodsite, D. Heard, M. Hutterli, H.-W. Jacobi, L. Kaleschke, B. Neff, J. Plane, U. Platt, A. Richter, H. Roscoe, R. Sander, P. Shepson, J. Sodeau, A. Steffen, T. Wagner, and E. Wolff. Halogens and their role in polar boundary-layer ozone depletion. *Atmospheric Chemistry and Physics*, 7(16):4375–4418, 2007.
- W. C. Skamarock, J. B. Klemp, J. Dudhia, D. O. Gill, D. M. Barker, M. G. Duda, X.-Y. Huang, W. Wang, and J. G. Powers. A description of the advanced research WRF model version 4. *National Center for Atmospheric Research: Boulder, CO, USA*, 145:145, 2019.
- M. M. Smith, L. von Albedyll, I. A. Raphael, B. A. Lange, I. Matero, E. Salganik, M. A. Webster, M. A. Granskog, A. Fong, R. Lei, and B. Light. Quantifying false bottoms and under-ice meltwater layers beneath Arctic summer sea ice with fine-scale observations. *Elem Sci Anth*, 10(1):000116, 2022.
- E. Sofen, D. Bowdalo, and M. Evans. How to most effectively expand the global surface ozone observing network. *Atmospheric Chemistry and Physics*, 16(3):1445–1457, 2016.
- A. Solomon, M. D. Shupe, G. Svensson, N. P. Barton, Y. Batrak, E. Bazile, J. J. Day, J. D. Doyle, H. P. Frank, S. Keeley, T. Remes, and M. Tolstykh. The winter central Arctic surface energy budget: A model evaluation using observations from the MOSAiC campaign. *Elem Sci Anth*, 11(1):00104, 2023.
- S. Solomon, D. Qin, M. Manning, K. Averyt, and M. Marquis. *Climate change 2007-the physical science basis: Working group I contribution to the fourth assessment report of the IPCC*, volume 4. Cambridge university press, 2007.
- G. Spreen, L. Kaleschke, and G. Heygster. Sea ice remote sensing using AMSR-E 89-GHz channels. *Journal of Geophysical Research: Oceans*, 113(C2), 2008.
- J. Stefels, M. Steinke, S. Turner, G. Malin, and S. Belviso. Environmental constraints on the production and removal of the climatically active gas dimethylsulphide (DMS) and implications for ecosystem modelling. *Biogeochemistry*, 83(1-3):245–275, 2007.
- S. R. Stephenson, W. Wang, C. S. Zender, H. Wang, S. J. Davis, and P. J. Rasch. Climatic responses to future trans-Arctic shipping. *Geophysical Research Letters*, 45(18):9898–9908, 2018.
- H. A. M. Sterk, G.-J. Steeneveld, T. Vihma, P. S. Anderson, F. C. Bosveld, and A. A. M. Holtslag. Clear-sky stable boundary layers with low winds over snow-covered surfaces. Part 1: WRF model evaluation. *Quarterly Journal of the Royal Meteorological Society*, 141(691):2165–2184, 2015.
- D. S. Stevenson, A. Zhao, V. Naik, F. M. O'Connor, S. Tilmes, G. Zeng, L. T. Murray, W. J. Collins, P. T. Griffiths, S. Shim, L. W. Horowitz, L. T. Sentman, and L. Emmons. Trends in global tropospheric hydroxyl radical and methane lifetime since 1850 from AerChemMIP. *Atmospheric Chemistry and Physics*, 20(21):12905–12920,

- 2020.
- D. S. Stevenson, R. G. Derwent, O. Wild, and W. J. Collins. COVID-19 lockdown NO_x emission reductions can explain most of the coincident increase in global atmospheric methane. *Atmospheric Chemistry & Physics Discussions*, 2021.
- A. Stohl, B. Aamaas, M. Amann, L. H. Baker, N. Bellouin, T. K. Berntsen, O. Boucher, R. Cherian, W. Collins, N. Daskalakis, M. Dusinska, S. Eckhardt, J. S. Fuglestedt, M. Harju, C. Heyes, Ø. Hodnebrog, J. Hao, U. Im, M. Kanakidou, Z. Klimont, K. Kupiainen, K. S. Law, M. T. Lund, R. Maas, C. R. MacIntosh, G. Myhre, S. Myriokefalitakis, D. Oliv  , J. Quaas, B. Quennehen, J.-C. Raut, S. T. Rumbold, B. H. Samset, M. Schulz, Ø. Seland, K. P. Shine, R. B. Skeie, S. Wang, K. E. Yttri, and T. Zhu. Evaluating the climate and air quality impacts of short-lived pollutants. *Atmospheric Chemistry and Physics*, 15(18):10529–10566, 2015.
- J. Stroeve and D. Notz. Changing state of Arctic sea ice across all seasons. *Environmental Research Letters*, 13(10):103001, 2018.
- R. B. Stull. *An introduction to boundary layer meteorology*, volume 13. Springer Science & Business Media, 1988.
- L. Su, Z. Yuan, J. C. H. Fung, and A. K. H. Lau. A comparison of HYSPLIT backward trajectories generated from two GDAS datasets. *Science of the Total Environment*, 506:527–537, 2015.
- W. F. Swanson, C. D. Holmes, W. R. Simpson, K. Confer, L. Marelle, J. L. Thomas, L. Jaegl  , B. Alexander, S. Zhai, Q. Chen, X. Wang, and T. Sherwen. Comparison of model and ground observations finds snowpack and blowing snow aerosols both contribute to Arctic tropospheric reactive bromine. *Atmospheric Chemistry and Physics*, 22(22):14467–14488, 2022.
- T. Takahashi, S. C. Sutherland, R. Wanninkhof, C. Sweeney, R. A. Feely, D. W. Chipman, B. Hales, G. Friederich, F. Chavez, C. Sabine, A. Watson, D. C. E. Bakker, U. Schuster, N. Metzl, H. Yoshikawa-Inoue, M. Ishii, T. Midorikawa, Y. Nojiri, A. K  rtzinger, T. Steinhoff, M. Hoppema, J. Olafsson, T. S. Arnarson, B. Tilbrook, T. Johannessen, A. Olsen, R. Bellerby, C. S. Wong, B. Delille, N. R. Bates, and H. J. de Baar. Climatological mean and decadal change in surface ocean pCO_2 , and net sea–air CO_2 flux over the global oceans. *Deep Sea Research Part II: Topical Studies in Oceanography*, 56(8-10):554–577, 2009.
- G. Tang, X. Zhu, J. Xin, B. Hu, T. Song, Y. Sun, J. Zhang, L. Wang, M. Cheng, N. Chao, L. Kong, X. Li, and Y. Wang. Modelling study of boundary-layer ozone over northern China-Part I: Ozone budget in summer. *Atmospheric Research*, 187:128–137, 2017.
- D. Tarasick, I. E. Galbally, O. R. Cooper, M. G. Schultz, G. Ancellet, T. Leblanc, T. J. Wallington, J. Ziemke, X. Liu, M. Steinbacher, J. Staehelin, C. Vigouroux, J. W. Hannigan, O. Garc  a, G. Foret, P. Zanis, E. Weatherhead, I. Petropavlovskikh, H. Worden, M. Osman, J. Liu, K.-L. Chang, A. Gaudel, M. Lin, M. Granados-Mu  oz, A. M. Thompson, S. J. Oltmans, J. Cuesta, G. Dufour, V. Thouret, B. Hassler, T. Trickl, and J. L. Neu. Tropospheric Ozone Assessment Report: Tropospheric ozone from 1877 to 2016, observed levels, trends and uncertainties. *Elementa: Science of the Anthropocene*, 7, 2019.
- N. Theys, M. van Roozendaal, F. Hendrick, X. Yang, I. de Smedt, A. Richter, M. Begoin, Q. Errera, P. V. Johnston, K. Kreher, and M. de Mazi  re. Global observations of tropospheric BrO columns using GOME-2 satellite data. *Atmospheric Chemistry and Physics*, 11(4):1791–1811, 2011.
- L. Thielke, M. Huntemann, S. Hendricks, A. Jutila, R. Ricker, and G. Spreen. Sea ice surface temperatures from helicopter-borne thermal infrared imaging during the MOSAiC expedition. *Scientific Data*, 9(1):364, 2022.
- D. N. Thomas. *Arctic ecology*. John Wiley & Sons, 2020.
- J. L. Thomas, J. Stutz, B. Lefer, L. G. Huey, K. Toyota, J. E. Dibb, and R. von Glasow. Modeling chemistry in and

- above snow at Summit, Greenland – Part 1: Model description and results. *Atmospheric Chemistry and Physics*, 11(10):4899–4914, 2011.
- C. R. Thompson, P. B. Shepson, J. Liao, L. G. Huey, C. Cantrell, F. Flocke, and J. Orlando. Bromine atom production and chain propagation during springtime Arctic ozone depletion events in Barrow, Alaska. *Atmospheric Chemistry and Physics*, 17(5):3401, 2017.
- G. Thompson, M. Tewari, K. Ikeda, S. Tessendorf, C. Weeks, J. Otkin, and F. Kong. Explicitly-coupled cloud physics and radiation parameterizations and subsequent evaluation in WRF high-resolution convective forecasts. *Atmospheric Research*, 168:92–104, 2016.
- B. F. Thornton, M. C. Geibel, P. M. Crill, C. Humborg, and C.-M. Mörrh. Methane fluxes from the sea to the atmosphere across the Siberian shelf seas. *Geophysical Research Letters*, 43(11):5869–5877, 2016.
- B. F. Thornton, J. Prytherch, K. Andersson, I. M. Brooks, D. Salisbury, M. Tjernström, and P. M. Crill. Shipborne eddy covariance observations of methane fluxes constrain Arctic sea emissions. *Science advances*, 6(5):eaay7934, 2020.
- M.-L. Timmermans, J. Toole, and R. Krishfield. Warming of the interior Arctic Ocean linked to sea ice losses at the basin margins. *Science advances*, 4(8):eaat6773, 2018.
- M. Tjernström. The summer Arctic boundary layer during the Arctic Ocean Experiment 2001 (AOE-2001). *Boundary-Layer Meteorology*, 117:5–36, 2005.
- M. Tjernström, C. E. Birch, I. M. Brooks, M. D. Shupe, P. O. G. Persson, J. Sedlar, T. Mauritsen, C. Leck, J. Paatero, M. Szczodrak, and C. R. Wheeler. Meteorological conditions in the central Arctic summer during the Arctic Summer Cloud Ocean Study (ASCOS). *Atmospheric Chemistry and Physics*, 12(15):6863–6889, 2012.
- M. Tjernström, C. Leck, C. E. Birch, J. W. Bottenheim, B. J. Brooks, I. M. Brooks, L. Bäcklin, R. Y.-W. Chang, G. de Leeuw, L. Di Liberto, S. de la Rosa, E. Granath, M. Graus, A. Hansel, J. Heintzenberg, A. Held, A. Hind, P. Johnston, J. Knulst, M. Martin, P. A. Matrai, T. Mauritsen, M. Müller, S. J. Norris, M. V. Orellana, D. A. Orsini, J. Paatero, P. O. G. Persson, Q. Gao, C. Rauschenberg, Z. Ristovski, J. Sedlar, M. D. Shupe, B. Sierau, A. Sirevaag, S. Sjogren, O. Stetzer, E. Swietlicki, M. Szczodrak, P. Vaattovaara, N. Wahlberg, M. Westberg, and C. R. Wheeler. The arctic summer cloud ocean study (ASCOS): Overview and experimental design. *Atmospheric Chemistry and Physics*, 14(6):2823–2869, 2014.
- M. Tjernström, M. D. Shupe, I. M. Brooks, P. Achtert, J. Prytherch, and J. Sedlar. Arctic summer air mass transformation, surface inversions, and the surface energy budget. *Journal of Climate*, 32(3):769–789, 2019.
- M. Tjernström, G. Svensson, L. Magnusson, I. M. Brooks, J. Prytherch, J. Vüllers, and G. Young. Central Arctic weather forecasting: Confronting the ECMWF IFS with observations from the Arctic Ocean 2018 expedition. *Quarterly Journal of the Royal Meteorological Society*, 147(735):1278–1299, 2021.
- C. Torrence and G. P. Compo. A practical guide to wavelet analysis. *Bulletin of the American Meteorological society*, 79(1):61–78, 1998.
- K. Toyota, J. C. McConnell, R. M. Staebler, and A. P. Dastoor. Air–snowpack exchange of bromine, ozone and mercury in the springtime Arctic simulated by the 1-D model PHANTAS – Part 1: In-snow bromine activation and its impact on ozone. *Atmospheric Chemistry and Physics*, 14(8):4101–4133, 2014.
- K. Toyota, A. P. Dastoor, and A. Ryzhkov. Parameterization of gaseous dry deposition in atmospheric chemistry models: Sensitivity to aerodynamic resistance formulations under statically stable conditions. *Atmospheric Environment*, 147:409–422, 2016.
- A. J. Turner, C. Frankenberg, and E. A. Kort. Interpreting contemporary trends in atmospheric methane. *Proceedings*

- of the *National Academy of Sciences*, 116(8):2805–2813, 2019.
- A. Ukhov, S. Mostamandi, A. Da Silva, J. Flemming, Y. Alshehri, I. Shevchenko, and G. Stenchikov. Assessment of natural and anthropogenic aerosol air pollution in the Middle East using MERRA-2, CAMS data assimilation products, and high-resolution WRF-Chem model simulations. *Atmospheric Chemistry and Physics*, 20(15): 9281–9310, 2020.
- M. Val Martin, C. L. Heald, and S. R. Arnold. Coupling dry deposition to vegetation phenology in the Community Earth System Model: Implications for the simulation of surface O₃. *Geophysical Research Letters*, 41(8): 2988–2996, 2014.
- B. van Dam, D. Helmig, C. Toro, P. Doskey, L. Kramer, K. Murray, L. Ganzeveld, and B. Seok. Dynamics of ozone and nitrogen oxides at Summit, Greenland: I. Multi-year observations in the snowpack. *Atmospheric Environment*, 123:268–284, 2015.
- B. van Dam, D. Helmig, P. V. Doskey, and S. J. Oltmans. Summertime surface O₃ behavior and deposition to tundra in the Alaskan Arctic. *Journal of Geophysical Research: Atmospheres*, 121(13):8055–8066, 2016.
- S. J. A. van der Linden, B. J. H. van de Wiel, I. Petenko, C. C. van Heerwaarden, P. Baas, and H. J. Jonker. A Businger mechanism for intermittent bursting in the stable boundary layer. *Journal of the Atmospheric Sciences*, 77(10):3343–3360, 2020.
- D. Vikhamar-Schuler, K. Isaksen, J. E. Haugen, H. Tømmervik, B. Luks, T. V. Schuler, and J. W. Bjerke. Changes in winter warming events in the Nordic Arctic Region. *Journal of climate*, 29(17):6223–6244, 2016.
- W. F. Vincent. Arctic climate change: Local impacts, global consequences, and policy implications. *The Palgrave handbook of Arctic policy and politics*, pages 507–526, 2020.
- W. F. Vincent, J. Boike, V. R. Buschman, F. Bouchard, S. Zolkos, G. H. Henry, B. B. Wolfe, and J. Canário. Terrestrial geosystems, ecosystems, and human systems in the fast-changing Arctic: research themes and connections to the Arctic Ocean. *Arctic Science*, 9(2):258–265, 2023.
- A. J. Visser, K. F. Boersma, L. N. Ganzeveld, and M. C. Krol. European NO_x emissions in WRF-Chem derived from OMI: impacts on summertime surface ozone. *Atmospheric Chemistry and Physics*, 19(18):11821–11841, 2019.
- B. Vogel and R. C. Bullock. Institutions, indigenous peoples, and climate change adaptation in the Canadian Arctic. *GeoJournal*, 86(6):2555–2572, 2021.
- P. von der Gathen and M. Maturilli. Ozone sonde profiles during MOSAiC Leg 1-2-3, 2020. doi: 10.1594/PANGAEA.919538.
- P. von der Gathen and M. Maturilli. Ozone sonde profiles during MOSAiC Leg 4-5, 2022. doi: 10.1594/PANGAEA.941294.
- D. A. Walker, M. K. Reynolds, F. J. A. Daniëls, E. Einarsson, A. Elvebakk, W. A. Gould, A. E. Katenin, S. S. Kholod, C. J. Markon, E. S. Melnikov, N. G. Moskalenko, S. S. Talbot, and B. A. Yurtsev. The circumpolar Arctic vegetation map. *Journal of Vegetation Science*, 16(3):267–282, 2005.
- C. Wang, R. M. Graham, K. Wang, S. Gerland, and M. A. Granskog. Comparison of ERA5 and ERA-Interim near-surface air temperature, snowfall and precipitation over Arctic sea ice: effects on sea ice thermodynamics and evolution. *The Cryosphere*, 13(6):1661–1679, 2019.
- Y. Wang, Y.-F. Ma, H. Eskes, A. Inness, J. Flemming, and G. P. Brasseur. Evaluation of the CAMS global atmospheric trace gas reanalysis 2003–2016 using aircraft campaign observations. *Atmospheric Chemistry and*

- Physics*, 20(7):4493–4521, 2020.
- T. T. Warner. Quality assurance in atmospheric modeling. *Bulletin of the American Meteorological Society*, 92(12):1601–1610, 2011.
- M. Watson, D. M. Holman, and M. Maguire-Eisen. Ultraviolet radiation exposure and its impact on skin cancer risk. *Seminars in Oncology Nursing*, 32(3):241–254, 2016.
- N. Weigum, N. Schutgens, and P. Stier. Effect of aerosol subgrid variability on aerosol optical depth and cloud condensation nuclei: implications for global aerosol modelling. *Atmospheric Chemistry and Physics*, 16(21):13619–13639, 2016.
- F. Wentz and T. Meissner. AMSR-E/Aqua Daily L3 Global Ascending/Descending .25x.25 deg Ocean Grids, Version 2., 2004.
- M. L. Wesely. Parameterization of surface resistances to gaseous dry deposition in regional-scale numerical models. *Atmospheric Environment (1967)*, 23(6):1293–1304, 1989.
- M. L. Wesely and B. B. Hicks. A review of the current status of knowledge on dry deposition. *Atmospheric environment*, 34(12-14):2261–2282, 2000.
- C. H. Whaley, R. Mahmood, K. von Salzen, B. Winter, S. Eckhardt, S. Arnold, S. Beagley, S. Becagli, R.-Y. Chien, J. Christensen, S. M. Damani, X. Dong, K. Eleftheriadis, N. Evangeliou, G. Faluvegi, M. Flanner, J. S. Fu, M. Gauss, F. Giardi, W. Gong, J. L. Hjorth, L. Huang, U. Im, Y. Kanaya, S. Krishnan, Z. Klimont, T. Kühn, J. Langner, K. S. Law, L. Marelle, A. Massling, D. Olivíé, T. Onishi, N. Oshima, Y. Peng, D. A. Plummer, O. Popovicheva, L. Pozzoli, J.-C. Raut, M. Sand, L. N. Saunders, J. Schmale, S. Sharma, R. B. Skeie, H. Skov, F. Taketani, M. A. Thomas, R. Traversi, K. Tsigaridis, S. Tsyro, S. Turnock, V. Vitale, K. A. Walker, M. Wang, D. Watson-Parris, and T. Weiss-Gibbons. Model evaluation of short-lived climate forcers for the Arctic Monitoring and Assessment Programme: a multi-species, multi-model study. *Atmospheric Chemistry and Physics*, 22(9):5775–5828, 2022.
- C. H. Whaley, K. S. Law, J. L. Hjorth, H. Skov, S. R. Arnold, J. Langner, J. B. Pernov, G. Bergeron, I. Bourgeois, J. H. Christensen, R.-Y. Chien, M. Deushi, X. Dong, P. Effertz, G. Faluvegi, M. Flanner, J. S. Fu, M. Gauss, G. Huey, U. Im, R. Kivi, L. Marelle, T. Onishi, N. Oshima, I. Petropavlovskikh, J. Peischl, D. A. Plummer, L. Pozzoli, J.-C. Raut, T. Ryerson, R. Skeie, S. Solberg, M. A. Thomas, C. Thompson, K. Tsigaridis, S. Tsyro, S. T. Turnock, K. von Salzen, and D. W. Tarasick. Arctic tropospheric ozone: assessment of current knowledge and model performance. *Atmospheric Chemistry and Physics*, 23(1):637–661, 2023.
- O. Wild, X. Zhu, and M. J. Prather. Fast-J: Accurate simulation of in-and below-cloud photolysis in tropospheric chemical models. *Journal of Atmospheric Chemistry*, 37(3):245–282, 2000.
- I. Wohltmann, P. von der Gathen, R. Lehmann, M. Maturilli, H. Deckelmann, G. L. Manney, J. Davies, D. Tarasick, N. Jepsen, R. Kivi, N. Lyall, and M. Rex. Near-complete local reduction of Arctic stratospheric ozone by severe chemical loss in spring 2020. *Geophysical Research Letters*, 47(20):e2020GL089547, 2020.
- G. M. Wolfe, J. A. Thornton, M. McKay, and A. H. Goldstein. Forest-atmosphere exchange of ozone: sensitivity to very reactive biogenic VOC emissions and implications for in-canopy photochemistry. *Atmospheric Chemistry and Physics*, 11(15):7875–7891, 2011.
- H. M. Worden, M. N. Deeter, C. Frankenberg, M. George, F. Nichitiu, J. Worden, I. Aben, K. W. Bowman, C. Clerbaux, P. F. Coheur, A. T. J. de Laat, R. Detweiler, J. R. Drummond, D. P. Edwards, J. C. Gille, D. Hurtmans, M. Luo, S. Martínez-Alonso, S. Massie, G. Pfister, and J. X. Warner. Decadal record of satellite carbon monoxide observations. *Atmospheric Chemistry and Physics*, 13(2):837–850, 2013.

- D. L. Wu and J. N. Lee. Arctic low cloud changes as observed by MISR and CALIOP: Implication for the enhanced autumnal warming and sea ice loss. *Journal of Geophysical Research: Atmospheres*, 117(D7), 2012.
- K. Wyser, C. Jones, P. Du, E. Girard, U. Willen, J. Cassano, J. Christensen, J. A. Curry, K. Dethloff, J.-E. Haugen, D. Jacob, M. K ltzow, R. Laprise, A. Lynch, S. Pfeifer, A. Rinke, M. Serreze, M. J. Shaw, M. Tjernstr m, and M.  agar. An evaluation of Arctic cloud and radiation processes during the SHEBA year: simulation results from eight Arctic regional climate models. *Climate Dynamics*, 30:203–223, 2008.
- X. Yang, J. A. Pyle, and R. A. Cox. Sea salt aerosol production and bromine release: Role of snow on sea ice. *Geophysical Research Letters*, 35(16), 2008.
- X. Yang, A.-M. Blechschmidt, K. Bognar, A. McClure-Begley, S. Morris, I. Petropavlovskikh, A. Richter, H. Skov, K. Strong, D. W. Tarasick, T. Uttal, M. Vestenius, and X. Zhao. Pan-Arctic surface ozone: modelling vs. measurements. *Atmospheric Chemistry and Physics*, 20(24):15937–15967, 2020.
- S. Yasunaka, A. Murata, E. Watanabe, M. Chierici, A. Fransson, S. van Heuven, M. Hoppema, M. Ishii, T. Johannessen, N. Kosugi, S. K. Lauvset, J. T. Mathis, S. Nishino, A. M. Omar, A. Olsen, D. Sasano, T. Takahashi, and R. Wanninkhof. Mapping of the air–sea CO₂ flux in the Arctic Ocean and its adjacent seas: Basin-wide distribution and seasonal to interannual variability. *Polar Science*, 10(3):323–334, 2016.
- C. You, M. Tjernstr m, and A. Devasthale. Eulerian and Lagrangian views of warm and moist air intrusions into summer Arctic. *Atmospheric research*, 256:105586, 2021.
- C. You, M. Tjernstr m, and A. Devasthale. Warm and moist air intrusions into the winter Arctic: a Lagrangian view on the near-surface energy budgets. *Atmospheric Chemistry and Physics*, 22(12):8037–8057, 2022.
- P. J. Young, V. Naik, A. M. Fiore, A. Gaudel, J. Guo, M. Y. Lin, J. L. Neu, D. D. Parrish, H. E. Rieder, J. L. Schnell, S. Tilmes, O. Wild, L. Zhang, J. Ziemke, J. Brandt, A. Delcloo, R. M. Doherty, C. Geels, M. I. Hegglin, L. Hu, U. Im, R. Kumar, A. Luhar, L. Murray, D. Plummer, J. Rodriguez, A. Saiz-Lopez, M. G. Schultz, M. T. Woodhouse, and G. Zeng. Tropospheric Ozone Assessment Report: Assessment of global-scale model performance for global and regional ozone distributions, variability, and trends. *Elementa: Science of the Anthropocene*, 6, 2018.
- Y. Yu, A. Katsoyiannis, P. Bohlin-Nizzetto, E. Brorstr m-Lund n, J. Ma, Y. Zhao, Z. Wu, W. Tych, D. Mindham, E. Sverko, E. Barresi, H. Dryfhout-Clark, P. Fellin, and H. Hung. Polycyclic aromatic hydrocarbons not declining in Arctic air despite global emission reduction. *Environmental science & technology*, 53(5):2375–2382, 2019.
- D. Yumashev, C. Hope, K. Schaefer, K. Riemann-Campe, F. Iglesias-Suarez, E. Jafarov, E. J. Burke, P. J. Young, Y. Elshorbany, and G. Whiteman. Climate policy implications of nonlinear decline of Arctic land permafrost and other cryosphere elements. *Nature communications*, 10(1):1–11, 2019.
- R. A. Zaveri and L. K. Peters. A new lumped structure photochemical mechanism for large-scale applications. *Journal of Geophysical Research: Atmospheres*, 104(D23):30387–30415, 1999.
- K. Zeller. Wintertime ozone fluxes and profiles above a subalpine spruce–fir forest. *Journal of Applied Meteorology*, 39(1):92–101, 2000.
- H. J. Zemmellink, B. Delille, J.-L. Tison, E. J. Hintsa, L. Houghton, and J. W. H. Dacey. CO₂ deposition over the multi-year ice of the western Weddell Sea. *Geophysical Research Letters*, 33(13), 2006.
- J. Zhang, F. Xie, W. Tian, Y. Han, K. Zhang, Y. Qi, M. Chipperfield, W. Feng, J. Huang, and J. Shu. Influence of the Arctic Oscillation on the vertical distribution of wintertime ozone in the stratosphere and upper troposphere over the northern hemisphere. *Journal of Climate*, 30(8):2905–2919, 2017.
- Y. Zhang, D. J. Seidel, J.-C. Golaz, C. Deser, and R. A. Tomas. Climatological characteristics of Arctic and


-
- Antarctic surface-based inversions. *Journal of Climate*, 24(19):5167–5186, 2011.
- Y. Zhang, Z. Gao, D. Li, Y. Li, N. Zhang, X. Zhao, and J. Chen. On the computation of planetary boundary-layer height using the bulk Richardson number method. *Geoscientific Model Development*, 7(6):2599–2611, 2014.
- W. Zhao, G. Tang, H. Yu, Y. Yang, Y. Wang, L. Wang, J. An, W. Gao, B. Hu, M. Cheng, X. An, X. Li, and Y. Wang. Evolution of boundary layer ozone in Shijiazhuang, a suburban site on the North China Plain. *Journal of Environmental Sciences*, 83:152–160, 2019.
- B. Zheng, F. Chevallier, Y. Yin, P. Ciais, A. Fortems-Cheiney, M. N. Deeter, R. J. Parker, Y. Wang, H. M. Worden, and Y. Zhao. Global atmospheric carbon monoxide budget 2000–2017 inferred from multi-species atmospheric inversions. *Earth System Science Data*, 11(3):1411–1436, 2019.
- J. Zhou, L. Cao, and S. Li. Influence of the Background Nitrogen Oxides on the Tropospheric Ozone depletion events in the Arctic during springtime. *Atmosphere*, 11(4):344, 2020.
- S. Zilitinkevich and A. Baklanov. Calculation of the height of the stable boundary layer in practical applications. *Boundary-Layer Meteorology*, 105(3):389–409, 2002.

About the author

Johannes Gerardus Martinus (Sjoerd) Barten was born on April 20th, 1994 in Nijmegen, The Netherlands. He grew up in Wijchen, The Netherlands before starting to study BSc Soil, Water, Atmosphere at Wageningen University in 2013. After receiving his BSc degree in 2016 he went on to study MSc Earth and Environment at Wageningen University. During his studies he was an active member of study association Pyrus and student association W.S.R. Argo. Also, he worked for the Wageningen University as student assistant for the "Introduction Atmosphere" and "Meteorology & Climate" courses and as a hospitality host during the bi-annual Open Days.



His interest to pursue a PhD degree started during his MSc thesis which resulted in a peer-reviewed journal publication. The project "Multi-scale model analysis of Arctic surface-boundary layer exchange of climate-active trace gases and aerosol precursors", supervised by Laurens Ganzeveld and Gert-Jan Steeneveld, combined his interest for computer programming and atmospheric sciences. The results of his PhD project can be found in the PhD thesis you are now reading. During his PhD he was active as a PhD representative of the Meteorology & Air Quality group. Also, he supported teaching in the courses "Introduction Atmosphere", "Meteorology & Climate" and "Atmospheric Modelling" and (co-)supervised numerous BSc and MSc thesis projects.

Sjoerd lives together with his partner Sarah and  Lotje in Wageningen. In his free time he enjoys cooking, hiking and board games. From March 2023 onwards, he works at the Meteorology & Air Quality group at Wageningen University as a System Administrator & Data Steward.

Peer-reviewed journal publications

J. G. M. Barten, L. N. Ganzeveld, A. J. Visser, R. Jiménez, and M. C. Krol (2020). Evaluation of nitrogen oxides (NO_x) sources and sinks and ozone production in Colombia and surrounding areas. *Atmospheric Chemistry and Physics*, 20, 9441–9458. DOI: 10.5194/acp-20-9441-2020

J. G. M. Barten, L. N. Ganzeveld, G.-J. Steeneveld and M. C. Krol (2021). Role of oceanic ozone deposition in explaining temporal variability in surface ozone at High Arctic sites. *Atmospheric Chemistry and Physics*, 21, 10229–10248. DOI: 10.5194/acp-21-10229-2021

J. G. M. Barten, L. N. Ganzeveld, G.-J. Steeneveld, B. W. Blomquist, H. Angot, S. D. Archer, L. Bariteau, I. Beck, M. Boyer, P. von der Gathen, D. Helmig, D. Howard, J. Hueber, H.-W. Jacobi, T. Jokinen, T. Laurila, K. M. Posman, L. Quéléver, J. Schmale, M. D. Shupe and M. C. Krol (2023). Low ozone dry deposition rates to sea ice during the MOSAiC field campaign: Implications for the Arctic boundary layer ozone budget. *Elementa: Science of the Anthropocene* 11(1). DOI: 10.1525/elementa.2022.00086

Published datasets & model code

J. G. M. Barten and L. N. Ganzeveld (2022). Single-Column atmospheric chemistry and meteorological Model simulations for MOSAiC. *Zenodo*. <https://doi.org/10.5281/zenodo.6546452>

Awards

Mechanistic Ocean-Atmosphere exchange of trace gases in Polar-WRF-Chem: Implications for Arctic surface ozone. AGU Fall Meeting. 01/12/2020. Online. **44/50 Outstanding Student Poster Award**

Mechanistic Ocean-Atmosphere exchange of trace gases in Polar-WRF-Chem: Implications for Arctic tropospheric ozone. IGAC Virtual Conference. 12/09/2021. Online. **Awarded Best Early Career Poster presentation in PACES session.**

Process-based representation of Arctic oceanic ozone uptake: weaker sink than we think? BBOS symposium. 20/10/2021. Soesterberg, The Netherlands. **Honorable mention (oral).**

Acknowledgements

Writing these acknowledgements marks the end of an intense journey. A journey to discover and learn, but also a journey that was frustrating and difficult at parts. Thank you for reading this thesis, and thank you for being part of my journey in whatever way. I want to keep it short, so if you do not find yourself on this page don't worry. You being interested in this thesis means a lot to me.

Laurens, dank voor je professionele en menselijke aanpak. De werksfeer die je creëert voelt enorm fijn en veilig. Je had altijd tijd voor werkgerelateerde vragen of gewoon een goede bak koffie. Ook tijdens corona was je altijd bereid voor een korte of lange pauze bij een van de Wageningse koffietentjes. De discussies die we hier voerden, over werk, politiek of op persoonlijk vlak, hebben enorm bijgedragen aan mijn werkplezier tijdens mijn PhD. Het is bewonderingswaardig hoe je precies de goede balans weet te vinden tussen werk en prive tijdens dit project.

Gert-Jan, dank voor je kennis en geduld. Je wist altijd de juiste vragen tijdens onze wekelijkse meetings. Ik ben nog steeds onder de indruk hoe je altijd al wist wat de reviewers aan gingen kaarten voordat we een paper opstuurde voor review. Met veel plezier heb ik met jou samengewerkt in dit project, maar ook in het onderwijs bij Meteorology & Climate en Atmospheric Modelling.

Maarten, dank voor je kritische blik. Hoewel we, zeker in het begin van het project, weinig inhoudelijk contact hadden wist je met jouw feedback altijd de analyses naar een hoger niveau te tillen.


Thanks to everybody at MAQ for providing a very warm and welcoming environment. Thank you for the coffee breaks, cake, Biertjeklaas, uitjes, soccer and beach volleyball matches. I feel extremely privileged to have been working with you over the past years, and being able to continue working with you in the future.

Thanks to the entire MOSAiC community for your dedication and enthusiasm to tackle all the intricate problems of the current and future Arctic. Thank you for the fruitful meetings in

Potsdam, Boulder and online to discuss all your wonderful measurements and modelling results. Special thanks to the MOSAiC trace gas flux team for your experimental efforts and the detailed discussions on the flux measurements.

Shout-out to coffee company MAAS International BV.

Thanks to my friends from Wijchen and Wageningen for providing the much needed distraction from my PhD in the form of holidays, board game nights, pubquizzes and many more. Special thanks to Tom and Sam for your sincere kindness and being my paranymphs during the defence.

Mijn allergrootste dankbetuiging gaat uit naar mijn (schoon-)familie en in het specifiek naar Sarah. Het is een onmogelijke taak om alles wat je voor mij betekend hebt de afgelopen jaren op papier te zetten en dat ga ik ook niet proberen. Jouw sociale karakter is bewonderingswaardig en iets waar ik nog veel van moet leren. Jij wist vaak beter wat ik nodig had dan ikzelf, en was de enige die mijn eigenwijze karakter met regelmaat wist te overtroeven. Dank voor het vragen, luisteren en je onvoorwaardelijke steun. Dank voor je keuze om  Lotje te adopteren. Bij jullie vond rust, geborgenheid en nieuwe energie. Op naar het volgende avontuur samen.





*Netherlands Research School for the
Socio-Economic and Natural Sciences of the Environment*

D I P L O M A

for specialised PhD training

The Netherlands research school for the
Socio-Economic and Natural Sciences of the Environment
(SENSE) declares that

***Johannes Gerardus Martinus
Barten***

born on 20 April 1994, in Nijmegen, The Netherlands

has successfully fulfilled all requirements of the
educational PhD programme of SENSE.

Wageningen, 26 April 2024

Chair of the SENSE board



Prof. dr. Martin Wassen

The SENSE Director



Prof. Philipp Pattberg

The SENSE Research School has been accredited by the Royal Netherlands Academy of Arts and Sciences (KNAW)



K O N I N K L I J K E N E D E R L A N D S E
A K A D E M I E V A N W E T E N S C H A P P E N



The SENSE Research School declares that **Johannes Gerardus Martinus Barten** has successfully fulfilled all requirements of the educational PhD programme of SENSE with a work load of 41.8 EC, including the following activities:

SENSE PhD Courses

- o Environmental research in context (2019)
- o Research in context activity: 'Arctic climate change': A practical assignment for high school students' (2022)

Other PhD and Advanced MSc Courses

- o Communication with the Media and the General Public & Reviewing a scientific manuscript, Wageningen Graduate Schools (2019)
- o Winter School: Our connection with a fast-changing Arctic, Arctic Centre, University of Groningen (2023)

External training at a foreign research institute

- o Early Career Researcher Collaboration and Networking Capacity Building (Online), IGAC, University of Colorado, United States of America (2021)

Management and Didactic Skills Training

- o PhD representative MAQ department (2019-2021)
- o Co-organization of Early Career Session at International MOSAiC Science Conference/Workshop (2022) & of session "Dynamical and Chemical Controls on Arctic Atmospheric Composition and Aerosols" at 2nd MOSAiC Science Conference (2023)
- o Supervising four BSc student (2020-2021) and two MSc students (2021-2022) with thesis
- o Teaching in the BSc courses 'Meteorology and climate' (2019) and 'Introduction Atmosphere' (2019); and the MSc course 'Atmospheric modelling (2020-2021)'

Oral Presentations

- o *Ocean-atmosphere exchange of CO₂, CH₄, O₃, DMS: From separate emission/deposition schemes to process-based exchange routines in (Polar-)WRF-Chem.* Arctic chemical-aerosol modelling workshop, 7-8 March 2019, Paris, France
- o *Process-based representation of Arctic oceanic ozone uptake: weaker sink than we think?* Process-based representation of Arctic oceanic ozone uptake: weaker sink than we think?, 20-22 October 2021, Soesterberg, The Netherlands
- o *Ozone flux observations and its effect on atmospheric boundary layer ozone: A 1-D model analysis.* International MOSAiC Science Conference/Workshop, 25-29 April 2022, Potsdam, Germany
- o *Polar-WRF-Chem simulations of the April warm air intrusion event.* 2nd MOSAiC Science Conference, 13-17 February 2023, Boulder, United States of America

SENSE coordinator PhD education

Dr. ir. Peter Vermeulen

This research received funding from the Nederlandse Organisatie voor Wetenschappelijk Onderzoek (NWO) as part of the Nederlands Polair Programma (NPP) under the project name "Multi-scale model analysis of Arctic surface-boundary layer exchange of climate-active trace gases and aerosol precursors" with grant no. 866.18.04.

Data used in this thesis was produced as part of the international Multidisciplinary drifting Observatory for the Study of the Arctic Climate (MOSAiC) with the tag MOSAiC20192020.

Financial support from Wageningen University & Research for printing this thesis is gratefully acknowledged.

Cover design by Johannes G. M. Barten using Midjourney AI

Printed by ProefschriftMaken on FSC-certified paper

